Nonlinear Optical Studies of Natural and Artificial Light Harvesting Antennae

Jordan Maxwell Womick

A dissertation submitted to the faculty of the University of North Carolina at Chapel Hill in partial fulfillment of the requirements for the degree of Doctor of Philosophy in the Department of Chemistry

Chapel Hill
2012

Approved by:

Dr. Andrew Moran

Dr. James Cahoon

Dr. Chris Fecko

Dr. Yosuke Kanai

Dr. Amy Oldenburg

ABSTRACT

Jordan Maxwell Womick: Nonlinear Optical Studies of Natural and Artificial Light Harvesting Antennae
(Under the direction of Andrew Moran)

This dissertation investigates the influence of nuclear motion on energy transfer processes in natural and artificial light harvesting antennae. In natural systems, light harvesting antennae increase the efficiency of photosynthesis by absorbing light and transferring electronic excitations to the reaction center. These antennae are highly optimized through evolution, and it is estimated that energy transfers to the reaction center through these structures with exceptional efficiency, motivating their investigation. Light harvesting proteins derived from cyanobacteria and red algae enable the study of the simplest possible energy transfer network: pigment "dimers" composed of one donor and one acceptor. Double walled cylindrical molecular aggregates, which are inspired by the chlorosome of green sulfur bacteria, are used as models for the investigation of many-body coherent electronic relaxation dynamics.

Evidence of electronic relaxation is gained through pulsed laser experiments. Many processes like energy transfer, solvation, and the dephasing of coherence take place on the tens to hundreds of femtosecond timescale. Femtosecond time resolved experiments investigate the initial events of these processes using a variety of advanced spectroscopic methods. Additional insight into electronic relaxation dynamics is gained by varying aspects

of the radiation fields (e.g., frequency, electric field polarizations). In all cases, the interpretation of experimental data is aided by comparison to theoretical calculations.

Chapters 1 – 3 introduce the systems, theory, and experimental methods used in this dissertation. Chapters 4 – 8 present a series of studies on light harvesting antennae from cyanobacteria and red algae. Advanced spectroscopies in chapters 4 – 7 lead to a unified treatment of electronic and nuclear relaxation dynamics using a vibronic exciton model originally derived for the treatment of organic semiconductor crystals. Chapter 8 studies the complex pigment network of the highest energy absorber in the light harvesting complex of red algae. Chapters 9 – 10 investigate the presence and origin of an elusive coherent relaxation process (i.e., coherence transfer) in cylindrical molecular aggregates.

To my parents, Jerry and Melisa Womick, and to my wife, Stephanie Womick, for their constant support and wisdom.

ACKNOWLEDGEMENTS

I wish to thank my advisor Dr. Andrew Moran for his leadership and patience in my pursuit of science. I also thank my friends who are past and current members of the Moran group; especially Stephen Miller, Brant West, Haoming Liu, Paul Giokas, and Brian Molesky.

TABLE OF CONTENTS

LIST OF TABLES

LIST OF FIGURES

LIST OF SYMBOLS

a	lowering operator
$a^{\dagger}$	raising operator
B	lowering operator
$B^{\dagger}$	raising operator
c	speed of light in vacuum
$c^{(N)}$	eigenvector coefficient of order N (Section 2.6.2)
c	eigenvector coefficient (Section 2.2.1)
C	eigenvector coefficient
$C(\omega)$	temperature independent spectral density
C^{OD}	overdamped spectral density
C^{UD}	underdamped spectral density
d	dimensionless displacement
D	dipole strength
D	doorway function (Chapter 4)
E	energy gap
$\vec{E}$	electric field vector
f	auxiliary line broadening function
f_D	fluorescence spectrum (Chapter 8)
F	Franck-condon factor (Chapter 4)
$\mathbf{F}$	derivative coupling vector
g	line broadening function
G	Green function
G	superoperator for Green function
$\hbar$	Dirac constant
H	Hamiltonian
$H^{(i)}$	Hamiltonian of order i
H_0	system Hamiltonian

H_B	bath Hamiltonian
H_{SB}	system-bath Hamiltonian
I	intensity
I	propagation function (Chapter 10)
J	dipole-dipole Coulombic coupling
J	term in first order response function (Chapter 2)
$\mathbf{k}$	wavevector
k_B	Boltzmann constant
k_v	vibrational cooling rate
K	rate constant
K	propagation function with coherence transfer (Chapter 10)
K''	spectral density of secondary bath coordinate
m_α	mass of secondary bath coordinate
M	solvation correlation function
M_j	mass of primary bath coordinate
n	real part of refractive index
p_α	momentum of seconday bath coordinate
P	probability
$P^{(N)}$	polarization at order N
P_j	momentum of primary bath coordinate
PR	participation ratio
q	bath operator
q_α	secondary bath coordinate
Q_j	primary bath coordinate
r	anisotropy
R	term in second order response function
R	displacement from equilibrium (Chapter 2)
S	Huang-Rhys factor
S	third order experimental signal

$S^{(N)}$	response function at order N
t	field-matter interaction time interval
T	delay between centers second and third pulses a third order experiment
T	group delay
$\hat{T}$	nuclear kinetic energy operator
U	time evolution operator
V	perturbation
$\mathbb{V}$	superoperator for commutators
$\vec{V}$	material dipole vector
w	pulse bandwidth
W	window function (Chapter 4)
W	overlap between fluorescence and absorbance spectra (Chapter 8)
Z	vibrational coupling term (Chapter 4)
γ	friction between primary and secondary bath coordinate
Γ	damping constant
δ	delta function
Δ	dimensionless displacement
ε	energy gap
ε_A	absorption spectrum (Chapter 8)
η	correlation constant
η	constant in Förster rate formula
θ	Heaviside step function
θ	angle
κ	orientation factor
κ	coherence transfer rate (Chapter 10)
λ	wavelength
λ	reorganization energy
λ	perturbation strength (Chapter 2)
Λ	inverse of nuclear timescale
Λ	damping constant (Chapter 10)

$\hat{\Lambda}$	nonadiabatic coupling operator
μ	transition dipole
$\xi(t)$	electric field envelope
ξ	eigenvector coefficient for double excition manifold
ξ	lineshape function (Chapter 10)
ρ_{mk}	density matrix element at index m and k
$\hat{\rho}$	density operator (Chapter 3)
σ_{abs}	linear absorption spectrum
σ_f	fluorescence spectrum
τ	delay between centers of first two pulses in a third order experiment
τ	time constant (Chapter 8)
$\bar{\tau}$	center of pulse
ϕ	basis function
ϕ	eigenvector coefficient for single excition manifold
Φ	lifetime broadening
χ	nuclear wavefunction
χ	collective coherence transfer damping constant (Chapter 10)
ψ	wavefunction
Ψ	wavefunction
ω	angular frequency
ω^0	thermally averaged energy gap
$\bar{\omega}_\alpha$	frequency of secondary bath coordinate
Ω	bath coordinate in exciton basis
$\bar{\Omega}_j$	frequency of primary bath coordinate

CHAPTER 1. INTRODUCTION

1.1. MOTIVATION

Light-induced energy transport is prevalent throughout nature[1] and in synthetic systems[2]. Radiative dynamics govern photosynthesis[3], DNA photoprotection[4], photovoltaic devices[5-8], and human vision[9,10]. It is a longstanding goal of physical chemistry to draw connections between these processes and elementary motions of electrons and nuclei. However, the elucidation of mechanisms is challenged by the complexity of condensed phases at ambient conditions. Thermal fluctuations give rise to broad distributions in molecular geometries whose motions span vast ranges of timescales. Thus, realistic models for energy transport in condensed phases must ultimately treat the behaviors of ensembles. Pulsed laser spectroscopies synchronize energy transfer events for all members in an ensemble then monitor the subsequent relaxation dynamics. In such experiments, it is essential to have laser pulses with durations short compared to the process of interest. Advances in laser technology have now pushed the time resolution limit to 10's of femtoseconds (10^{-15} seconds), thereby making even the fastest energy transport dynamics accessible[11-13].

This dissertation investigates the influence of nuclear motion on energy transfer processes in natural and artificial light harvesting antennae. Light harvesting proteins derived from cyanobacteria and red algae enable the study of the simplest possible energy transfer network: pigment "dimers" composed of one donor and one acceptor. Double walled cylindrical molecular aggregates, which are inspired by the chlorosome of green

sulfur bacteria, exemplify the beauty and power of self-assembly. Also, the quasi-periodic structures of these aggregates compete against the disorder imposed by thermal fluctuations. Crystal structures of these light harvesting systems are leveraged as a framework for the models employed in this work. In all cases, the interpretation of experimental data is aided by comparison to theoretical calculations.

Of primary interest are the dynamics of electronic states known as Frenkel excitons. A Frenkel exciton involves the "sharing" or "delocalization" of an electronic excitation between two or more molecules. Such delocalization is quantum mechanical in nature, but parallels the vibrational modes of classical coupled oscillators[14]. Vibrational amplitude generally spreads among classical oscillators when they possess similar force constants and/or when the mechanical coupling between oscillators is large. By analogy, excitons readily delocalize in molecular aggregates when they share similar energy gaps and/or when the intermolecular Coulombic coupling is large. It will be explained later that fluctuations complicate this simple comparison. Nonetheless this analogy is a useful starting point. In fact, recent literature refers to Frenkel excitons as "electronic modes" and vibrational states and "vibrational excitons"[2,15].

Evidence of transitions between exciton states is gained through pulsed laser experiments. These measurements initiate energy transfer dynamics using pulses of electromagnetic radiation. A simplified example of such an experiment follows. First, a pulse of light interacts with a system to promote population into an excited state. The excited state population evolves in time according to the forces within the system until it is interrogated with a second laser pulse. This "probe" pulse effectively records a snapshot of the excited state population through quasi-instantaneous stimulation of radiation, the signal field, from

the system. Changes in the excited state population affect the waveform of the signal field. A plot of signal amplitude versus time is produced by detecting the signal and experimentally controlling the delay between the first and second pulses. Additional insight into the dynamics of the system is gained by varying aspects of the radiation fields (e.g., color, electric field polarizations). Studies in this dissertation use a variety of advanced spectroscopies.

1.2. ELECTRONIC ENERGY TRANSFER

Electronic energy transfer is a process by which an electronic excitation moves from a donor molecule to an acceptor molecule. The quantum states of the donor and acceptor are spatially separated in this limiting view of the transition. Energy transfer occurs most rapidly when the (average) acceptor molecule's energy gap is smaller than that of the donor's. This rule, known as detailed balance, ensures that equilibrium is ultimately established[16]. The rate of energy transfer generally increases with the strength of Coulombic coupling between the donor and acceptor. In addition, energy conservation requires that fluctuations at the two sites must occasionally bring the energy gaps of the donor and acceptor into degeneracy. For molecules in close proximity the time scale of the transition ranges from 100s of femtoseconds to 100s of picoseconds (10^{-12} seconds).

An understanding of energy transfer in light harvesting proteins requires careful examination of the interplay between intermolecular Coulombic coupling and thermal fluctuations of the pigments. The physics behind this competition is made transparent by considering two limiting cases. In strongly coupled systems, an excitation behaves coherently, and the excitation will move from donor to acceptor and back again in a wavelike fashion. Oscillations occur indefinitely when there are no fluctuating forces present (i.e.,

Rabi oscillations). This fully coherent limit of energy transfer is more naturally formulated in a delocalized basis of Frenkel excitons states, which are analogous to classical normal modes. In the exciton picture, the excitation never localizes on a particular molecule so, strictly speaking, energy is never transferred. By contrast, in the weak coupling limit, the environment induces fluctuations in the energy levels of the donor and acceptor, which are large compared to the size of the Coulombic coupling. The excitation localizes onto a particular molecule because random motion in the surroundings is a source of quantum mechanical decoherence. From the classical perspective, the weak coupling limit is analogous to a pair of classical oscillators for which the difference in force constants is large compared to the mechanical coupling, which restricts concerted motion.

Energy transfer in many light harvesting proteins occurs in a regime that is intermediate between the weak and strong coupling limits. In this regime, thermal fluctuations compete with intermolecular Coulombic coupling to localize electronic excitations on a time scale that is comparable to the non-radiative transition. As a result, the trajectory of the excitation possesses a (partially) wavelike character for a short amount of time (e.g., hundreds of femtoseconds). Such partially coherent energy transfer has been detected in proteins isolated from green sulfur bacteria and cryptophyte algae[17,18]. It is suggested that correlated thermal fluctuations at the donor and acceptor sites are the key factor making coherent energy transfer possible[19-21]. In a sense, these spatially correlated fluctuations promote (temporary) exciton delocalization by making the environment appear less noisy than it actually is. Unambiguous evidence of correlated energy level fluctuations is challenged by the lack of a direct spectroscopic signature.

1.3. LIGHT HARVESTING IN PHOTOSYNTHESIS

Photosynthetic organisms produce chemical fuel by harnessing solar energy. It is estimated that a chlorophyll pigment located in photosynthetic reaction centers absorbs 10 photons per second[3]. Organisms have evolved exquisite light harvesting architectures to survive under such low light levels. To increase the light collection efficiency, pigment-protein complexes, called light harvesting antennae, absorb light and transfer electronic excitations to the reaction center. It is estimated that the energy transfer of solar energy to the reaction center is exceptionally efficient, which motivates their investigation[22].

Bilin pigments are a class of molecules responsible for light harvesting in cyanobacteria and red algae[3,23-25]. Bilins are unique among light harvesting pigments in that their absorbance spectra span much of the visible spectral range. The molecules are composed of four pyrrole rings linked by conjugated π orbitals. Bilins tune their absorbance spectra by varying their effective double-bond conjugation lengths. The lowest energy light absorber, phycocyanobilin, possesses three conjugated linkers between rings; phycoerythrobilin has two; the highest energy absorber, phycourobilin, has only one conjugate linker. As shown in chapter 5, the linear structure of bilins allows for "kinks" which fine tune their energy gaps. Chlorophyll molecules are also found in many light harvesting antennae and have a structure similar to bilins except they are cyclic with a metal atom bound at the center. Chlorophyll molecules absorb light primarily at blue and red frequencies and show little variation in their absorbance spectra because of their rigid structures[3].

Phycobilisome light harvesting antennae are found in cyanobacteria and red algae. The phycobilisome is usually composed of three proteins stacked above the photosynthetic reaction center. As shown in Figure 1, allophycocyanin (APC) is closest to the reaction

center, C-phycocyanin (CPC) is in the middle of the antenna complex, and R-phycoerythrin (RPE) is at the top. The stacking arrangement of the phycobilisome promotes energy funneling to the reaction center. Each protein structure possesses a three-fold symmetry axis[26-28]. APC and CPC both contain only phycocyanobilin molecules and are structurally very similar. However, CPC's absorption spectra is blue shifted from that of APC's and it possesses extra phycocyanobilin molecules at its periphery. The similarity between APC and CPC makes them good models for comparison.

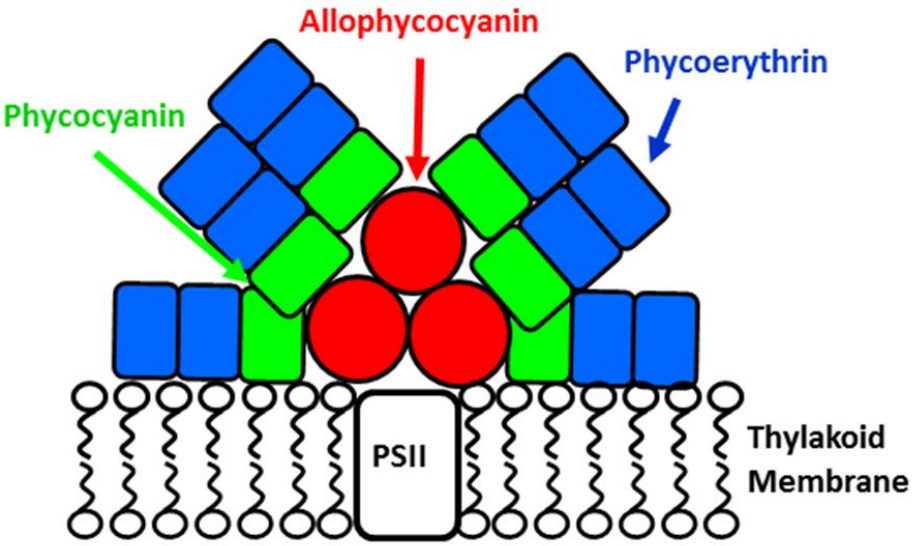

Figure 1.1: Phycobilisome antenna complex of cyanobacteria and red algae shown with reaction center. Excitations are funneled from the top of the antenna to the reaction center in the thylakoid membrane.

The fastest electronic energy transfer in both APC and CPC occurs between two closely spaced phycocyanobilin pigments (Figure 2). This simplest of donor-acceptor systems is considered at length in this dissertation. Even though the pigments are identical, differences in conformation and environment produce two distinct states. Work by Beck and coworkers found that in APC much of the population in the higher energy exciton state

transfers to the lowest energy state in approximately 100 fs[29]. However, in CPC energy transfer occurs in approximately a picosecond[24,25]. These results are surprising because of the similar geometries and electronic couplings of the two pigments in both APC and CPC. Furthermore, the energy gap between these two pigments in CPC is less than half of that in APC, so that the conventional models (e.g., Förster and Redfield) predict faster electronic population transfer in CPC (i.e., in the wrong system). My research aims to uncover the origin of this 10-fold difference in energy transfer rates.

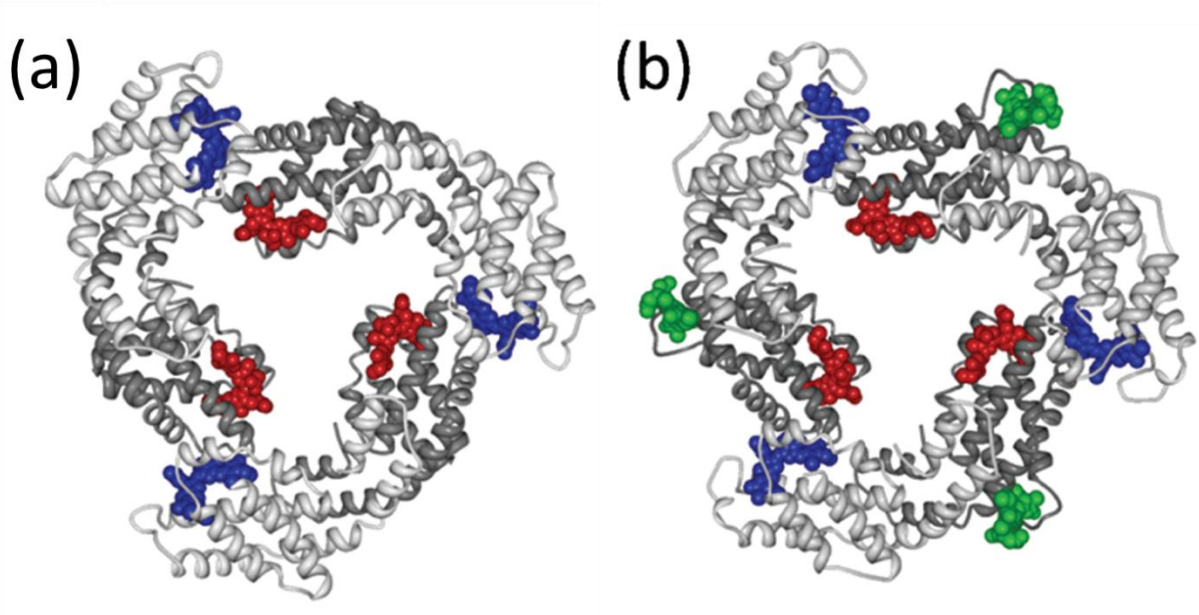

Figure 1.2: X-ray crystal structures of (a) allophycocyanin and (b) C-phycocyanin. Each protein possesses a three-fold axis of symmetry. The color of each pigment represents a unique binding site in each symmetric subunit. The pigment dimers considered in the text occur between nearest neighbor red and blue pigments.e binding site in each symmetric subunit. The pigment dimers considered in the text occur between nearest neighbor red and blue pigments.

1.4. LIGHT HARVESTING IN BIOLOGICALLY INSPIRED MOLECULAR AGGREGATES

Biologically inspired molecular aggregates are used as models for the investigation of coherent electronic relaxation dynamics. For example, recent experiments have detected

coherent energy transfer in complex biological photosystems[17-19,30]. Theoretical calculations suggest that coherent energy transfer is responsible for up to 20% of the transport efficiency in the Fenna-Matthews-Olson complex in green sulfur bacteria[20]. It is therefore interesting to look for such non-trivial quantum behavior elsewhere in nature. The molecular aggregates studied here are chosen with inspiration from the light harvesting chlorosome of green bacteria. The chlorosome of green bacteria and our artificial system both possess textbook excitonic structure (e.g., Davydov splittings)[1,31].

The aggregate is composed of "C8O3" monomers which self-assemble in solution to form nanotubes (Figure 3). A cross-section of the tube reveals a double-walled cylindrical structure where each "wall" is composed of tightly packed monomers (Figure 3b). The structure of the aggregate loosely resembles that of the light harvesting chlorosome of green sulfur bacteria[32]. The chlorosome contains thousands of tightly packed bacteriochlorophyll molecules. The large shift of the energy levels of the aggregate from those of the monomer and the narrow distribution of energy levels indicate that exciton states spread (i.e., delocalize) over many monomers (Figure 3a). Experimental control of the electronic structure is achieved by varying the solvent conditions. For example, the spacing between walls can be tuned in mixtures of water and alcohol while preserving the overall structure of the aggregate[33].

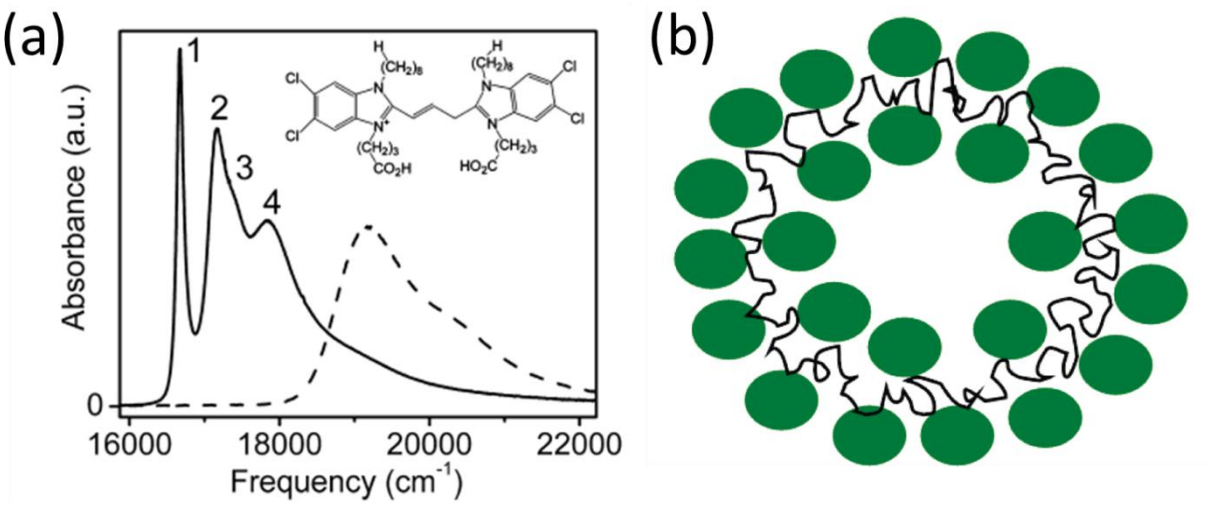

Figure 1.3: (a) Absorption spectrum of monomer (dashed) and C8O3 cylindrical molecular aggregate (solid). The inset shows the structure of monomer building block, 5,5',6,6'-tetrachlorobenzimidacarbocyanine (C8O3). (b) Cross section of the double-walled cylindrical structure of the aggregate in which the monomer core is represented by green circles and the hydrophobic chains (black lines) are bundled between cylinder walls.

My research concentrates on two aspects of coherent dynamics in the molecular aggregate. The first study in chapter 9 obtains evidence of spatially correlated thermal motion in the aggregate. The importance of these fluctuations for coherent, wavelike behavior is discussed above. The slow dephasing rates in the C8O3 aggregate, as evidenced by its narrow spectroscopic line widths, make it a good candidate for uncovering the physics behind these fluctuations. The second study in chapter 10 investigates a non-radiative transition known as "coherence transfer" within the aggregate. From the quantum mechanical perspective, coherence transfer is the process by which one superposition state transitions into another without loss of coherence. In the experiment, a pair of laser pulses initiates oscillations in the charge distribution within the aggregate. Coherence transfer essentially transforms the frequency and "shape" of this electronic mode (i.e., electronic wavepacket). Coherence transfer is difficult to detect in electronic spectroscopy because the transition is

often masked by stronger incoherent signals. The study in chapter 10 uses a specialized laser pulse sequence to suppress such undesired incoherent signals. Overall, the investigation of C8O3 informs the mechanism of coherent energy transfer.

1.5. NONLINEAR OPTICAL SPECTROSCOPY

Femtosecond time resolved experiments investigate the initial events of a variety of electronic relaxation processes. Many processes like energy transfer, solvation, and the dephasing of wavelike coherence take place on the tens to hundreds of femtosecond timescale[34]. Femtosecond pulsed laser spectroscopies are a valuable experimental tool for investigation of these dynamics. Pulses in the femtosecond regime were produced in 1975[34], and lasers became stable for practical use with the introduction of the self-modelocked laser in 1990[11]. Today, commercially available titanium sapphire laser systems can reliably produce sub-100 fs pulses with millijoule energies. Optical parametric amplifiers (OPAs) became popular to expand the tuning range and bandwidth of lasers to generate femtosecond pulses in the visible region of the spectrum with significant power (Figure 4b)[12,13,35]. Similar effects are produced using optical parametric oscillators and gas filled hollow core fibers[36,37]. Compression down to only several optical cycles from these amplifiers occurred in the late 1980s[38].

The pulsed laser experiments used in this dissertation initiate and follow energy transfer dynamics using three pulses of electromagnetic radiation. The first pulse marks the beginning of the light absorption process by creating a quantum mechanical superposition between the ground and excited state. A second pulse completes the light absorption process by forcing the system to populate either its ground or excited state. These populations evolve until a third pulse returns the system to an optical coherence, which radiates the electric field

measured in the experiment. The first two pulses are often termed the pump pulse and the third pulse is the probe. Scanning the delay between pump and probe provides information on population dynamics (e.g., electronic energy transfer). Controlling aspects of the input pulses (e.g., color, electric field polarizations) expose details in transport mechanisms.

To obtain additional information on which initial states were involved in the experiment, two dimensional photon echo spectroscopy is used below. This sophisticated experiment correlates the absorbing and emitting states using a Fourier transform technique. This two dimensional experiment is vitally important in uncovering relaxation mechanisms when the processes occur on the sub-picosecond time scale. A full description of this technique is given in later chapters.

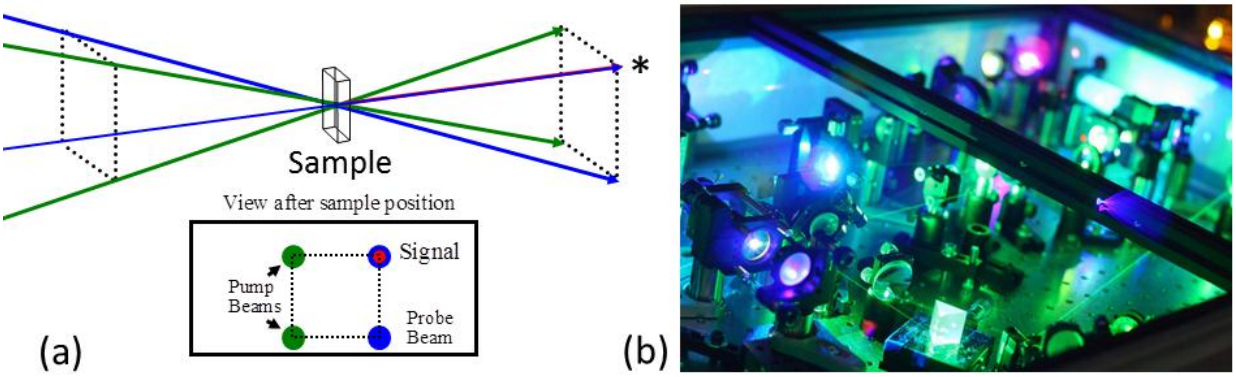

Figure 1.4: (a) Three laser pulses are incident on the sample with a fourth (in red) used as a reference beam in a transient grating experiment. A noncollinear geometry produces a signal in a background free direction. The position of the detector is marked with an asterisk. (b) Experiments require a variety of home-built equipment. An optical parametric amplifier with prism compressor is shown.

Signal to noise ratios are enhanced using spectral interferometry. Typically a signal pulse is mixed with a much stronger reference pulse and the two beams are dispersed onto an

array detector. The resulting interferogram contains an oscillating pattern due to constructive and destructive interferences. The amplitude of the signal is boosted because it scales linearly with the reference field. In addition, the pattern of interference fringes yields the phase of the signal waveform. Maintaining the phase stability needed for interferometry is difficult because of the short wavelength of visible light. Passively phase stabilized diffractive optic based interferometers introduced in 1998 offered an alternative to actively stabilized setups employing multiple interferometers[39-41]. The noncollinear geometry of pulses in the diffractive optic setup produces a signal that radiates in a background free direction (Figure 4a)[42]. The extremely high sensitivity afforded by interferometry and background free signal detection allows study of photosensitive samples, which normally operate under the low flux of sunlight.

In general, experiments are tailored to the information sought. Even though many of the components just described are now available commercially, most of the optical components in this dissertation are home-built to allow for flexibility in designing experiments. Chapter 3 provides an overview of the techniques and hardware used in experiments while details for each system are outlined in its respective chapter.

1.6. ORGANIZATION OF DISSERTATION

Chapter 2 provides a background on the theory used in later chapters. Chapter 3 describes the experimental setup and methods. Initial time resolved spectroscopic measurements are performed on APC in chapter 4 and CPC in chapter 5. Chapter 6 examines the possibility that correlated energy level fluctuations give rise to distinct behaviors in APC and CPC. Building on this work, chapter 7 investigates the influence of intramolecular nuclear motions on energy transfer using a vibronic exciton model originally derived for the

treatment of organic semiconductor crystals[43-46]. Chapter 8 studies the complex pigment network of the highest energy absorber in the phycobilisome, R-phycoerythrin. Chapter 9 probes quantum beating dynamics in cylindrical molecular aggregates. Chapter 10 develops a new pulse sequence with the goal of detecting an elusive coherent relaxation process (e.g., coherence transfer) in the same molecular aggregates.

REFERENCES

(1) van Amerongen, H.; Valkunas, L.; van Grondelle, R. *Photosynthetic Excitons*; World Scientific: Singapore, 2000.

(2) Abramavicius, D.; Palmieri, B.; Voronine, D. V.; Sanda, F.; Mukamel, S. *Chem. Rev.* 2009, *109*, 2350.

(3) Blankenship, R. E. *Molecular Mechanisms of Photosynthesis*; Blackwell Science Ltd.: Oxford, 2002.

(4) Middleton, C. T.; de La Harpe, K.; Su, C.; Law, Y. K.; Crespo-Hernandez, C. E.; Kohler, B. *Annu. Rev. Phys. Chem.* 2009, *60*, 217.

(5) Anderson, N. A.; Lian, T. *Annu. Rev. Phys. Chem.* 2005, *56*, 491.

(6) Haque, S. A.; Tachibana, Y.; Willis, R. L.; Moser, J. E.; Gratzel, M.; Klug, D. R.; Durrant, J. R. *J. phys. Chem. B* 2000, *104*, 538.

(7) Nozik, A. J. *Annu. Rev. Phys. Chem.* 2001, *52*, 193.

(8) Pandey, A.; Guyot-Sionnest, P. *J. Phys. Chem. Lett.* 2010, *1*, 45.

(9) Yoshizawa, T.; Wald, G. *Nature* 1963, *197*, 1279.

(10) Birge, R. *Ann. Rev. Biophys. Bioeng.* 1981, *10*, 315.

(11) Backus, S.; Durfee, C. G. I.; Murnane, M. M.; Kapteyn, H. C. *Rev. Sci. Instrum.* 1998, *69*, 1207.

(12) Riedle, E.; Beutter, M.; Lochbrunner, S.; Piel, J.; Schenkl, S.; Spörlein, S.; Zinth, W. *Appl. Phys. B* 2000, *71*, 457.

(13) Baltuska, A.; Fuji, T.; Kobayashi, T. *Optics Letters* 2002, *27*, 306.

(14) Taylor, J. R. *Classical Mechanics*; University Science Books: Sausalito, 2005.

(15) Tretiak, S.; Mukamel, S. *Chem. Rev.* 2002, *102*, 3171.

(16) Nitzan, A. *Chemical Dynamics in Condensed Phases*; Oxford University Press: New York, 2006.

(17) Engel, G. S.; Calhoun, T. R.; Read, E. L.; Ahn, T. K.; Mancal, T.; Cheng, Y. C.; Blankenship, R. E.; Fleming, G. R. *Nature* 2007, *446*, 782.

(18) Collini, E.; Wong, C. Y.; Wilk, K. E.; Curmi, P. M.; Brumer, P.; Scholes, G. D. *Nature* 2010, *463*, 644.

(19) Lee, H.; Cheng, Y.-C.; Fleming, G. R. *Science* 2007, *316*, 1462.

(20) Rebentrost, P.; Mohseni, M.; Aspuru-Guzik, A. *J. Phys. Chem B* 2009, *113*, 9942.

(21) Panitchayangkoon, G.; Hayes, D.; Fransted, K. A.; Caram, J. R.; Harel, E.; Wen, J.; Blankenship, R. E.; Engel, G. S. *PNAS* 2010, *107*, 12766.

(22) Wraight, C. A.; Clayton, R. K. *Biochim. Biophys. Acta* 1973, *333*, 246.

(23) MacColl, R. *Biochim. Biophys. Acta* 2004, *1657*, 73.

(24) Debreczeny, M. P.; Sauer, K.; Zhou, J.; Bryant, D. A. *J. Phys. Chem.* 1995, *99*, 8412.

(25) Debreczeny, M. P.; Sauer, K.; Zhou, J.; Bryant, D. A. *J. Phys. Chem.* 1995, *99*, 8420.

(26) Brejc, K.; Ficner, R.; Huber, R.; Steinbacher, S. *J. Mol. Biol.* 1995, *249*, 424.

(27) Wang, X.-Q.; Li, L.-N.; Chang, W.-R.; Zhang, J.-P.; Gui, L.-L.; Guo, B.-J.; Liang, D.-C. *Acta Cryst.* 2001, *D57*, 784.

(28) Ritter, S.; Hiller, R. G.; Wrench, P. M.; Welte, W.; Diederichs, K. *J. Struct. Biol.* 1999, *126*, 86.

(29) Edington, M. D.; Riter, R. E.; Beck, W. F. *J. Phys. Chem.* 1995, *99*, 15699.

(30) Calhoun, T. R.; Ginsberg, N. S.; Schlau-Cohen, G. S.; Cheng, Y.-C.; Ballottari, M.; Bassi, R.; Fleming, G. R. *J. Phys. Chem. B* 2009, *xx*, dd.

(31) Davydov, A. S. *J. Exp. Theor. Phys. USSR* 1948, *18*, 210.

(32) Egawa, A.; Fujiwara, T.; Mizoguchi, T.; Kakitani, Y.; Koyama, Y.; Akutsu, H. *PNAS* 2007, *104*, 790.

(33) von Berlepsch, H.; Kirstein, S.; Böttcher, C. *Langmuir* 2002, *18*, 7699.

(34) Fleming, G. R. *Chemical Applications of Ultrafast Spectroscopy*; University Press: New York, 1986.

(35) Cerullo, G.; De Silvestri, S. *Rev. Sci. Instrum.* 2003, *74*, 1.

(36) Tang, C. L.; Bosenberg, W. R.; Ukachi, T.; Lane, R. J.; Cheng, L. K. *Proc. IEEE* 1992, *80*, 365.

(37) Durfee, C. G. I.; Backus, S.; Murnane, M. M.; Kapteyn, H. C. *Opt. Lett.* 1997, *22*.

(38) Fork, R. L.; Brito Cruz, C. H.; Becker, P. C.; Shank, C. V. *Opt. Lett.* 1987, *12*, 483.

(39) Maznev, A. A.; Nelson, K. A.; Rogers, J. A. *Opt. Lett.* 1998, *23*, 1319.

(40) Goodno, G. D.; Dadusc, G.; Miller, R. J. D. *J. Opt. Soc. Am. B* 1998, *15*, 1791.

(41) Scherer, N. F.; Carlson, R. J.; Matro, A.; Du, M.; Ruggiero, A. J.; Romero-Rochin, V.; Cina, J. A.; Fleming, G. R.; Rice, S. A. *J. Chem. Phys.* 1991, *95*, 1487.

(42) Hybl, J. D.; Albrecht Ferro, A.; Jonas, D. M. *J. Chem. Phys.* 2001, *115*, 6606.

(43) Philpott, M. R. *J. Chem. Phys.* 1967, *47*, 4437.

(44) Philpott, M. R. *J. Chem. Phys.* 1971, *55*, 2039.

(45) West, B. A.; Womick, J. W.; McNeil, L. E.; Tan, K. J.; Moran, A. M. *J. Phys. Chem. B* 2011, *1*, 5157.

(46) West, B. A.; Womick, J. W.; McNeil, L. E.; Tan, K. J.; Moran, A. M. *J. Phys. Chem. C* 2010, *114*, 10580.

CHAPTER 2. THEORY OF DYNAMCIS AND SPECTROSCOPY IN CONDENSED PHASES

2.1. INTRODUCTION

Condensed phase theory must be able to relate the dynamics of the system of interest to the signals acquired during experiments. Descriptions of condensed phase systems are complicated by the abundance of thermal fluctuations. Coulombic couplings between molecules tend to delocalize excitations while thermal fluctuations disrupt phase relationships between molecules and have a localizing effect. For systems studied in this dissertation, the Coulombic coupling and the fluctuation strength are of comparable magnitude; consequently, the electronic structure cannot be assumed from the beginning. For all cases, solutions are sought in a reduced description with only a few states of the system being explicitly considered and the effect of other states enter through time-dependent fluctuations. Fluctuations originate from the random motions of the bath which are dark states and not directly experimentally measured. However, spectroscopy is sensitive to the modulation of the energy gap of the system through system-bath interactions. The system-bath interaction, along with the electronic and nuclear states of the system itself, governs electronic relaxation. Time-resolved spectroscopy monitors the observables of the system which are then equated to specific dynamics (e.g., energy transfer) as well as their microscopic (e.g., electronic and nuclear) origin.

Experimental observables come from the electric field radiated by the induced polarization. Linear spectroscopy refers to events that are linearly dependent on the applied

electric field strength (i.e., absorption). Nonlinear effects require more electric field interactions. The polarization is expanded in orders of the electric field below

$$\boldsymbol{P} = \chi^{(1)}\boldsymbol{E} + \chi^{(2)}\boldsymbol{E}^2 + \chi^{(3)}\boldsymbol{E}^3 + \cdots \tag{2.1}$$

where $\chi^{(N)}$ is the Nth-order susceptibility which contains information on the response of the material (e.g., energy transfer, resonant frequencies). The first order susceptibility governs linear absorption. The second order susceptibility describes effects such as second harmonic generation and the third term describes fluorescence, Raman, and pump-probe techniques. Recasting this susceptibility in terms of experimental observables will be discussed later in this chapter. Experiments use the electric fields to isolate parts of interest of the susceptibility. Conclusions are drawn from comparing experimental data to theoretical models.

This chapter provides a background of the theory used in chapters 4 – 10. The first section (section 2.1) explains the macroscopic polarization detected in experiments with diagrammatic representations of the optical response function. Section 2.2 describes the treatment of electronic and nuclear structure of the system. Section 2.3 presents a Frenkel exciton electronic structure model whose molecular fluctuations are treated in section 2.4. Förster and Redfield-type descriptions of electronic energy transfer are given from a reduced description of Fermi's golden rule in section 2.5. Many of the theoretical treatments in this chapter come from the following references[1-7].

2.2. TIME DEPENDENT PERTURBATION THEORY

In this section the microscopic origins of the electric field signal are described using a perturbative approach. The polarization is separated into a response function which depends only on the dynamics of the system and the input electric fields which synchronize the time

evolution in the experiment. This section ends by presenting the mathematics in an intuitive diagrammatic fashion.

2.2.1. Density Operator

For the discussion of time dependent perturbation theory, a density matrix approach is more convenient than using wavefunctions. The expectation values of observables are easily calculated with the density operator, $\hat{\rho}$, and operator $\hat{\mathrm{A}}$ as $\langle \mathrm{A} \rangle = \mathrm{Tr}\left(\hat{\rho} \cdot \hat{\mathrm{A}}\right)$. The wavefunction in a complete set of basis functions, $\phi_k(\vec{r})$, is

$$\psi(\vec{r},t) = \sum_k c_k \phi_k(\vec{r}) \exp(-i\omega_k t) \tag{2.2}$$

where ω_k is the frequency of state k. The probability density is obtained by taking the square modulus of the wavefunction as

$$\left|\psi(\vec{r},t)\right|^2 = \sum_k \sum_m c_m c_k^* \phi_k^*(\vec{r}) \phi_m(\vec{r}) \exp\left(i(\omega_k - \omega_m)t\right) \tag{2.3}$$

The elements of the density matrix reflect the coefficients and time dependence of the wavefunction and are given as

$$\rho_{mk}(t) = c_m c_k^* \exp\left(i(\omega_k - \omega_m)t\right) \tag{2.4}$$

Diagonal elements ($m = k$) are called populations and off-diagonal elements ($m \neq k$) are known as coherences. Switching to Dirac notation, the density operator in a set of basis functions is given as

$$\hat{\rho}(t) = \sum_m \sum_k \rho_{mk}(t) |m\rangle\langle k| \tag{2.5}$$

where $\langle k|$ is known as the bra and $|m\rangle$ as the ket.

2.2.2. Time Dependent Perturbation Theory

This section solves the time dependent Liouville equation for small changes or perturbations from equilibrium. The quantum Liouville equation

$$i\hbar\frac{\partial\rho}{\partial t}=[H,\rho] \tag{2.6}$$

is the density matrix analogue to the wavefunction-based Schrodinger equation. The matrix representation of the Liouville equation is $i\hbar\frac{\partial\rho_{mk}}{\partial t}=\langle m|[H,\rho]|k\rangle$. The Hamilitonian is divided into a time independent and dependent part as

$$H=H^{(0)}+\lambda H^{(1)}(t) \tag{2.7}$$

with λ as a parameter which determines the strength of the perturbation. An element of the density matrix is expanded with the same perturbation as

$$\rho_{mk}(t)=\sum_{N=0}\lambda^N\rho_{mk}^{(N)}(t)=\rho_{mk}^{(0)}(t)+\lambda\rho_{mk}^{(1)}(t)+\lambda^2\rho_{mk}^{(2)}(t)+\cdots \tag{2.8}$$

Substituting these terms in the Liouville equation and grouping terms with a common λ yields a series of equations which gives the time dependence of the density matrix at order N. Integrating this equation gives the value of the density matrix at order N

$$\rho_{mk}^{(N)}(t)=-\frac{i}{\hbar}\int_0^{\infty}\langle m|\left[H^{(1)}(t-t_N),\rho^{(N-1)}(t-t_N)\right]|k\rangle\exp(-i\omega_{mk}t_N)dt_N \tag{2.9}$$

where t_N represents time intervals between interactions and $\omega_{mk}=(E_m-E_k)/\hbar$. This form of the density matrix is analogous to that obtained for the time dependence of the coefficients in

the wavefunction representation. The density matrix at order N is dependent on N nested commutators and 2^N terms total.

The interaction Hamiltonian for an external electric field, $\vec{E}(t)$, with a material dipole, $\vec{V}$, is $H^{(1)}(t) = -\vec{V} \cdot \vec{E}(t)$. The general form of the transition dipole operator is $V = \sum_{a,b} \mu_{ab} |a\rangle\langle b|$.where μ_{ab} is the dipole matrix element $\langle a|\mu|b\rangle$. From Maxwell's equations, the electric field produced by the polarization under ideal conditions is given by

$$E_s(t) = \frac{i2\pi\omega_s l}{n(\omega_s)c} P_s(t) \tag{2.10}$$

where $n(\omega_s)$ is the real part of the refractive index at frequency and l is the pathlength. The factors in front of the polarization are time independent. Therefore, to a good approximation, the electric field measured in a spectroscopic experiment directly informs on the polarization. The polarization is given at Nth order by projecting with the dipole operator and taking a trace over the density matrix:

$$P^{(N)}(t) = \mathrm{Tr}\left[V\rho^{(N)}(t)\right] \tag{2.11}$$

Rewriting the above equation using the density operator gives

$$\begin{aligned} P^{(N)}(t) = \int_0^\infty dt_N \int_0^\infty dt_{N-1} \ldots \int_0^\infty dt_1 S^{(N)}(t_N, t_{N-1}, \ldots, t_1) \\ \times E_N(t - t_N) E_{N-1}(t - t_N - t_{N-1}) \cdots E_1(t - t_N - t_{N-1} \cdots t_1) \end{aligned} \tag{2.12}$$

with Nth-order nonlinear response function given as a time correlation function of transition dipoles as

$$S^{(N)}\left(t_N, t_{N-1}, \ldots, t_1\right) \equiv \left(\frac{i}{\hbar}\right)^N \mathrm{Tr}\left[VG\left(t_N\right)VG\left(t_{N-1}\right)\cdots VG\left(t_1\right)V\,\rho^{(0)}\left(-\infty\right)\right] \qquad (2.13)$$

where V and G are superoperators defined as

$$\begin{aligned} V\,A &= \left[V, A\right] \\ G\left(t\right)A &= \theta\left(t\right)\exp\left(\frac{-i}{\hbar}H^{(0)}t\right)A\exp\left(\frac{i}{\hbar}H^{(0)}t\right) \\ \theta\left(t\right) &= \begin{cases} 1 & t \geq 0 \\ 0 & t < 0 \end{cases} \end{aligned} \qquad (2.14)$$

The benefit of this equation is that paths through the density matrix can now be calculated from start to finish before integration. Equation 2.12 is read starting in a population at equilibrium, $\rho^{(0)}\left(-\infty\right)$. This state then interacts with an electric field E_1 at time $t - t_N - t_{N-1}\cdots - t_1$ and transitions to one of the state defined by V. The system oscillates in the absence of the electric field in time t_1 according to the Hamiltonian $H^{(0)}$ until another interaction occurs at time $t - t_N - t_{N-1}\cdots - t_2$ with another transition dipole contained in V. This process continues until at time *t* a final transition occurs and the trace is taken. The Heavyside step function enforces causality (i.e., time evolution occurs after a transition to a new state).

Physically, the time correlation function reflects the macroscopic decay of the system's dipole oscillations during free evolution intervals. The electric fields start (and synchronize) the motion of each dipole. The sum of the dipole response decays as random, thermally driven interactions adjust the phase of each oscillation. From this information the polarization can be thought of as a process where radiation fields synchronize and select

which states participate while time evolution is controlled solely by the dynamics of the system itself.

Only a few of the possible response functions and electric fields sequences contribute in most third order experiments. One way of determining the path through the density matrix is by controlling the wave vector of the electric field. The electric field is treated classically since its wavelength is over an order of magnitude larger than that of the system of interest. The electric field is given by

$$\mathbf{E}_n(\mathbf{r},t) = \xi_n(t)\left(\exp\left[i\left(\mathbf{k_n}\mathbf{r} - \omega_n t\right)\right] + c.c.\right) \tag{2.15}$$

where $\xi_n(t)$ is a slowly-varying envelope function, $\mathbf{k_n}$ is the wave vector, and ω_n is the frequency. In third order experiments, there are three fields applied which can act in any order yielding $6\times6\times6$, or 216, possible combinations. By conservation of momentum, only the signal wave vector must come from the input electric fields, that is

$$\mathbf{k_{sig}} = \sum_n \pm\mathbf{k_n} \tag{2.16}$$

By detecting the signal in a phase matched direction ($\mathbf{k_s = -k_1 + k_2 + k_3}$ for most experiments at third order) and ordering pulses in time, the number of possible combinations drops significantly. Also, not all interactions with an electric field produce a response from the system. For example, at first order in perturbation theory, there are two terms in the response function

$$S^{(1)}(t_N, t_{N-1}, \ldots, t_1) \equiv \frac{i}{\hbar}\theta(t_1)\left[J_1(t_1) - J_2(t_1)\right] \tag{2.17}$$

The first term represents linear absorption and the second term represents emission from an excited state at equilibrium. Since virtually all population is in the ground state at equilibrium, electric fields cannot induce stimulated emission and the term $J_2(t_1)$ does not contribute. With these observations there are six electric field and response functions combinations which describe third order spectroscopic experiments[8].

All of the time resolved experiments in this dissertation can be described at third order in perturbation theory. In first order (linear) spectroscopy, the response is given by two point time correlation functions and at third order there is a four point correlation function. These four point correlation functions can be put into a collection of two point time correlation functions known as line broadening functions. At third order, there are eight terms in the response function

$$\begin{aligned} S^{(3)}(t) = & \left(\frac{i}{\hbar}\right)^3 \theta(t_1)\theta(t_2)\theta(t_3) \\ & \times \sum_{\alpha=1}^{4} \left[R_\alpha(t_1,t_2,t_3) - R_\alpha^*(t_1,t_2,t_3) \right] \end{aligned} \tag{2.18}$$

where R^* terms are the complex conjugates of R. Terms in the response function for R_1 to R_4 are

$$\begin{aligned} R_1(t_1,t_2,t_3) &= |\mu_{eg}|^4 \exp(-i\omega_{eg}t_1 - i\omega_{eg}t_3) \exp\left[-g^*(t_3) - g(t_1) - f_+(t_1,t_2,t_3)\right] \\ R_2(t_1,t_2,t_3) &= |\mu_{eg}|^4 \exp(i\omega_{eg}t_1 - i\omega_{eg}t_3) \exp\left[-g^*(t_3) - g^*(t_1) + f_+^*(t_1,t_2,t_3)\right] \\ R_3(t_1,t_2,t_3) &= |\mu_{eg}|^4 \exp(i\omega_{eg}t_1 - i\omega_{eg}t_3) \exp\left[-g(t_3) - g^*(t_1) + f_-^*(t_1,t_2,t_3)\right] \\ R_4(t_1,t_2,t_3) &= |\mu_{eg}|^4 \exp(-i\omega_{eg}t_1 - i\omega_{eg}t_3) \exp\left[-g(t_3) - g(t_1) - f_-(t_1,t_2,t_3)\right] \end{aligned} \tag{2.19}$$

with auxiliary functions

$$f_{-}(t_1,t_2,t_3) = g(t_2) - g(t_2+t_3) - g(t_1+t_2) + g(t_1+t_2+t_3)$$
$$f_{+}(t_1,t_2,t_3) = g^{*}(t_2) - g^{*}(t_2+t_3) - g(t_1+t_2) + g(t_1+t_2+t_3) \quad (2.20)$$

where $g(t)$ is the line broadening function (section 2.5). The strength of interaction and orientation is given by the transition dipole. The frequency ω_{eg} represents the peak of the linear absorption spectrum and $g(t)$ contains all information on fluctuations.

2.2.3. Feynman Diagrams

The mathematics of time dependent perturbation theory can be described in a more accessible way using diagrams. Feynman diagrams are a shorthand method of tracking the microscopic pathways that lead to the emitted signal. Figure 2.1 explains the Feynman diagram for linear absorption. The lines that run vertically represent the density operator. The left line represents the ket and the right line represents the bra. Time runs vertically from bottom to top. Interactions with the electric field are represented by arrows and change the index of either the bra or ket through the transition dipole. Arrows pointing toward the diagram represent increases in energy and those pointing away represent decreases in energy. Horizontal dotted lines represent time intervals during which the system evolves according to the zero-order Hamiltonian. The signal emits from the ket after the last interaction. The sign of the response function is given by $(-1)^m$ where m is the number of interactions on the right (bra) side of the diagram. The diagrams begin and end in populations. The signal frequency and wavevector are given by the sum of the electric field frequency and wavevector respectively.

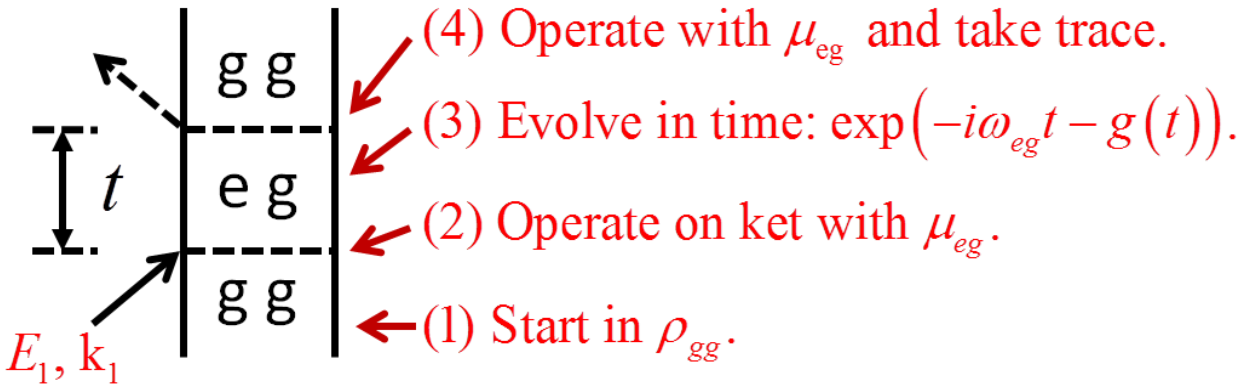

Figure 2.1: Feynman diagram of response term $J_1(t)$ (black) with mathematical description (red) for linear absorption in a two level system of ground "g" and excited state "e".

Feynman diagrams for the third order response are given in Figure 2.2 for the $k_s = -k_1 + k_2 + k_3$ wavevector. Only six of the eight terms are shown since the other two are forbidden in the specified wavevector geometry. States of the system are dummy indicies with state "g" reserved for the ground state, "a" and "b" for states with one excitation, and state "c" for states with two excitations. The systems are in optical coherences in the t_1 and t_3 time intervals. Terms with a ground state population in t_2 are called ground state bleach (GSB) terms. Terms that have an excited state population in t_2 are called excited state emission (ESE) if the diagram terminates in the ground state and are called excited state absorption (ESA) if the diagram ends in an excited state. It is important to note that GSB and ESE terms destructively interfere with ESA terms. In following chapters Feynman diagrams provide an intuitive way of tracing the path of the density matrix.

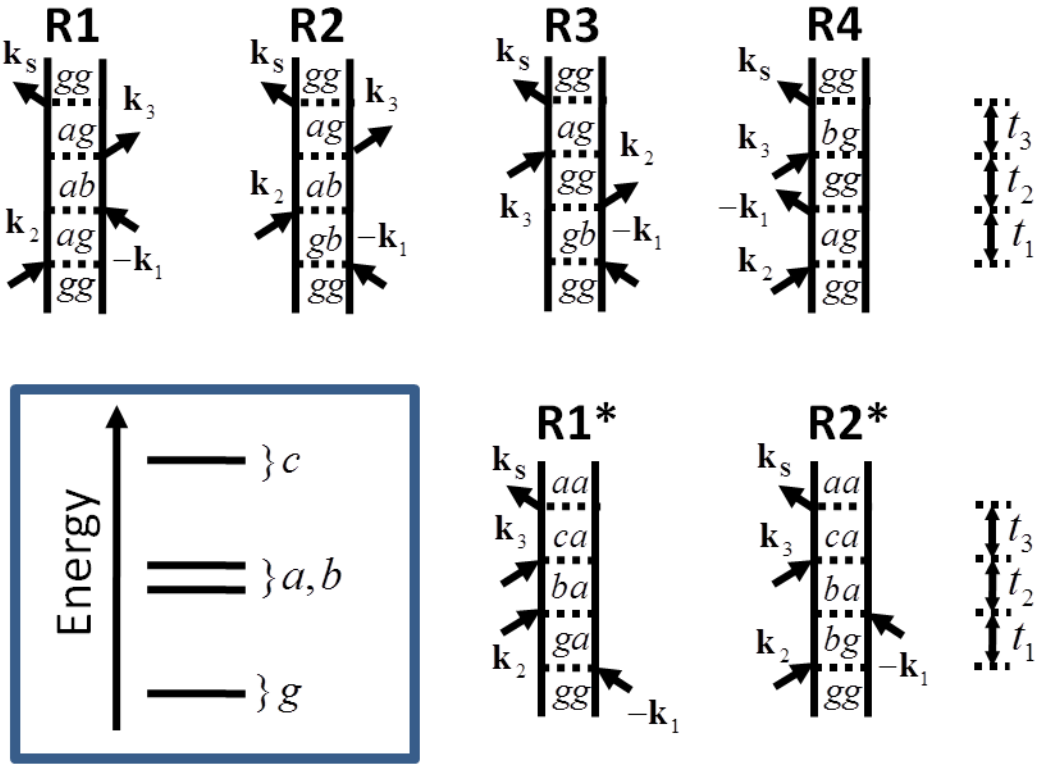

Figure 2.2: Feynmann diagrams commonly encountered at third order. The wavevectors of the electric field is given as ks = -k1 + k2 + k3.

2.3. VIBRONIC COUPLING

In time dependent perturbation theory, transitions occur between states. In general, these states have mixed electronic and nuclear character and the information of the nuclear coordinates of the bath are encoded in the fluctuation of these energy levels. The treatment of nuclear modes is important since they describe important relaxation effects (e.g., Stokes shift) and are important for energy transfer. The Born-Oppenheimer approximation and the Condon approximation effectively allow electronic and nuclear processes of the system to be treated separately. While chapter 7 discusses joint electronic and nuclear states for a high frequency mode, the present treatment of states is important for the theory of later chapters.

2.3.1. The Born-Oppenheimer Approximation

The Born-Oppenheimer approximation provides a picture of nuclei moving over a potential energy surface of an electronic state. The solution to the Schrodinger equation

$$i\hbar \frac{\partial \Psi}{\partial t} = \hat{H}\Psi \tag{2.21}$$

where $\hat{H}$ is the molecular Hamiltonian and Ψ the wavefunction contains all the information about the molecule. Even though solving the full Schrodinger equation is not feasible for large systems, progress is made by noting the large difference between the mass of the electrons and nuclei. The following treatment of the Born-Oppenheimer approximation is similar to that found in References[9,10]. The total Hamiltonian is given by

$$\hat{H}\left(\mathbf{R},\mathbf{r}\right) = \hat{T}_n\left(\mathbf{R}\right) + \hat{H}_{el}\left(\mathbf{R},\mathbf{r}\right) \tag{2.22}$$

where $\hat{T}_n$ is the nuclear kinetic energy operator, $\hat{H}_{el}$ is the electronic Hamiltonian which contains all other terms, $\mathbf{R}$ denotes all nuclear coordinates and $\mathbf{r}$ all electronic coordinates. Solving the electronic equation

$$\hat{H}_{el}\Psi_I^{el}\left(\mathbf{r};\mathbf{R}\right) = E_I^{el}\left(\mathbf{R}\right)\Psi_I^{el}\left(\mathbf{r};\mathbf{R}\right) \tag{2.23}$$

with fixed nuclear geometry produces electronic energy eigenvalues. Continuously varying the nuclear coordinate and resolving the equation creates a potential energy surface. The total wavefunction is given by

$$\Psi_I\left(\mathbf{r},\mathbf{R}\right) = \sum_I \Psi_I^{el}\left(\mathbf{r};\mathbf{R}\right)\chi_I\left(\mathbf{R}\right) \tag{2.24}$$

where χ is the nuclear wavefunction. This form of the wavefunction is exact if the summation is not truncated. Inserting equation 2.24 into the Schrodinger equation yields a solution in matrix notation

$$\left[\hat{T}_n + E_J^{el}\right]\chi_J - \sum_I \hat{\Lambda}_{JI}\chi_I = i\hbar\frac{\partial\chi_J}{\partial t} \tag{2.25}$$

where $\hat{\Lambda}_{JI}$ are nonadiabatic coupling operators. These nonadiabatic operators depend inversely on mass and the Born-Oppenheimer (BO) approximation ignores all but one state in equation 2.25 since the electron mass is orders of magnitude smaller than that of the nucleus. The nonadiabatic operators can be omitted yielding the solution for a single state

$$\left[\hat{T}_n + E^{el}\right]\chi = E\chi \tag{2.26}$$

where E is the total energy of the system. It should be noted that $\hat{\Lambda}_{JI}$ is also proportional to the derivative coupling vector

$$\mathbf{F}_{JI} = \frac{\left\langle \Psi_J^{el} \middle| (\nabla \hat{H}_{el}) \middle| \Psi_I^{el} \right\rangle}{E_I^{el} - E_J^{el}} \qquad \text{for } i \neq j \tag{2.27}$$

which becomes large when potential energy surfaces become close or cross in energy, and the BO approximation fails. At these points radiationless transitions may occur, which is discussed in more detail in Section 2.6.

It is useful to consider a simple model with one nuclear mode since these concepts generalize to an arbitrary number of electronic and nuclear states. Solving equation 2.23 and keeping the two lowest energy states will give eigenvalues $E_g^{el}(R)$ and $E_e^{el}(R)$ for the ground, $\Psi_g^{el}(\mathbf{r};R)$, and excited, $\Psi_e^{el}(\mathbf{r};R)$, state wavefunctions, respectively. For small displacements from equilibrium in R, potential energy surfaces can be approximated as harmonic with energies

$$E_g^{el} = \frac{1}{2} k_g \left(R + d/2 \right)^2$$
$$E_e^{el} = \hbar \omega_{eg}^0 + \frac{1}{2} k_e \left(R - d/2 \right)^2 \qquad (2.28)$$

where d is the dimensionless displacement between equilibrium positions, ω_{eg}^0 represents the vertical transition frequency at the equilibrium nuclear position, and k_i determines the surface curvature. The greater the coupling of the excited state to the nuclear mode, the greater will be the displacement d between the nuclear geometry. Solving the Schrodinger equation with harmonic surfaces yields harmonic oscillator nuclear eigenfunctions. A schematic diagram of equation 2.28 is presented in Figure 2.3. Transitions between states are outlined in the next section.

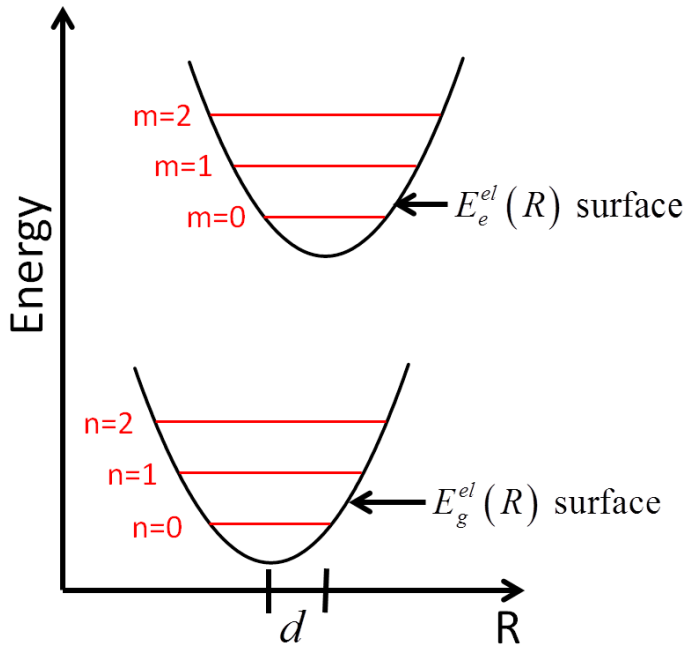

Figure 2.3: Potential energy surfaces created by equation 2.28 with nuclear energy levels. The nuclear coordinate is given by R and the displacement between equilibrium positions is given by d.

2.3.2. Electronic Excitation and Franck-Condon Factors

The probability of a radiation induced transition from a vibrational level in the ground electronic state "g" to a vibrational level in the excited electronic state "e" is proportional to the transition dipole

$$\boldsymbol{\mu}_{em,gn} = \langle \Psi_e \chi_m | \mu | \Psi_g \chi_n \rangle \tag{2.29}$$

where $\tilde{\mu}$ is the dipole operator. The above is rewritten considering integration separately over electronic and nuclear coordinates

$$\langle \Psi_e \chi_m | \mu | \Psi_g \chi_n \rangle = \langle \chi_m | \langle \Psi_e | \mu | \Psi_g \rangle | \chi_n \rangle = \langle \chi_m | \mu_{eg}^{el}(\mathbf{R}) | \chi_n \rangle \tag{2.30}$$

where $\mu_{eg}^{el}(\mathbf{R})$ is an electronic transition dipole that is a function of nuclear coordinates. To simplify the equation $\mu_{eg}^{el}(\mathbf{R})$ is expanded in a Taylor series

$$\mu_{eg}^{el}(\mathbf{R}) = \mu_{eg}^{el}(\mathbf{R}_0) + \left(\frac{\partial \mu_{eg}^{el}(\mathbf{R})}{\partial \mathbf{R}} \right)_{\mathbf{R}_0} \mathbf{R} + \cdots \tag{2.31}$$

and inserted the leading term into equation 2.30 to get

$$\boldsymbol{\mu}_{em,gn} = \mu_{eg}^{el}(\mathbf{R}_0) \langle \chi_m | \chi_n \rangle. \tag{2.32}$$

Ignoring the nuclear dependence of the transition produces an electronic transition dipole $\mu_{eg}^{el}(\mathbf{R_0})$ averaged over nuclear coordinates and multiplied by a nuclear overlap factor in equation 2.32. This truncation is called the Condon approximation.

The square of the nuclear overlap integral, $|\langle \chi_m | \chi_n \rangle|^2$, is called a Franck-Condon factor and represents that nuclear motion is frozen on the timescale of an electronic transition. At room temperature, thermal motions of the solvent induce nuclear motion with timescales greater than 100 fs. In condensed phases, inverse linewidths of linear absorption

spectra reveal electronic transitions on the order of 10 fs, making the Franck-Condon approximation adequate for these thermally driven frequencies.

The Franck-Condon factor explains the vibronic progressions seen in absorption spectra. Returning to the example of BO surfaces in Figure 2.3, electronic transition strengths depends on the square of the nuclear overlap integral between electronic states. Since the harmonic oscillator solutions are orthogonal, only transitions between wavefunctions of the same quantum number are allowed when there is no equilibrium displacement between surfaces. A nonzero displacement between the surfaces allows excitations into all states. An analytical solution of the Franck-Condon factor from the zero quantum state of the ground state to the m quantum state of the excited state is given as

$$\left|\langle \chi_m | \chi_0 \rangle\right|^2 = \frac{S^m \exp(-S)}{m!} \tag{2.33}$$

where $S = \frac{1}{2} d^2$ represents the coupling strength to nuclear modes. This equation is plotted for a few values of d in Figure 2.4. The high frequency nuclear modes described by Franck-Condon factors are important since they can open up fast relaxation channels for nonradiative transitions over large differences in electronic energy. Nuclear modes which have the strongest coupling to the excited state are good candidates for these relaxation channels. In Figure 2.4, large displacements ($d \approx 2$) are needed to produce significant amplitude in nuclear modes with one quanta or greater. However, even nuclear modes with modest values of the Franck-Condon factor can have an important impact on nonradiative relaxation by forming superposition states with other electronic states. The physics of these superposition states are outlined in the next section.

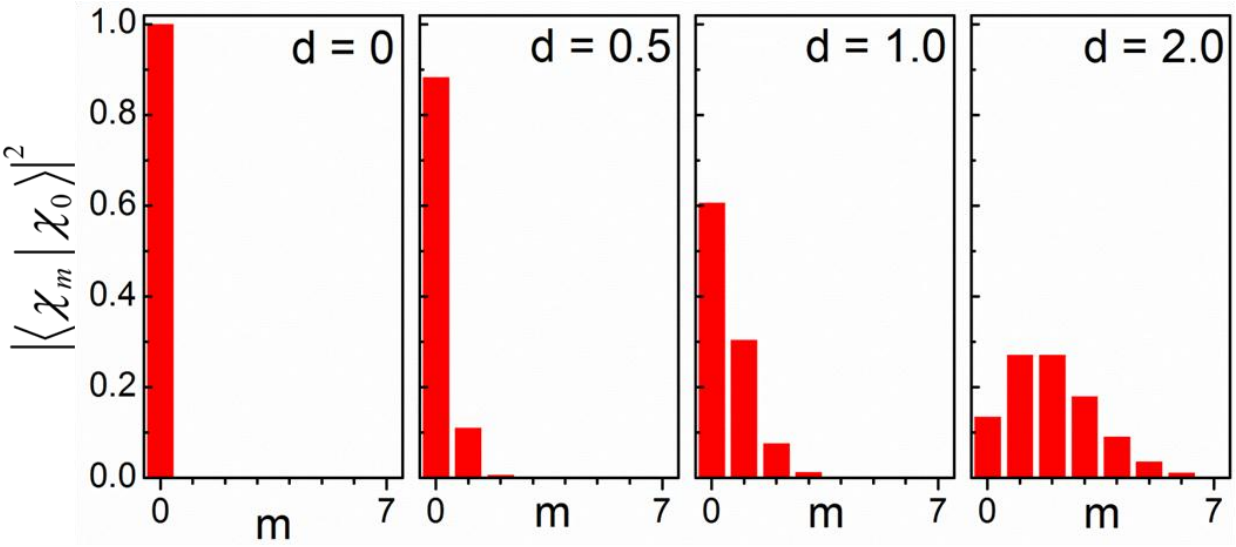

Figure 2.4: Franck-Condon factors between the n = 0 and m vibrational levels for given values of the dimensionless displacement, d.

2.4. FRENKEL EXCITONS

Optical excitations delocalized over more than one molecule are described as excitons. An excitation into the lowest energy resonances in a system excites an electron from the highest occupied molecular orbital to the lowest unoccupied orbital. The exciton is bound so that the HOMO and LUMO are associated with the same molecule. This excitation is called a Frenkel exciton[11]. The electronic structure of excitons differs significantly from that of the sum of their individual systems. This is particularly evident in absorption spectra from Davydov (or resonance) splitting and exchange narrowing. Energy transfer is typically much fast in systems which form excitons due to strong coupling between pigments. The Frenkel exciton model applies to molecules with non-ovelapping charge distributions and treats each molecule as a two level system of a ground and excited state with Coulombic intermolecular coupling. A direct product of the eigenstates of each system provides the basis for the exciton states. Diagonalizing these basis states with their couplings produces a set of

stationary states (i.e., excitons). This description is relevant to the electronic structure of light harvesting antennae and molecular aggregates.

2.4.1. Dimer System

This section describes the mathematical framework for describing the exciton state of a coupled two level system which can be generalized to larger systems. The Hamiltonian is given by

$$H = \varepsilon_a a_1^\dagger a_1 + \varepsilon_b a_2^\dagger a_2 + J_{ab}\left(a_1^\dagger a_2 + a_2^\dagger a_1\right) \tag{2.34}$$

where ε_a (ε_b) represents the energy gap at site 1 (2) and $a_m^\dagger$ and a_m are raising and lowering operators, respectively. The lowest order interaction between two pigments is described as "dipole-dipole" and is given by

$$J_{\alpha\beta} = \frac{5.04\text{cm}^{-1}\text{nm}^3}{\text{D}^2}\frac{\vec{\mu}_\alpha \cdot \vec{\mu}_\beta - 3\left(\vec{\mu}_\alpha \cdot \hat{n}_{\alpha\beta}\right)\left(\vec{\mu}_\beta \cdot \hat{n}_{\alpha\beta}\right)}{R_{\alpha\beta}^3} \tag{2.35}$$

where $\vec{\mu}_\alpha$ a dipole between the ground and first excited state centered at molecule α, $\hat{n}_{\alpha\beta}$ is a unit vector connecting sites α and β, and $R_{\alpha\beta}^3$ is the distance between dipoles. The coupling is zero for perpendicular transition dipoles and the magnitude increases as they become parallel. The basis states are given by taking the direct product of states. The states with a single excitation are given by $|10\rangle$ and $|01\rangle$ where the ket $|mn\rangle$ represents that molecule 1 contains m excitations and molecule 2 contains n excitations. Applying the above Hamiltonian to these basis states yields the following matrix,

$$H = \begin{pmatrix} \varepsilon_a & J_{ab} \\ J_{ab} & \varepsilon_b \end{pmatrix} \tag{2.36}$$

where $\varepsilon_a = \langle 10|H|10\rangle$, $\varepsilon_b = \langle 01|H|01\rangle$, and $J_{ab} = \langle 10|H|01\rangle$. Diagonalization of this matrix yields the following eigenstates and eigenvalues

$$\begin{aligned}
\varepsilon_{\pm} &= \frac{1}{2}\left(\varepsilon_a + \varepsilon_b\right) \pm \frac{1}{2}\sqrt{\left(\varepsilon_a - \varepsilon_b\right)^2 + 4\left|J_{ab}\right|^2} \\
|\psi_+\rangle &= \cos(\theta)|a\rangle + \sin(\theta)|b\rangle \\
|\psi_-\rangle &= -\sin(\theta)|a\rangle + \cos(\theta)|b\rangle \\
\tan(2\theta) &= \frac{2|J_{ab}|}{\varepsilon_a - \varepsilon_b}
\end{aligned} \tag{2.37}$$

This equation shows that when, $|\varepsilon_a - \varepsilon_b| \gg |J_{ab}|$ the wavefunctions will localize onto different sites. When $\tan(2\theta) \to 0$, $|\psi_+\rangle \approx |a\rangle$ and $|\psi_-\rangle \approx |b\rangle$ and the eigenvalues will converge to their site values as $\varepsilon_+ \approx \varepsilon_a$ and $\varepsilon_- \approx \varepsilon_b$. As the coupling becomes comparable to the energy gap, the eigenvalues begin to significantly deviate from their site values. The increased energy difference between of the superposition states compared to that of the individual states is called resonance or Davydov splitting. Also, as the coupling becomes larger than the energy gap between molecules, the wavefunction completely delocalizes over both molecules and the resonance splitting approaches $2|J_{ab}|$. In the limit of degeneracy or $|\varepsilon_a - \varepsilon_b| \ll |J_{ab}|$ the eigenvalues and eigenstates are given as

$$\begin{aligned}
\varepsilon_{\pm} &= \varepsilon_a \pm J_{ab} \\
|\psi_+\rangle &= \frac{1}{\sqrt{2}}\left(|a\rangle + |b\rangle\right) \\
|\psi_-\rangle &= \frac{1}{\sqrt{2}}\left(|a\rangle - |b\rangle\right)
\end{aligned} \tag{2.38}$$

In this equation, the sign of the coupling will have implications on the absorbance spectra as shown in Figure 2.5.

Radiation induced transitions between states is given by adding the following term to the Hamiltonian

$$\tilde{H}(t) = -\tilde{\mu} \cdot E(t) \tag{2.39}$$

For this part, analysis will concentrate on the time independent dipole operator. The dipole operator for a dimer is given by

$$\tilde{\mu} = \vec{\mu}_1 \left(a_1^{\dagger} + a_1 \right) + \vec{\mu}_2 \left(a_2^{\dagger} - a_2 \right) \tag{2.40}$$

The transition dipoles between ground and excited states in the degenerate case are

$$\mu_{\pm} = \langle \psi_{\pm} | \tilde{\mu} | \psi_0 \rangle = \frac{1}{\sqrt{2}} \left(\vec{\mu}_1 \pm \vec{\mu}_2 \right) \tag{2.41}$$

where $|\psi_0\rangle = |00\rangle$ is the ground state of the exciton. Due to the sum and difference between vectors, the transition dipoles of fully delocalized excitons are always perpendicular. In time resolved spectroscopy, this property is taken advantage of by using the different orientation of each exciton to identify transitions between electronic transitions in the Condon approximation. This technique works well since electronic transitions typically occur faster than the time for molecular rotation in solution (>10ps).

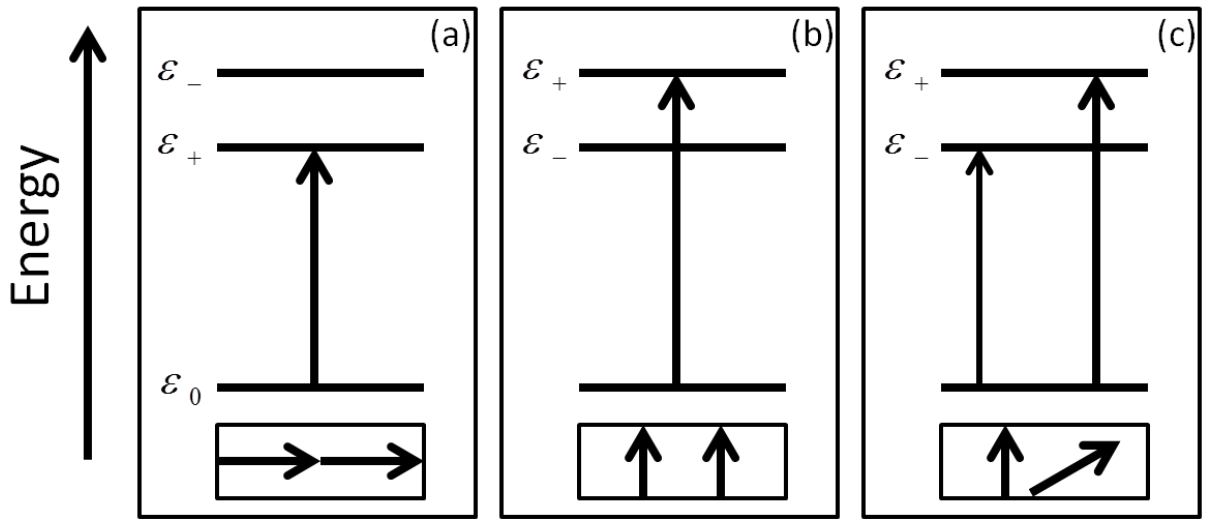

Figure 2.5: A sketch showing the exciton levels ($\varepsilon_0, \varepsilon_+, \varepsilon_-$) formed between states of a dimer of identical molecules with three different dipole geometries (inset at bottom). Vertical arrows overlaid on the energy diagram connect states with nonzero transition dipole strength. (a) In the tip-to-tail geometry, only the lowest energy state has transition dipole strength. (b) Side-by-side dipoles provide strength to only the higher energy state. (c) At 60º both states are accessible to excitation with the higher energy state having three times the strength as the lower transition.

The dipole strength is given as the square modulus of the transition dipole, $D_a = |\vec{\mu}_a|^2$, and has units of Debye. For localized excitons, the transition dipoles and dipole strength closely resemble that of the sites. When states begin to mix, dipole strength will be redistributed. Squaring equation 2.41 and assuming $D_1 = D_2$ gives the dipole strength for identical dimers as

$$D_{\pm} = D_1\left(1 \pm \cos\left(\theta_{12}\right)\right) \tag{2.42}$$

where θ_{12} is the angle between the two dipoles. When dipoles are parallel ($\theta_{12} = 0$), one transition will contain all of the oscillator strength. Special cases of transitions are given in Figure 2.5. For dipoles that are "tip to tail", the coupling between identical molecules is negative allowing only ground state transitions to the lowest single excited state. For dipoles that are "side by side", the coupling for identical molecules is positive and the transition to the higher energy state dominates. These effects are especially pronounced in molecular aggregates which have exciton spectra red-shifted (J-aggregate) or blue-shifted (H-aggregate) with respect to the monomer.

2.4.2. Generalization to Larger Systems

The properties discussed in a dimer system are analogous to those in larger systems. For example, a chromophore's state will mix with those of other chromophores depending on

the magnitude of coupling relative to their energy separation. Generalizing to larger systems, the Hamiltonian is given as

$$H = \sum_{m=1}^{N} \varepsilon_m a_m^\dagger a_m + \sum_{m}^{N} \sum_{n \neq m}^{N} J_{mn} a_m^\dagger a_n \tag{2.43}$$

for chromophores, m and n. Upon diagonalization, the eigenstates of the single exciton manifold are given as

$$\left| e_j \right\rangle = \sum_m C_{jm} \left| m \right\rangle \tag{2.44}$$

where $\left| e_j \right\rangle$ is the jth exciton state and $\left| m \right\rangle = a_m^\dagger \left| 0 \right\rangle$.[5] The participation ratio

$$PR_j = \left[\sum_{m=1}^{N} C_{jm}^4 \right]^{-1} \tag{2.45}$$

provides a succinct way to describe exciton delocalization by describing the effective number of chromophores involved in the exciton. This quantity varies from 1 for excitations localized to one site to N for a completely delocalized exciton.

2.5. CONDENSED PHASE ENVIRONMENT AND LINE BROADENING

In this section, fluctuations of the system's energy levels are described using a time correlation approach. Absorbance spectra of molecules in the gas phase have many well resolved transitions while spectra in condensed phase are broad and have few features. The width of the condensed phase absorbance spectra stems from interactions between the system and its surroundings. Pigment-pigment and solvent-pigment nuclear motions produce shifts in the energy of the system compared to that of the non-interacting (gas phase) system. The shifts in energy of the individual systems lead to a macroscopic damping of the time domain

response. The microscopic description of these system-bath interactions is given in this section.

2.5.1. Interaction with Surroundings: Spectral Density

The system Hamiltonian is described by a sum of three terms

$$H = H_0 + H_{SB} + H_B \tag{2.46}$$

where H_0 represents the system Hamiltonian, H_{SB} the system-bath interaction, and H_B the bath. The general form for the system-bath interaction Hamiltonian is[5]

$$H_{SB} = \sum_m \sum_n q_{mn}(\boldsymbol{Q}) a_m^\dagger a_n \tag{2.47}$$

where $q_{mn}(\boldsymbol{Q})$ is an operator of bath coordinates, $\boldsymbol{Q}$ and contains all information on fluctuations. Terms in which $m = n$ cause energy gaps to fluctuate, and terms with $m \neq n$ cause the coupling between states to fluctuate. Due to the extremely large number of modes in the bath, explicitly expressing each state is not possible or necessary. Equation 2.47 becomes easier to solve by using the ergodic hypothesis which states that the time average of a property is equivalent to the ensemble average. Knowledge of the bath states is not needed in this time dependent method which tracks the behavior of a representative coordinate over a long period of time using a time correlation function.

It is assumed that the expectation value of the operator is zero (i.e., $\langle q_{mn}(\boldsymbol{Q}) \rangle_0 = 0$) and any constant interaction could be included in the zero-order Hamiltonian. Typically the mean square fluctuations of the site energies are larger than the fluctuation of the couplings, so the development will concentrate on terms where $m = n$. The amplitude of populations will vary according to

$$\langle q_{mm}(t)\, q_{nn}(0)\rangle \tag{2.48}$$

It is further assumed that fluctuations are independent for each site and that all sites experience the same fluctuations. These approximations give

$$\langle q_{mm}(t)\, q_{nn}(0)\rangle = \langle q_{mm}(t)\, q_{mm}(0)\rangle \quad \text{(for all } m\text{)} \tag{2.49}$$

The term on the right is given as

$$\begin{aligned} C(t) &= \langle q_{mm}(t)\, q_{mm}(0)\rangle = a(t) + ib(t) \\ a(t) &= \int_0^\infty d\omega \cos(\omega t) \coth\left(\hbar\omega / 2k_B T\right) C(\omega) \\ b(t) &= \int_0^\infty d\omega \sin(\omega t) C(\omega) \end{aligned} \tag{2.50}$$

where $C(\omega)$ is the temperature independent spectral density. Here the spectral density represents each nuclear mode that modulates the energy gap of the chromophore weighted by the strength of its interaction. Integrating over the spectral density yields the coupling strength to the nuclear modes known as the reorganization energy

$$\lambda = \int_0^\infty d\omega \frac{C(\omega)}{\omega} \tag{2.51}$$

Adding the temperature dependence produces the linewidth parameter which when nuclear modes are sufficiently populated ($k_B T \gg \hbar\omega$) has a simplified form given as

$$\Delta^2 = \frac{2\lambda k_B T}{\hbar} \tag{2.52}$$

The line broadening function is given by

$$g(t) = \frac{1}{2\pi}\int_{-\infty}^{\infty} d\omega \frac{1-\cos(\omega t)}{\omega^2}\coth(\hbar\omega / 2k_B T)C(\omega) + \frac{i}{2\pi}\int_{-\infty}^{\infty} d\omega \frac{\sin(\omega t)-\omega t}{\omega^2} C(\omega) \tag{2.53}$$

which describes system-bath coupling spectroscopy and plays an important role in energy transfer rate theories (Section 2.5). The line broadening function controls the line width in a linear absorption spectrum by

$$\sigma_{abs}(\omega) = \frac{1}{\pi}\mathrm{Re}\int_0^{\infty} dt \exp\left[i\left(\omega - \omega_{eg}^0\right)t - g\left(t\right)\right] \tag{2.54}$$

where ω_{eg}^0 is the average energy gap between the zero quantum vibrational level of the ground and excited states. The above equation shows that the real part of the line broadening function controls the width in absorption spectra and the imaginary part causes shifts in the peak frequency.

There are two limits to the spectral density under this model. When a vibration is underdamped, the spectral density assumes the form

$$C^{UD}(\omega) = \sum_j S_j \omega_j^2 \left[\delta\left(\omega - \omega_j\right) - \delta\left(\omega + \omega_j\right)\right] \tag{2.55}$$

where S_j is the Huang-Rhys factor and $S_j\omega_j$ is the reorganization energy for mode j. The Huang-Rhys factor describes the coupling strength of a nuclear mode to an electronic transition. For harmonic vibrations, the Huang-Rhys factor is proportional to the equilibrium displacement of a nuclear mode (equation 2.28). The abundance of low frequency modes in the spectral density prevents treating each mode explicitly. Fortunately, a single overdamped mode models the effect of a continuous distribution of individual modes. The overdamped spectral density is given as

$$C^{OD}(\omega) = 2\lambda \frac{\omega\Lambda}{\omega^2 + \Lambda^2} \tag{2.56}$$

where Λ^{-1} describes the nuclear correlation time which decays according to a single exponential in this model. The total spectral density is given as a sum of the two limits: $C(\omega) = C^{UD}(\omega) + C^{OD}(\omega)$. Solvent and intermolecular modes are generally low in frequency and are described in the overdamped regime. Intramolecular modes which have typical frequencies > 500 cm^{-1} are generally underdamped as evidenced by their narrow widths in Raman spectra.

When the spectral densities are put into equation 2.53, the low frequency (overdamped) modes dominate the real part of $g(t)$ and the higher frequency (underdamped) modes contribute mainly to the imaginary part. Figure 2.6 shows the total spectral density obtained with an overdamped and one underdamped mode with corresponding absorption spectrum with parameters given in Table 2.1. Multiple peaks represent transitions occurring between vibrational levels of the high frequency mode in the ground and excited state. Peak amplitudes closely match those of Figure 2.4 for d = 1.0. Each peak of the Franck-Condon

progression is broadened by the overdamped part of the spectral density.

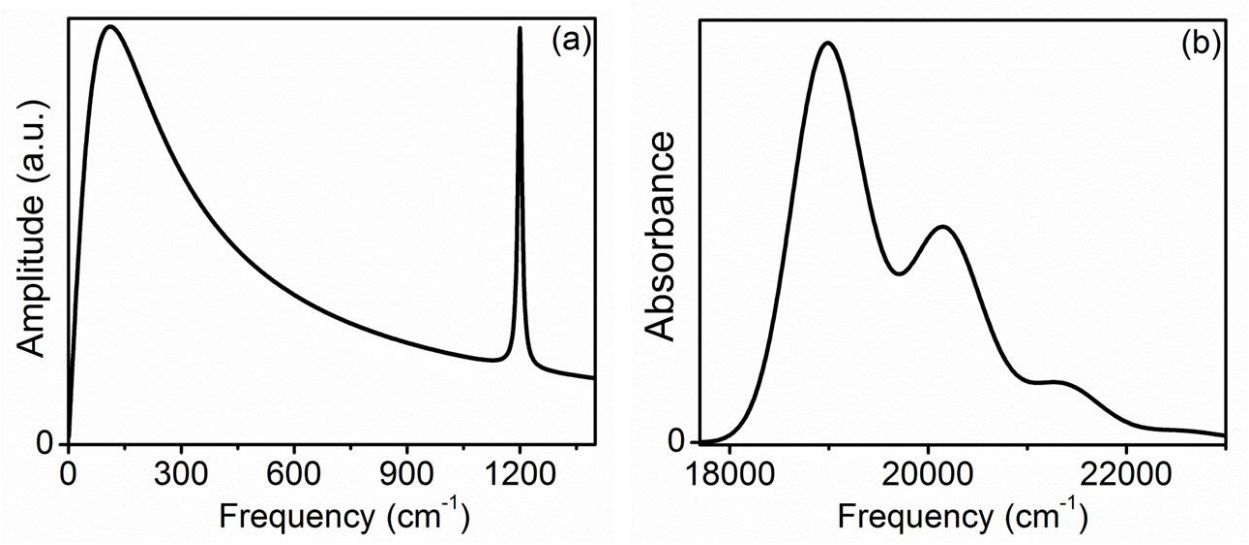

Figure 2.6: (a) Spectral density obtained by summing the overdamped and underdamped contributions. The underdamped contribution is given at 1200 cm^{-1} and has a finite width for illustration. The overdamped portion peaks at Λ. (b) Absorption spectra obtained from equation 2.54. The spectrum shows a Franck-Condon progression of vibrational modes and each peak is broadened by COD(w). Parameters are given in Table 2.1.

Table 2.1: Parameters used in calculation of absorbance and spectral density

parameter	value
ω	19000 cm^{-1}
λ	400 cm^{-1}
Λ^{-1}	300 fs
ω_{vib}	1200 cm^{-1}
S	0.5
T	300 K

2.5.2. Limits of Line Broadening

The overdamped spectral density is useful because the timescale and coupling strength of nuclear motion are all that is needed to parameterize line broadening and the

equations reduce to simple forms in opposing limits. Solving the line broadening function above with the overdamped spectral density in the high temperature limit yields

$$g(t) = \left(\frac{2\lambda k_B T}{\Lambda^2} - i\frac{\lambda}{\Lambda} \right) \left(\exp\left(-\Lambda |t|\right) + \Lambda t - 1 \right) \tag{2.57}$$

The real part describes line broadening and the imaginary part is responsible for changes in the average energy of a state. When the inverse of the nuclear correlation time is small compared to coupling between states ($\Lambda \ll \Delta$), $g(t)$ simplifies to

$$g(t) = \frac{1}{2}\Delta^2 t^2 \tag{2.58}$$

Inserting this equation into the above gives the following absorbance and fluorescence profiles

$$\begin{aligned} \sigma_a(\omega) &= \sqrt{2\pi\Delta^2}\, \exp\left[-\left(\omega - \omega_{eg}^0\right)^2 / 2\Delta^2 \right] \\ \sigma_f(\omega) &= \sqrt{2\pi\Delta^2}\, \exp\left[-\left(\omega - \omega_{eg}^0 + 2\lambda\right)^2 / 2\Delta^2 \right] \end{aligned} \tag{2.59}$$

Since the Fourier transform of the Gaussian line shape produces another Gaussian, the line shapes are Gaussian with a standard deviation that reflects the coupling to nuclear modes. The peak of the fluorescence line shape is red shifted by 2λ, the Stokes shift. The fluorescence line shape is just the mirror image of the absorption line shape for a two level system. This limit is known as the inhomogeneous or static limit of linebroadening and is often seen in laser dyes in solution.

In the opposite limit, nuclear fluctuation amplitudes are small and the inverse timescale is fast, ($\Lambda \gg \Delta$) and the above equation reduces to

$$g(t) = \Gamma t - i\lambda t \tag{2.60}$$

where $\Gamma = \lambda k_B T / \hbar\Lambda$. The absorption and fluorescence line shapes are now equal and are given by

$$\sigma_a(\omega) = \sigma_f(\omega) = \frac{1}{\pi} \frac{\Gamma}{\left(\omega - \omega_{eg}^0\right)^2 + \Gamma^2} \tag{2.61}$$

No Stokes shift is observed due to the weak coupling to the environment. The line width of this Lorentzian is 2Γ.

These equations provide a link between the microscopic nuclear environment and an easily obtainable absorption spectrum. For molecules in solution at 300 K, the slow modulation limit is an acceptable approximation. Typical nuclear time scales (Λ^{-1}) are on the order 100 fs in condensed phase. Laser dyes in solution have inverse linewidths on the order of 10fs which put them in the inhomogeneous limit of line broadening. Narrow linewidths can be achieved through exchange coupling where excitons delocalize over many pigments (i.e., possess a high participation ratio) and have smaller reorganization energies. This is especially true in J-aggregates which have narrow features in absorption spectra.

2.6. RELAXATION IN GAS PHASE AND CONDENSED MEDIA

Calculations up to this point have concentrated on stationary states of the system and their fluctuations. The following section outlines limits of electronic relaxation. The case of a coherent system is given by the Rabi formula. Fluctuations from other states are considered using a time correlation function form of Fermi's Golden Rule. Specific cases of Fermi's Golden Rule are given for limiting cases of intermolecular Coulombic coupling and system-bath coupling.

2.6.1. Rabi Formula

The first case is the exact solution to the time dependence of a two level system. The time evolution operator is useful here since the complete set of eigenfunctions is known. The time dependence of the wavefunction is given as

$$\begin{aligned} |\psi(t)\rangle &= U(t,0)|\psi(0)\rangle \\ U(t,0) &= \sum_n |n\rangle \exp(-iE_n t/\hbar)\langle n| \end{aligned} \tag{2.62}$$

where $U(t,0)$ is the time evolution operator and $|n\rangle$ is a basis state of $|\psi(t)\rangle$. Expanding the form of the wavefunction from above yields

$$U(t,0) = |\psi_+\rangle \exp[-i\varepsilon_+ t/\hbar]\langle\psi_+| + |\psi_-\rangle \exp[-i\varepsilon_- t/\hbar]\langle\psi_-| \tag{2.63}$$

The probability that a system starting in state $|n\rangle$ is in state $|m\rangle$ at time t is given by

$$P_{mn}(t) = \left|\langle m|U(t,0)|n\rangle\right|^2 \tag{2.64}$$

If the probability of moving between exciton states is calculated, $\left|\langle\psi_+|U(t,0)|\psi_-\rangle\right|^2$, $P_{mn}(t)$ is zero. This is because these states are eigenstates of the Hamiltonian. Calculating the probability between coupled states, $\left|\langle b|U(t,0)|a\rangle\right|^2$, and performing some algebra yields the Rabi formula

$$P_{ba}(t) = \frac{4|V_{ab}|^2}{4|V_{ab}|^2 + (\varepsilon_a - \varepsilon_b)^2} \sin^2\left[\frac{t}{2\hbar}\sqrt{(\varepsilon_a - \varepsilon_b)^2 + 4|V_{ab}|^2}\right] \tag{2.65}$$

The case of a degenerate system is given as

$$P_{ba}(t) = \sin^2\left[|V_{ab}|t/\hbar\right] \tag{2.66}$$

This equation shows that for a degenerate system even a weak perturbation can cause the population to fully transfer between states. Also, the stronger the coupling, the faster the population will oscillate between states. In the opposite limit, $(\varepsilon_a - \varepsilon_b)^2 \gg 4|V_{ab}|^2$, and

$$P_{ba}(t) \approx \frac{4|V_{ab}|^2}{(\varepsilon_a - \varepsilon_b)^2} \sin^2\left[\frac{t}{2\hbar}(\varepsilon_a - \varepsilon_b)\right] \tag{2.67}$$

Now the probability amplitude oscillates independent of the coupling and has a small maximum value. This result motivates that the coupling strength must be comparable to the energy separation between states to obtain a high maximum probability value.

2.6.2. Golden Rule: Standard Form and Reduced Description

To move beyond the two level system in the Rabi formula consider a wavefunction of m levels after N perturbations have been applied

$$\Psi^{(N)}(t) = \sum_m c_m^{(N)}(t) \exp(-i\omega_m t) \tag{2.68}$$

and separate the Hamiltonian into a time dependent and independent part, so

$$H = H^{(0)} + H^{(1)}(t) \tag{2.69}$$

Solving the time-dependent Schrodinger equation from the initial value of the coefficients to t after one perturbation, gives

$$c_m^{(1)}(t) = -\frac{i}{\hbar} \sum_k \int_0^t c_k^{(0)}(t') H_{mk}^{(1)}(t') \exp(i\omega_{mk} t') dt' \tag{2.70}$$

This equation allows the coefficients to be determined from the coefficients before the perturbation is applied. Progress is made by assuming that the system starts in state $|i\rangle$ and that the perturbation is so weak that the coefficients can be approximated by their initial

values. All coefficients are set to zero throughout the calculation except for $|i\rangle$ which has a value $c_i^{(0)} = 1$. This approximation means that an experimentalist must maintain low laser fluences to produce signals that have meaning in the perturbative regime. Now consider an oscillating perturbation like that of an electric field

$$H^{(1)}(t) = 2H^{(1)} \cos \omega t \tag{2.71}$$

Using this equation along with the coefficients in the previous equation, a formula for the probability of transition between states can be derived[7]. At times long compared to the perturbation timescale the transition rate from state $|i\rangle$ to a quasi-continuum of states $\{|f\rangle\}$ is

$$K_i^{GR} = \frac{2\pi}{\hbar^2} \sum_i \sum_f P_i \left| H_{if}^{(1)} \right|^2 \delta(\omega_i - \omega_f) \tag{2.72}$$

where $P_i = \exp(-E_i / k_B T) \Big/ \sum_i \exp(-E_i / k_B T)$ represents a thermal distribution of initial states. This equation says that only the square modulus of the coupling between states and the number of states is needed to calculate a transition rate. Typically an average coupling term is used for all states. Also, in this form all states, including the bath states are needed to specify the set of states $\{|f\rangle\}$. A useful form of the golden rule recasts the above equation[6,12] as an integral over a time correlation function given by

$$K_i^{GR} = \frac{1}{\hbar^2} \mathrm{Re} \int_{-\infty}^{\infty} dt \left\langle H^{(1)}(t) H^{(1)}(0) \right\rangle \tag{2.73}$$

where $H^{(1)}(t)$ represents the time dependence of the perturbation and $H^{(1)}(0)$ represents the initial thermal distribution. The brackets represent averaging over the states of the bath. Later in this Chapter, specific cases of the perturbative part of the Hamiltonian will be considered.

2.6.3. Förster Theory

The theory developed by Förster is widely used and its appeal lies in its simple and intuitive final form[13]. In this model, the Coulombic coupling, H^{Coul}, is taken as the perturbation. This choice has the immediate consequence that no states are coupled in the zeroeth order Hamiltonian (i.e., $J_{ab}=0$ in equation 2.34). Assuming that molecules are far apart with respect to their dimensions, the dipole approximation can be used to write the coupling equivalent to the form of equation 2.35. It is important to note that the coupling is an average over the nuclear coordinates. Partitioning the Coulombic coupling into nuclear modes is performed in chapter 7. Inserting the coupling into equation 2.73, the transition dipoles become the main contribution to the correlation function since they are time dependent. Fluctuations in the transition dipoles are governed by the same system-bath fluctuations as in equation 2.50. The resulting equation leads to an absorption or fluorescence spectrum. The Förster rate can now be written between sites 1 and 2 as

$$K_{1\leftarrow 2}^{F}=\frac{\eta^2\kappa^2}{\hbar^2 R_{12}^6}\left|\mu_{eg,1}\right|^2\left|\mu_{eg,2}\right|^2\int_{-\infty}^{\infty}\sigma_{fl,1}(\omega)\sigma_{abs,2}(\omega)\,d\omega \qquad (2.74)$$

where $\mu_{eg,i}$ is the transition dipole between ground and excited states for site i, $\sigma_{abs,2}(\omega)$ and $\sigma_{fl,1}(\omega)$ are the absorption and fluorescence spectra given by equation 2.54, κ^2 is an orientation factor, and η^2 is a constant approximately equal to $25\,\mathrm{cm^{-2}nm^6D^{-4}}$. The

orientational factor controls the sign of the coupling and is similar to the numerator in equation 2.35 except the transition dipoles are unit vectors,

$$\kappa^2 = \left[\hat{\mu}_{eg,1} \cdot \hat{\mu}_{eg,2} - 3\left(\hat{\mu}_{eg,1} \cdot \hat{n}_{12} \right)\left(\hat{\mu}_{eg,2} \cdot \hat{n}_{12} \right) \right]^2 \tag{2.75}$$

The dependence of the coupling on orientation is outlined in a previous section.

2.6.4. Redfield Theory

Redfield theory takes the electron-phonon coupling as the perturbation.[14] Doing this puts the Coulombic coupling between states into the zeroeth order Hamiltonian and eigenstates are given as in equation 2.44. Transitions are computed between excitons and the correlation function contains terms similar to equation 2.48. The correlation function then yields the spectral density function. The Redfield rate is given as

$$K^R_{k \leftarrow k'} = \sum_{n=1}^{N} \left| c^*_{kn} c_{k'n} \right|^2 C_n\left(\omega_{k'k} \right) \tag{2.76}$$

where $c^*_{kn} c_{k'n}$ are coefficients of the monomer n contributing to exciton state k' and k, and $C_n\left(\omega_{k'k} \right)$ is the spectral density at monomer n. The spectral density satisfies detailed balance so that $C_n\left(-\omega \right) = \exp\left(-\hbar\omega / k_B T \right) C_n\left(\omega \right)$. The electron-phonon coupling is treated such that only single quantum transitions are allowed. This neglects contributions from overtones and combination bands which are important for downhill energy transfer across large energy gaps.

The rate in equation 2.76 increases linearly with the reorganization energy. This dependence is invalid for systems where the coupling to nuclear modes becomes comparable to or greater than the Coulombic coupling between sites. This is a consequence from using

the commonly invoked secular approximation where it is assumed the inverse of the relaxation rate is much slower than the coherent oscillations between exciton states. Using the full Redfield equation with no secular approximation, the transition rate becomes independent of reorganization energy when $\lambda \geq J_{12}$.[15]

2.6.5. Modified Redfield Theory

Modified Redfield theory is of interest because it reduces to the Förster rate and traditional Redfield in their applicable limits in one equation[6]. Describing the regime intermediate between the two theories is important since many times in photosynthetic systems the reorganization energy and Coulombic coupling are of comparable magnitude. Modified Redfield theory, introduced by Zhang et.al[16], is similar to Redfield theory since it takes part of the electron-phonon coupling, in this case the off-diagonal part, as the perturbation. The off diagonal part of this term induces transitions between states while the diagonal part is responsible for line broadening. The consequence is that modified Redfield theory is valid when the spatial overlap between excitons is minimal. Including the diagonal part of the electron-phonon coupling into the zeroeth order Hamiltonian also removes the restriction on single quantum transitions found in traditional Redfield theory. The form of the rate is

$$K_{k\leftarrow k'}^{MR} = \frac{1}{4\pi^2}\int_{-\infty}^{\infty} d\omega \int_{-\infty}^{\infty} d\omega' F_{k'}(\omega) A_k(\omega') N_{kk'}(\omega-\omega') \qquad (2.77)$$

where $F_{k'}(\omega)$ and $A_k(\omega')$ represent absorption and fluorescence lineshapes and $N_{kk'}(\omega-\omega')$ describes overlap of the excitons and phonons from the spectral density.

2.7. SUMMARY

The nonlinear polarization has been described at arbitrary order using a perturbative approach from the Liouville equation. At third order, the response function tracks the path through the density matrix and time evolution of each path is synchronized by three interactions from external electric fields. The time correlation function is used in time perturbation theory and elsewhere to describe ensemble effects. The Born-Oppenheimer and Condon approximations delineate the role of electronic and nuclear states of the system. Electronic states are then described using a Frenkel exciton approach where all information on fluctuations is given by the line broadening function. Energy transfer is described in three different perturbative regimes. The limit of small spatial exciton overlap in modifield Redfield theory is found to interpolate between the Förster and traditional Redfield limits.

REFERENCES

(1) Mukamel, S. *Principles of Nonlinear Optical Spectroscopy*; Oxford University Press: New York, 1995.

(2) Parson, W. W. *Modern Optical Spectroscopy*; Springer-Verlag: Berlin, 2007.

(3) Boyd, R. W. *Nonlinear Optics, Second Edition*; Academic Press: San Diego, 2003.

(4) Schwoerer, M.; Wolf, H. C. *Organic Molecular Solids*; Wiley-VCH: Weinheim, 2007.

(5) Cho, M. *Chem. Rev.* 2008, *108*, 1331.

(6) Yang, M.; Fleming, G. R. *Chem. Phys.* 2002, *282*, 163.

(7) Atkins, P.; Friedman, R. *Molecular Quantum Mechanics Fourth Edition*; Oxford University Press: Oxford, 2005.

(8) Brixner, T.; Mancal, T.; Stiopkin, I. V.; Fleming, G. R. *J. Chem. Phys.* 2004, *121*, 4221.

(9) Matsika, S.; Krause, P. *Annu. Rev. Phys. Chem.* 2011, *62*, 621.

(10) Worth, G. A.; Cederbaum, L. S. *Annu. Rev. Phys. Chem.* 2004, *55*, 127.

(11) Abramavicius, D.; Palmieri, B.; Voronine, D. V.; Sanda, F.; Mukamel, S. *Chem. Rev.* 2009, *109*, 2350.

(12) Nitzan, A. *Chemical Dynamics in Condensed Phases*; Oxford University Press: New York, 2006.

(13) Förster, T. *Ann. Physik* 1948, *437*, 55.

(14) *The Theory of Relaxation Processes*; Redfield, A. G., Ed.; Academic Press Inc.: New York, 1965; Vol. 1, pp 1.

(15) Ishizaki, A.; Fleming, G. R. *J. Chem. Phys.* 2009, *130*, 234110.

(16) Zhang, W. M.; Meier, T.; Chernyak, V.; Mukamel, S. *J. Chem. Phys.* 1998, *7763*, 7763.

CHAPTER 3. NONLINEAR TIME RESOLVED SPECTROSCOPY INSTRUMENTATION AND TECHNIQUES

3.1. INTRODUCTION

The investigation of femtosecond time-resolved electronic relaxation processes relies on electric fields as the main source of information. Succinctly stated, the experiments in this dissertation need the electric fields to be short, coherent, tunable, with low fluence at the sample. Pulsed coherent sources became available with the laser[1]. Until the 1990s experiments involving pulsed lasers were especially tedious since the operating conditions for the laser had to be extremely stable[2]. In 1991, Sibbet and coworkers demonstrated a robust self-modelocked titanium sapphire laser[3]. The titanium sapphire gain medium produces a large bandwidth but its fixed frequency limits the number of samples that can be measured. Increased control of the bandwidth and frequency of pulses is given by an optical parametric amplifier which uses the high power from the laser as a source of gain[4]. Low fluence at the sample prevents photodamage and higher order signals. A diffractive optic based interferometer introduced in 1998 provides the signal to noise ratios needed for low fluence measurements[5,6].

In this dissertation, stable laser outputs are highly desired while flexibility in all other optical components is needed for a variety of experiments. To this end, the titanium sapphire laser (Quantronix Integra C) was purchased commercially for its stability and ease of use and all other optical components in this dissertation are home-built for its adjustable parts. This chapter provides an overview of the techniques and hardware used in experiments while details for each system are outlined later in its respective chapter.

Section 3.2 describes the optical parametric amplifier concept and setup. Pulse characterization and compression is described in Section 3.3. Section 3.4 describes the diffractive optic based interferometer for transient grating and two-dimensional photon echo spectroscopy. Simulated signals describe the output of transient grating and two-dimensional photon echo spectroscopy for a two level system.

3.2. OPTICAL PARAMETRIC AMPLIFICATION

The optical parametric amplifier (OPA) used in this section amplifies a weak continuum pulse with a high energy pulse from a titanium sapphire laser in a second order nonlinear process. There are three nonlinear processes present in the OPA induced by the high power laser. In the first process, continuum generation in a sapphire plate produces a broadband pulse. The energy of this pulse is very low since the incident power on the sapphire must not exceed the damage threshold. A second nonlinear event called second harmonic generation doubles the frequency of the residual laser power not used in continuum generation. Frequency doubling is important since the third nonlinear process, difference frequency generation, amplifies by "splitting" the high frequency, high energy pulse into two lower frequency pulses. The frequencies of the splitting are determined by the broadband pulse from the sapphire. Noncentrosymmetric media (crystals without an inversion symmetry) are needed to produce a polarization in second harmonic and difference frequency generation[7]. The pathlength of these crystals creates inverse effects on the power and bandwidth of the amplified pulse.

In the amplification stage, a high energy, high frequency "pump" pulse acts as a gain for a weaker "seed" pulse in difference frequency generation. In the first step, the pump and seed interact to produce a low frequency "idler" photon. The idler photon then interacts with

the pump again to produce a photon at the seed frequency (Figure 3.1)[7]. The efficiency of this process is determined by many factors. Gain is given as the intensity after passing through a medium of length L with initial intensity I_{s0}, as

$$G = \frac{I_s(L)}{I_{s0}} = \frac{1}{4}\exp(2\Gamma L) \tag{3.1}$$

and

$$\Gamma \propto \sqrt{I_p \omega_i \omega_s} \tag{3.2}$$

where Γ is the nonlinear coefficient, I_p is the pump irradiance, and ω_i and ω_s are the frequency of the idler and signal, respectively[4]. This equation shows that the gain depends exponentially on crystal length and exponentially on the square root of the pump intensity. The gain also increases as the frequency of signal and idler increases, but since the pump frequency, ω_p, is fixed the seed and idler frequencies are constrained by $\omega_p = \omega_s + \omega_i$. Maximum gain is found when the signal and idler approach the same value. In practice limitations occur since the pump irradiance can only increase up to the damage threshold of the crystal, and amplified bandwidth decreases as the length of the medium increases.

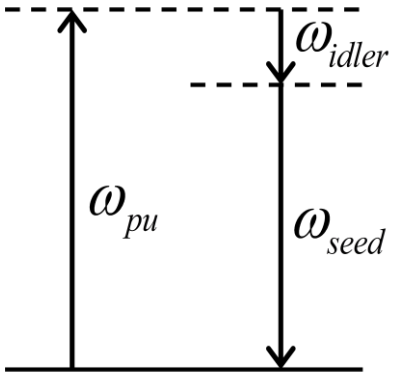

Figure 3.1: Energy level diagram for difference frequency generation. Pump and idler frequencies interact using virtual states to produce a photon at the seed frequency.

For pulses to remain overlapped in the gain medium, their wavevectors k_i, must match the phase matching condition

$$\Delta k = k_p - k_s + k_i = 0 \tag{3.3}$$

where p, s, and i stand for the pump, signal, and idler respectively. Analyzing the magnitude of the vector, this means $n_p < n_s$ for the refractive index n which is not possible in isotropic media. Birefringent crystals provide a solution to this problem by allowing the pump pulse to be polarized along the crystal axis with the lower refractive index. In reality, only one frequency can be phase matched; frequencies further from this condition separate according to their group velocity mismatch. Pulses will be overlapped in the crystal for some time, though, due to their finite duration while frequencies which are phase matched will be amplified for the entire length of the crystal. The net effect is a narrowing of the amplified signal bandwidth around the phase matched frequency. The full width at half maximum of the phase matched bandwidth scales as the inverse of the square root of the crystal length[4]. A noncollinear setup is used to amplify pulses with the largest bandwidth since it causes the group velocities of all three pulses become similar. The idler pulse emits at an angle larger than that between the pump and seed in this geometry. Increasing the pump-seed angle causes the projection of the group velocity of the idler in the seed direction to decrease until it matches that of the seed at an angle of 6.4 in the OPA described below. Phase matching more bandwidth generally means that the energy at any given frequency is lowered since pump energy is used to amplify a larger number of frequencies. In general, crystal length and

the angle between pump and seed beams are adjusted to obtain the desired amplification and bandwidth for the experiment.

When focusing the pump and signal beams, the duration of the pump pulse at the crystal must be much longer than that of the seed. If this condition is not met, the full bandwidth of the seed will not be amplified due to the non-uniform spreading of frequencies (chirp) of the pulse. Passing the pump through 20 cm of high optical quality glass provides the dispersion necessary to stretch the pump in the OPA design below. Also, the pump spot size at the crystal is larger than the spot size of the seed. This allows for uniform amplification of the seed which contains spatially dispersed frequencies called "spatial chirp".

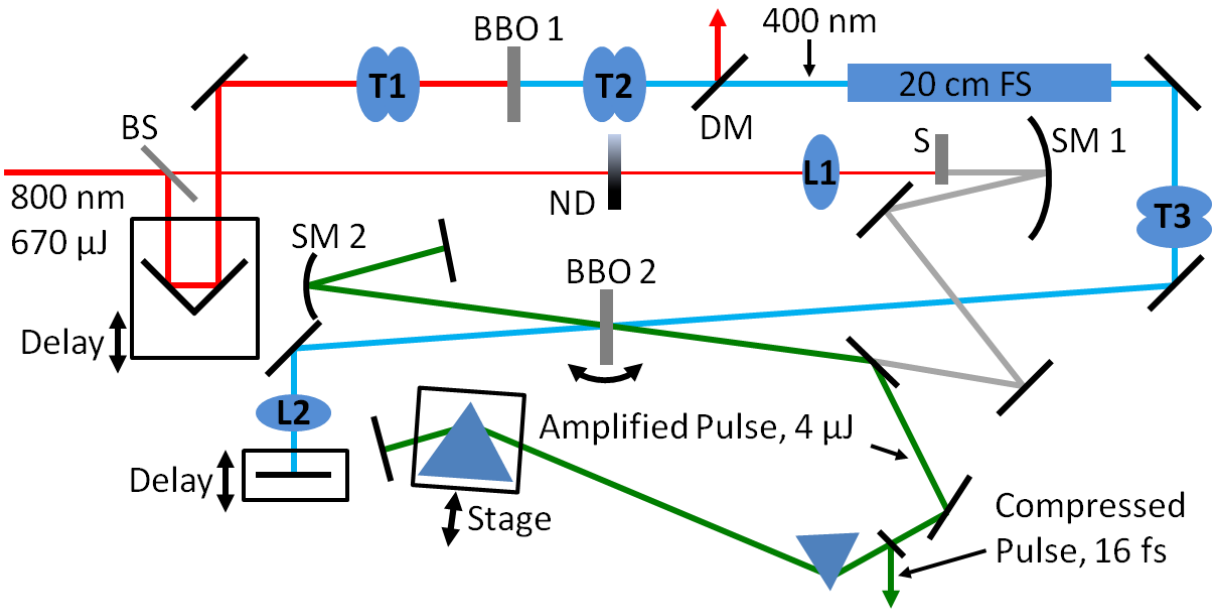

Figure 3.2: Schematic of OPA design with prism compressor. An explanation of all components is given in the text.

A schematic of the OPA used in the experiments is given in Figure 3.2. The incoming pulse (800 nm, 130 fs, 0.67 mJ) is incident on a beam splitter (BS). A small, 2%, portion of

the energy from this beam splitter passes through a variable neutral density filter (ND, OD 0 – 2) and is focused with a 10 cm lens (L1) onto a 1 mm sapphire plate (S). Unless otherwise noted, all lenses are one inch diameter, planoconvex, and made from BK7 glass. Continuum generation in the sapphire produces a pulse (~1 nJ, 490 – 1100 nm) that is focused onto the difference frequency beta-barium borate (BBO 2) crystal using a two inch diameter, 4 cm focal length spherical mirror (SM 1). The remaining energy (0.65 mJ) from the beam splitter (BS) is delayed on a stage with micrometer precision. This beam is down-collimated using a telescope (T1) with a 5 cm planoconcave and 7.5 cm planoconvex lens combination. The 800 nm input beam undergoes second harmonic generation in a type 1, 1 mm thick, $\theta = 32°$ BBO crystal (BBO 1). The output at 400 nm is expanded using a telescope that is complimentary to the down-collimation telescope. Residual 800 nm light is dumped by using a special dichroic mirror (DM) designed to reflect near the second harmonic frequency and transmit near 800 nm. The second harmonic (pump) pulse is stretched in time by passing through 20 cm of fused silica glass which allows it to have a duration longer than that of the continuum. A telescope (T3) focuses the pump over approximately 25 cm to spot at a couple of centimeters before the difference frequency BBO (BBO 2). High pump energies prevent focusing on the crystal. The angle between pump and seed beams is adjusted from one to six degrees as experimental demands dictate. The difference frequency BBO crystal is a 1mm thick, type 1 crystal, cut at $\theta = 32°$ with an angle that is tuned horizontally to the optical table since the pump polarization is also horizontal. A second pass is achieved by reflecting the amplified seed and pump along the same path as the first pass. The continuum uses a 25 cm concave mirror (SM 2) and the pump uses a 30 cm lens (L2) for collimating and focusing on this second pass. A delay stage is placed in the path of the pump for the second pass. A small

vertical displacement in the second pass alignment allows the amplified seed to be spatially picked off. For pump-seed angles near 6.4º, the OPA produces a bandwidth of 490 – 750 nm. Smaller pump-seed angles phase match less bandwidth but produce more energy.

3.3. DISPERSION MANAGEMENT

3.3.1. Phase

From time dependent perturbation theory, it is seen that the phase of the input electric fields are imparted on the electric field signal. Therefore, characterization of the phase of input electric fields is needed to isolate phase changes originating from the signal itself. In the frequency domain, the group delay is expanded in a Taylor series as

$$T(\omega) = \frac{\partial \phi(\omega)}{\partial \omega} = \phi'(\omega_0) + \phi''(\omega_0)(\omega - \omega_0) + \frac{1}{2}\phi'''(\omega_0)(\omega - \omega_0)^2 + \cdots \tag{3.4}$$

where ϕ', ϕ'', ϕ''' and are the derivatives of the phase and are known as the group delay, chirp, and third-order dispersion, respectively. The group delay changes the time a pulse arrives but does not change the shape of a pulse. Chirp is a linear dependence of the group velocity with respect to frequency, and third-order dispersion possesses a quadratic dependence with frequency. Positive chirp is defined as lower frequencies travelling faster than higher ones which is the type of chirp imparted by glass. Pulse duration depends primarily on chirp and to a lesser extent on higher order phases. This is seen by calculating the effects of broadening from glass. After passing through 1 mm of BK7 glass, a pulse centered at 600 nm will accumulate 71 fs^2 of group velocity dispersion and 27 fs^3 of third order dispersion. At a bandwidth of 1200 cm^{-1} (pulse duration 12.3 fs), this corresponds to a broadening of 36 fs and 5.5 fs from chirp and third order dispersion, respectively.

Pulse compression occurs when chirp and higher order phases are minimized. A useful parameter for determining compression is the time bandwidth product which gives the theoretical limit of compression. It is computed as the width of the intensity of a pulse in time multiplied by its corresponding spectral width intensity. Assuming the spectrum of the intensity of an electric field is Gaussian and contains a flat phase, the time bandwidth product is given as 0.44. For example, a 1200 cm^{-1} full width at half maximum Gaussian intensity profile compresses to an electric field duration of no less than 12.3 fs by this formula. Pulses with nonzero phase will have higher values of the time bandwidth product. The time bandwidth product also implies that bandwidth and pulse duration are inversely related, so a pulse will need twice the bandwidth to compress to (ideally) twice as short.

3.3.2. Pulse Compression

Conventional methods of pulse compression include the use of prisms and gratings[8]. These methods are useful for their ease of use. The drawback for prisms is that their ratio of compensation for chirp and third-order dispersion is fixed so that pulses of large bandwidth cannot be compressed over their entire frequency range[2]. Grating compressors can adjust this ratio but they provide low throughputs. Specially engineered dielectric mirrors, deformable mirror-prism pairs, and pulse shapers provide optimal pulse compression but are complex and a prism compressor is sufficient for the systems of interest in this work[9,10].

The amplified seed from the OPA is compressed using prism pairs mounted on delay stages placed approximately 100 cm apart from tip to tip. Prisms are rotated to Brewster's angle to prevent loss from reflections. The second prism is larger than the first to accommodate the large bandwidth dispersed by the first prism. A mirror redirects the pulse through the prism pair to recombine all frequencies. The prism spacing is large enough to

impart an excessive amount of negative chirp. During compression, the prisms are inserted into the pulse using the delay stages to provide a fine adjustment of positive chirp.

3.3.3. Frequency Resolved Optical Gating

Characterization of the electric field for compression typically involves using the field to measure itself. Pulses are mixed in a fast responding (i.e., off-resonant) medium and their arrival times are scanned. The resulting signal is spectrally resolved. For a transient grating signal with an instantaneously responding medium, the signal of the electric field is approximated by $E_{sig}(t,\tau) = E_1^*(t)E_2(t)E_3(t)$. The frequency resolved optical gating (FROG)[8] spectrogram is given by

$$I_{FROG}^{TG}(\omega,\tau) = \left| \int_{-\infty}^{\infty} E(t)\left|E(t-\tau)\right|^2 \exp(-i\omega t)\,dt \right|^2 \tag{3.5}$$

where the delay between pulses is given by τ and it is assumed that all pulses are the same. Two pulses, $\left|E(t-\tau)\right|^2$, act as a gating function for the third field. Since the spectrogram is resolved in frequency and time, the phase of the pulse can easily be estimated by observation. For instance, frequencies which are linearly delayed in time (showing "tilt") in the spectrogram come from chirp (Figure 3.3). The value of transient grating FROG over a two pulse autocorrelation is that FROG yields the sign of the chirp and third order dispersion. Also, since the gating pulse is the square modulus of the electric field, the phase of the gating pulse does not change the shape of the investigated field in the frequency domain. This makes it possible to use a pulse other than the investigated pulse as the gate pulse. Lengthening the gate pulse will cause loss of information in the time domain that manifests as an equal broadening in time for all frequencies in the spectrogram. FROG does not

measure the absolute phase or group delay. Interferometric measurements outlined in the next chapter provide a way to determine the absolute phase which is necessary to determine the real and imaginary components of the electric field signal.

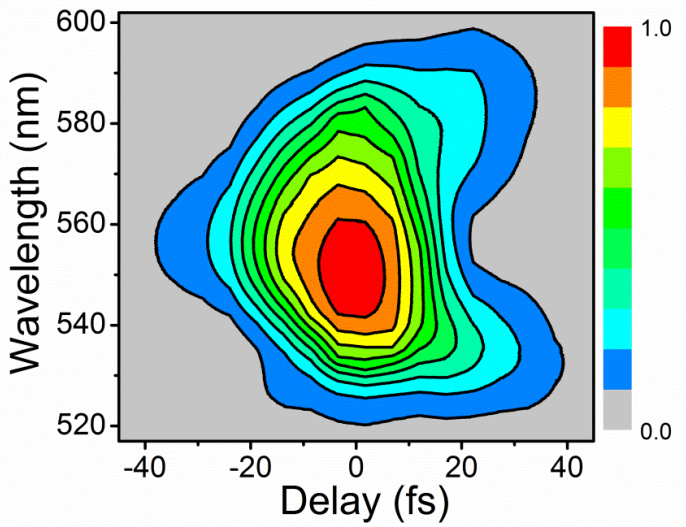

Figure 3.3: Example of a spectrogram taken using transient grating frequency resolved optical gating. The prism pair used to compress this pulse has minimized chirp but does not compensate for third order dispersion which is seen as the quadratic dependence of peak amplitude verses frequency. Contours are spaced at 10% intervals.

3.4. HETERODYNE FOUR WAVE MIXING

3.4.1. Diffractive Optic Based Interferometer

Heterodyne detection involves mixing the signal electric field with a reference electric field. There are two key advantages to this setup over homodyne detection. First, the signal will be amplified linearly with to the power of the reference. The intensity of the signal $E_s(\omega)$ and reference $E_4(\omega)$ electric fields is read by a detector as the square modulus of the combined fields as

$$I(\omega) = |E_s(\omega)|^2 + |E_4(\omega)|^2 + |E_s(\omega)E_4(\omega)|\exp[-i(\phi_s - \phi_4)] + |E_s(\omega)E_4(\omega)|\exp[i(\phi_s - \phi_4)] \quad (3.6)$$

where ϕ_s and ϕ_4 represents the phase of the reference and signal respectively. The signal strength of the heterodyne signal is $|E_4(\omega)/E_s(\omega)|$ greater than that of the homodyne signal. This enhancement makes it possible to measure weak transient grating signals using low (~ 1 nJ) pulse energies.

The second advantage of heterodyne detection is that the absolute phase can be retrieved. This is important since the absolute phase carries details of the real and imaginary parts of the electric field. The frequency domain allows facile determination of the phase for broad bandwidth pulses. The reference field is delayed with respect to the signal and the frequencies are dispersed onto an array detector to produce an interferogram given by equation 3.6 and shown in Figure 3.4. The interferogram is then Fourier transformed into the time domain and only the contribution at the delay between reference and signal is kept[11]. Transforming back to the frequency domain yields the last term in equation 3.6. The phase of the signal is found by determining the phase of the reference pulse and subtracting it out. The phase of the reference pulse is found by taking a second measurement under identical conditions as the experiment of interest. Measurements are typically taken at the point where all pulses are overlapped in a transparent medium since the signal from the electric field will be imaginary with a phase equal to $\frac{\pi}{2}$.

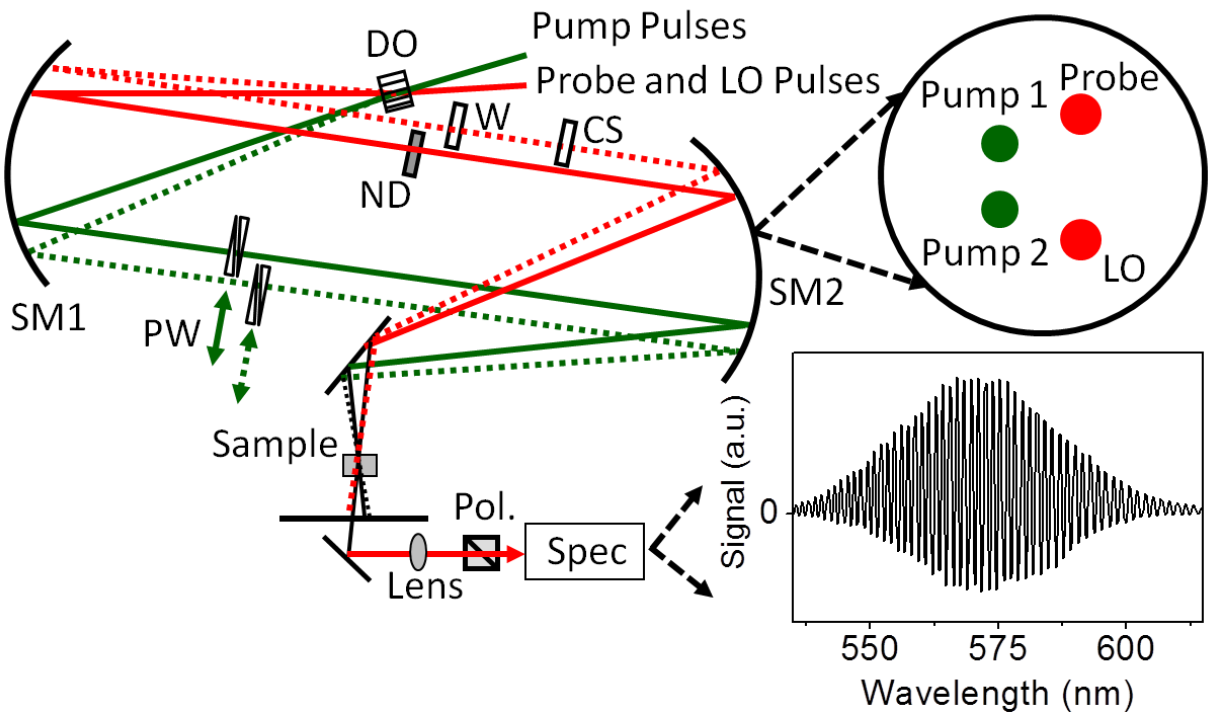

Figure 3.4: Schematic of diffractive optic based interferometer used in TG and 2DPE experiments. For TG, SM1 and SM2 are spherical mirrors located at a distance equal to the sum of their focal lengths; DO is the diffractive optic; ND is a neutral density filter; W is a fused silica window; CS is a cover slip. 2DPE spectroscopy uses prism wedges (PW) to control the delay between pulses. At top right are the locations of the beams on SM2. Bottom right shows a sample interferogram after using a shutter to eliminate the background from probe and local oscillator (reference) fields.

It is important that the phase of the input electric fields remain constant over the course of the experiment since phase fluctuations in these pulses will contribute to the signal phase. In practice, phase stability is difficult to maintain since a change of 16 nm in optical path length produces a shift of approximately 10º in the phase for visible pulses. Minimizing phase drift can be achieved actively by monitoring the phase of each pulse with an interferometer[12]. A simpler setup passively locks the phases of the pulses. A stabilized output is found when the changes in phase $\Delta\phi_i$ for pulse i sum to zero as

$$-\Delta\phi_1 + \Delta\phi_2 + \Delta\phi_3 - \Delta\phi_4 = 0 \qquad (3.7)$$

Focusing two pulses on to a diffractive optic (DO),[5,6] provides two pairs of pulses, $E_1 \& E_2$ and $E_3 \& E_4$, with identical phase fluctuations. These pulses then interact with the same mirrors until they reach the sample. Using the phase relationship above, the path-length fluctuations from the vibration of the mirrors will cancel. The transmissive optics placed in individual pulse paths are thin and produce negligible phase fluctuations. Boxes are put around the interferometer to prevent disturbance from air currents.

The diffractive optic based interferometer used in the experiments is given in Figure 3.4. Pump and probe pulses are focused onto a diffractive optic designed for high efficiency in the ±1 diffraction orders. A spatial filter (not shown) is used to keep only the ±1 diffraction orders as depicted by the inset in Figure 3.4. Pulses of different frequency will diffract at slightly different angles off the diffractive optic. Two spherical mirrors (SM1, SM2) collimate and refocus all four pulses and are placed at the sum of their focal lengths apart to maintain a 4f setup. The reference or local oscillator (LO) electric field is attenuated approximately 1000 times by a 2 mm thick fused silica variable neutral density filter (ND) and arrives at the sample 800 fs before the probe pulse. The probe pulse is delayed by a 2 mm thick fused silica window (W) and two 175 μm thick microscope cover slips (CS). The signal is collimated by a lens after the sample and passes through a polarizer before being dispersed in a spectrograph on to an array detector. Polarizations of all input pulses are controlled by half waveplates (not shown). Photon echo include the use of prism wedges (PW) with a 1º wedge angle mounted on translation stages with computer controlled linear actuators. The wedges impart a delay of 30 fs for each millimeter of prism insertion. An

identical prism pair is placed in the probe path to match dispersion when pump and probe pulses are split from the same pulse.

3.4.2. Transient Grating Spectroscopy

Transient grating (TG) experiments are taken with the diffractive optic based interferometer described above with signals acquired in the $\vec{k}_s = -\vec{k}_1 + \vec{k}_2 + \vec{k}_3$ background free direction. The pulse sequence is given in Figure 3.5. Two pump pulses (E_1, E_2) arrive simultaneously at the sample ($\tau = 0$). The experimentally controlled delay of the probe pulse (E_3) is given as T which is positive when the pump arrives before the probe. The signal emits in time t. The local oscillator arrives approximately a picosecond before the probe pulse. Transient grating spectroscopy with dispersed detection varies the pump-probe delay T and disperses the signal field onto an array detector. The dispersed detection effectively Fourier transforms the signal field into the frequency domain. Transient grating spectra are then represented as a function of T and the Fourier transformed signal ω_t.

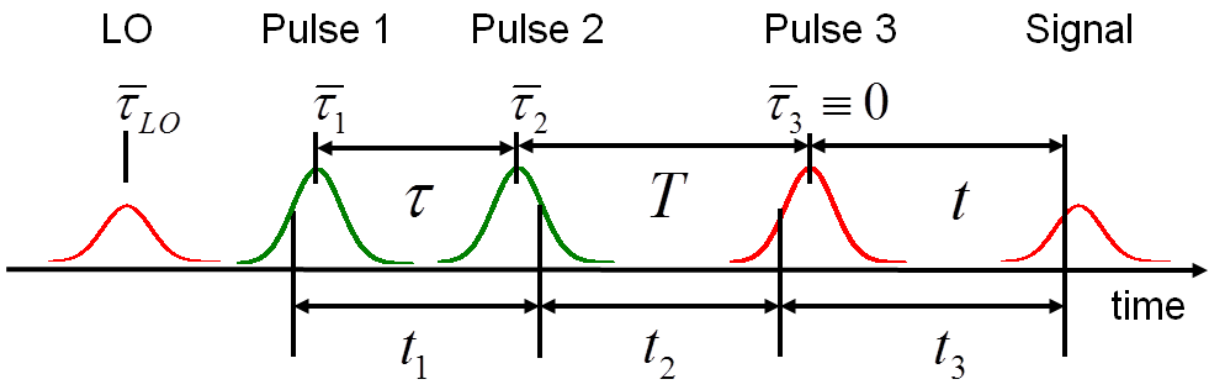

Figure 3.5: Pulse sequence with times used in experiments. Pulse centers are given as $\bar{\tau}_i$ with delays between pulses defined as $\tau = \bar{\tau}_2 - \bar{\tau}_1$ and $T = \bar{\tau}_3 - \bar{\tau}_2$. Field-matter interaction occur at times intervals t_1, t_2, and t_3. The local oscillator (LO) pulse arrives approximately a picosecond before the probe. The colors match the pulses in Figure 3.4.

When a wavepacket is excited into a higher lying state, a "hole" is left in the ground state. This hole is monitored by GSB terms and reveals how long it takes an excited wavepacket to return to the ground state. For dyes in solution, where the fluorescence relaxation pathway dominates, complete recovery occurs on the timescale of fluorescence which is typically several nanoseconds. ESE terms can have excited state population in t_2. This excited state wavepacket will relax according to the nuclear reorganization energy so that at long times, ESE signals will have a profile that matches the fluorescence spectrum. ESA terms are similar to ESE terms except the probe is absorbed into a higher lying state in t_3. ESA terms have an opposite sign than that of GSB and ESE and deconstructively interfere in spectra.

Recasting the response function in equation 2.18 into a function of spectroscopic parameters is important for illustrative purposes. Taking the slow modulation limit of line broadening and that pulses are well separated in time gives the transient grating spectrum with dispersed detection for a two level system as

$$S_{TG}^{DD}\left(\omega_{pu},\omega_{pr};T\right)=\frac{2\pi}{\sqrt{\left(\Delta^2+w_{pu}^2\right)\sigma^2\left(T\right)}}\exp\left[-\frac{\left(\omega_{pu}-\omega_{eg}^0-\lambda\right)^2}{2\left(\Delta^2+w_{pu}^2\right)}\right]$$
$$\times\left\{\exp\left[-\frac{\left(\omega_{pr}-\omega_g\left(T\right)\right)^2}{2\sigma^2\left(T\right)}\right]+\exp\left[-\frac{\left(\omega_{pr}-\omega_e\left(T\right)\right)^2}{2\sigma^2\left(T\right)}\right]\right\} \tag{3.9a}$$

where

$$\omega_g(T) \equiv \omega_{eg}^0 + \lambda + M(T)\left(\omega_0 - \omega_{eg}^0 - \lambda\right)$$
$$\omega_e(T) \equiv \omega_{eg}^0 - \lambda + M(T)\left(\omega_0 - \omega_{eg}^0 + \lambda\right)$$
$$\omega_0 \equiv \omega_{pu}\frac{\Delta^2}{\Delta^2 + w_{pu}^2} + \left(\omega_{eg}^0 + \lambda\right)\frac{w_{pu}^2}{\Delta^2 + w_{pu}^2} \qquad (3.9b)$$
$$\sigma^2(T) \equiv \Delta^2\left[1 - \frac{\Delta^2}{\Delta^2 + w_{pu}^2}M^2(T)\right]$$

and ω_{eg}^0 is the frequency corresponding to the energy gap between ground and excited states, w_i is the bandwidth of pulse i, and $M(T)$ is the solvation correlation function[13]. The solvation correlation function assumes the form of a decaying exponential with time constant Λ^{-1} as

$$M(T) = \exp(-\Lambda T) \qquad (3.9c)$$

The electric fields in equation 3.9 are assumed to have Gaussian envelope functions. The last term equation 3.9a captures ground state bleach (R_1 and R_2) and the next to last term describes excited state emission (R_3 and R_4).

A simulation of equation 3.9 is given in Figure 3.6. The dispersed detection signal width increases while simultaneously redshifting. The timescale of these processes is given by the nuclear timescale, Λ^{-1} and their magnitude is proportional to the reorganization energy. In this model the redshift comes completely from the ESE term since the pump pulse spectrum is centered at the peak of the absorbance spectrum. The wavelength integrated amplitude decays for both ESE and GSB terms according to the nuclear timescale. Only nuclear reorganization takes effect during the delay so the ground state population does not

recover and is given as an offset at long times. This simulation points out the effect of nuclear relaxation and shows that it causes a variety of changes in the spectrum.

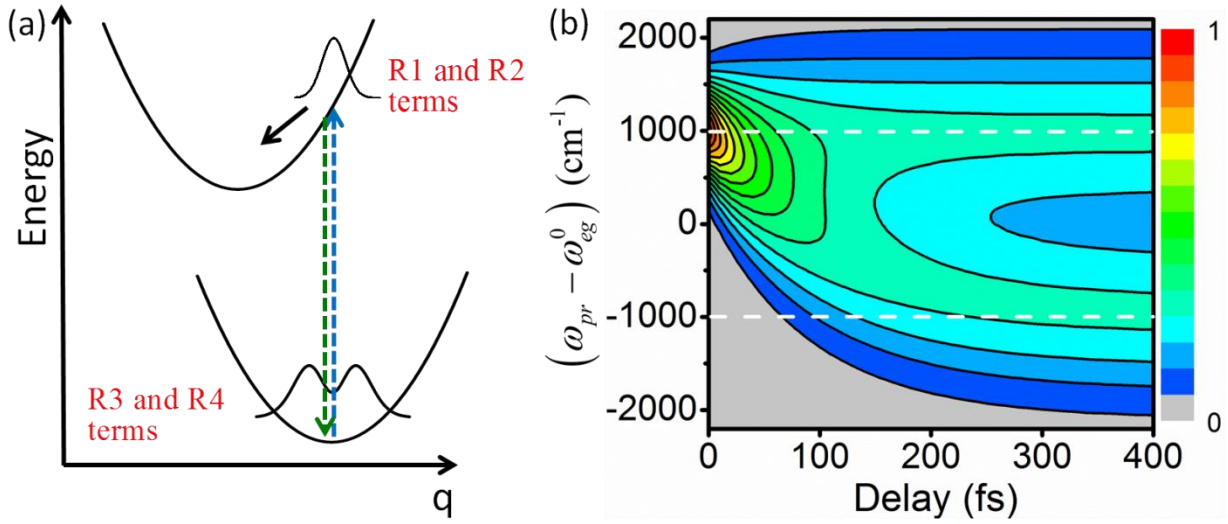

Figure 3.6: Diagram and simulation of nuclear relaxation in a two level system described by equation 3.9. (a) The pump pulse (blue) is tuned to the peak of the absorption spectrum and induced dynamics in both wells monitored by the probe pulse (green). The excited state wavepacket is described by R_1 and R_2 terms; the ground state evolution is described by R_3 and R_4 terms. (b) Dispersed transient grating signal as a function of delay. The y axis is the signal frequency difference from the zero-zero frequency difference between excited and ground state and the x axis is the delay T. The ESE signal moves from the peak of the absorbance at $\omega_{eg}^0 + \lambda$ to the peak of the fluorescence at $\omega_{eg}^0 - \lambda$ shown as white lines in the spectrum. Contours are placed at 6.7% intervals.

If other electronic states are present, excited state wavepackets in t_2 can relax according to rates given by Fermi's Golden Rule. Distinguishing between electronic and nuclear relaxation processes is difficult since they share similar spectroscopic signatures and timescales. Experiments employing specific polarization conditions can distinguish between electronic population transfer and solvation effects[14-16]. The anisotropy is computed as

$$r(T) = \frac{S_{ZZ}(T) - S_{XZ}(T)}{S_{ZZ}(T) + 2S_{XZ}(T)} \tag{3.10}$$

where $S_{ZZ}(T)$ and $S_{XZ}(T)$ represents the real TG signals obtained with all parallel and perpendicular pump and probe pulses, respectively. The anisotropy value decreases when the pump and probe interact with different transition dipole orientations. For a two level system, the anisotropy remains constant in time because only one dipole orientation is present. Nuclear relaxation dynamics do not show up because changes in nuclear state manifest only as a scalar quantity in the transisiton dipole under the Condon approximation. With two excited states, electronic population in t_2 can transfer in time and show up in the anisotropy. It is important to note that nuclear vibrations in the ground state can contribute to the anisotropy when excited state potentials are displaced from each other[16]. Experimentally, pulses are linearly polarized from the laser and 2 mm thick fused silica waveplates rotate the polarization of the input electric fields. A polarizer after the sample selects the signal polarization.

3.4.3. Two-Dimensional Photon Echo Spectroscopy

Transient grating spectroscopy with dispersed detection effectively Fourier transforms the t_3 time interval while information regarding t_1 is averaged. In two-dimensional spectroscopy (2DPE), the pump pulse is effectively dispersed using a Fourier transform technique. The delay, τ, between pulses 1 and 2 is scanned at fixed T. Taking the Fourier transform of this one-dimensional delay provides information during the t_1 time interval[17]. The resulting two-dimensional spectrum is plotted with pump frequency, ω_τ, on the x-axis and probe frequency, ω_t, on the y-axis (Figures 3.7b and 3.8)[17].

During the experiment glass is removed from one pump pulse at a time to keep the delay, T, constant. When glass is removed from pulse 1, R_2 and R_3 terms dominate, while R_1 and R_4 terms dominate when glass is removed from pulse 2 due to the pulse order. Terms R_2 and R_3 are known as rephasing terms since the elements of the density matrix are reversed in time t_3 compared to time t_1 while R_1 and R_4 are known as nonrephasing terms. To obtain a projection where the real part of the electric field signal is purely absorptive, rephasing and nonrephasing terms are summed[17,18].

Two-dimensional spectra provide a detailed map for tracking population transfer. Wavepackets excited at a certain energy in t_1 and emitted at a different in t_3 energy show up as off-diagonal peaks in two dimensional spectra. The transient grating signal is a projection of the two dimensional signal onto the probe axis which hides the presence of these cross peaks. In Figure 3.7, the higher energy state directly transfers population to the lower energy state and appears as a cross peak in the two-dimensional spectrum. In systems with several excited states, two-dimensional photon echoes can distinguish detailed relaxation pathways between resonances where it would not be possible to do so with transient grating spectroscopy[19].

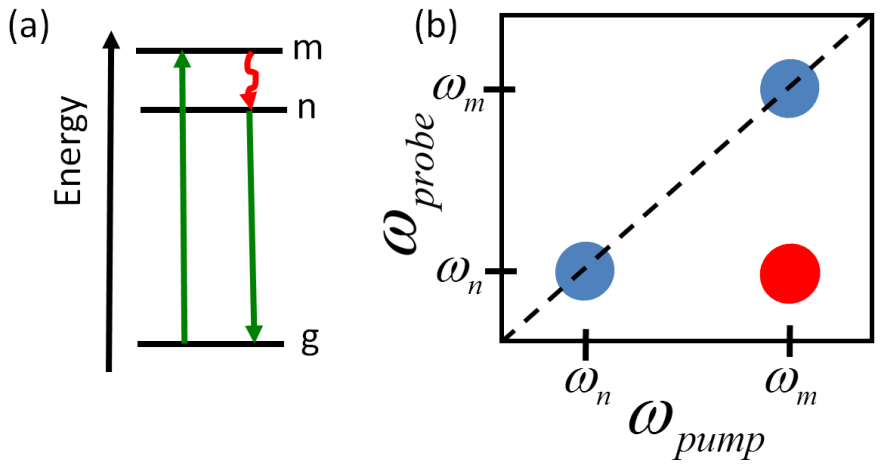

Figure 3.7: Energy level diagram showing ground, g, and excited states m and n. A red arrow symbolizes population transfer from state m to n. (b) Schematic of two dimensional diagram produced by an experiment in which electric field bandwidth spans states m and n. The interaction of pulse energies leading to the formation of the red cross-peak is given by green arrows in (a).

In the rephasing terms, the phase evolves in an opposite direction in t_1 compared to t_3 and cancels out, leaving only the homogeneous linewidth. This cancellation is called a photon echo from its similarity to spin echoes in NMR spectroscopy[20]. To explain the effect of rephasing, consider the terms in the response function for the same system described in equation 3.9,

$$
\begin{aligned}
R_1(t_1,t_2,t_3) &= \exp\left(-i\omega_{eg}t_1 - i\omega_{eg}t_3\right)\exp\left[-\frac{1}{2}\Delta^2 t_1^2 - \frac{1}{2}\Delta^2 t_3^2 - 2i\lambda\left[M(t_2)-1\right]t_3 - \Delta^2 M(t_2)t_1t_3\right] \\
R_2(t_1,t_2,t_3) &= \exp\left(i\omega_{eg}t_1 - i\omega_{eg}t_3\right)\exp\left[-\frac{1}{2}\Delta^2 t_1^2 - \frac{1}{2}\Delta^2 t_3^2 - 2i\lambda\left[M(t_2)-1\right]t_3 + \Delta^2 M(t_2)t_1t_3\right] \\
R_3(t_1,t_2,t_3) &= \exp\left(i\omega_{eg}t_1 - i\omega_{eg}t_3\right)\exp\left[-\frac{1}{2}\Delta^2 t_1^2 - \frac{1}{2}\Delta^2 t_3^2 + \Delta^2 M(t_2)t_1t_3\right] \\
R_4(t_1,t_2,t_3) &= \exp\left(-i\omega_{eg}t_1 - i\omega_{eg}t_3\right)\exp\left[-\frac{1}{2}\Delta^2 t_1^2 - \frac{1}{2}\Delta^2 t_3^2 - \Delta^2 M(t_2)t_1t_3\right]
\end{aligned}
\tag{3.11}
$$

This equation assumes pulses are well separated compared to their width and all line broadening comes from inhomogeneous broadening. The real and imaginary parts of the

equation above are responsible for line broadening and peak positions, respectively. The last term in the equations convolutes the dynamics in t_1 and t_3 time intervals with the inhomogeneous broadening. At short delays in the rephasing equations R_2 and R_3, this term will cancel the broadening terms before it. This cancellation is manifest in the two-dimensional Fourier transform spectra as only having amplitude when $\omega_\tau = \omega_t$. A simulation of this effect is given in Figure 3.8 using equation 3.9 with resolution in the pump dimension given by setting the pump width to zero ($w_{pu} = 0$). Inhomogeneous broadening is given by the projection onto the probe axis and the antidiagonal width reflects homogeneous broadening which is narrow due to cancellation in the rephasing terms. No homogeneous broadening is present in the equation above since it was derived in the slow modulation limit. At long times the correlation function decays to zero which causes a redshift in the ESE terms and the spectrum to appear round. Photon echoes are one of the few employed spectroscopies which can directly measure homogeneous broadening.

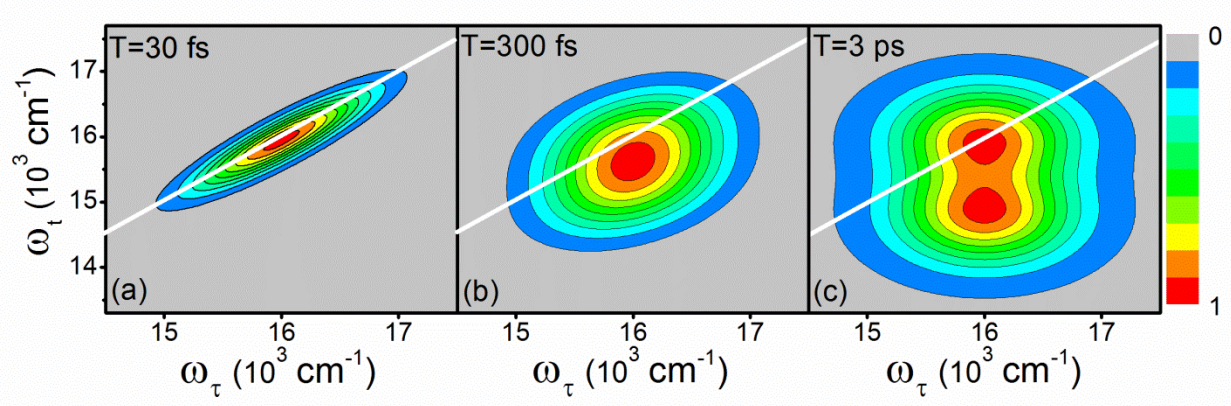

Figure 3.8: Simulated two-dimensional photon echo spectra on a two level system at times short (T=30 fs) to long (T=3 ps) compared to the bath timescale. (a) At short times frequencies remain correlated over the course of the experiment and the spectrum is elongated along the diagonal. (b) At 300 fs the shape becomes more round as the correlation function decays. (c) At times long compared to the timescale of the bath, no tilt is observed in the spectrum. Also, the excited state wavepacket has moved to 2λ giving a separate peak at

$\omega_\tau = 14800$ cm^{-1} and $\omega_t = 16000$ cm^{-1}. The white line represents $\omega_\tau = \omega_t$. These simulations are formed from equation 3.9 with resolution added in the pump dimension (i.e., $w_{pu} = 0$).

3.5. CONCLUSION

For the systems presented in this dissertation, the above techniques are essential to look at sensitive samples absorbing in the visible spectrum. Commercial Ti:sapphire self-modelocked oscillators provide stability for long experiments. OPAs provide broad bandwidth pulses over the visible region with ample pulse energies. Pulse compression to several femtoseconds is achieved through prism pairs and characterization is provided by frequency resolved optical gating methods. Signal to noise ratios are improved using heterodyne detection and a noncollinear experimental geometry to induce signals in a background free direction. Even with these advantages, many events such as solvation and electronic energy transfer, share a similar timescale and spectroscopic signature. Sophisticated experiments employing control over the incident electric field frequency, bandwidth, or polarization and experiments such as two dimensional photon echo spectroscopy are useful in this regard. In general, a variety of experiments are combined to investigate a system.

REFERENCES

(1) Siegman, A. E. *Lasers*; University Science Books: Sausalito, 1986.

(2) Backus, S.; Durfee, C. G. I.; Murnane, M. M.; Kapteyn, H. C. *Rev. Sci. Instrum.* 1998, *69*, 1207.

(3) Spence, D. E.; Kean, P. N.; Sibbett, W. *Opt. Lett.* 1991, *16*, 42.

(4) Cerullo, G.; De Silvestri, S. *Rev. Sci. Instrum.* 2003, *74*, 1.

(5) Goodno, G. D.; Dadusc, G.; Miller, R. J. D. *J. Opt. Soc. Am. B* 1998, *15*, 1791.

(6) Maznev, A. A.; Nelson, K. A.; Rogers, J. A. *Opt. Lett.* 1998, *23*, 1319.

(7) Boyd, R. W. *Nonlinear Optics, Second Edition*; Academic Press: San Diego, 2003.

(8) Trebino, R. *Frequency Resolved Optical Gating: The Measurement of Ultrashort Laser Pulses*; Kluwer Academic Publishers: Boston, Dordrecht, London, 2000.

(9) Riedle, E.; Beutter, M.; Lochbrunner, S.; Piel, J.; Schenkl, S.; Spörlein, S.; Zinth, W. *Appl. Phys. B* 2000, *71*, 457.

(10) Baltuska, A.; Fuji, T.; Kobayashi, T. *Optics Letters* 2002, *27*, 306.

(11) Brixner, T.; Mancal, T.; Stiopkin, I. V.; Fleming, G. R. *J. Chem. Phys.* 2004, *121*, 4221.

(12) Scherer, N. F.; Carlson, R. J.; Matro, A.; Du, M.; Ruggiero, A. J.; Romero-Rochin, V.; Cina, J. A.; Fleming, G. R.; Rice, S. A. *J. Chem. Phys.* 1991, *95*, 1487.

(13) Mukamel, S. *Principles of Nonlinear Optical Spectroscopy*; Oxford University Press: New York, 1995.

(14) Qian, W.; Jonas, D. M. *J. Chem. Phys.* 2003, *119*, 1611.

(15) Fleming, G. R. *Chemical Applications of Ultrafast Spectroscopy*; University Press: New York, 1986.

(16) Farrow, D. A.; Smith, E. R.; Qian, W.; Jonas, D. M. *J. Chem. Phys.* 2008, *129*, 174509:1.

(17) Hybl, J. D.; Albrecht Ferro, A.; Jonas, D. M. *J. Chem. Phys.* 2001, *115*, 6606.

(18) Khalil, M.; Demirdöven, N.; Tokmakoff, A. *J. Phys. Chem. A* 2003, *107*, 5258.

(19) Cho, M.; Vaswani, H. M.; Brixner, T.; Stenger, J.; Fleming, G. R. *J. Phys. Chem. B* 2005, *109*, 10542.

(20) Ernst, R. R.; Bodenhausen, G.; Wokaun, A. *Principles of Nuclear Magnetic Resonance in One and Two Dimensions*; Oxford University Press: New York, 1987.

CHAPTER 4. EXCITON COHERENCE AND ENERGY TRASPORT IN THE LIGHT-HARVESTING DIMERS OF ALLOPHYCOCYANIN

4.1. INTRODUCTION

Underlying photosynthetic light harvesting is a complicated world of fluctuating nuclei whose amplitudes, rates and many-body correlations govern the fate of electronic excitations.[1-3] It is well-established that interactions between pigments and the surrounding environment (e.g., protein matrix, aqueous solvent) span a range of strengths and time scales.[4-6] Spatially correlated environmental fluctuations add a particularly rich dimension to the picture.[7-13] Correlations in the environment-induced fluctuations of energy gaps and couplings in systems composed of multiple pigments can, in principal, range from full correlation to full anti-correlation. The complexity of this phenomenon challenges modern experimental techniques and theory. Nonetheless, the impact of correlated dynamics can be substantial and have been found to boost the contribution of coherent light harvesting mechanisms by 20% in the Fenna-Matthews-Olson protein.[10] Further theoretical and experimental investigations are required to fully understand how biological antennae use correlations to enhance function. This understanding will likely apply to artificial systems.[14,15]

Correlated dynamics influence energy transfer kinetics in both weak and intermediate coupling regimes. Recent work illustrates how correlated excited state (i.e., exciton) energy level fluctuations give rise to recurrences in energy transfer.[15-17] These recurrences reflect

partially correlated fluctuations at the donor and acceptor sites, where the requirement for partial correlation can be understood with consideration of two well-defined limits. In the strong-coupling limit, full energy donor and acceptor correlation manifests as "Rabi-like" oscillations in electronic populations, whereas irreversible relaxation takes hold when coupling between the donor and acceptor is weak compared to the system-bath interaction strength. It is also important to recognize that donor and acceptor units can possess internal structure whose dynamics can influence energy transfer kinetics through correlated line broadening.[18-21] That is, the spectroscopic line shapes entering Förster's rate formula generally reflect the extent to which spatially correlated dynamics occur within the molecular complexes comprising the donor and/or acceptor units.[22] Nonlinear spectroscopies have proven useful for uncovering many aspects of line broadening,[23,24] whereas spatial correlations remain elusive due to their complex many-body nature.[25,26] Advances in the understanding of correlated line broadening will require the application of specialized experimental techniques to appropriate model systems.[22,27]

In this chapter, we investigate photoinduced relaxation dynamics in Allophycocyanin (APC) using transient grating and photon echo spectroscopies. Signals are analyzed using a theoretical model to obtain the parameters of a Frenkel exciton Hamiltonian. APC is a particularly good model for the study of exciton dynamics because of its well-defined geometry and electronic structure.[28-30] Figure 4.1 shows that the X-ray crystal structure of APC possesses a three-fold axis of symmetry consisting of three dimers with phycocyanobilin pigments separated by 2.1 nm.[31] Pairs of dimers interact weakly because they are separated by distances of approximately 5 nm. Thus, to a good approximation, coupling between pairs of phycocyanobilin transforms the electronic structure into an

"exciton" basis consisting of four levels, where the linear absorption spectrum presented in Figure 4.1c corresponds to transitions between the ground state and the two single exciton levels. The peak at 15300 cm^{-1} predominantly represents the lower energy transition to $e+$, whereas the higher energy transition to $e-$ appears as a broad "shoulder" centered at 16200 cm^{-1}. Although vibronic structure is not well-resolved in the linear absorption spectrum, this chapter will show that vibronic coupling is essential to fitting the absorption line shape and also to the description of internal conversion between exciton states. For example, a significant portion of the intensity underneath the 16200 cm^{-1} band is associated with the Franck-Condon progression of the $e+$ transition if the fluorescence spectrum is taken to be the mirror image of the $e+$ absorption line shape,[32] where mirror image symmetry assumes identical vibronic structure for the absorption and fluorescence spectra (i.e., equivalent normal modes and vibrational frequencies for the ground and excited states).[6,33]

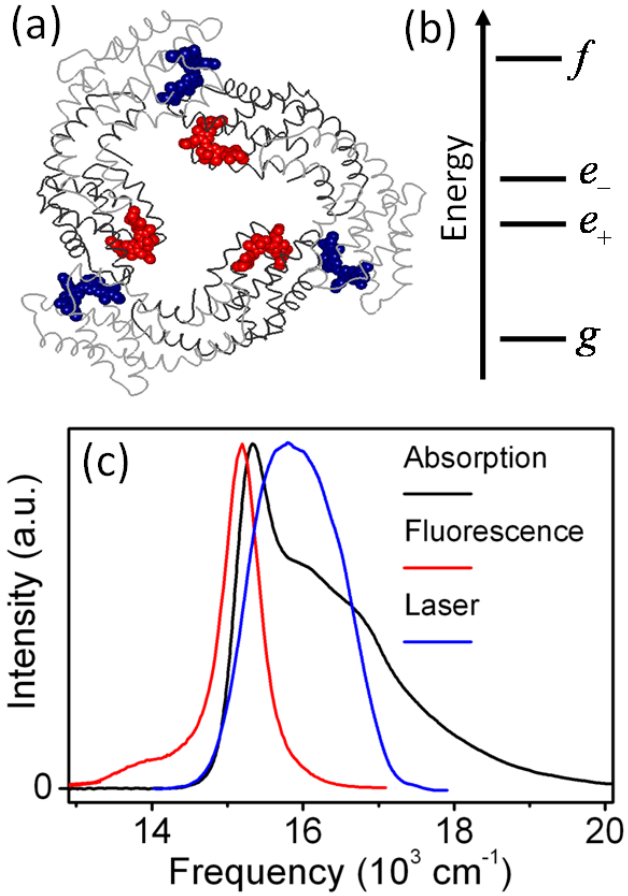

Figure 4.1. (a) Structure of APC trimer in which blue and red respectively signify α84 and β84 subunits. (b) Each pigment dimer possesses four-level exciton electronic structure. (c) Absorption (black) and fluorescence emission (red) spectra ofAPC. Overlaid in blue is the spectrum of the 15 fs laser pulse used in this work

Spectroscopic signatures of correlated line broadening are difficult to ascertain. In principal, the analysis of two-dimensional photon echo line shapes measured at a fixed population time is a direct route to uncovering these dynamics.[18-22] However, interference between transitions (i.e., spectral overlap) prevents this approach for most pigment complexes because energy gaps between the multiple exciton levels are generally comparable to the spectroscopic line widths. Alternative approaches first prepare coherent superpositions of electronic states, then monitor the loss of correlation in the time domain

(e.g., pump-probe anisotropy).[9,14,17,22,34-39] The rate of decoherence for a pair of excitons generally increases with decreasing exciton correlation. In essence, the instantaneous distribution of energy gaps in an ensemble broadens in the absence of correlation; fast damping is the natural outcome of superposing many oscillators with incommensurate frequencies. Here we examine signatures of correlated line broadening encoded in the dephasing rates of photoexcited coherent superposition states. Correlation within the dimer of APC is quantitatively evaluated with the support of a theoretical model.

Beck and co-workers have investigated femtosecond dynamics of APC with a variety of four-wave mixing spectroscopies.[28,32,40,41] It was firmly established that the 15300 cm^{-1} and 16200 cm^{-1} absorption bands in APC correspond to exciton states associated with the phycocyanobilin dimers. Pump-probe anisotropy experiments found that internal conversion between exciton states occurs with time constants of 30-56 fs and 280 fs,[28] whereas photon echo spectroscopy identified an additional 220 fs relaxation process.[41] Sub-picosecond red-shifting of the transient absorption signal spectrum was attributed to inertial solvation processes and relaxation within the manifold of photoexcited intramolecular nuclear coordinates (i.e., vibrational cooling).[40] Of particular relevance to the present chapter is the suggestion of imperfect correlation between exciton states discussed in Reference [41]. Technical advances in nonlinear optics and spectroscopic techniques occurring in the last decade now allow this issue to be more carefully examined here.

Strong vibronic coupling of a large number of intramolecular modes is known to occur APC[42-44] as well as other phycobiliproteins.[45-47] Resonance Raman experiments observe a large number of transitions in the vibrational fingerprint region.[43,44] In addition, the analysis of earlier pump-probe measurements performed with 16 fs pulses yielded large

Huang-Rhys factors for several vibrations.[42] The strong vibronic coupling observed in these experiments reflects the displacement of equilibrium nuclear coordinates for the ground state compared to the single exciton states. However, efficient internal conversion between $e-$ and $e+$ requires that significant geometric distortion occurs in the transition between excited states. Below we suggest that a promoting mode near 800 cm^{-1} assists in the sub-picosecond internal conversion of APC because the energy gap between the $e+$ and $e-$ exciton states exceeds the characteristic frequency of overdamped nuclear motion in the bath (i.e., spectral density).

4.2. EXPERIMENT

Allophycocyanin (APC) was purchased from Prozyme as a suspension in 60% ammonium sulfate. Spectroscopic measurements used solutions of APC in 100 mM potassium phosphate buffer at pH 7.0. All experiments were performed within 12 hours of solution preparation. Optical experiments circulated the solutions at a rate of 10 mL/s in flow system using a peristaltic pump with reservoir of 10 mL. The absorbance of the solution was 0.15 at 15300 cm^{-1} in the 0.5 mm path length flow cell. Absorbance spectra were measured before and after optical experiments to confirm the absence of sample degradation.

Transient grating (TG) and photon echo (PE) experiments utilize a Quantronix Integra C Titanium Sapphire amplifier producing 800 nm, 120 fs laser pulses at 1 kHz. The laser system pumps a home-built noncollinear optical parametric amplifier (NOPA) yielding pulses with a spectrum spanning 500-750 nm. The portion of the full spectrum shown in Figure 4.1c is obtained by filtering the higher and lower frequency spectral content in a fused

silica prism compressor. Pulses are compressed to 15 fs duration and characterized using transient grating frequency resolved optical gating.[48]

TG and PE experiments are performed using the same passively phase-stabilized, diffractive optic-based interferometer for which a detailed description is given in Reference [22]. The interferometer design resembles that reported in several earlier publications.[49-57] Briefly, a boxcars (i.e., square) laser beam geometry is used to generate a signal in the $\mathbf{k_S} = -\mathbf{k}_1 + \mathbf{k}_2 + \mathbf{k}_3$ phase matched direction. All three pulses and a local oscillator field are derived from the same NOPA. Times at which the E_1 and E_2 pulses arrive at the sample are varied by inserting independent prism wedges in the paths of both beams, whereas a conventional optical delay line controls the arrival of the E_3 and local oscillator pulses. The E_3 and local oscillator pulses pass through an identical pair of prism wedges to ensure that all four pulses possess identical dispersion. Pulses with energies of 5 nJ are focused to a120 um spot size at the sample for a fluence of 1.4×10^{14} photons/cm^2. Increasing the pulse energies by a factor of four has no effect on the measured dynamics. Signals are detected using spectral interferometry with a back-illuminated CCD array (Princeton Instruments PIXIS 100B) mounted on a 0.3 meter spectrograph (Princeton Instruments). Integration times are 100-200 ms. A Fourier transform algorithm is used to process the measured interferograms.[52 ,53,58-60]

The TG signals presented here represent the average of 15 scans of the optical delay line. Anisotropies compare tensor elements for real (absorptive) signal components measured in immediate succession, where data acquisition for one tensor element requires approximately 25 minutes. The experiments were repeated several times and suggest that this procedure yields an error of approximately +/- 0.03 in the anisotropy. PE scans acquire

two-dimensional spectra at a series of population times, T, as described in Reference [22]. Rephasing and non-rephasing signals are superposed to obtain absorptive spectra.[60,61] Scans of photon echo spectra at a series of population times are repeated 10 times and averaged for a total data acquisition time of 5 hours.

The real and imaginary components of the TG and PE signals are defined by reference to the pure buffer solution, which is taken to possess a fully dispersive (imaginary) signal phase because it is transparent to visible light. The phases are calibrated by measuring TG signal fields with the buffer, then exchanging the sample reservoir with APC solution without moving the flow cell. With the known phase of the TG signal for APC, the PE signal phase is readily obtained using the projection slice theorem of Fourier transforms.[62] Two-dimensional PE signals are integrated over the ω_τ dimension (i.e., Fourier transform of τ delay), and the phase of this projection is adjusted for agreement with the TG signal phase. Earlier investigations successfully use this same phasing procedure.[52,63]

4.3. MODELING SPECTROSCOPIC SIGNALS

This Section presents a theoretical model that will be used to interpret all linear and nonlinear spectroscopic measurements in this chapter. The foundation of the model is taken from Sections 5.1 and 5.2 of Reference [25], where the cumulant expansion of Gaussian fluctuations (CGF) yields line broadening functions and incoherent exciton transport rates. The CGF model is chosen because of its demonstrated success in the simulation of correlated line broadening dynamics.[18] Experimentally detected signals in the following Sections will show that vibronic coupling is an important component of the optical response of APC. Below, the model of Reference [25] is supplemented to capture these vibronic coupling effects.

4.3.1. Description of Correlated Line Broadening in the Basis of Pigment Sites

The Frenkel exciton model with CGF line broadening dynamics has been presented in full detail elsewhere.[25,26] Here we present some of the fundamental equations to establish notation and aspects of the model specific to the present treatment. The equations are written for general application to systems with arbitrary numbers of molecules. The Hamiltonian of the pigment complex is partitioned into three components as

$$H = H_{Sys} + H_{Bath} + H_{Sys-Bath} \tag{4.1}$$

where the system Hamiltonian is given by

$$H_{Sys} = \sum_{m}^{N} E_m B_m^{\dagger} B_m + \sum_{m}^{N} \sum_{n \neq m}^{N} J_{mn} B_m^{\dagger} B_n \tag{4.2}$$

Here E_m is the energy gap of molecule m and J_{mn} is the electrostatic coupling between molecules m and n, and N is the number of molecules in the complex. The CGF treatment of line broadening describes the time scale and magnitude of fluctuations in E_m with the parameters Λ_{mm}^{-1} and Δ_{mm}, respectively. Correlated fluctuations at different pigment sites are found with the Cauchy-Schwartz inequality[18]

$$\Delta_{mn}^2 = \eta_{mn} \Delta_{mm} \Delta_{nn} \tag{4.3}$$

where η_{mn} interpolates between the fully correlated, $\eta_{mn} = 1$, and anti-correlated, $\eta_{mn} = -1$, limits. To minimize the number of adjustable parameters in this chapter, we assume that all Λ_{mn} and Δ_{mn} possess the same ratio $\kappa = \Lambda_{mn} / \Delta_{mn}$. Therefore, fluctuations at a pair of molecular sites, m and n, are fully described with four parameters: Δ_{mm}; Δ_{nn}; η_{mn}; κ. Our model calculations further assume the overdamped Brownian oscillator line broadening function in the high temperature limit

$$g'_{mn}(t) = g'_{nm}(t) = \frac{1}{\kappa^2} \left(1 - i \frac{\kappa \Delta_{mn}}{2 k_B T} \right) \left[\exp\left(-\Lambda_{mn} |t| \right) + \Lambda_{mn} t - 1 \right] \tag{4.4}$$

4.3.2. Transforming Line Broadening Functions into the Exiton Basis

The Hamiltonian matrix is diagonalized in a basis of zero, one and two excitations yielding a ground state, N single exciton states, and $N(N-1)/2$ double exciton states.[21,25,26] Eigenvectors of the single and double exciton states are respectively written as

$$|a\rangle = \sum_{m}^{N} \phi_{am} |m\rangle \tag{4.5}$$

and

$$|c\rangle = \sum_{m=1}^{N-1} \sum_{n+1}^{N} \xi_{c,mn} |m\rangle |n\rangle \tag{4.6}$$

This chapter reserves the dummy indices a *and* b *for single exciton states and* c *for the double exciton manifold.* Transformation of the line broadening functions from the local to exciton basis is accomplished using

$$g'_{ab}(t) = g'_{ba}(t) = \sum_{n=1}^{N} \sum_{m=1}^{N} \phi_{am}^2 \phi_{bn}^2 g'_{mn}(t) \tag{4.7}$$

$$g'_{ac}(t) = g'_{ca}(t) = \sum_{n=1}^{N} \sum_{m=1}^{N-1} \sum_{k=m+1}^{N} \phi_{a,m}^2 \xi_{c,nk}^2 \left[g'_{mn}(t) + g'_{mk}(t) \right] \tag{4.8}$$

$$g'_{cd}(t) = g'_{dc}(t) = \sum_{m=1}^{N-1} \sum_{n=m+1}^{N} \sum_{k=1}^{N-1} \sum_{l=k+1}^{N} \xi_{c,mn}^2 \xi_{d,kl}^2 \left[g'_{mk}(t) + g'_{ml}(t) + g'_{nk}(t) + g'_{nl}(t) \right] \tag{4.9}$$

where the symmetrized line broadening function is defined as $g_{mn}(t) \equiv g'_{mn}(t) + g'_{nm}(t)$.[24] Damping imposed by loss of correlation between a pair of single exciton states is described by $g_{ab}(t)$; $g_{ac}(t)$ corresponds to single exciton a and double exciton c; $g_{cd}(t)$ refers to double excitons c and d.

4.3.3. Nonlinear Response Functions

Under perfect phase-matching conditions, the signal field is related to the third-order polarization by

$$E_S(t) = \frac{i2\pi l\omega_t}{n(\omega_t)c} P^{(3)}(t), \tag{4.10}$$

where $n(\omega_t)$ is the refractive index, l is the sample thickness, and c is the speed of light. The polarization, $P^{(3)}(t)$, is induced with three applied fields, E_j, which can be written as[62]

$$E_j(t) = \varepsilon(t-\bar{\tau}_j)\cos\left[\omega_j(t-\bar{\tau}_j)\right] \tag{4.11}$$

where $\varepsilon(t-\bar{\tau}_j)$ is a Gaussian envelope centered at time $\bar{\tau}_j$ (see Figure 4.2) and ω_j is the carrier frequency of the field. The Feynman diagrams shown in Figure 4.3 represent the 10 dominant terms in the nonlinear response function, where all terms assume that the two "pump" pulses, E_1 and E_2, interact with the sample before the "probe" pulse, E_3.[25] This assumption is inherent to the "doorway-window" treatment of exciton transport introduced below.

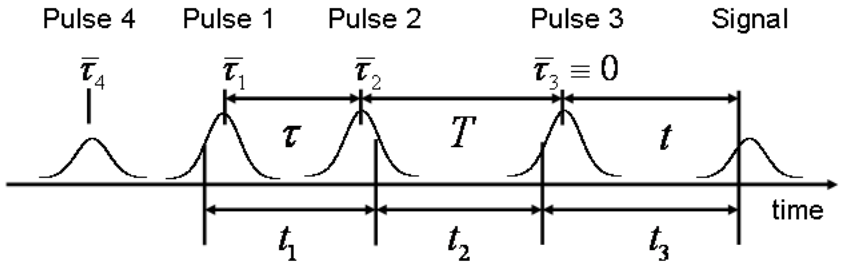

Figure 4.2. Pulse sequence used for TG and PE spectroscopies. Arrival times of the four pulses (at their peaks) are represented by $\bar{\tau}_i$. The delays, $\tau = \bar{\tau}_2 - \bar{\tau}_1$ and $T = \bar{\tau}_3 - \bar{\tau}_2$, are experimentally controlled. Intervals between field-matter interaction times are given by t_1,

t_2 and t_3. Pulse 4 is a reference field (i.e., local oscillator) used for interferometric signal dection.

This chapter finds that the accurate fitting of spectroscopic signals for APC must account for vibronic coupling. Vibronic structure is described *ad hoc* by adding two nuclear modes to the exciton basis. Below it is shown that, although the vibronic manifold is introduced in the exciton basis, the model still yields a microscopic interpretation because the vibrations are localized to the phycocyanobilin pigments comprising the dimers of APC. Response functions for terms in the first two rows of Figure 4.3 are given in Reference [25]. To make clear the specifics of the present treatment, we demonstrate how vibronic levels and electric field polarization effects are addressed using the $R_1(t_1,t_2,t_3)$ term as an example. The expression

$$R_1(t_1,t_2,t_3)=\sum_{ab}\mu_{ag}^2\mu_{bg}^2\exp\left(-i\omega_{ag}t_1+i\omega_{ba}t_2-i\omega_{ag}t_3-\frac{1}{2}f_1(t_1,t_1+t_2,t_1+t_2+t_3,0)\right) \quad (4.12)$$

is obtained directly from Equations (5.26) in Reference [25], where a sum of line broadening functions is obtained by expansion of $f_1(t_1,t_1+t_2,t_1+t_2+t_3,0)$, using Equation (5.27). Electric field polarizations and vibronic coupling are incorporated by rewriting Equation (4.12) as

$$\begin{aligned}R_1(t_1,t_2,t_3)=\sum_{ab}\left\langle\alpha_{gb}\beta_{ag}\gamma_{bg}\chi_{ga}\right\rangle Z_{ab}^1(t_1,t_2,t_3)\exp\Big(&-i\omega_{ag}t_1-i\omega_{ab}t_2-i\omega_{ag}t_3\\&-\frac{1}{2}f_1(t_1,t_1+t_2,t_1+t_2+t_3,0)\Big)\end{aligned} \quad (4.13)$$

The orientational factor, $\left\langle\alpha_{gb}\beta_{ag}\gamma_{bg}\chi_{ga}\right\rangle$, is given in Appendix A and vibronic coupling is described by

$$
\begin{aligned}
Z^{1}_{ab}\left(t_1,t_2,t_3\right) = {} & F^{00}_{a}F^{00}_{b} + \sum_{\nu=1}^{2} F^{01}_{a\nu}F^{00}_{b}\exp\left[-\left(i\omega_{\nu}+k_{\nu}\right)\left(t_1+t_2+t_3\right)\right] \\
& + F^{00}_{a}F^{01}_{b\nu}\exp\left[\left(i\omega_{\nu}-k_{\nu}\right)t_2\right] \\
& + \delta_{ab}F^{01}_{a\nu}F^{00}_{b\nu}\exp\left(-i\omega_{\nu}t_1-k_{\nu}\left(t_1+t_2\right)\right)\left[\exp\left(-i\omega_{\nu}t_3-k_{\nu}t_3\right)+\left(\exp\left(k_{\nu}t_2\right)-1\right)\right]
\end{aligned}
\tag{4.14}
$$

where ω_{ν} is the frequency of mode ν, F^{00}_{a} is the Franck-Condon factor coupling the ground state to the electronic origin of excited state a, $F^{01}_{a\nu}$ is the Franck-Condon factor corresponding to a process in which photoexcitation initiates at the ground state and terminates in the first excited vibronic level of electronic state a and mode ν, and k_{ν} represents the inverse lifetime of mode ν (i.e., vibrational cooling rate). Equation (4.14) keeps only the dominant terms in which at least two field matter interactions couple the electronic origins of the ground and excited states. Neglect of higher-order terms is appropriate for systems, such as APC, in which the 0-0 transitions possess the largest Franck-Condon factors. Signal components evolving as excited state nuclear coherences in t_2 can also be envisioned for diagrams in which $a=b$ and/or $a\neq b$.[64,65] However, the TG and PE signals of APC are well-captured without this additional complexity because terms with four field-matter interactions coupling the electronic origins of g and a (or g and b) possess the largest nonlinearities.

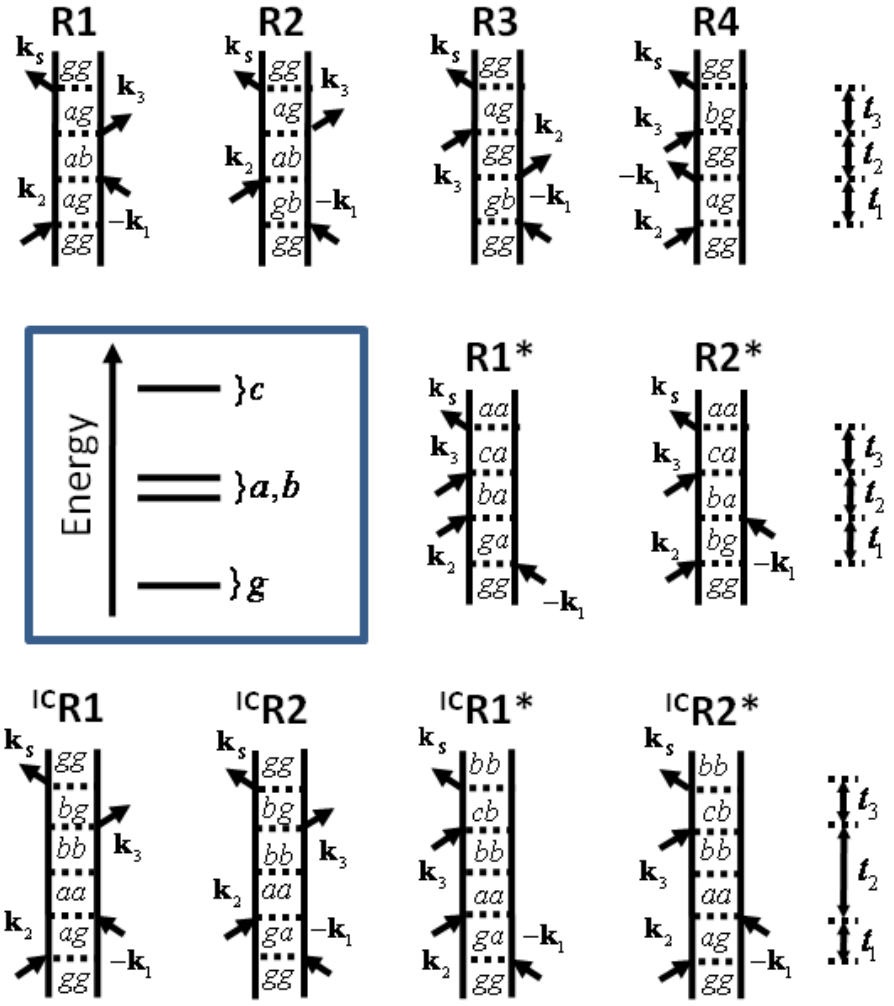

Figure 4.3. Feynman diagrams for dominant terms in the transient grating and photon echo spectroscopies in this chapter. The dummy indices a and b are used for single exciton states, whereas c is reserved for the double exciton manifold. The superscript IC used in the bottom row denotes incoherent exciton transport. Terms in the nonlinear response function corresponding to these diagrams are presented in Section 4.3.3 and Appendix B.

The physical significance of $Z_{ab}^{1}(t_1,t_2,t_3)$ is made clear by considering it as the sum of three terms. The first term, which is simply equal to $F_a^{00}F_b^{00}$, represents a sequence in which all four field-matter interactions couple the electronic origins (i.e., 0-0 transitions). The second term accounts for all field-matter interaction sequences evolving in a vibronic coherence during the t_2 interval. Finally the third term, which is linear in the delta function,

δ_{ab}, populates the first vibronic level of mode ν at t_2 =0, then relaxes to the electronic origin at the rate k_ν. This term captures the short and long time limits of intramolecular nuclear relaxation by ensuring that stimulated emission occurs from hot vibronic states at short t_2, and from the electronic origins of the excited states at long t_2. Expressions for the terms in the response function corresponding to the five other diagrams in the first two rows of Figure 4.3 are given in Appendix B.

The CGF model describes fluctuations of the exciton energies and captures essential aspects of spectroscopic line shapes. However, fluctuations in the exciton couplings are needed for simulation of exciton transport. The doorway-window treatment of the nonlinear response, which is valid for well-separated pump and probe pulses, describes line broadening and population transfer on the same footing.[66] The doorway-window model is appropriate for APC because the dominant population transfer channel occurs with a time constant over 18 times larger than the experimental laser pulse duration. For convenience, the response function is partitioned into rephasing and nonrephasing terms. The rephasing, S_{OD}^{RP}, and nonrephasing, S_{OD}^{NRP}, components of the response function are respectively given by

$$S_{OD}^{RP}(t_1,t_2,t_3)=\sum_{ab}\left[W_{ab}^{ESE}(t_3)-W_{ab}^{ESA}(t_3)\right]D_a(-t_1)\left[G_{ba}(t_2)-1\right]-S_D^{RP}(t_1,\infty,t_3) \tag{4.15}$$

and

$$S_{OD}^{NRP}(t_1,t_2,t_3)=\sum_{ab}\left[W_{ab}^{ESE}(t_3)-W_{ab}^{ESA}(t_3)\right]D_a(t_1)\left[G_{ba}(t_2)-1\right]-S_D^{NRP}(t_1,\infty,t_3) \tag{4.16}$$

where the subscript, OD, refers to off-diagonal elements of the Hamiltonian (i.e., inter-exciton couplings). In $S_{OD}^{RP}(t_1,t_2,t_3)$ [$S_{OD}^{NRP}(t_1,t_2,t_3)$], the terms linear in the window

functions, $W_{ab}^{ESE}(t_3)$ and $W_{ab}^{ESA}(t_3)$, respectively correspond to the ^{IC}R2 and ^{IC}R1* [^{IC}R1 and ^{IC}R2*] terms in Figure 4.3. The doorway function is written as

$$D_a(t_1) = \exp\left[-i\omega_{ag}t_1 - g_{aa}(t_1)\right]\left\{F_a^{00} + \sum_{\nu=1}^{2} F_{a\nu}^{01}\exp\left(-i\omega_\nu t_1 - k_\nu|t_1|\right)\right\} \tag{4.17}$$

where the vibronic manifold is consistent with that used for $Z_{ab}^{1}(t_1,t_2,t_3)$ in Equation (4.14). The window functions are given by

$$\begin{aligned} W_{ab}^{ESE}(t_3) &= \left\langle \alpha_{ga}\beta_{ag}\gamma_{bg}\chi_{gb}\right\rangle \\ &\times\exp\left[-i\omega_{bg}t_3 - g_{bb}(t_1) + 2i\lambda_{bb}t_3\right]\left\{F_b^{00} + \sum_{\nu=1}^{2} F_{b\nu}^{01}\exp\left(i\omega_\nu t_3 - k_\nu t_3\right)\right\} \end{aligned} \tag{4.18}$$

and

$$\begin{aligned} W_{ab}^{ESA}(t_3) &= \sum_c \left\langle \alpha_{ga}\beta_{ag}\gamma_{cb}\chi_{bc}\right\rangle \\ &\times\exp\left[-i\omega_{cb}t_3 - g_{bb}(t_3) - g_{cc}(t_3) + 2g_{cb}(t_3) + 2i\left(\lambda_{cb}-\lambda_{bb}\right)t_3\right] \end{aligned} \tag{4.19}$$

where the vibronic structure of $W_{ab}^{ESE}(t_3)$ is consistent with that of $Z_{ab}^{1}(t_1,t_2,t_3)$ and $D_a(t_1)$. The linear absorbance and fluorescence spectra impose valuable constraints for parameterization of the vibronic couplings strengths, $F_{a\nu}$. However, the experimental data presented here does not provide information sufficient to determine the vibronic couplings associated with transitions between the single and double exciton manifolds. For this reason, vibronic coupling effects are neglected in $W_{ab}^{ESA}(t_3)$.

Expressions for the response functions are convoluted with the applied electric fields to obtain the third-order polarization as

$$
\begin{aligned}
P^{(3)}(t) = \int_0^\infty dt_1 \int_0^\infty dt_2 \int_0^\infty dt_3 \left[S_D^{NRP}(t_1,t_2,t_3) + S_{OD}^{NRP}(t_1,t_2,t_3) \right] \\
\times E_3(t-t_3) E_1^*(t-t_3-t_2) E_2(t-t_3-t_2-t_1) \\
+ \left[S_D^{RP}(t_1,t_2,t_3) + S_{OD}^{RP}(t_1,t_2,t_3) \right] E_3(t-t_3) \\
\times E_2(t-t_3-t_2) E_1^*(t-t_3-t_2-t_1)
\end{aligned}
\tag{4.20}
$$

where the rephasing and nonrephasing terms associated with (diagonal) energy level fluctuations are given by

$$
S_D^{RP}(t_1,t_2,t_3) = R_2(t_1,t_2,t_3) + R_3(t_1,t_2,t_3) - R_1^*(t_1,t_2,t_3) \tag{4.21}
$$

$$
S_D^{NRP}(t_1,t_2,t_3) = R_1(t_1,t_2,t_3) + R_4(t_1,t_2,t_3) - R_2^*(t_1,t_2,t_3) \tag{4.22}
$$

Equation (4.20) will be used to model transient grating and photon echo experiments. The model calculations below constrain parameters by simultaneous fitting of absorbance and fluorescence spectra, which are calculated with

$$
\sigma_A(\omega) = \sum_{a=1}^{N} \mu_{ag}^2 \int_0^\infty dt \left\{ F_a^{00} + \sum_{\nu=1}^{2} F_{a\nu}^{01} \exp(-i\omega_\nu t) \right\} \exp\left[i(\omega - \omega_{ag})t - \frac{1}{2} g_{aa}(t) \right] \Phi_a(t) \tag{4.23}
$$

and

$$
\sigma_F(\omega) = \sum_{a=1}^{1} \mu_{ag}^2 \int_0^\infty dt \left\{ F_a^{00} + \sum_{\nu=1}^{2} F_{a\nu}^{01} \exp(i\omega_\nu t) \right\} \exp\left[i(\omega - \omega_{ag})t - \frac{1}{2} g_{aa}^*(t) \right] \Phi_a(t) \tag{4.24}
$$

where $\Phi_a(t)$ accounts for lifetime broadening and is obtained by summing the Green function, $G_{ba}(t)$, over all population transfer channels as

$$
\Phi_a(t) = \sum_b G_{ba}(t) \tag{4.25}
$$

The Green function used here is parameterized phenomenologically as

$$
G_{12}(t) = 0.35 \exp(-t/35) + 0.65 \exp(-t/280) \tag{4.26}
$$

and population transfer from the lower to higher energy exciton state is neglected because of the large energy gap between the exciton states. Section 4.5 discusses why this

phenomenological parameterization of $G_{12}(t)$ is performed in lieu of modified Redfield theory.[66,67]

4.4. RESULTS AND DISCUSSION

4.4.1. Linear Absorption and Flouresence Spectra

Fits to the linear absorption and fluorescence spectra of APC are presented in Figure 4.4, where parameters of the model are given in Table 4.1. The spectra are quite similar to those found by Edington et al.[32] The line shape of the $e+$ transition exhibits well-resolved vibronic structure, whereas vibronic transitions are obscured by lifetime broadening in the $e-$ band. Resonance Raman measurements show that many vibrational modes couple to the excitations.[43,44] However, fitting of the present experimental data is accomplished with two high-frequency modes at 800 cm^{-1} and 1500 cm^{-1}. In essence, this treatment sums the intramolecular reorganization energy for all displaced modes with similar frequencies onto the two coordinates with the goal of minimizing adjustable parameters. It should be emphasized that this pair of measurements only partially constrains the model parameters. The nonlinear spectroscopies discussed below are also taken into account. For example, the Green function that causes lifetime broadening of the $e-$ band [see Equation (4.26)] is parameterized to simultaneously fit the transient grating signal spectra and anisotropies presented in the following Section.

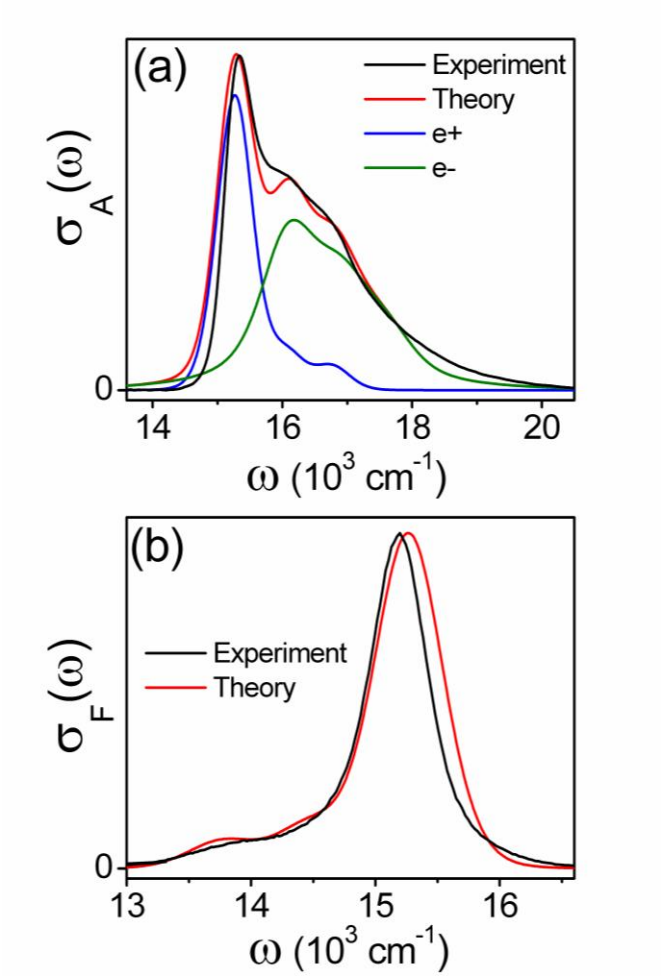

Figure 4.4. (a) Experimental (black) and theoretical (red) linear absorption spectra. Also shown are the line shapes of the transitions to the e_+ (blue) and e_- (green) single exciton states. (b) Experimental (black) and theoretical (red) fluorescence spectra. Calculations use the parameters in Table 4.1.

4.4.2. Dynamics in the Transient Grating Signal Spectrum

The transient grating (TG) measurements shown in Figure 4.5 separate real (absorptive) and imaginary (dispersive) signals components for both ZZZZ and ZZXX tensor elements. This tensor notation denotes the electric field polarizations involved in the sequence of four field-matter interactions (see Appendix A). The real signal components provide information equivalent to a conventional pump-pump experiment (i.e., transient

absorption), whereas the interpretation of dispersive signal components is more complicated. In the limit of laser pulses with infinite bandwidths, the real and imaginary signals are (exactly) related by a Kramers-Kronig transformation. However, because finite bandwidth pulses are actually used, the imaginary signal components in Figure 4.5 report on dynamics taking place outside of the spectral window defined by the probe laser spectrum.[63,68,69] Therefore, the dynamics measured at different signal phase angles provide complementary information.

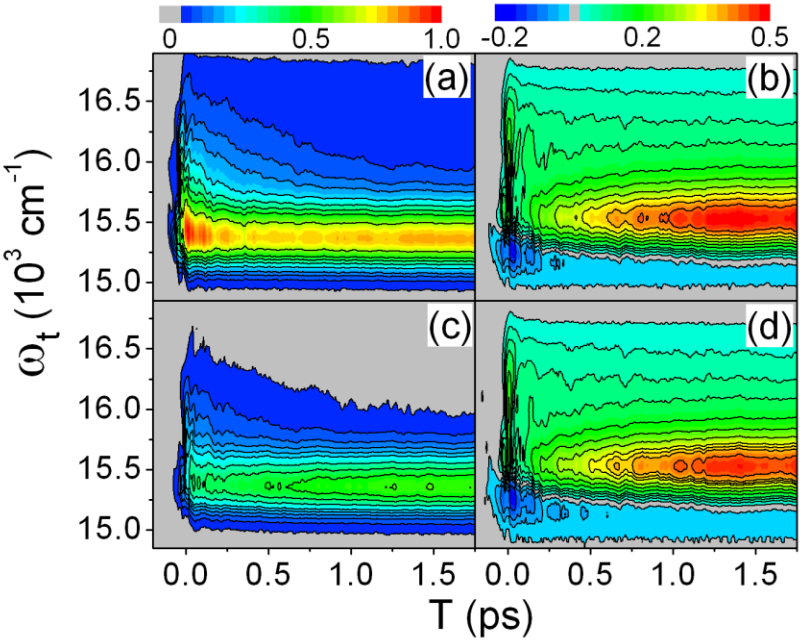

Figure 4.5. Real (a), (c) and imaginary (b), (d) parts of transient grating signal field measured for the ZZZZ (a)-(b) and ZZXX (c)-(d) tensor elements. Amplitudes of the four spectra are normalized to the same value and can be directly compared.

The real TG signals shown in Figure 4.5 display a red-shift in the signal spectrum taking place within the first several hundred femtoseconds. The red-shift observed in the real signal component is consistent with previous pump-probe measurements for APC in which the dynamics were assigned to both electronic and nuclear relaxation.[32,40,42] By contrast,

significant red-shifting is not found in the imaginary signal components. Rather, the imaginary amplitude at ω_t=15400 cm^{-1} rises on a time scale similar to that with which the real spectrum red-shifts. This rise in amplitude is quite significant with an increase of more than a factor of 5 between T=0 and T=0.5 ps. In addition to population dynamics of the excitons, the imaginary signal component possesses enhanced sensitivity to the Raman response of the surrounding protein environment and solvent (i.e., as in an optical Kerr effect).[70,71] We make no attempt to extract this information here, but focus on coherent dynamics found in the imaginary signal component in Section 4.4.4.

The model calculation shown in Figure 4.6 suggests that both electronic and nuclear relaxation contributes to the red-shift measured in the transient grating signal spectrum. Interpretation is facilitated by decomposing the signal into three contributions: ground state bleach (GSB); excited state emission (ESE); excited state absorption (ESA). Figure 4.6a shows that the GSB component is essentially independent of the pulse delay T, whereas the ESE and ESA terms respectively shift to lower and higher frequencies with increasing T. It is essential that interference between the ESE and ESA terms is considered to understand the dynamics in the total signal spectrum shown in Figure 4.6d. The excited state emission terms in the response function radiate as hot vibronic states with spectra resembling the line shapes shown in Figure 4.4a at T=0, whereas the signals converge to mirror images of the absorption spectrum when T is long compared to the vibrational cooling time of 50 fs. Internal conversion between $e-$ and $e+$ is also partly responsible for the red-shift in the signal field, where the 35 fs relaxation channel represents the major contribution. Electronic relaxation dominates the response at T>100 fs because the internal conversion rate possesses a significant (65%) 280 fs component.

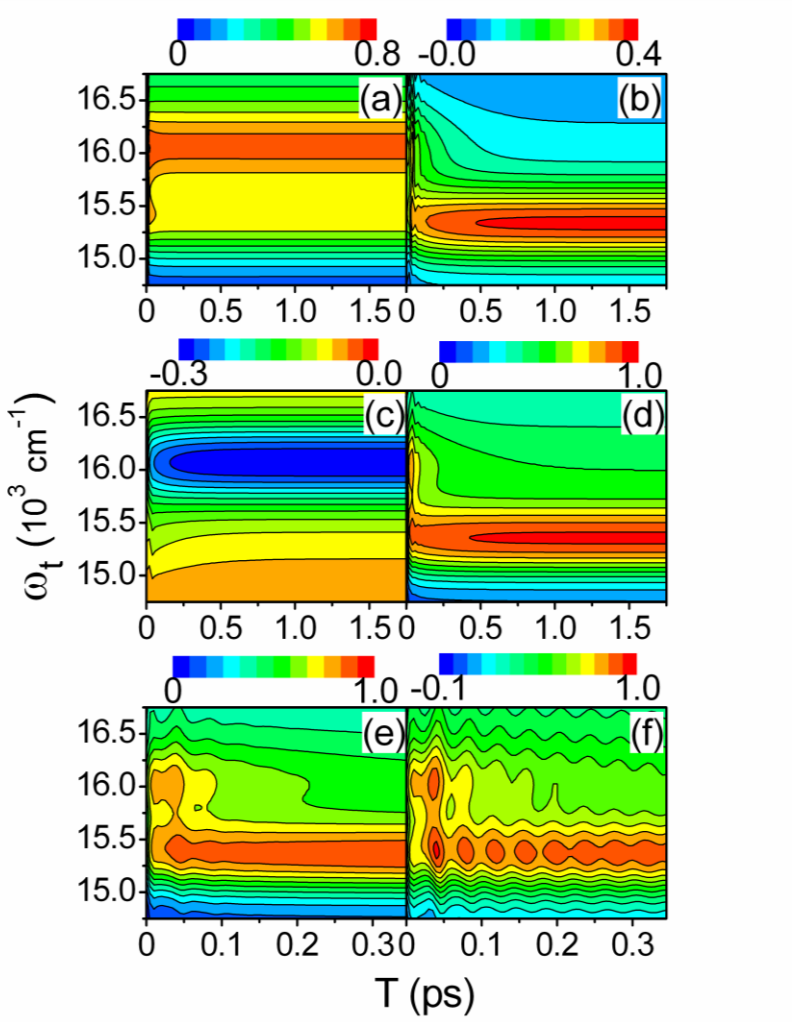

Figure 4.6. Panels (a)-(c) present the real part of calculated transient grating signals for terms; (a) R3, R4; (b) R1, R2, ^{IC}R1, ^{IC}R2; (c) R1*, R2*, ^{IC}R1*, ^{IC}R2*. Panels (d)-(f) are computed using Equation (4.20), where (d) and (e) show the same calculation plotted on different time scales. The parameters of Table 4.1 are used with the exception that panel (f) sets the correlation parameter, η, equal to 1 (see Equation 4.3).

Figure 4.6e and 4.6f present TG signals computed without (η=0) and with (η=1) fully correlated fluctuations at the individual pigment sites. Full correlation gives rise to a long-lived electronic coherence between the e_+ and e_- exciton states; this coherence manifests as oscillations in the signal amplitude with a period of 40 fs. By contrast, recurrences in the signal amplitude are not observed with η=0. In fact, indistinguishable

signals are obtained with $0<\eta<0.5$. An essential finding of this model is that, with the exception of the coherent quantum beating dynamics shown in Figure 4.6f, spectroscopic signatures of excition correlations are quite subtle and not readily detected with the present configurations of TG and PE spectroscopy. We parameterize the model with $\eta=0$ on the basis of these calculations and the absence of electronic quantum beating in the measurements.

4.4.3. Incoherent Dynamics in the Transient Grating Signal Anisotropy

Analysis of electric field polarization effects is useful for distinguishing electronic population transfer from nuclear relaxation.[36,72-76] The anisotropy is calculated with real TG tensor elements using

$$r(T)=\frac{S_{ZZZZ}(T)-S_{ZZXX}(T)}{S_{ZZZZ}(T)+2S_{ZZXX}(T)} \tag{4.27}$$

We reiterate that the anisotropy computed with real TG signal components give information equivalent to that obtained with conventional pump-probe experiments. Figures 4.7a and 4.7b display the anisotropy at ω_t=16000 cm^{-1}. The signal amplitude decays significantly on the sub-picosecond time-scale, whereas the anisotropy remains at approximately 0.36 for T <0.5 ps (see Table 4.2). The anisotropy in panel 7b measured at T >0.5 ps is not meaningful due to limitations in the dynamic range of our instrument. Figures 4.7g and 4.7h present real TG tensor elements and the anisotropy measured at the low frequency edge of the signal spectrum, ω_t=15270 cm^{-1}. The signal amplitudes exhibit a rise concomitant with the red-shift shown in Figures 4.5a and 4.5c. The anisotropy decays with a 280 fs time constant, which is in exact agreement with that previously measured by Beck and co-workers (see Table 4.2).[28] Real TG signals detected at the intermediate frequency, ω_t=15750 cm^{-1}, are

shown in Figures 4.7c and 4.7d. The anisotropy decays with the time constant of 550 fs which is almost twice that found at ω_t=15270 cm^{-1}. It is possible that population transfer and nuclear relaxation both contribute to the 550 fs time constant. In addition, the model calculations suggest that the dynamics measured at ω_t=15750 cm^{-1} are complicated by the interference between ESE and ESA (see Figure 4.7). Parameters in Table 4.2 describing coherences in the anisotropies are discussed in the following Section.

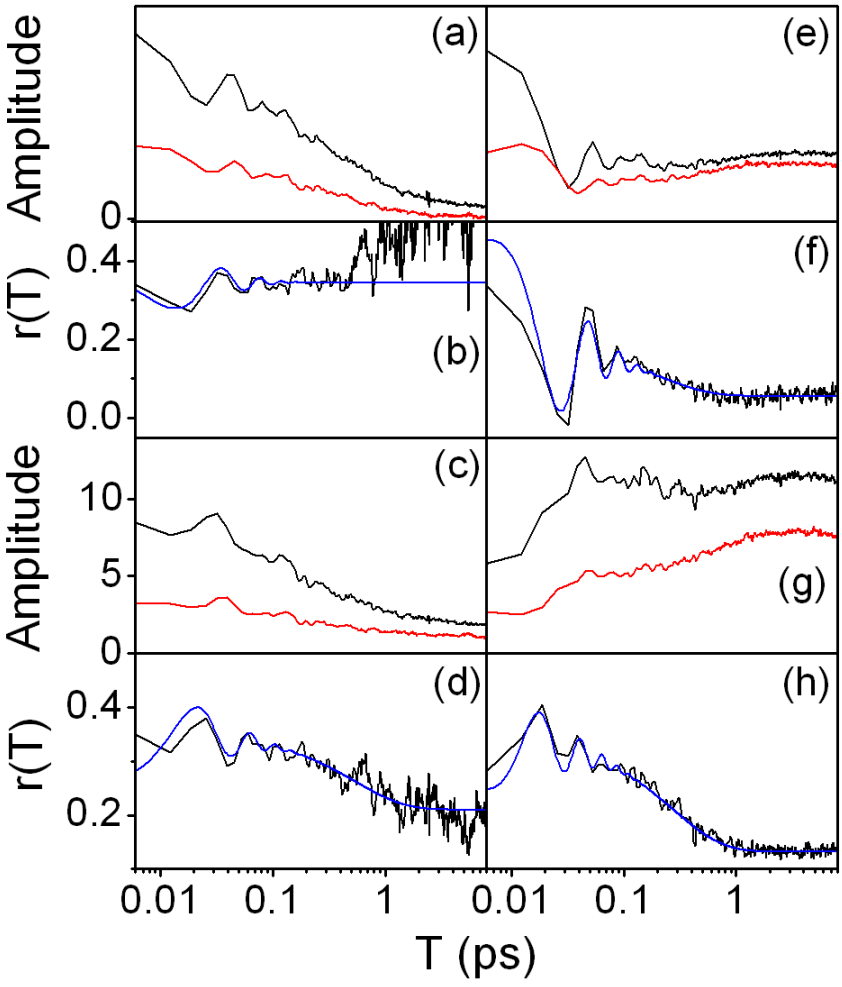

Figure 4.7. Tensor elements measured with ZZZZ (black) and ZZXX (red) tensor elements along the with the corresponding anisotropy are shown in four pairs of panel: (a)-(b); (c)-(d); (e)-(f); (g)-(h). Panels (e) and (f) represent the imaginary part of the transient grating signal

field, whereas all other data correspond to the real component. The panels in all rows use the same scale and can be compared. Signal detection frequencies for the four pairs of panels are: (a)-(b) 16000 cm^{-1}; (c)-(d) 15750 cm^{-1}; (e)-(f) 16000 cm^{-1}; (g)-(h) 15270 cm^{-1}. Fitting parameters are given in Table 4.2.

The imaginary signal components detected at ω_t =16000 cm^{-1}, are plotted primarily to emphasize the coherences discussed in the following Section. However, the measured time constant of 220 fs deserves mention because it is in exact agreement with the time constant found using photon echo spectroscopy by Homoelle et al.[41] We believe that this time constant is most likely associated with internal conversion between the exciton states. For example, it may be that the 220 fs and 280 fs population transfer time constants represent distinct (heterogeneous) configurations of the dimer. The fact that this time constant is detected only in the imaginary signal component may also be significant; Reference [41] measures the photon echo signal intensity, and therefore informs on dynamics occurring in both the real and imaginary components of the signal field.

The parameters of Table 4.1 capture the ω_t dependence of the anisotropies presented in Figure 4.7. Figure 4.8 overlays experimental and calculated anisotropies at three difference pulse delays. The calculations are performed with and without the ESA terms to explain why the measured anisotropies do not decay significantly at ω_t >15800 cm^{-1}. The anisotropy is reasonably well-fit at T =0, where the fast 35 fs component of the Green function in Equation (4.26) is essential for obtaining an anisotropy of approximately 0.35 at T =0. The effect of the ESA signal component becomes clear at T =200 fs, where it suppresses decay in the anisotropy on the high frequency side of the signal spectrum. At T =3 ps, experimental limitations prevent accurate measurement of the anisotropy at ω_t >15800 cm^{-1}. The measured anisotropy is also slightly smaller than that predicted by the model. One

explanation for this discrepancy is that incoherent energy transfer between the initially photoexcited dimer and the two others dimers (see Figure 4.1a) contributes to the dynamics at T >1 ps.

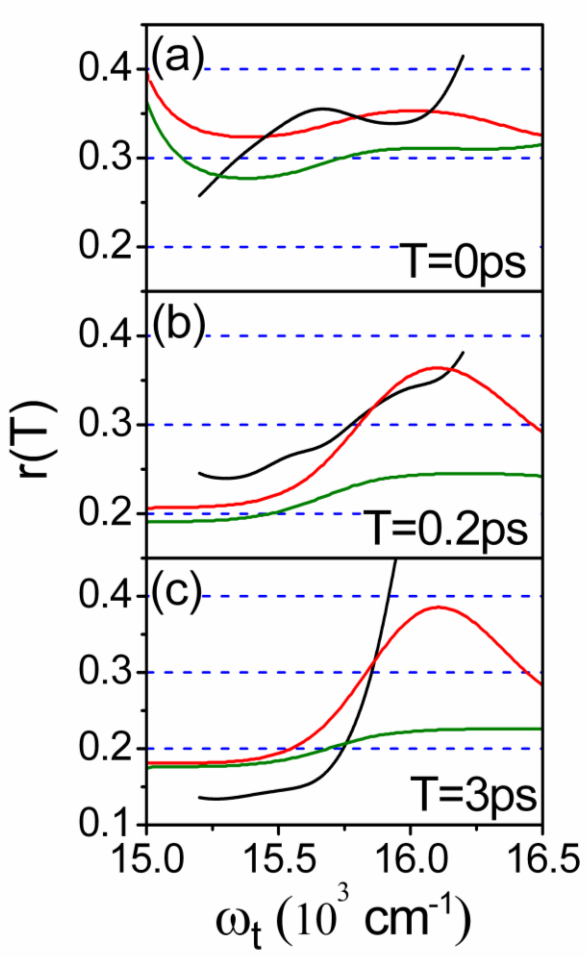

Figure 4.8. Experimental (black) and calculated (red and green) anisotropies with (a) $_T$ =0 fs, (b) $_T$ =0.2 fs, (c) $_T$ =3 ps. The anisotropies are computed with the real part of the signal field. Calculations represented with the red line use all terms in the response function, whereas the green line omits the excited state absorption terms R1*, R2*, ^{IC}R1*, ^{IC}R2*.

To summarize, contributions of electronic and nuclear relaxation to the TG signal spectrum and anisotropy have been investigated by comparing experimental and calculated signals. Important aspects of the measured signals include a red-shift in the signal spectrum

taking place at T <500 fs and a signal anisotropy for which the amount of depolarization increases with decreasing signal detection frequency, ω_t. The anisotropy decay occurs with time constants of 220, 280 and 550 fs. The 220 fs and 280 fs time constants agree with previous work and may represent electronic population transfer channels corresponding to different geometric configurations of the dimer. It is interesting that the present work obtains these same time constants as those found in Reference [28] despite the broader distributions of photoexcited vibronic states produced by our 15 fs laser pulses. Apparently, this means that internal conversion occurs from the electronic origin of $e-$ because vibrational cooling is fast compared to these time constants. Interpretation of the 550 fs time constant is complicated by interference between the ESE and ESA signal components; nuclear relaxation may be an important contribution. We find that the sub-100 fs dynamics involve dephasing of electronic and nuclear coherences in addition to more than 35% of the total internal conversion between the $e-$ to $e+$ exciton states, whereas internal conversion dominates evolution in the TG signal spectrum at T >100 fs.

4.4.4. Coherent Dynamics in the Transient Grating Signal Anisotropy

This Section focuses on recurrences measured in the TG tensor elements and anisotropy. Nuclear coherences in APC have previously been investigated with high-quality pump-probe measurements employing 16 fs laser pulses.[42] However, recurrences in the anisotropy signals have not been reported in earlier papers. Table 4.2 summarizes fitting parameters for the anisotropy data in Figure 4.7 where all fits possess coherent components that damp in approximately 35 fs.

At the signal emission frequency ω_t =16000 cm^{-1}, a recurrence frequency of 800 cm^{-1} is found in both the real and imaginary signal components. Conventional transient

absorption anisotropy uses the real signal component. The anisotropy found with the imaginary signal components is displayed in Figure 4.7f because the large modulation depth gives strong support to the finding of anisotropic coherent dynamics. Signals detected at ω_t =15750 cm^{-1} are consistent with those at ω_t =16000 cm^{-1}.

The central issue in interpretation of the 800 cm^{-1} coherence measured at ω_t =15750 cm^{-1} and ω_t =16000 cm^{-1} is whether the coherence corresponds to a pair of electronic or nuclear states. To address this point, Figure 4.9 presents the Fourier transformation of a TG signal measured for the ZZZZ tensor element at 15625 cm^{-1}, where we measure the greatest coherence amplitude. This Raman spectrum exhibits significant amplitude at 800 cm^{-1}. On the basis of Resonance Raman studies for a related bilin chromophore, phytochrome, we assign the 800 cm^{-1} mode to a hydrogen out-of-plane (HOOP) wagging mode analogous to those observed in retinal polyenes.[77-79] It is quite interesting that this is the only nuclear mode producing modulation in the anisotropies of Figure 4.7. Figure 4.9 clearly shows that lower frequency modes at 205 cm^{-1} and 285 cm^{-1} couple more strongly to photoexcitation. However, these modes are apparently more symmetric in nature such that their contributions cancel in the numerator of Equation (4.27).

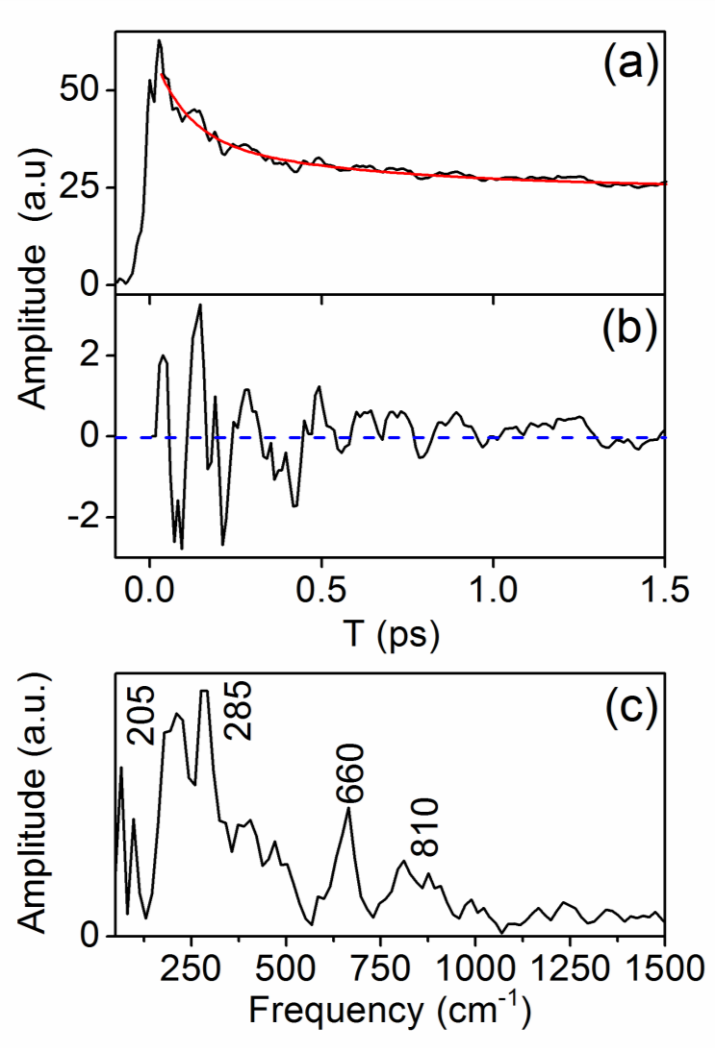

Figure 4.9. (a) Real part of transient grating signal field measured with a 15 fs pump and probe pulses centered at 15870 cm^{-1}. Signal is detected at 15625 cm^{-1}. (b) Nuclear coherences are isolated by subtracting a decaying exponential function (red) from the data (black) in panel (a). (c) Absolute value of Fourier transform of residual signal in panel (b). The noise level in (c) is approximately 10% of the peak amplitude at 660 cm^{-1}.

Assignment of the dynamics to electronic coherence in APC is finally ruled out by the measurement of a recurrence with a frequency of 1450 cm^{-1} at ω_t =15270 cm^{-1}. Resonance Raman spectroscopy observes a transition at 1450 cm^{-1}.[44] The fact that the two coherence frequencies detected in the anisotropy agree with vibrational modes known to have large Franck-Condon factors leads us to conclude that the recurrences in the anisotropy correspond

to impulsively excited vibrations. This finding has important implications for our interest in correlated line broadening. As shown in Figure 4.6, strongly correlated pigment fluctuations should promote long-lasting electronic coherences, which are readily detected with transient absorption anisotropy.[35]

4.4.5. Photon Echo Spectroscopy

Photon echo (PE) spectra obtained in the delay range T =0-120 fs are presented in Figure 4.10. Inhomogeneity in the sample produces a peak shape elongated with respect to the diagonal, $\omega_\tau = \omega_t$ at T <30 fs. This elongated peak shape quickly subsides as nuclear relaxation takes hold (e.g., solvation and dephasing of vibronic coherences). Most interesting is the presence of a fairly well-resolved cross peak located at ω_τ =16400 cm^{-1} and ω_t =15300 cm^{-1}. The model calculations shown in Figure 4.11 assign this cross peak to two signal generation mechanisms: (i) the first two field matter interactions produce a population in the 800 cm^{-1} or 1500 cm^{-1} mode of state $e+$ which then relaxes to the electronic origin; (ii) excitation into the electronic origin of state $e-$ is followed by internal conversion to state $e+$. The amplitude of the calculated cross peak is slightly underestimated and centered closer to ω_τ =16200 cm^{-1} and ω_t =15300 cm^{-1} at T =0. Apparently, a small amount of relaxation not accounted for by the model takes place within the 18 fs time resolution of the experiment. However, the simulated cross peak intensity quickly grows and the agreement between experiment and theory is quite good in the range T =10-30 fs.

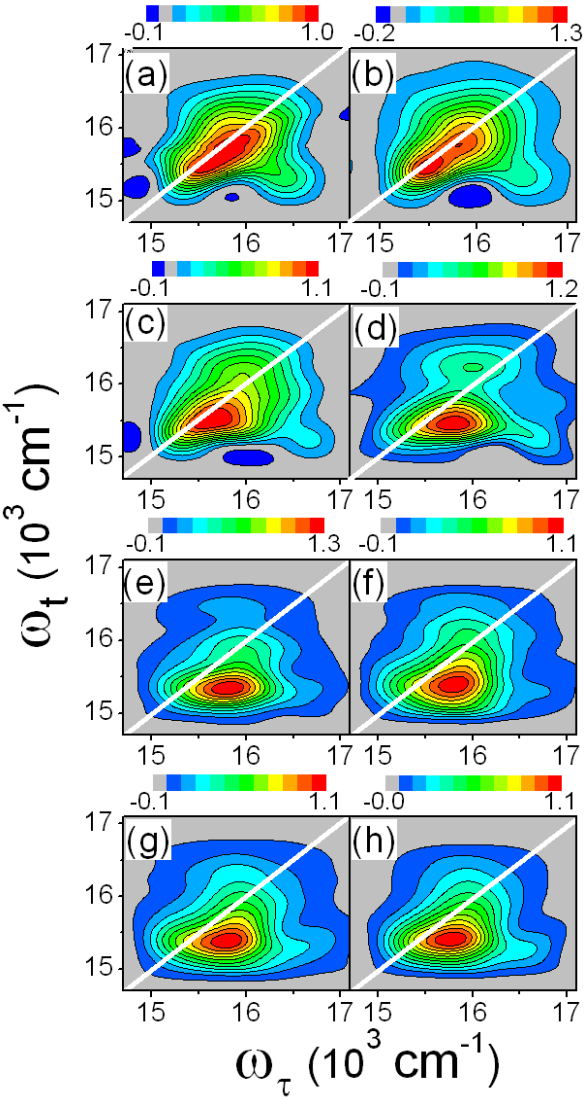

Figure 4.10. Real part of experimental photon echo spectra measured at pulse delays, T: (a) 0 fs; (b) 10 fs; (c) 20 fs; (d) 30 fs; (e) 50 fs; (f) 70 fs; (g) 90 fs;(h) 120 fs. Pump (E_1 & E_3) and probe pulses (E_3 & E_4) are configured with magic angle polarizations. Amplitudes are scaled with respect to peak signal at T = 0 fs. The contour lines in each panel are linearly spaced.

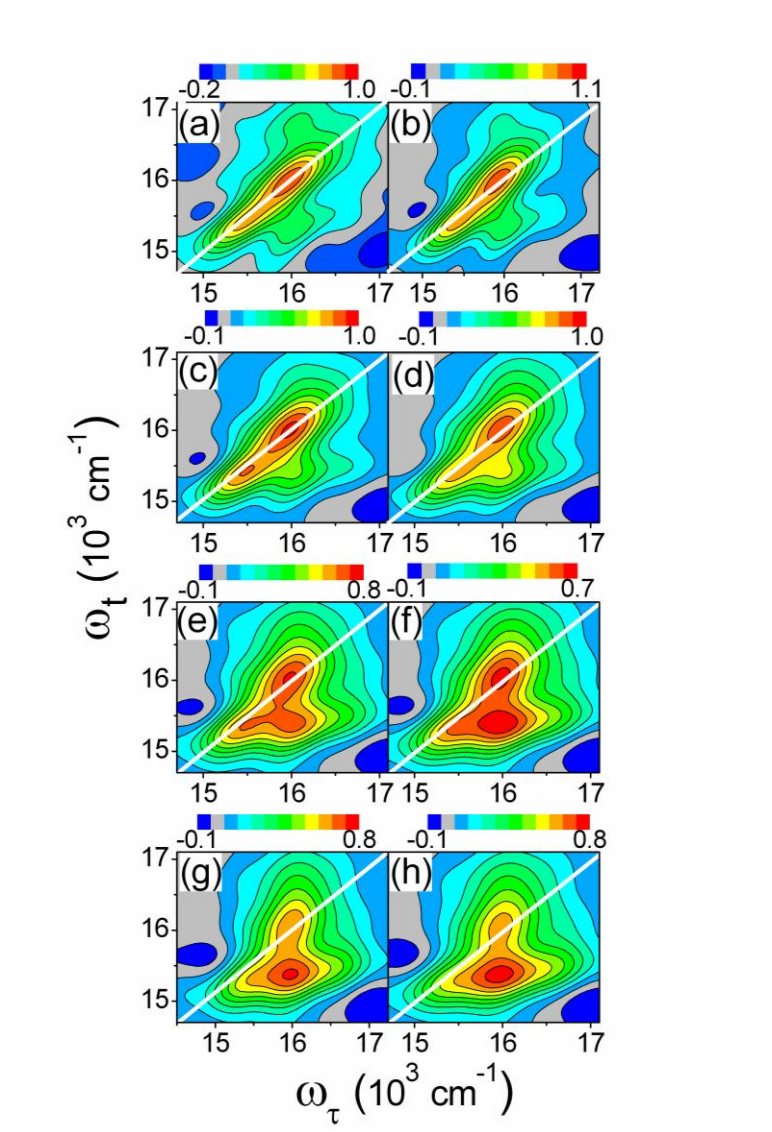

Figure 4.11. Real part of calculated photon echo spectra measured at pulse delays, T: (a) 0 fs; (b) 10 fs; (c) 20 fs; (d) 30 fs; (e) 50 fs; (f) 70 fs; (g) 90 fs;(h) 120 fs. Pump (E_1 & E_3) and probe pulses (E_3 & E_4) are configured with magic angle polarizations. Amplitudes are scaled with respect to peak signal at T = 0 fs. Calculations use Equation (4.20) and the parameters of Table 4.1. The contour lines in each panel are linearly spaced.

For T >60 fs, the PE line shape exhibits increasing spectral width with decreasing ω_t. The time scale of relaxation in the peak shape is well-captured by the model. Overall, the dynamics in the PE spectrum reflect processes in which the excitation of a broad distribution

of initial states terminates in the electronic origin of the $e+$ exciton level. The most prominent internal conversion channel possesses a 280 fs time constant, whereas the PE spectrum changes little for T >120 fs. Therefore, evolution of the PE spectrum found in Figure 4.10 must mainly reflect solvation and intramolecular nuclear relaxation within the $e+$ exciton level. The small Stokes shift between the absorption and fluorescence spectra of Figure 4.1c suggests that solvation is probably a minor contribution.

4.5. CONCLUSION

4.5.1. Correlated Line Broadening

TG and PE measurements in this chapter do not detect coherent quantum beating between the $e+$ and $e-$ excitons. Furthermore, we have shown that the present configurations of TG and PE are fairly insensitive to these dynamics because quantum beats in the TG signal are not observed unless the correlation parameter, η, is greater than 0.5; it should be noted that the PE line shapes are also indistinguishable for signals computed in the range 0< η <0.5. To better understand the present observations, we consider the initial amplitudes of the exciton-exciton cross-correlation function of APC[18]

$$\left\langle E_{e+}(0)E_{e-}(0)\right\rangle = \left\langle E_{e+}E_{e-}\right\rangle = \phi_{e+,1}^2\phi_{e-,1}^2\Delta_{11}^2 + \phi_{e+,2}^2\phi_{e-,2}^2\Delta_{22}^2 + \eta_{12}\left[\phi_{e+,1}^2\phi_{e-,2}^2 + \phi_{e+,2}^2\phi_{e-,1}^2\right]\Delta_{11}\Delta_{22} \quad (4.28)$$

where

$$\left\langle E_{e+}E_{e-}\right\rangle / \mathrm{cm}^{-2} = 20093 + \eta_{12}\,232378 \quad (4.29)$$

is obtained with the parameters of Table 4.1. The component of $\left\langle E_{e+}E_{e-}\right\rangle$ linear in η_{12} is 11.5 times larger than the first term under the condition of full correlation, η_{12}=1. It is useful to compare this situation with that of a dimer possessing degenerate pigment energies where

$$\left\langle E_{e+}E_{e-}\right\rangle = \frac{1}{4}\left[\Delta_{11}^2 + \Delta_{22}^2\right] + \frac{\eta_{12}}{2}\Delta_{11}\Delta_{22} \tag{4.30}$$

is obtained. Here the third term is closer in magnitude to the sum of the first two. In fact, the autocorrelation functions and cross correlation functions possess equal weight when $\Delta_{11} = \Delta_{22}$, i.e., $2\left\langle E_{e+}E_{e-}\right\rangle = \Delta_{11}^2\left(1+\eta_{12}\right)$.

Together, Equations (4.28)-(4.30) suggest that the non-degenerate basis of APC facilitates the spectroscopic observation of electronic coherence if the pigment fluctuations of APC are indeed correlated. First, the term in Equation (4.28) linear in η_{12} makes a significant contribution. Secondly, non-degeneracy of the pigment basis allows oscillator strength to be shared evenly between the two exciton transitions. Thus, an electronic coherence between $e+$ and $e-$ should be readily photoexcited and monitored with TG or PE. These factors promoting the observation of electronic coherences compete with fast dephasing dynamics imposed by vibrational cooling and electronic population transfer. On the basis of the present measurements and modeling, we can only conclude that η_{12}<0.5. Chapter 6 will address this issue with a nonlinear spectroscopy specially designed to isolate coherences between exciton states by suppressing the detection of electronic populations.[27]

4.5.2. Importance of Promoting Modes

Geometry changes in the nuclear coordinates of the $e+$ and $e-$ exciton states are important because large Franck-Condon factors of "promoting modes" can potentially open efficient vibronic relaxation channels. Promoting modes are essential to explaining fast internal conversion in APC because the 827 cm^{-1} energy gap between exciton states is large compared to the characteristic frequency of the bath. For example, population transfer rates computed with a modified Redfield theory yield time constants of approximtely 13.2 ps,

which is more than 50 times slower than the observed time scale. This slow rate reflects the fact that the spectral density of the solvent environment possesses little amplitude near 827 cm^{-1}. We suggest that a high frequency promoting mode of APC must enhance its internal conversion rate by accepting a portion of this excess energy.

One requirement for effective rate enhancement by way of a promoting mode is a large displacement in the coordinate for the $e+$ and $e-$ states. The displacement can be calculated using the vibronic coupling strengths in Table 4.1. For the 800 cm^{-1} mode, the vibronic coupling strength of the 0-0 transition is 8.3 and 1.7 larger than that of the 0-1 transition for the e_+ and e_- states, respectively. These ratios correspond to dimensionless displacements (Huang-Rhys factors) of 0.63 (.20) and 1.1 (0.63) for e_+ and e_-. Thus, we estimate a dimensionless displacement of approximately 1.73 between the two exciton states. The rate enhancement can then be estimated by calculating the ratio of internal conversion rates found for cases in which the final state possesses either 0 or 1 quanta of energy in the 800 cm^{-1} mode of electronic state $e+$, where the transition is taken to initiate at the electronic origin of the e_- state.[80,81] This ratio, $k_{0\to1}/k_{0\to0}$, is given by

$$\frac{k_{0\to1}}{k_{0\to0}} = \frac{\Delta^2}{2}\exp\left[\frac{-\left(E_{00}-\hbar\omega_p\right)^2+E_{00}^2}{2\sigma^2}\right] \tag{4.31}$$

where Δ is the dimensionless displacement in the nuclear coordinate, E_{00} is the 827 cm^{-1} energy gap between the electronic origins of the $e+$ and $e-$ states, σ is the bandwidth of the transition imposed with system-bath interactions, and the Gaussian line shape is assumed for convenience. The spectroscopic line widths are used to estimate a 275 cm^{-1} bandwidth, σ.

The point of Equation (4.31) is only to obtain an order of magnitude estimate the rate enhancement. Internal conversion rates of APC calculated with full rigor reach essentially the same conclusion.[42] Equation (4.31) yields a ratio $k_{0\to1}/k_{0\to0}$=137, which puts the estimated internal conversion rate on the sub-picosecond time scale. For example, a time constant of 96 fs is obtained if the rate enhancement factor of 137 is applied to the 13.2 ps time constant obtained by Redfield theory. On the basis these calculations, we interpret the fast internal conversion dynamics of APC as proceeding through the vibronic relaxation channel of the 800 cm^{-1} HOOP vibrational mode shown in the Raman spectrum of Figure 4.9c (see Section 4.4.4). It should be noted that extremely rapid, promoting mode-assisted internal conversion is not unique to APC. Sub-picosecond internal conversion rates across energy gaps close to the 900 cm^{-1} have been found in various photosynthetic reaction centers.[35,82]

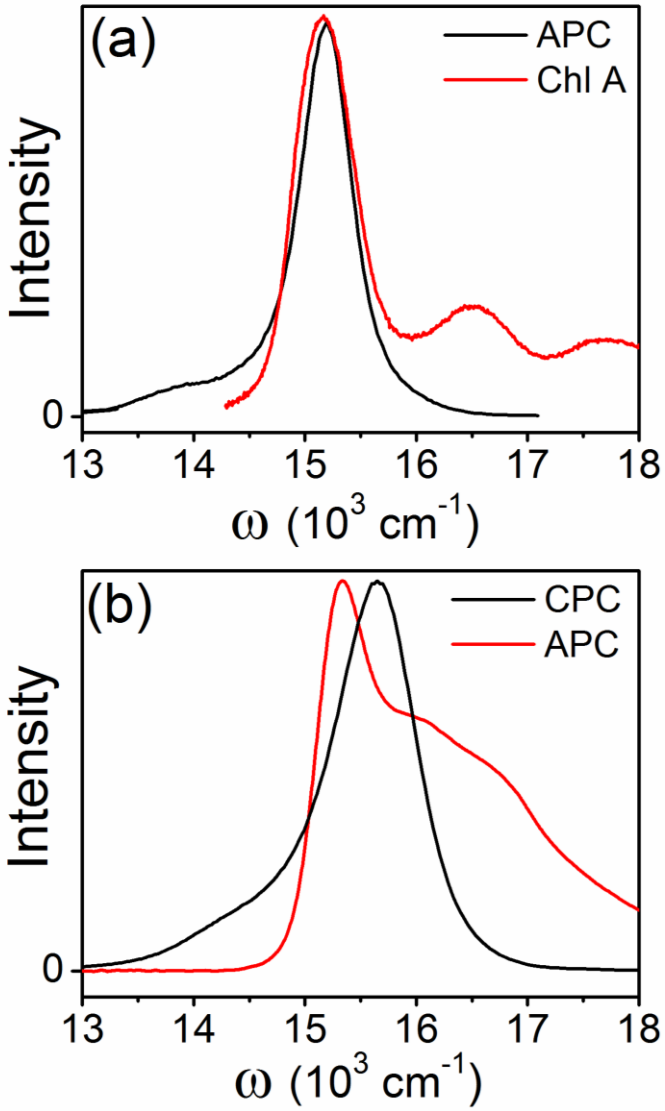

Figure 4.12. Overlap of spectral line shapes for donor and acceptor pairs in the phycobilisome light harvesting antenna of cyanobacteria. (a) Fluorescence spectrum of Allophycocyanin (APC, black) and absorption spectrum of Chlorophyll A (Chl A, red). (b) Fluorescence spectrum of C-Phycocyanin (CPC, black) and absorption spectrum of Allophycocyanin (APC, red).

4.5.3. Implications for Function of the Phycobilisome

Delivery of excitation energy from APC to the reaction center requires that light absorbed by the e_- state transfers quickly and efficiently to $e+$. Indeed, the excellent

overlap between the fluorescence spectrum of APC and the absorption spectrum of the chlorophyll energy acceptor shown in Figure 4.12a suggests that the distribution of nuclear states in $e+$ is optimally configured for energy transfer to the reaction center. The parameters of Table 4.1 find that $e+$ and $e-$ exciton states are respectively 96% localized to β84 and α84 pigments because the pigments comprising the dimer have non-degenerate energy levels. We suggest that this exciton localization facilitates function of the phycobilisome in the following two ways. First, localization of the transition densities onto the individual pigments enhances the Franck-Condon factors essential to promoting mode-assisted internal conversion between $e-$ and $e+$. A second advantage to the non-degenerate basis is that oscillator strength distributes fairly evenly between the two exciton transitions. Overlap in the fluorescence emission spectrum of C-Phycocyanin (CPC) and the absorption spectrum of APC presented in Figure 4.12b suggests that this distribution of oscillator strength promotes energy transfer between this donor-acceptor pair by allowing the transition moments of both the $e+$ and $e-$ states of APC to couple with the energy donating state of CPC. By contrast, Förster energy transfer from CPC to the $e-$ state of APC would be less efficient if APC possessed degenerate pigments because the transition dipole connecting the ground state to $e-$ would have smaller magnitude.

Table 4.1. Parameters of Spectroscopic Model

Parameter	Value
[(a)] E_1 / hc	15300 cm^{-1}
[(a)] E_2 / hc	16060 cm^{-1}
J_{12}	-163 cm^{-1}
Δ_{11}	450 cm^{-1}
Δ_{22}	560 cm^{-1}
η_{12}	0
κ	0.25
$\omega_\nu \left(\nu = 1\right)$	800 cm^{-1}
$\omega_\nu \left(\nu = 2\right)$	1500 cm^{-1}
[(b)] $F_a^{00} \left(a = 1\right)$	2.05
[(b)] $F_a^{00} \left(a = 2\right)$	0.64
$F_{a\nu}^{01} \left(a = 1, \nu = 1\right)$	0.24
$F_{a\nu}^{01} \left(a = 1, \nu = 2\right)$	0.16
$F_{a\nu}^{01} \left(a = 2, \nu = 1\right)$	0.38
$F_{a\nu}^{01} \left(a = 2, \nu = 2\right)$	0.09

k_ν^{-1} (all ν)	50 fs
$\omega_1 = \omega_2 = \omega_3$	15940 cm^{-1}

[a]Energy gap of pigment in Equation (4.2)

[b] a =1 and a =2 respectively denote the $e+$ and $e-$ excitons

Table 4.2. Fits to anisotropy profiles in Figure 4.7

[a]Parameter	[b] ω_t =16000 cm^{-1}	[b] ω_t =15750 cm^{-1}	[c] ω_t =16000 cm^{-1}	[b] ω_t =15270 cm^{-1}
r_0	0.36	0.21	0.06	0.13
r_1	0	0.14	0.13	0.21
r_2	0.1	0.10	0.33	0.11
τ_1	----------	550fs	220fs	280fs
τ_2	35fs	37fs	36fs	30fs
ω	800 cm^{-1}	800 cm^{-1}	800 cm^{-1}	1450 cm^{-1}
φ	0.9 rad.	2.9 rad.	5.1 rad.	1.4 rad.

[a] Fit to Equation $r(T) = r_0 + r_1 \exp(-T/\tau_1) + r_2 \cos(\omega T + \varphi)\exp(-T/\tau_2)$

[b] Real component of signal.

[c] Imaginary component of signal.

REFERENCES

(1) van Amerongen, H.; Valkunas, L.; van Grondelle, R. *Photosynthetic Excitons*; World Scientific: Singapore, 2000.

(2) Blankenship, R. E. *Molecular Mechanisms of Photosynthesis*; Blackwell Science Ltd.: Oxford, 2002.

(3) *Light Harvesting Antennas*; Green, B. R.; Parson, W. W., Eds.; Kluwer Academic Publishers: Dordrecht, 2003; Vol. 13.

(4) Sundström, V.; Pullerits, T.; van Grondelle, R. *J. Phys. Chem. B* 1999, *103*, 2327.

(5) Fleming, G. R.; Scholes, G. D. *Nature* 2004, *121*, 4221.

(6) Parson, W. W. *Modern Optical Spectroscopy*; Springer-Verlag: Berlin, 2007.

(7) Soules, T. F.; Duke, C. B. *Phys. Rev. B* 1971, *3*, 262.

(8) Parson, W. W. *Science* 2007, *316*, 1438.

(9) Lee, H.; Cheng, Y.-C.; Fleming, G. R. *Science* 2007, *316*, 1462.

(10) Rebentrost, P.; Mohseni, M.; Aspuru-Guzik, A. *J. Phys. Chem B* 2009, *113*, 9942.

(11) Yu, Z. G.; Berding, M. A.; Wang, H. *Phys. Rev. E* 2008, *78*, 0509902.

(12) Hennebicq, E.; Beljonne, D.; Curutchet, C.; Scholes, G. D.; Silbey, R. J. *J. Chem. Phys.* 2009, *130*, 214505.

(13) Nazir, A. *Phys. Rev. Lett.* 2009, *103*, 146404.

(14) Collini, E.; Scholes, G. D. *Science* 2009, *323*, 369.

(15) Collini, E.; Scholes, G. D. *J. Phys. Chem. A* 2009, *113*, 4223.

(16) Kimura, A.; Kakitani, T. *J. Phys. Chem. A* 2007, *111*, 12042.

(17) Engel, G. S.; Calhoun, T. R.; Read, E. L.; Ahn, T. K.; Mancal, T.; Cheng, Y. C.; Blankenship, R. E.; Fleming, G. R. *Nature* 2007, *446*, 782.

(18) Venkatramani, R.; Mukamel, S. *J. Chem. Phys.* 2002, *117*, 11089.

(19) Demirdöven, N.; Khalil, M.; Tokmakoff, A. *J. Phys. Chem. A* 2001, *105*, 8025.

(20) Pisliakov, A. V.; Mancal, T.; Fleming, G. R. *J. Chem. Phys.* 2006, *124*, 234505.

(21) Cho, M. *Chem. Rev.* 2008, *108*, 1331.

(22) Womick, J. M.; Miller, S. A.; Moran, A. M. *J. Phys. Chem. B* 2009, *113*, 6630.

(23) Joo, T.; Jia, Y.; Yu, J.-Y.; Lang, M. J.; Fleming, G. R. *J. Chem. Phys.* 1996, *104*, 6089.

(24) Mukamel, S. *Principles of Nonlinear Optical Spectroscopy*; Oxford University Press: New York, 1995.

(25) Abramavicius, D.; Mukamel, S. *Chem. Rev.* 2004, *104*, 2073.

(26) Abramavicius, D.; Palmieri, B.; Voronine, D. V.; Sanda, F. *Chem. Rev.* 2009, *109*, 2350.

(27) Womick, J. M.; Miller, S. A.; Moran, A. M. *J. Phys. Chem. A* 2009, *113*, 6587.

(28) Edington, M. D.; Riter, R. E.; Beck, W. F. *J. Phys. Chem.* 1995, *99*, 15699.

(29) MacColl, R. *J. Struct. Biol.* 1998, *124*, 311.

(30) Ying, L.; Sunney, X. *J. Phys. Chem B* 1998, *102*, 10399.

(31) Brejc, K.; Ficner, R.; Huber, R.; Steinbacher, S. *J. Mol. Biol.* 1995, *249*, 424.

(32) Edington, M. D.; Riter, R. E.; Beck, W. F. *J. Phys. Chem B* 1996, *100*, 14206.

(33) McHale, J. *Molecular Spectroscopy*; Prentice Hall: Upper Saddle Creek River, NJ, 1999.

(34) Savikhin, S.; Buck, D. R.; Struve, W. S. *Chem. Phys.* 1997, *223*, 303.

(35) Arnett, D. C.; Moser, C. C.; Dutton, P. L.; Scherer, N. F. *J. Phys. Chem. B* 1999, *103*, 2014.

(36) Qian, W.; Jonas, D. M. *J. Chem. Phys.* 2003, *119*, 1611.

(37) Milota, F.; Sperling, J.; Nemeth, A.; Kauffman, L. J. *Chem. Phys.* 2008, *357*, 45.

(38) Pakoulev, A. V.; Rickard, M. A.; Meyer, K. A.; Kornau, K. M.; Mathew, N. A.; Thompson, D. E.; Wright, J. C. *J. Phys. Chem. A* 2006, *110*, 3352.

(39) Pakoulev, A. V.; Rickard, M. A.; Mathew, N. A.; Kornau, K. M.; Wright, J. C. *J. Phys. Chem A* 2007, *111*, 6999.

(40) Edington, M. D.; Riter, R. E.; Beck, W. F. *J. Phys. Chem. B* 1997, *101*, 4473.

(41) Homoelle, B. J.; Edington, M. D.; Diffey, W. M.; Beck, W. F. *102* 1998, 3044.

(42) Zhang, J. M.; Shiu, Y. J.; Hayashi, M.; Liang, K. K.; Chang, C. H.; Gulbinas, V.; Yang, C. M.; Yang, T.-S.; Wang, H. Z.; Chen, Y.-T.; Lin, S. H. *J. Phys. Chem. A* 2001, *105*, 8878.

(43) Szalontai, B.; Gombos, Z.; Csizmadia, V.; Csatorday, K.; Lutz, M. *Biochemistry* 1989, *28*, 6467.

(44) Szalontai, B.; Gombos, Z.; Csizmadia, V.; Bagyinka, C.; Lutz, M. *Biochemistry* 1994, *33*, 11823.

(45) Kneip, C.; Parbel, A.; Foerstendorf, H.; Scheer, H.; Siebert, F.; Hildebrandt, P. *J. Raman. Spectrosc.* 1998, *29*, 939.

(46) Mroginski, M. A.; Mark, F.; Thiel, W.; Hildebrandt, P. *Biophys. J.* 2007, *93*, 1885.

(47) Doust, A. B.; Marai, C. N. J.; Harrop, S. J.; Wilk, K. E.; Curmi, P. M. G.; Scholes, G. D. *J. Mol. Biol.* 2004, *344*, 135.

(48) Trebino, R. *Frequency Resolved Optical Gating: The Measurement of Ultrashort Laser Pulses*; Kluwer Academic Publishers: Boston, Dordrecht, London, 2000.

(49) Cowan, M. L.; Ogilvie, J. P.; Miller, R. J. D. *Chem. Phys. Lett.* 2004, *386*, 184.

(50) Goodno, G. D.; Dadusc, G.; Miller, R. J. D. *J. Opt. Soc. Am. B* 1998, *15*, 1791.

(51) Maznev, A. A.; Nelson, K. A.; Rogers, J. A. *Opt. Lett.* 1998, *23*, 1319.

(52) Moran, A. M.; Maddox, J. B.; Hong, J. W.; Kim, J.; Nome, R. A.; Bazan, G. C.; Scherer, N. F. *J. Chem. Phys.* 2006, *124*, 194904.

(53) Brixner, T.; Mancal, T.; Stiopkin, I. V.; Fleming, G. R. *J. Chem. Phys.* 2004, *121*, 4221.

(54) Khurmi, C.; Berg, M. A. *J. Phys. Chem. A* 2008, *112*, 3364.

(55) Underwood, D. F.; Blank, D. A. *J. Phys. Chem. A* 2003, *107*, 956.

(56) Gundogdu, K.; Stone, K. W.; Turner, D. B.; Nelson, K. A. *Chem. Phys.* 2007, *341*, 89.

(57) Kim, J.; Wong, C. Y.; Nair, P. S.; Fritz, K. P.; Kumar, S.; Scholes, G. D. *J. Phys. Chem. B* 2006, *110*, 25371.

(58) Lepetit, L.; Chériaux, G.; Joffre, M. *J. Opt. Soc. Am. B* 1995, *12*, 2467.

(59) Gallagher, S. M.; Albrecht, A. W.; Hybl, J. D.; Landin, B. L.; Rajaram, B.; Jonas, D. M. *J. Opt. Soc. Am. B* 1998, *15*, 2338.

(60) Hybl, J. D.; Albrecht Ferro, A.; Jonas, D. M. *J. Chem. Phys.* 2001, *115*, 6606.

(61) Khalil, M.; Demirdöven, N.; Tokmakoff, A. *J. Phys. Chem. A* 2003, *107*, 5258.

(62) Jonas, D. M. *Annu. Rev. Phys. Chem.* 2003, *54*, 425.

(63) Moran, A. M.; Park, S.; Scherer, N. F. *J. Phys. Chem. B* 2006, *110*, 19771.

(64) Gallagher Faeder, S. M.; Jonas, D. M. *J. Phys. Chem. A* 1999, *103*, 10489.

(65) Gallagher Faeder, S. M.; Jonas, D. M. *Phys. Rev. A* 2000, *62*, 033820:1.

(66) Zhang, W. M.; Meier, T.; Chernyak, V.; Mukamel, S. *J. Chem. Phys.* 1998, *7763*, 7763.

(67) Yang, M.; Fleming, G. R. *Chem. Phys.* 2002, *282*, 163.

(68) Nelson, K. A.; Casalegno, R.; Miller, R. J. D.; Fayer, M. D. *J. Chem. Phys.* 1982, *77*, 1144.

(69) Hybl, J. D.; Yu, A.; Farrow, D. A.; Jonas, D. M. *J. Phys. Chem A* 2002, *106*, 7651.

(70) Park, S.; Flanders, B. N.; Shang, X.; Westervelt, R. A.; Kim, J.; Scherer, N. F. *J. Chem. Phys.* 2003, *118*, 3917.

(71) Goodno, G. D.; Astinov, V.; Miller, R. J. D. *J. Phys. Chem. B* 1999, *103*, 603.

(72) Fleming, G. R. *Chemical Applications of Ultrafast Spectroscopy*; University Press: New York, 1986.

(73) Wynne, K.; Hochstrasser, R. M. *Chem. Phys.* 1993, *171*, 179.

(74) Farrow, D. A.; Smith, E. R.; Qian, W.; Jonas, D. M. *J. Chem. Phys.* 2008, *129*, 174509:1.

(75) Matro, A.; Cina, J. A. *J. Phys. Chem* 1995, *99*, 2568.

(76) Nagarajan, V.; Johnson, E. T.; Williams, J. C.; Parson, W. W. *J. Phys. Chem. B* 1999, *103*, 2297.

(77) Lin, S. W.; Groesbeek, M.; van der Hoef, I.; Verdegem, P.; Lugtenburg, J.; Mathies, R. A. *Biochemistry* 1998, *28*, 1498.

(78) Andel III, F.; Murphy, J. T.; Haas, J. A.; McDowell, M. T.; van der Hoef, I.; Lugtenburg, J.; Lagarias, J. C.; Mathies, R. A. *Biochemistry* 2000, *39*, 2667.

(79) Fodor, S. P.; Lagarias, J. C.; Mathies, R. A. *Biochemistry* 1990, *29*, 11141.

(80) Freed, K. F. *Top. Appl. Phys.* 1976, *15*, 23.

(81) Morse, M. D.; Puiu, A. C.; Smalley, R. E. *J. Chem. Phys.* 1982, *78*, 3435.

(82) Jonas, D. M.; Lang, M. J.; Nagasawa, Y.; Joo, T.; Fleming, G. R. *J. Phys. Chem* 1996, *100*, 12660.

CHAPTER 5. NATURE OF EXCITED STATES AND RELAXATION MECHANISMS IN C-PHYCOCYANIN

5.1. INTRODUCTION

Essential to the understanding of photoinduced relaxation in multi-chromophore systems is the composition of excited states.[1-4] When wavefunctions delocalize among multiple chromophores, transitions between exciton states proceed through solvent fluctuations and vibronic internal conversion channels. By contrast, incoherent energy transfer dynamics take hold for systems in which excited state wavefunctions are localized to the individual molecules comprising the complex.[5-8] Frenkel exciton models applied to photosynthetic proteins, molecular aggregates and organic crystals show that (delocalized) exciton wavefunctions originate in interactions between molecular transition moments.[1-4,9-11] The appropriate view of electronic structure is governed by the relative sizes of these intermolecular couplings and system-bath interaction strengths, where the latter tend to localize wavefunctions to the individual pigment sites.[12,13] The delineation of relaxation mechanisms is not always clear in photosynthetic proteins because the interactions between pigments separated by less than a few nanometers are generally comparable to the amplitudes of environment-induced energy level fluctuations.[14-17] Understanding the nature of excited states in such systems generally relies on the application of advanced theory and experiments.

Adapted with permission from Womick, J.M.; Moran, A.M. *J. Phys. Chem. B* 2009, *113*, 15771-15782.

In this chapter, the nature of the excited states and relaxation mechanisms of C-Phycocyanin (CPC) are investigated using femtosecond laser spectroscopies. As shown in Figure 5.1, the structure of CPC consists of 9 phycocyanobilin pigments arranged about a three-fold axis of symmetry.[18-20] The structure is considered as a "trimer" composed of three α (light gray) and three β (dark gray) monomer sub-units. Upon trimer formation, the α84 and β84 pigments of adjacent monomer units come into close contact. Excited state delocalization in these pairs of α84 and β84 pigments (i.e., dimers) is the central issue addressed in this work. The α84 and β84 pigments within a particular dimer are separated by only 2.1 nm, whereas the separation between all other pairs of pigments in CPC is > 5 nm. Close proximity of pigments within the dimer opens the possibility that intermolecular interactions give rise to exciton formation. In fact, several investigations find evidence of exciton formation in the α84-β84 pigments of a closely related protein, Allophycocyanin (APC), in which geometry of the dimer is quite similar to that of CPC.[21-25] Experiments conducted in this chapter closely examine the interplay between intermolecular couplings and the thermal fluctuations of the environment that compete to localize electronic wavefunctions. These results are discussed in the context of our recent study of APC.[26] Together, these investigations provide insight into how phycobiliproteins configure their pigments and use environment-induced fluctuations to optimize the efficiency of the phycobilisome antenna.

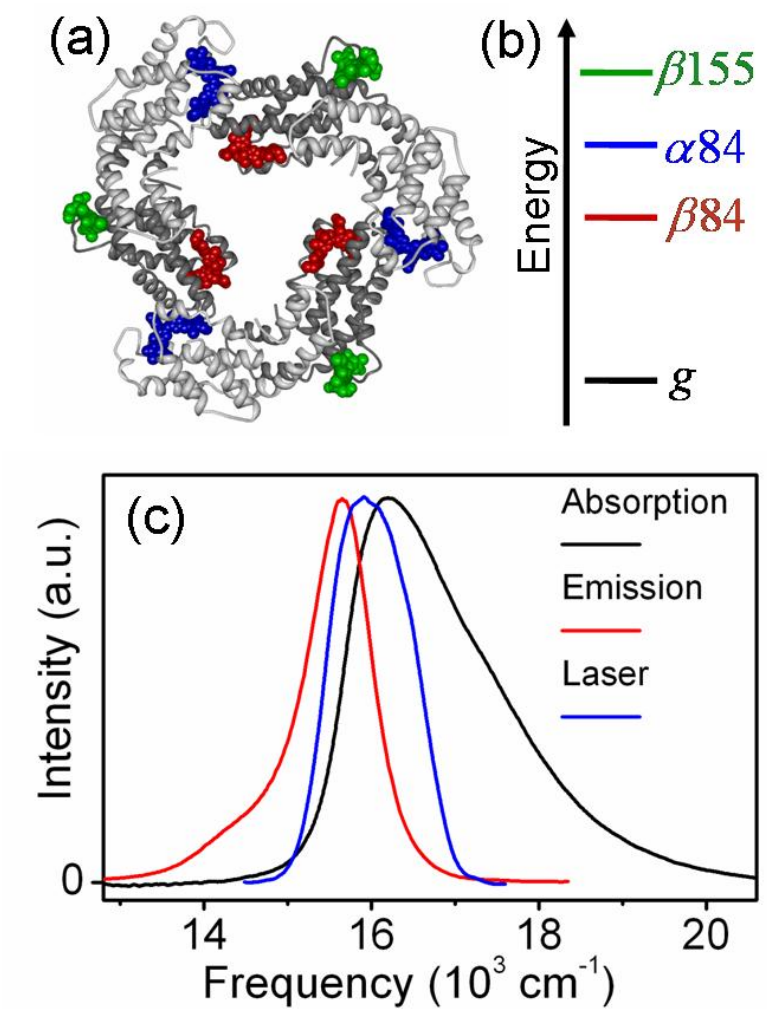

Figure 5.1. (a) Structure of CPC trimer in which red, blue and green respectively represent the β84, α84, and β155 pigments. (b) Energy levels diagram for three pigments. (c) Absorption (black) and fluorescence emission (red) spectra for CPC overlaid with spectrum of laser pulses used for most of the measurements.

Electronic relaxation dynamics of CPC have been investigated using spectroscopies that measure anisotropy in either transient absorption or fluorescence emission.[27-30] Although these anisotropy techniques provide similar information, different conclusions have been reached by various authors regarding the nature of relaxation mechanisms (i.e.,

incoherent energy transfer versus inter-exciton population decay). One aspect of the dynamics for which there is broad agreement is the presence of a sub-picosecond non-radiative transition involving the α84-β84 pigment dimers, which is over 50 times faster than that the electronic relaxation processes associated with any other pair of pigments. Much of the present understanding of CPC photophysics is owed to Sauer and co-workers who carefully examined both monomers and trimers using a variety of theoretical and experimental methods.[28,29] It was concluded that the time scale of the transition involving the α84-β84 dimer is well-described with Förster theory. Zhang et al. interpreted fluorescence upconversion measurements using an exciton model, but acknowledged that heterogeneity in the molecular site energies, which were unknown at the time, could motivate a description of electronic relaxation based on Förster energy transfer.[31] Gillbro et al. applied transient absorption anisotropy measurements to CPC and assigned a 0.5 ps decay component to Förster energy transfer between the α84 and β84 pigments.[27] The Förster model was deemed appropriate because the spectroscopic line widths of CPC are larger than the estimated 112 cm^{-1} intermolecular coupling in the dimer. By contrast, the transient absorption anisotropy measurements of Riter et al. assigned a 35 fs time constant internal conversion between exciton states.[30] This research agrees with Riter et al. that the sub-100 fs dynamics in the anisotropy are particularly important for elucidating the electronic relaxation mechanisms of CPC. Our transient absorption anisotropy measurements provide new information on these sub-100 fs dynamics with a 7.5-fold improvement in time resolution.

Theoretical and experimental advances occurring in the last decade allow CPC to be examined with improved time resolution and sensitivity. First, the time resolution available in ultrafast spectroscopies has substantially improved because of advances in nonlinear

optics.[32-34] The generation of sub-20 fs pulses is now routine in the region of the visible spectrum where CPC absorbs light. Technical developments have also made possible the application of a variety of nonlinear spectroscopies analogous to multidimensional NMR techniques.[35-44] For example, two-dimensional photon echo spectra correlate photoexcited and relaxed states without the compromise in time and frequency resolution inherent to conventional pump-probe techniques.[45-50] In addition, the "cross peaks" resolved in these 2D spectra are particularly sensitive to exciton formation.[51-54] Here we leverage these technical advances for improved physical insight into CPC electronic structure.

The present investigation of CPC complements our recent study of APC in which transient grating and two-dimensional photon echo signals were used to constrain the parameters of a Frenkel exciton Hamiltonian.[26] We found that energy gaps at the β84 and α84 sites of APC were respectively 15300 and 16060 cm^{-1} with an intermolecular coupling of -163 cm^{-1}. This basis of non-degenerate pigments gives rise to excitons that are 96% localized to the individual pigments comprising the dimer. Nonetheless, unambiguous signatures of exciton formation were found in transient absorption anisotropy and photon echo signals. For example, excited state absorption between delocalized single and double exciton states causes the transient absorption anisotropy to increase with the signal emission frequency. Further support of exciton formation in APC derives from the observation of cross peaks in photon echo spectra. In addition, nuclear coherences observed in transient absorption anisotropy signals enabled assignment of the dominant relaxation channel to an 800 cm^{-1} promoting mode representing a hydrogen out-of-plane wagging vibration similar to those found in phytochrome and retinal proteins.[55-58] Overall, the results suggest that APC

uses delocalized electronic states to enhance electronic relaxation rates and quickly configure itself for efficient energy transfer to the reaction center.

5.2. EXPERIMENT

C-Phycocyanin (CPC), isolated from *Spirulina*, was purchased from Prozyme as a suspension in 60% ammonium sulfate. Spectroscopic measurements used solutions of CPC in 50 mM potassium phosphate buffer at pH 7.0. All experiments were performed within 12 hours of solution preparation. Optical experiments circulated the solutions at a rate of 4 mL/s in flow system using a peristaltic pump with reservoir of 10 mL. The flow rate was set at the maximum value for which turbulence in the flow cell did not appreciably degrade the signal-to-noise ratio. The absorbance of the solution was 0.15 at 16200 cm^{-1} in a 0.5 mm path length flow cell. Absorbance spectra were measured before and after experiments to confirm the absence of sample degradation.

The one-color transient grating (TG) and photon echo (PE) experiments in this chapter use the same equipment and procedures described elsewhere.[59-61] Briefly, the TG and PE experiments use a diffractive optic-based interferometer similar to those reported in several earlier publications.[39,40,62-65] The apparatus applies four pulses in a boxcars (square) laser beam geometry. Pulses with durations of 17 fs and energies of 5 nJ are focused to 120 um spot size at the sample for a fluence of $1.4x10^{14}$ photons/cm^2. Increasing the pulse energies by a factor of four has no effect on the measured dynamics. Signals are detected by spectral interferometry using a back-illuminated CCD array (Princeton Instruments PIXIS 100B) mounted on a 0.3 meter spectrograph. Integration times are 100-200 ms. Signals are processed using a Fourier transform algorithm.[35,66,67]

Anisotropies compare tensor elements for real (absorptive) TG signal components measured in immediate succession, where each tensor element represents an average of 15 scans of the optical delay line (25 minutes total data acquisition time). The experiments were repeated several times and suggest that this procedure yields an error of approximately +/- 0.03 in the anisotropy. The photon echo spectra presented here are performed under the magic angle polarization condition. Rephasing and non-rephasing signals are superposed to obtain absorptive line shapes.[46,48,68] Scans of photon echo spectra at a series of population times are repeated 10 times and averaged for a total data acquisition time of 5 hours.

Phase angles of TG and PE signals are defined by reference to the pure buffer solution, which is taken to possess a fully dispersive (imaginary) signal phase because it is transparent to visible light. TG signal fields are first measured with the pure buffer. Calibration of the TG signal phase for CPC is achieved by exchanging the sample reservoir for the CPC solution without moving the flow cell. The PE signal phase is then readily obtained using the projection slice theorem of Fourier transforms.[36] That is, two-dimensional PE signals are integrated over the ω_τ dimension (i.e., Fourier transform of τ delay shown in Figure 5.2), and the phase of this projection is adjusted for agreement with the TG signal phase. Earlier investigations successfully use this same phasing procedure.[69,70]

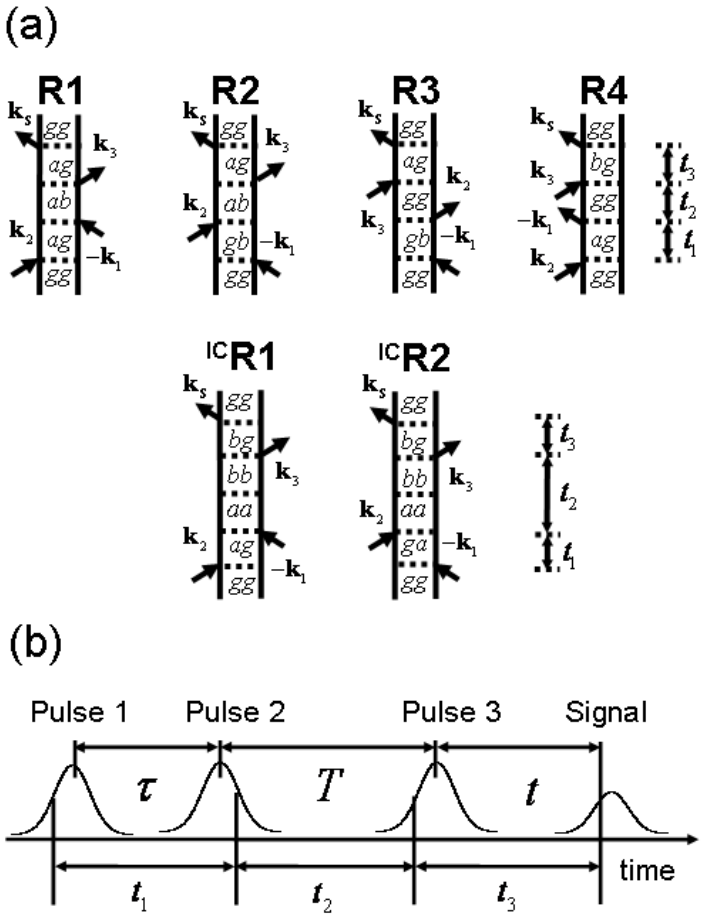

Figure 5.2. (a) Feynman diagrams for dominant terms in the transient grating and photon echo spectroscopies in this chapter. R1, R2, R3 and R4 are restricted to terms in which $a = b$ when the zeroeth order Hamiltonian of Equation (5.1) does not include (weak) intermolecular interactions. The superscript IC used in the bottom row denotes incoherent exciton transport. Terms in the nonlinear response function corresponding to these diagrams are presented in Appendix D. (b) Pulse sequence used for TG and PE spectroscopies. The delays, τ and T, are experimentally controlled. Intervals between field-matter interactions are given by t_1, t_2 and t_3.

The two-color TG measurements presented in Figure 5.5 use an $E_1 \& E_2$ pulse-pair and an E_3 pulse (see Figure 5.2) derived from separate optical parametric amplifiers. The spectrum of the E_3 "probe" pulse spans the 500-750 nm range and we are unable to fully compensate for the dispersion over this broad bandwidth using a prism compressor. The

frequency-dependent time overlap of E_3 with the compressed $E_1 \& E_2$ pulse-pair is taken into account numerically using a procedure already well-established for conventional two-pulse transient absorption spectroscopy with a continuum probe.[71] TG signals obtained with the transparent buffer solution are used as a reference to numerically correct the dependence of "time-zero" on the signal emission frequency. We obtain a full-width half maximum instrument response of <60 fs at signal emission frequencies of 14500-18500 cm^{-1} using a prism compressor configured to minimize dispersion at 16800 cm^{-1}. Experiments in this chapter use laser pulses with time-bandwidth products less than 0.52.

5.3. THEORETICAL MODEL FOR C-PHYCOCYANIN

5.3.1. Parameterization of the Hamiltionian

The site energies and inter-pigment couplings in CPC have been examined with comprehensive studies of monomers, trimers and mutant proteins.[28,29] Our parameterization of the system Hamiltonian is guided by these earlier investigations. In addition, spectroscopic line widths and Franck-Condon factors are obtained with consideration the present measurements. Here, it is necessary to consider a basis of only the three unique pigments, α84, β84 and β155, because the measurements examine dynamics on a short time scale (< 10 ps) for which electronic relaxation occurs only within the α84-β84 dimers. Here the α84 and β84 pigments refer to the closely spaced (2.1 nm) dimers of adjacent peptide units (see Section 5.1). It is irrelevant with which peptide unit β155 is taken to be associated because it transfers energy to other pigments at a rate slow compared to the time scale for which signals are measured and simulated.

Under the assumption of localized electronic states, the zeroeth-order Hamiltonian of the system simply sums over the three pigment sites as

$$H_{Sys}^{(0)} = \sum_{a}^{3} E_a \left|a\right\rangle\left\langle a\right| \tag{5.1}$$

where E_a is the energy gap of pigment a (i.e., α84, β84 or β155). This chapter regards the intermolecular interactions neglected in Equation (5.1) as weak perturbation inducing incoherent energy transfer between pigment sites.[5-8,14] Because $H_{Sys}^{(0)}$ is diagonal in the local basis, the energy levels and transition dipoles entering the optical response function are independent of intermolecular couplings. Throughout this chapter Equation (5.1) is referred to as the zeroeth-order Hamiltonian to emphasize that intermolecular interactions influence spectroscopic signals only through their promotion of incoherent energy transfer; the applied fields interact with localized electronic states.

The time scale and magnitude of environment-induced fluctuations in E_a are described with Λ_{aa}^{-1} and Δ_{aa}, respectively. Spectroscopic line broadening is modeled with a single overdamped Brownian oscillator coordinate in the high-temperature limit

$$g'_{ab}(t) = g'_{ba}(t) = \frac{1}{\kappa_a^2}\left(1 - i\frac{\kappa_a \Delta_{ab}}{2k_B T}\right)\left[\exp\left(-\Lambda_{ab}\left|t\right|\right) + \Lambda_{ab} t - 1\right] \tag{5.2}$$

where the symmetrized line broadening function is defined as $g_{ab}(t) \equiv g'_{ab}(t) + g'_{ba}(t)$ and $\kappa_a = \Lambda_{aa} / \Delta_{aa}$.[2,10,72] The optical response functions assume that all vibronic transitions for a pair of electronic states, a and b, share the same $g_{ab}(t)$ function. Essentially, this treatment says that environment-induced fluctuations particular to vibrational coordinates are negligible compared to fluctuations of the electronic energy levels. The parameters of Equations (5.1) and (5.2) are given in Table 5.1. Note that no transformation of Equation (5.2) is necessary because the states of the individual pigments are eigenstates of $H_{Sys}^{(0)}$. We

assume a 60° angle between transition dipoles for the α84 and β84 pigments. This angle is consistent with the present measurements and also within the 52°-65° range suggested by earlier spectroscopic investigations.[27,29]

5.3.2. Computation of Spectroscopic Signals

Modern methods for computing spectroscopic signals of photosynthetic proteins and molecular aggregates can be found in recent literature.[2-4,7,73] The model used here is a modified version of that presented in Sections 5.1 and 5.2 of Reference [74], where line broadening and exciton transport are described with a cumulant expansion of Gaussian fluctuations. In our recent study of APC, quantized nuclear modes were added to the model of Reference [74] to account for vibronic coupling. Here we model experiments using a similar approach with one important difference; signal contributions requiring the inclusion of intermolecular interactions in the zeroeth-order Hamiltonian, $H_{Sys}^{(0)}$, are neglected. It will be shown below that the transient absorption anisotropy is particularly sensitive to the composition of $H_{Sys}^{(0)}$.

Figure 5.2 presents Feynman diagrams representing all terms in the nonlinear response function. Sensitivity of the optical response to exciton formation centers on the two dummy indices, a and b, involved in the summations of the R1, R2, R3 and R4 terms. Recognizing which terms are forbidden and allowed in these summations is the key to distinguishing exciton electronic structure from states localized to the individual pigments. Specifically, we suggest a rule that terms in which $a \neq b$ must be neglected when intermolecular couplings are not part of $H_{Sys}^{(0)}$ (see Equation (5.1)). Under this condition, intermolecular interactions influence the optical response only through the ^{IC}R1 and ^{IC}R2

terms by promoting incoherent energy transfer between pigment sites.[5-8] Alternatively, with intermediate and/or strong intermolecular interactions, the couplings are taken into account at zeroeth-order. The Hamiltonian must then be transformed into the exciton basis and the nonlinear response does not restrict the R1, R2, R3 and R4 summations to terms in which $a = b$.[2,4,10,74]

Figure 5.3 further explains the type of nonlinearity neglected under the zeroeth-order assumption of uncoupled pigments (Equation (5.1)). The key point is that, in the absence of zeroeth-order intermolecular coupling, the R4 nonlinearity can be generated only when all four field-matter interactions occurs with the same molecule. Terms in which pairs of interactions occur with the transition dipoles of different pigments cannot contribute because, in essence, these sites do not share the same ground state. By contrast, coherent "cross terms" in which $a \neq b$ contribute when pigment coupling gives rise to exciton electronic structure. Thus, signatures of electronic relaxation mechanisms in the R1, R2, R3 and R4 nonlinearities are quite well-defined. Pigment complexes undergoing Förster energy transfer restrict summations to terms in which $a = b$, whereas systems relaxing by internal conversion between exciton states have unrestricted summations (i.e., $a \neq b$ is allowed).

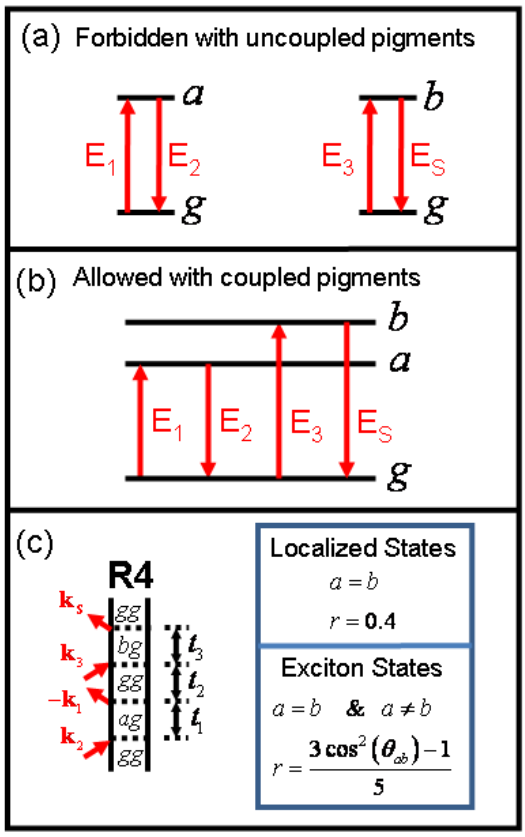

Figure 5.3. (a) Sequences with pairs of interactions on pigments uncoupled in the zeroeth order Hamiltonian, $H_{Sys}^{(0)}$, are forbidden. (b) Pairs of interactions with separate resonances are allowed in the exciton basis. (c) Field-matter interaction sequence expressed for the R4 diagram. Anisotropies depend on relative transition dipole orientations only in the (coupled) exciton basis.

The ^{IC}R1 and ^{IC}R2 terms represent incoherent non-radiative transitions between electronic states. These terms are particularly important for interpreting dynamics in transient absorption anisotropy experiments examining weakly coupled pigments because the first two field-matter interactions occur with different transition dipoles than the final two. The anisotropy obtained by summing the ^{IC}R1 and ^{IC}R2 terms is equal to 0.4 at t_2 =0 and decays to an asymptotic value determined by the relative orientations of the μ_{ga} and μ_{gb} dipoles. These are the only terms in Figure 5.2 for which summations over $a \neq b$ are

allowed with the zeroeth-order Hamiltonian of Equation (5.1). In this limit, the anisotropy obtained by summing over the R1, R2, R3 and R4 terms is equal to 0.4 at all pulse delays.

The nonlinear polarization is computed by convoluting the response function with the applied electric fields as

$$\begin{aligned} P^{(3)}(t) = \int_0^\infty dt_1 \int_0^\infty dt_2 \int_0^\infty dt_3 \Big[& R_1(t_1,t_2,t_3) + R_4(t_1,t_2,t_3) + {}^{IC}R_1(t_1,t_2,t_3) \Big] \\ & \times E_3(t-t_3) E_1^*(t-t_3-t_2) E_2(t-t_3-t_2-t_1) \\ & + \Big[R_2(t_1,t_2,t_3) + R_3(t_1,t_2,t_3) + {}^{IC}R_2(t_1,t_2,t_3) \Big] E_3(t-t_3) \\ & \times E_2(t-t_3-t_2) E_1^*(t-t_3-t_2-t_1) \end{aligned} \tag{5.3}$$

Transient grating and photon echo signals are related to $P^{(3)}(t)$ under perfect phase-matching conditions by

$$E_S(t) = \frac{i2\pi l \omega_t}{n(\omega_t) c} P^{(3)}(t), \tag{5.4}$$

where $n(\omega_t)$ is the refractive index, l is the sample thickness, and c is the speed of light. Expressions for all terms in the response function are given in Appendix D.

5.4. RESULTS AND DISCUSSION

5.4.1. Linear Absorption and Fluorescence Spectra

The linear absorption spectrum is decomposed into transitions at the three pigment sites in Figure 5.4a, where calculations are performed with the formulas in Appendix C. The site energies are blue-shifted by about 190-390 cm^{-1} compared to the values obtained by studies of monomers and a mutant protein.[28,29] The origin of this blue-shift could be associated with geometry changes induced by trimer formation. It is interesting that our recent investigation of a closely related phycobiliprotein, APC, found a 760 cm^{-1} gap between the transition energies of the two pigments comprising the dimer,[26] whereas that of

CPC is only 350 cm^{-1}. X-ray crystal structures for APC and CPC suggest that the energy gaps may be influenced by a difference in pigment conformations.[18-20,75] The fluorescence spectrum shown in Figure 5.4b is also used to constrain the parameters of the Hamiltonian given in Table 5.1. The site energies, line widths and Franck-Condon factors of the α84 and β84 pigments are well-determined by the fit of the fluorescence line shape. By contrast, the line widths and Franck Condon factors of the β155 pigment are not as well-constrained because β155 contributes very little to the steady state fluorescence spectrum. In any case, uncertainties associated with the β155 pigment do not impact the conclusions of this chapter because our experiments and model calculations use laser spectra that overlap little with the absorption spectrum of β155.

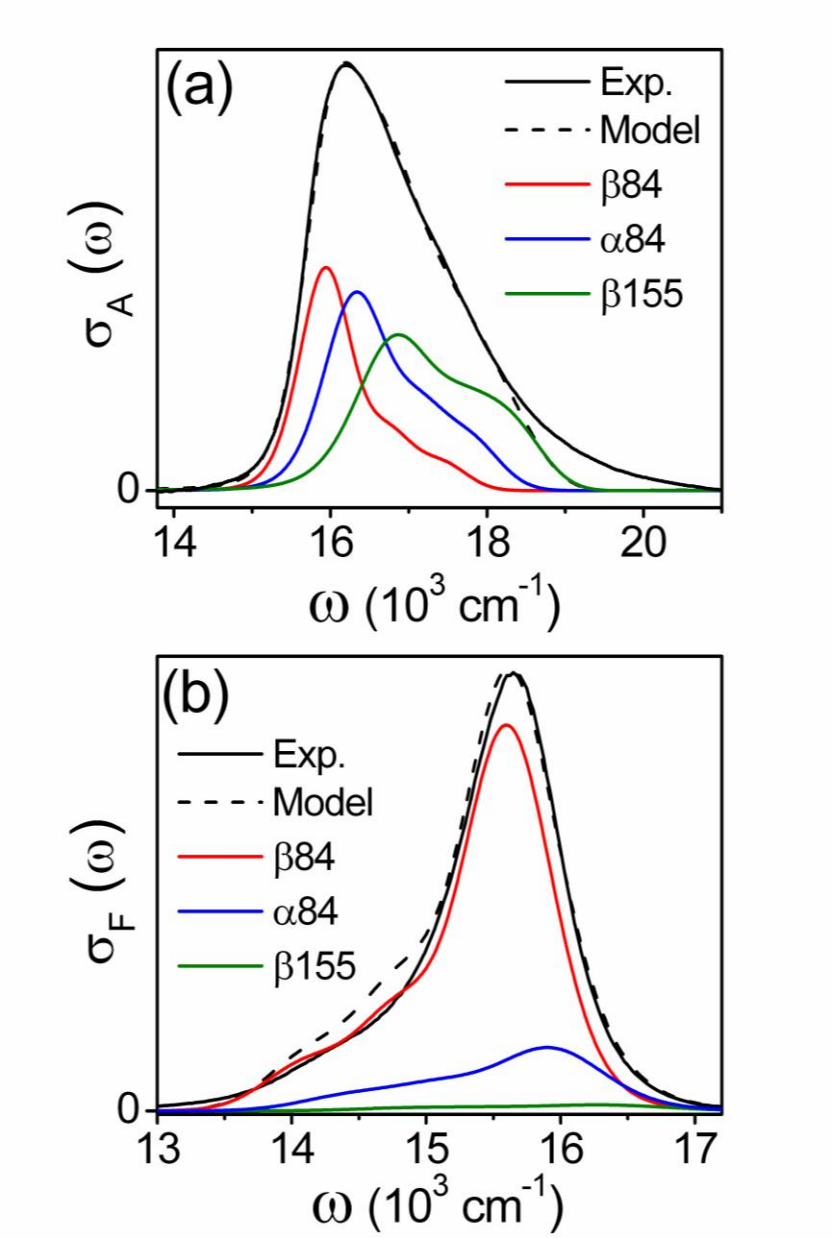

Figure 5.4. (a) Experimental (black solid) and theoretical (black dashed) linear absorption spectra. Also shown are the line shapes of the β84 (red), α84 (blue) and β155 (green) pigments. (b) Same as (a) for fluorescence spectrum. The same color scheme is used in Figure 5.1a.

5.4.2. Dynamics of Solvation and Vibrational Cooling

Nuclear relaxation in both CPC and its α-subunit have been examined using hole-burning spectroscopies employing 80 fs pump pulses and continuum probe pulses.[30,76] Red-

shifting of the signal spectrum was observed on the 50 fs time scale, whereas line broadening occurred with a time constant of 200 fs. Figure 5.5 presents transient grating signals aimed at uncovering nuclear relaxation dynamics with improved time-resolution (i.e., <60 fs FWHM instrument response over full probe bandwidth). Solvation dynamics cause significant sub-100 fs red-shifting of the signal spectrum with a concomitant decrease in signal amplitude occurring in the 16500-18000 cm^{-1} frequency range. The absence of dynamic line broadening in the measured signal spectrum is explained by the initiation of broad nuclear wavepackets. That is, the present 20 fs pump pulses degrade (frequency) resolution of the transient line broadening dynamics observed in the earlier "hole-burning" experiments.[30,76]

Both intramolecular vibrational energy redistribution (IVR) and solvation likely contribute to the red-shift observed in Figure 5.5. The solvation time scales are computed as $\Lambda_a^{-1} = 1/\kappa_a \Delta_{aa}$, where time constants of 327, 278 and 238 fs are found for β84, α84 and β155 using the parameters of Table 5.1, respectively. These calculated solvation time constants are about 5 times slower than the measured dynamics. It may be that the red-shift in the signal spectrum mainly reflects IVR. Another explanation is that this discrepancy reflects a shortcoming of the Brownian oscillator model. Indeed, modern computational solvation models have established the importance of explicitly treating intermolecular interactions in liquids (e.g., electrostatic coupling, hydrogen bonding).[77-82] The important point is that these data prove CPC to be well-configured for fast nuclear relaxation through a combination of IVR and solvation. The X-ray crystal structure indicates substantial access of water to the pockets in which the pigments are bound.[18-20] The ability of water to undergo fast structural reorganization is consistent with the sub-100 fs time scale of the dynamics.[50,83-85]

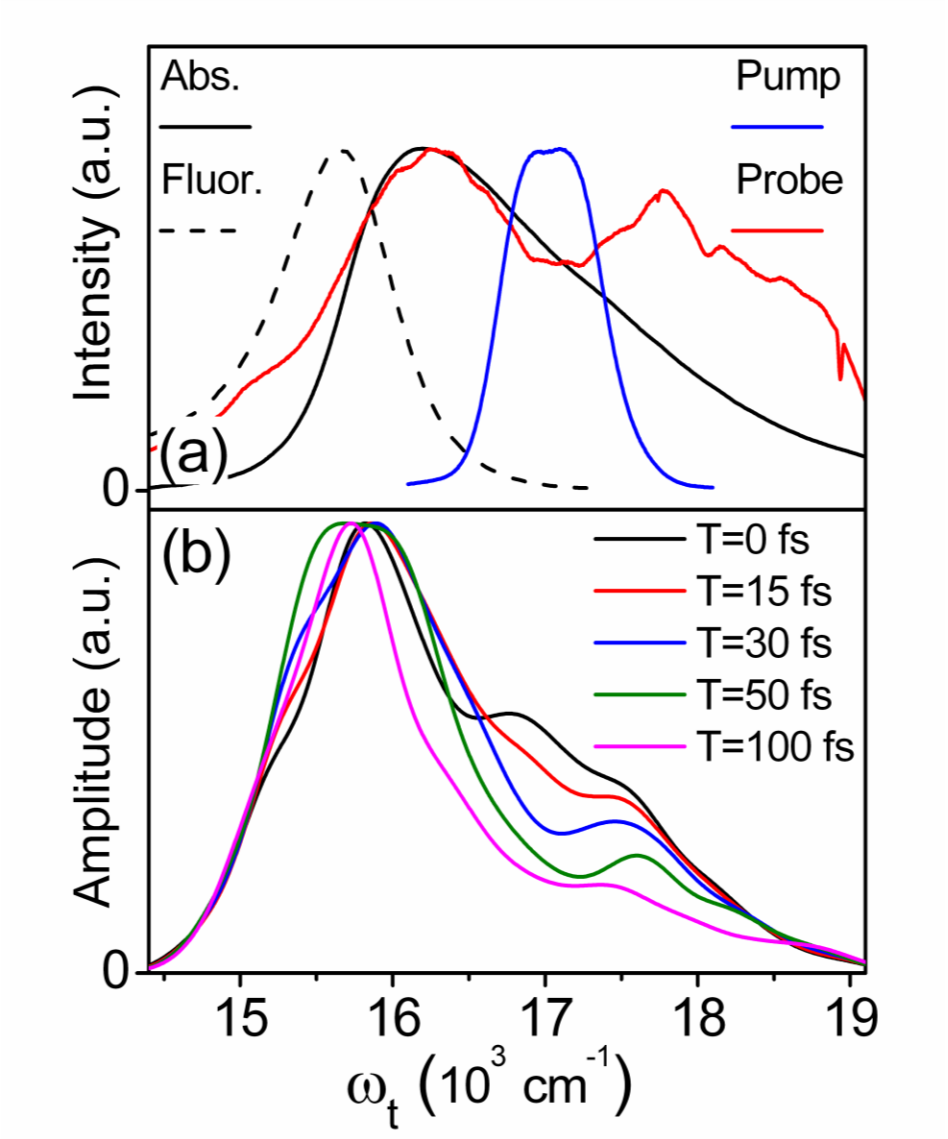

Figure 5.5. (a) Pump (blue) and probe (red) spectra overlaid on absorption and fluorescence spectra of CPC. (b) Absolute value of transient grating signal fields measured at the pump-probe delay times given in the legend. Signal amplitudes are normalized.

5.4.3. Transient Absorption Anisotropy

The transient absorption anisotropy presented in Figure 5.6 is obtained using the real (absorptive) part of the transient grating signal field measured for ZZZZ and ZZXX tensor elements. This representation is equivalent to that found with a conventional pump-probe laser beam geometry.[69] In Figure 5.6b, the decay profiles are fit with an exponential and

damped sinusoidal component for which parameters are given in Table 5.2. The 970 fs exponential decay represents incoherent energy transfer between the α84 and β84 pigments. The broadband pulses used here excite both the α84 and β84 pigments in roughly equal proportions judging by the overlap of the laser spectrum with the absorption line shapes of the individual pigments (see Figures 5.1 and 5.4). The energy gap between the excited states is 350 cm^{-1}. Therefore, the significant energy transfer occurs in both directions with the ratio of 5.26 governed by detailed balance. The 970 fs time constant measured here is slower than the time constants found in two earlier measurements for CPC where values of 500 and 690 fs were obtained.[27,30] We believe this difference in measured time constants reflects selective excitation of the α84 pigment in the earlier studies, where pulses with higher frequencies and narrower bandwidths were employed.

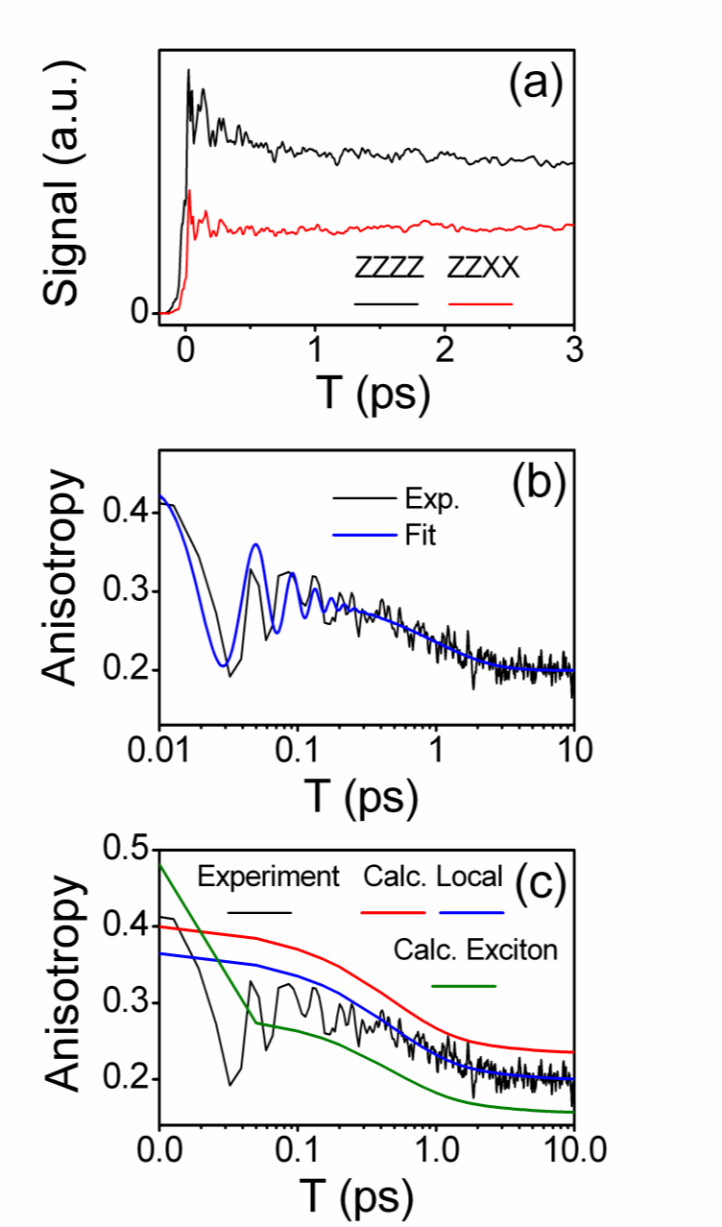

Figure 5.6. (a) Real part of transient grating signal field measured at ω_t =15625 cm^{-1} with ZZZZ (black) and ZZXX (red) polarization conditions. (b) Anisotropy computed using tensor elements in panel (a) and fit (blue, see Table 5.2). (c) Anisotropy calculated using parameters in Table 5.1 (red) and Equations in Appendix D where R1, R2, R3 and R4 are restricted to terms in which $a = b$; the blue line subtracts 0.035 from the red line. The green line assumes exciton formation and computes the anisotropy without restricting the summations of R1, R2, R3 and R4 terms (i.e., $a \neq b$ is allowed).

The experimental signal possesses a coherent component with a 795 cm^{-1} frequency, which we assign to a hydrogen out-of-plane (HOOP) wagging mode analogous to those observed in retinal polyenes. This assignment is based on comprehensive Resonance Raman studies of a related bilin chromophore, phytochrome, which has a structure similar to phycocyanobilin.[55-58] Transient absorption anisotropies measured for the phycobiliprotein APC also exhibit coherences at 800 cm^{-1} reflecting a HOOP vibration.[26] Our recent investigation assigns this coordinate as the promoting mode responsible for ultrafast internal conversion in APC.[26] Appearance of this mode in the transient absorption anisotropy underscores its asymmetric nature.[86]

In Figure 5.6c, model calculations consistent with the zeroeth-order Hamiltonian in Equation (5.1) sum over R1, R2, R3 and R4 with the restriction that $a = b$. The calculation predicts initial and asymptotic values of the anisotropy of 0.4 and 0.235, respectively. Differences between experiment and calculation are particularly apparent in that the measured r_0 and r_1 components do not sum to 0.4 at T =0 despite the model's prediction that they should. We attribute this discrepancy to a broadband excited state absorption (ESA) nonlinearity localized on the individual pigment. That is, the model calculation obtains an initial anisotropy of 0.4 under the assumption that each pigment is a two-level system, whereas ESA reduces the measured anisotropy because the "pump" and "probe" pulses can then interact with transition dipoles possessing different orientations. This interpretation is supported by transient absorption experiments for the isolated α subunit of CPC, which observed ESA in this frequency range.[76] We presently do not have enough information to accurately parameterize the line shapes of the excited state resonances. However, the contribution of ESA does not weaken the arguments regarding the electronic structure of

CPC put forth in this chapter. The 970 fs time constant is obtained with or without ESA because the nonlinearity is localized to the pigment site. In other words, ESA essentially produces an "offset" in the magnitude of the anisotropy. To emphasize this point, Figure 5.6c subtracts 0.035 from the calculated anisotropy to show that the shape of the exponential decay is well-captured by the model with the zeroeth-order Hamiltonian of Equation (5.1).

This chapter's primary conclusion of localized electronic states in the α84-β84 dimer is further supported by computing the anisotropy in an exciton basis where "cross terms" in which $a \neq b$ enter R1, R2, R3 and R4. The anisotropy then has an initial value of 0.48 and an asymptotic value of 0.16 (Figure 5.6c). This calculated decay profile clearly disagrees with the electronic relaxation dynamics measured at T <100 fs because the calculated R1 and R2 terms evolve as short-lived excited states coherences when $a \neq b$. The failure of the calculation to describe the anisotropy at long times is ascribed to the R3 and R4 ground state bleach terms, which are essentially independent of T. On the basis of the measurements and calculations in this Section, we conclude that CPC does not possess exciton electronic structure. We view this comparison of experiment and theory an important illustration of the power of transient absorption anisotropy for elucidating electronic structure.[87-90] Spectroscopic signatures of these coherent "cross terms" are unambiguous and clearly distinguish fundamentally different models of electronic structure.

The interpretation of localized electronic states reached in this Section conflicts with that of Riter et al. who also employed femtosecond transient absorption anisotropy measurements in an investigation of CPC.[30] The present apparatus leverages technical developments occurring in the last decade for a 7.5-fold improvement in time resolution. The time resolution is quite important because it enables assignment of the sub-100 fs

dynamics in the anisotropy to an impulsively excited vibration. The measured anisotropy is clearly distinct from the monotonic decay predicted with the response function appropriate for delocalized excited states (green line in Figure 5.6c). We attribute the vibration's 60 fs dephasing rate to heterogeneity in the ground state (i.e., Franck-Condon) geometry; the photoexcited nuclear coherence dephases quickly in t_2 because the nonlinear polarization radiates as a sum over many incommensurate vibrational frequencies. It should be acknowledged that we do not yet have conclusive evidence that ESA nonlinearities localized at the pigment sites are responsible for the fact that the measured r_0 and r_1 components do not sum to 0.4 at T=0. An alternative viewpoint would see this as a signature of exciton delocalization. However, we believe that the present experiments and analysis argue against this interpretation.

5.4.4. Impulsively Excited Vibrations

Figure 5.7 Fourier transforms recurrences in a transient absorption measurement to obtain a spectrum of impulsively excited vibrations. The spectrum in Figure 5.7 is similar to that measured for APC, where significant amplitude is measured near 250 cm^{-1}, 600 cm^{-1} and 800 cm^{-1}.[91] It should be noted that dominance of the low-frequency part of the spectrum reflects, in part, the finite time resolution of the experiment. The fact that the coherent signal components at 250 cm^{-1} and 600 cm^{-1} are not observed in the anisotropy suggests that these resonances represent nuclear motion imposing little distortion of the phycocyanobilin structural symmetry. Resonance Raman investigations of a related chromophore, phytochrome, indicate that resonances at 530 cm^{-1} and 635 cm^{-1} involve a mixture of hydrogen out-of-plane (HOOP) wagging and twisting of the methine bridge, whereas HOOP motion dominates the 810 cm^{-1} mode (see Section 5.4.3).[55] The mode near 250 cm^{-1} was not

assigned by earlier Resonance Raman studies. Because of its low frequency, we propose that it represents twisting the methine bridges (i.e., inter-ring torsion).

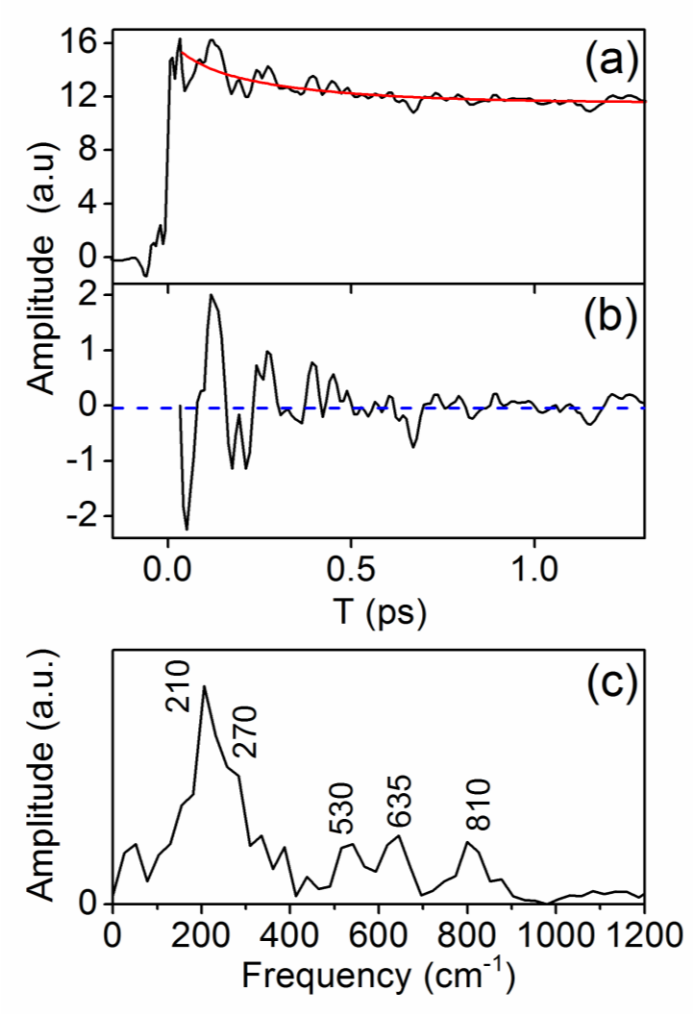

Figure 5.7. (a) Real part of transient grating signal field measured with a 17 fs pump and probe pulses centered at 15900 cm^{-1}. (b) Nuclear coherences are isolated be subtracting a decaying exponential function (red) from the data in panel (a). (c) Absolute value of Fourier transform of signals in panel (b). The noise level in (c) is approximately 15% of the peak amplitude at 635 cm^{-1}.

5.4.5. Photon Echo Spectroscopy

The photon echo (PE) signals in this Section further test our interpretation that the excited states of CPC are localized to the individual pigments. Figure 5.8 presents PE

spectra measured from T =0-120 fs. At T =0 fs, elongation of the spectrum with respect to the diagonal, $\omega_\tau = \omega_t$, represents correlation in the pumped, ω_τ, and probed, ω_t, transition frequencies.[4,36,46,48] The asymmetric peak shape enables separation of the homogeneous and inhomogeneous contributions to the line widths; the 490 cm^{-1} anti-diagonal width is the homogeneous contribution. Elongation of the line shape fully relaxes by T =30 fs, which is about 20-30 fs faster than relaxation of the PE spectrum for APC.[26] In addition, a 175 cm^{-1} red-shift in the PE peak maximum occurs on the same time scale as relaxation in the peak shape. The time scale is consistent with the red-shift observed in the transient grating (TG) signals shown in Figure 5.5 where the dynamics at T <50 fs dominate relaxation of the signal spectrum. Changes in the PE spectra from T =50-120 fs mainly involve a decrease in signal amplitude at ω_τ =16100 cm^{-1}, ω_t =16300 cm^{-1}. Consistent with this observation, the TG spectrum in Figure 5.5 exhibits a reduction in signal amplitude at ω_t =16300 cm^{-1} during this same time interval.

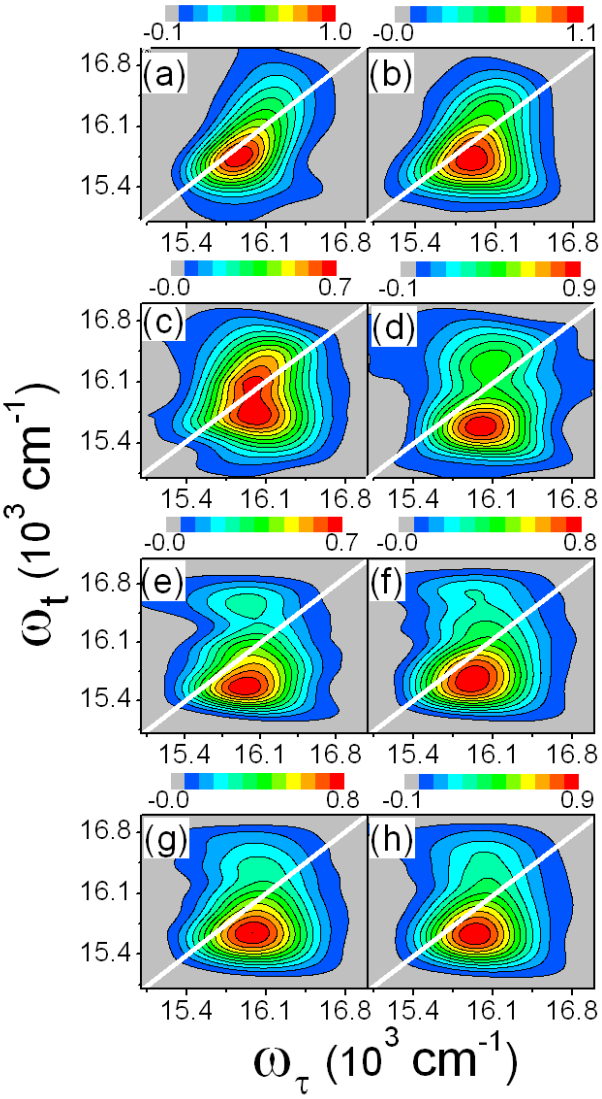

Figure 5.8. Real part of photon echo spectra measured at pulse delays, T : (a) 0 fs; (b) 10 fs; (c) 20 fs; (d) 30 fs; (e) 50 fs; (f) 70 fs; (g) 90 fs;(h) 120 fs. Pump (E_1 & E_3) and probe pulses (E_3 & E_4) are configured with magic angle polarizations. Amplitudes are scaled with respect to the peak signal amplitude at T = 0 fs. The contour lines in each panel are linearly spaced.

The calculated PE signals presented in Figure 5.9 capture the observed elongation of the PE spectrum at T <30 fs in addition to a portion of the red-shift (50 cm^{-1}) in the ω_t dimension. The simulations predict that solvation causes relaxation in the shape of PE spectrum (e.g., reduced elongation and red-shift in ω_t) at T >50 fs, whereas the

measurements in Figure 5.8 are dominated by dynamics at T <30 fs. We believe that disagreement between the measured and simulated solvation time scales mostly likely reflects limitations of the spectroscopic model.[72] That is, solvation dynamics of CPC must possess an inertial component not accounted for by the model in Appendix D, which couples a single primary Brownian oscillator coordinate to each pigment excitation. In fact, evidence for an inertial solvation process was found in earlier studies of APC and α-Phycocyanin.[25,30,76] Our PE measurements for APC and CPC suggest that the inertial solvent response is more prominent in CPC. This insight may be the key to understanding why exciton delocalization occurs in APC but not CPC.

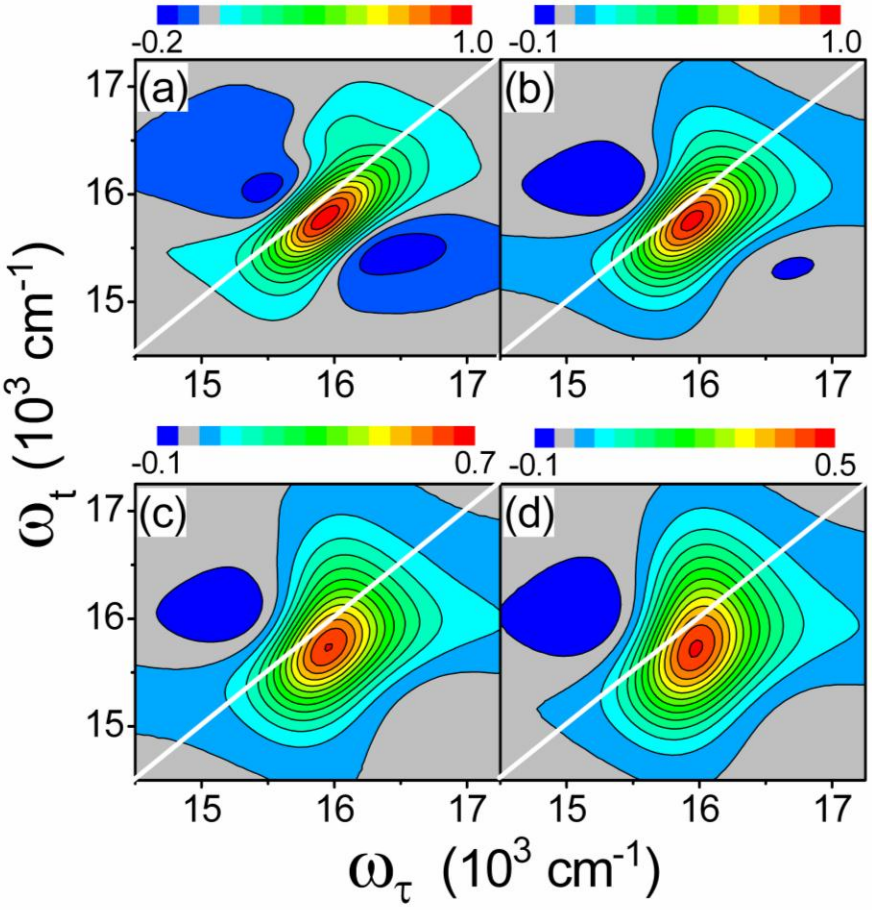

Figure 5.9. Real part of photon echo spectra calculated using parameters in Table 5.1 and Equations in Appendix D where R1, R2, R3 and R4 are restricted to terms in which $a = b$.

Pulse delays, T, are: (a) 0 fs; (b) 20 fs; (c) 50 fs; (d) 120 fs. Pump (E_1 & E_3) and probe pulses (E_3 & E_4) have magic angle polarizations. Amplitudes are scaled with respect to the spectrum at T = 0 fs. The contour lines in each panel are linearly spaced.

The assignment of the dynamics in Figure 5.9 to nuclear relaxation should be addressed here because earlier experimental work found evidence of exciton electronic structure in the α84-β84 dimers of CPC.[30] A view of the system assuming exciton states could assign the rapid red shift of the 2D spectrum to internal conversion between exciton states. We address this issue by simulating the experiment using the exciton model outlined in Appendix E. The Hamiltonian assumes exciton formation within the α84-β84 dimers, but neglects couplings (at zeroeth-order) between all other pairs of pigments. The approximations on which this model is based are consistent with experimental measurements as well as an analysis of inter-pigment interactions based on the X-ray crystal structure (see Appendix E).[28,29] The essence of the model is that the spectroscopic response can be decomposed into two independent systems: a two-level pigment ($\beta 155$) and a dimer possessing four-level exciton electronic structure (α84 and β84). Figure 5.10a presents the energy level scheme and Figure 5.10b shows a fit to the linear absorption spectrum obtained with the parameters described in Appendix E.

The calculated PE spectra in Figure 5.10c-10f clearly distinguish between predictions of the exciton model and experimental measurements. Excited state absorption (ESA) between the single exciton states, $e+$ and $e-$, and the double exciton state, f, produces interferences not found in our experimental data. It is even computed that the signal changes from positive to negative sign near ω_t =16000 cm^{-1}, whereas the sign of the measured signal is all-positive in this region. Furthermore, ESA produces interferences similar to those in

Figure 5.10 for a wide range of input parameters. We regard these calculations as strong evidence against exciton formation in CPC. Of course, different ways of writing the exciton model can be envisioned.[31] However, we believe the present to be most plausible. Similar treatments of exciton electronic structure have successfully described the spectroscopic responses of other light harvesting proteins, including APC,[26] with strongly coupled pigments.[2,4,51,92] It should also be emphasizd that the line widths and transition dipoles involving the resonances between the single and double exciton states are constrained by fits of the linear absorption and fluorescence spectra (Figure 5.4), which are in fair agreement with those of Sauer and co-workers.[28,29] Therefore, we rule out the possibility that the ESA signal component discussed in Section 5.4.3 reflects exciton electronic structure; these nonlinearities are localized to the pigment sites and are unrelated to the double exciton state f.

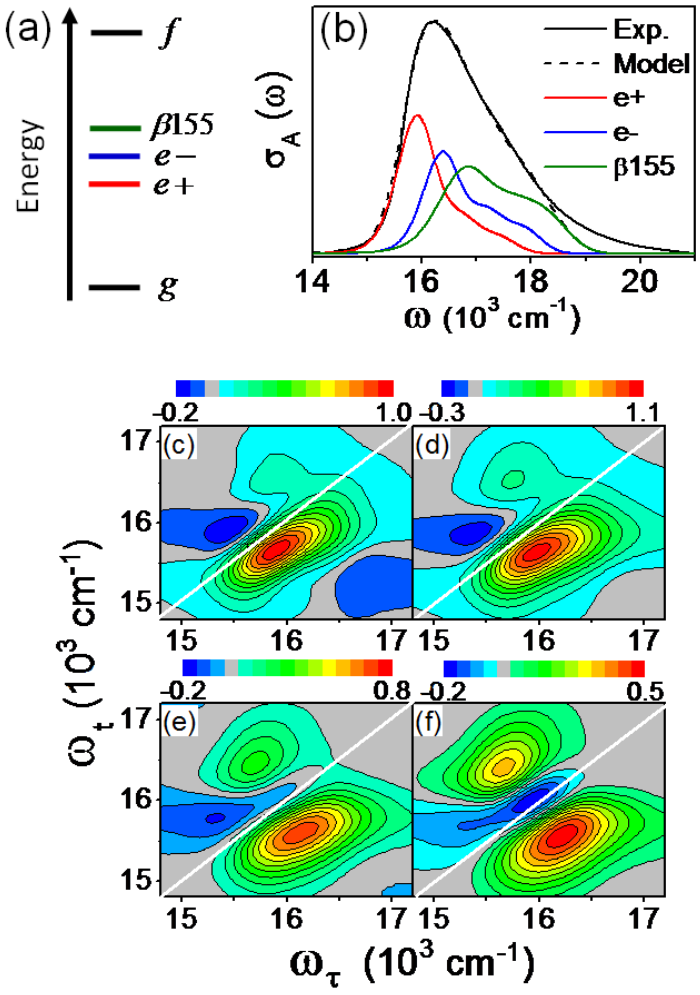

Figure 5.10. (a) Energy levels of system in which exciton formation occurs between α84 and β84 pigments. (b) Absorption spectrum of CPC overlaid with spectrum simulated using the parameters of Table 5.1. Calculated real part of photon echo spectra at pulse delays, T, are: (c) 0 fs; (d) 20 fs; (e) 50 fs; (f) 120 fs. The parameters in Table 5.1 and Equations in Appendix D are used where R1, R2, R3 and R4 are not restricted to terms in which $a = b$. Pump (E_1 & E_3) and probe pulses (E_3 & E_4) have magic angle polarizations.

5.5. CONCLUSIONS

The main conclusion of this chapter is that electronic relaxation in the α84-β84 dimers of CPC proceeds by way of incoherent energy transfer. This conclusion is supported by comparing two different experimental measurements with the predictions of a theoretical

model. (i) The anisotropy measurements and simulations shown in Figure 5.6 show that coherent cross terms in the response function give rise to a monotonically decaying anisotropy at $T < 100$ fs. By contrast, our experimental data find that the sub-100 fs time scale is dominated by an 795 cm^{-1} recurrence corresponding to an impulsively excited HOOP vibration similar to that used by retinal proteins to initiate signal transduction in vision.[55-58,93] The 60 fs dephasing time of this coherence is attributed to heterogeneity in the ground state (i.e., Franck-Condon) geometry of CPC rather than inter-exciton internal conversion. (ii) The measured PE line shapes in Figure 5.9 show no sign of theoretically predicted interferences associated with ESA signal components involving resonances between the single and double exciton levels depicted in Figure 5.10 (see also Appendix E). The presence of this higher energy excited state, f, imposes strong constraints on an interpretation that assumes exciton electronic structure because the line shapes of spectroscopic transitions involving f derive from the same parameters that control the line shapes of absorption and fluorescence spectra (Figure 5.4). Similar exciton models successfully describe double exciton electronic structure of strongly coupled chromophores,[2,51,74,92] including APC.[26] Therefore, we believe the new information obtained in the present chapter argues against exciton formation in CPC.

Insight into why CPC evolved with localized electronic states may be derived with consideration of its energy donor and acceptor pairs in the phycobilisome. CPC predominantly uses ß155 to accept energy from phycoerythrin, which has fluorescence maximum at 17400 cm^{-1}. Extremely fast solvation in CPC apparently serves to ensure that energy transfer in the phycobilisome is uni-directional. First, energy transfer from CPC to back to phycoerythrin is suppressed by solvation of the ß155 pigment. Similarly, solvation of the α84-ß84 dimer releases heat and guards against reversible energy transfer to the ß155

pigment. CPC is configured to direct energy to its α84-ß84 dimer, where energy transfer to APC initiates. This chapter suggests that inertial solvation processes are more prevalent in CPC than in APC, and are likely to be important for understanding the different photophysics present in these two proteins.

Table 5.1. Parameters of spectroscopic model

Parameter	Value	Parameter	Value
[(a)] $E_a(\beta 84)$	15890 cm^{-1}	[(b)] $F_a^{00}(\beta 84)$	0.69
[(a)] $E_a(\alpha 84)$	16240 cm^{-1}	[(b)] $F_a^{00}(\alpha 84)$	0.52
[(a)] $E_a(\beta 155)$	16640 cm^{-1}	[(b)] $F_a^{00}(\beta 155)$	0.37
$\Delta_{aa}(\beta 84)$	510 cm^{-1}	$F_{a\nu}^{01}(\nu=1,\beta 84)$	0.17
$\Delta_{aa}(\alpha 84)$	600 cm^{-1}	$F_{a\nu}^{01}(\nu=1,\alpha 84)$	0.21
$\Delta_{aa}(\beta 155)$	700 cm^{-1}	$F_{a\nu}^{01}(\nu=1,\beta 155)$	0.18
$\lvert\mu_{ga}\rvert(\beta 84)$	6.5 D	$F_{a\nu}^{01}(\nu=2,\beta 84)$	0.08
$\lvert\mu_{ga}\rvert(\alpha 84)$	6.5 D	$F_{a\nu}^{01}(\nu=2,\alpha 84)$	0.13
$\lvert\mu_{ga}\rvert(\beta 155)$	5.4 D	$F_{a\nu}^{01}(\nu=2,\beta 155)$	0.18
κ_a (all pigments)	0.2	$\omega_\nu(\nu=1)$	800 cm^{-1}
k_ν^{-1} (all ν)	10 fs	$\omega_\nu(\nu=2)$	1500 cm^{-1}

[(a)]Energy gap of pigment in Equation (5.1)

Table 5.2. Fits to Anisotropy Measurements Shown in Figure 5.6

[a]Parameter	Value
r_0	0.2
r_1	0.1
r_2	0.15
τ_1	970 fs
τ_2	60 fs
ω	795 cm^{-1}
φ	5.0 rad.

[a]Fit to Equation $r(T) = r_0 + r_1 \exp(-T/\tau_1) + r_2 \cos(\omega T + \varphi)\exp(-T/\tau_2)$

REFERENCES

(1) Capek, V.; Silinish, E. *Organic Molecular Crystals: Interaction, Localization, and Transport Phenomena*; AIP: New York, 1994.

(2) Abramavicius, D.; Palmieri, B.; Voronine, D. V.; Sanda, F.; Mukamel, S. *Chem. Rev.* 2009, *109*, 2350.

(3) Fleming, G. R.; Scholes, G. D. *Nature* 2004, *121*, 4221.

(4) Cho, M. *Chem. Rev.* 2008, *108*, 1331.

(5) *Resonance Energy Transfer*; Andrews, D. L.; Demidov, A. A., Eds.; Wiley: Chichester, 1999.

(6) Andrews, D. L. *Chem. Phys.* 1989, *135*, 195.

(7) van Amerongen, H.; Valkunas, L.; van Grondelle, R. *Photosynthetic Excitons*; World Scientific: Singapore, 2000.

(8) Scholes, G. D. *Annu. Rev. Phys. Chem.* 2003, *54*, 57.

(9) Davydov, A. *Theory of Molecular Excitons*; Plenum: New York, 1971.

(10) Mukamel, S.; Abramavicius, D.; Yang, L.; Zhuang, W.; Schweigert, I. V.; Voronine, D. V. *Acc. Chem. Res.* 2009, *42*, 553.

(11) Zhuang, W.; Hayashi, T.; Mukamel, S. *Angew. Chemie.* 2009, *48*, 3750.

(12) Kimura, A.; Kakitani, T. *J. Phys. Chem. A* 2007, *111*, 12042.

(13) Collini, E.; Scholes, G. D. *J. Phys. Chem. A* 2009, *113*, 4223.

(14) Beljonne, D.; Curutchet, C.; Scholes, G. D.; Silbey, R. J. *J. Phys. Chem. B* 2009, *113*, 6583.

(15) Sumi, H. *J. Phys. Chem. B* 1999, *103*, 252.

(16) Jang, S.; Newton, M. D.; Silbey, R. J. *Phys. Rev. Lett.* 2004, *92*, 218301.

(17) Scholes, G. D.; Jordanides, X. J.; Fleming, G. R. *J. Phys. Chem. B* 2001, *105*, 1640.

(18) Schirmer, T.; Bode, W.; Huber, R.; Sidler, W.; Zuber, H. *J. Mol. Biol.* 1985, *184*, 257.

(19) Schirmer, T.; Huber, R.; Schneider, M.; Bode, W.; Miller, M.; Hackert, M. L. *J. Mol. Biol.* 1986, *188*, 651.

(20) Schirmer, T.; Bode, W.; Huber, R. *J. Mol. Biol.* 1987, *196*, 677.

(21) Xie, X.; Due, M.; Mets, L.; Fleming, G. R. "Femtosecond Fluorescence Depolarization Study of Photosynthetic Antenna Proteins: Observation of Ultrafast Energy Transfer in Trimeric C-phycocyanin and Allophycocyanin"; SPIE Symposium, 1992.

(22) Edington, M. D.; Riter, R. E.; Beck, W. F. *J. Phys. Chem.* 1995, *99*, 15699.

(23) Edington, M. D.; Riter, R. E.; Beck, W. F. *J. Phys. Chem. B* 1997, *101*, 4473.

(24) Edington, M. D.; Riter, R. E.; Beck, W. F. *J. Phys. Chem B* 1996, *100*, 14206.

(25) Homoelle, B. J.; Edington, M. D.; Diffey, W. M.; Beck, W. F. *102* 1998, 3044.

(26) Womick, J. M.; Moran, A. M. *J. Phys. Chem. B (in press),* 2009.

(27) Gillbro, T.; Sharkov, A. V.; Kryukov, I. V.; Khoroshilov, E. V.; Kryukov, P. G.; Fischer, R.; Scheer, H. *Biochimica et Biophysica Acta* 1993, *1140*, 321.

(28) Debreczeny, M. P.; Sauer, K.; Zhou, J.; Bryant, D. A. *J. Phys. Chem.* 1995, *99*, 8412.

(29) Debreczeny, M. P.; Sauer, K.; Zhou, J.; Bryant, D. A. *J. Phys. Chem.* 1995, *99*, 8420.

(30) Riter, R. E.; Edington, M. D.; Beck, W. F. *J. Phys. Chem. B* 1997, *101*, 2366.

(31) Zhang, J. M.; Zhao, F. L.; Zheng, X. G.; Wang, H. Z.; Yang, T.-S.; Hayashi, M.; Lin, S. H. *J. Photochem. Photobiol. B: Biol.* 1999, *53*, 128.

(32) Kobayashi, T.; Baltuska, A. *Meas. Sci. Technol.* 2002, *13*, 1671.

(33) Cerullo, G.; Nisoli, M.; De Silvestri, S. *Appl. Phys. Lett.* 1997, *71*, 3616.

(34) Riedle, E.; Beutter, M.; Lochbrunner, S.; Piel, J.; Schenkl, S.; Spörlein, S.; Zinth, W. *Appl. Phys. B* 2000, *71*, 457.

(35) Gallagher, S. M.; Albrecht, A. W.; Hybl, J. D.; Landin, B. L.; Rajaram, B.; Jonas, D. M. *J. Opt. Soc. Am. B* 1998, *15*, 2338.

(36) Jonas, D. M. *Annu. Rev. Phys. Chem.* 2003, *54*, 425.

(37) Maznev, A. A.; Nelson, K. A.; Rogers, J. A. *Opt. Lett.* 1998, *23*, 1319.

(38) Goodno, G. D.; Dadusc, G.; Miller, R. J. D. *J. Opt. Soc. Am. B* 1998, *15*, 1791.

(39) Cowan, M. L.; Ogilvie, J. P.; Miller, R. J. D. *Chem. Phys. Lett.* 2004, *386*, 184.

(40) Brixner, T.; Mancal, T.; Stiopkin, I. V.; Fleming, G. R. *J. Chem. Phys.* 2004, *121*, 4221.

(41) Pakoulev, A. V.; Rickard, M. A.; Meyer, K. A.; Kornau, K. M.; Mathew, N. A.; Thompson, D. E.; Wright, J. C. *J. Phys. Chem. A* 2006, *110*, 3352.

(42) Mathew, N. A.; Yurs, L. A.; Block, S. B.; Pakoulev, A. V.; Kornau, K. M.; Wright, J. C. *J. Phys. Chem. A* 2009, *113*, 9261.

(43) Strasfeld, D. B.; Shim, S.-H.; Zanni, M. T. *Adv. Chem. Phys.* 2009, *141*, 1.

(44) Wright, J. C. *Int. Rev. Phys. Chem.* 2002, *21*, 185.

(45) Gallagher Faeder, S. M.; Jonas, D. M. *J. Phys. Chem. A* 1999, *103*, 10489.

(46) Hybl, J. D.; Albrecht Ferro, A.; Jonas, D. M. *J. Chem. Phys.* 2001, *115*, 6606.

(47) Hybl, J. D.; Yu, A.; Farrow, D. A.; Jonas, D. M. *J. Phys. Chem A* 2002, *106*, 7651.

(48) Khalil, M.; Demirdöven, N.; Tokmakoff, A. *J. Phys. Chem. A* 2003, *107*, 5258.

(49) Asplund, M. C.; Zanni, M. T.; Hochstrasser, R. M. *Proc. Natl. Acad. Sci.* 2000, *97*, 8219.

(50) Asbury, J.; Steinel, T.; Kwak, K.; Corcelli, S. A.; Lawrence, C. P.; Skinner, J. L.; Fayer, M. D. *J. Chem. Phys.* 2004, *121*, 12431.

(51) Brixner, T.; Stenger, J.; Vaswani, H. M.; Cho, M.; Blankenship, R. E.; Fleming, G. R. *Nature* 2005, *434*, 625.

(52) Read, E. L.; Engel, G. S.; Calhoun, T. R.; Mancal, T.; Ahn, T. K.; Blankenship, R. E.; Fleming, G. R. *Proc. Natl. Acad. Sci.* 2007, *104*, 14203.

(53) Moran, A. M.; Dreyer, J.; Mukamel, S. *J. Chem. Phys.* 2003, *118*, 1347.

(54) Zanni, M. T.; Ge, N. H.; Kim, Y. S.; Hochstrasser, R. M. *Proc. Natl. Acad. Sci.* 2001, *98*, 11265.

(55) Andel III, F.; Murphy, J. T.; Haas, J. A.; McDowell, M. T.; van der Hoef, I.; Lugtenburg, J.; Lagarias, J. C.; Mathies, R. A. *Biochemistry* 2000, *39*, 2667.

(56) Fodor, S. P.; Lagarias, J. C.; Mathies, R. A. *Biochemistry* 1990, *29*, 11141.

(57) Lin, S. W.; Groesbeek, M.; van der Hoef, I.; Verdegem, P.; Lugtenburg, J.; Mathies, R. A. *J. Phys. Chem. B* 1998, *102*, 2787.

(58) Lin, S. W.; Groesbeek, M.; van der Hoef, I.; Verdegem, P.; Lugtenburg, J.; Mathies, R. A. *Biochemistry* 1998, *28*, 1498.

(59) Womick, J. M.; Miller, S. A.; Moran, A. M. *J. Phys. Chem. B* 2009, *113*, 6630.

(60) Womick, J. M.; Miller, S. A.; Moran, A. M. *J. Phys. Chem. A* 2009, *113*, 6587.

(61) Miller, S. A.; Womick, J. M.; Parker, J. F.; Murray, R. W.; Moran, A. M. *J. Phys. Chem. C* 2009, *113,* 9440.

(62) Goodno, G. D.; Astinov, V.; Miller, R. J. D. *J. Phys. Chem. B* 1999, *103*, 603.

(63) Moran, A. M.; Nome, R. A.; Scherer, N. F. *J. Phys. Chem. A* 2006, *110*, 10925.

(64) Moran, A. M.; Nome, R. A.; Scherer, N. F. *J. Chem. Phys.* 2007, *127*, 184505:1.

(65) Milota, F.; Sperling, J.; Nemeth, A.; Kauffman, L. J. *Chem. Phys.* 2008, *357*, 45.

(66) Lepetit, L.; Chériaux, G.; Joffre, M. *J. Opt. Soc. Am. B* 1995, *12*, 2467.

(67) Tokunaga, E.; Terasaki, A.; Kobayashi, T. *J. Opt. Soc. Am. B* 1995, *12*, 753.

(68) Khalil, M.; Demirdoven, N.; Tokmakoff, A. *Phys. Rev. Lett.* 2003, *90*, 047401.

(69) Moran, A. M.; Maddox, J. B.; Hong, J. W.; Kim, J.; Nome, R. A.; Bazan, G. C.; Scherer, N. F. *J. Chem. Phys.* 2006, *124*, 194904.

(70) Moran, A. M.; Park, S.; Scherer, N. F. *J. Phys. Chem. B* 2006, *110*, 19771.

(71) Nakayama, T.; Amijima, Y.; Ibuki, K.; Hamanoue, K. *68* 1997, 4364.

(72) Mukamel, S. *Principles of Nonlinear Optical Spectroscopy*; Oxford University Press: New York, 1995.

(73) Sundström, V.; Pullerits, T.; van Grondelle, R. *J. Phys. Chem. B* 1999, *103*, 2327.

(74) Abramavicius, D.; Mukamel, S. *Chem. Rev.* 2004, *104*, 2073.

(75) Brejc, K.; Ficner, R.; Huber, R.; Steinbacher, S. *J. Mol. Biol.* 1995, *249*, 424.

(76) Riter, R. R.; Edington, M. D.; Beck, W. F. *J. Phys. Chem.* 1996, *100*, 14198.

(77) Corcelli, S. A.; Lawrence, C. P.; Asbury, J. B.; Steinel, T.; Fayer, M. D.; Skinner, J. L. *J. Chem. Phys.* 2004, *121*, 8897.

(78) Wang, C.; Stratt, R. M. *J. Chem. Phys.* 2007, *127*, 224503.

(79) Elola, M. D.; Ladyani, B. M. *J. Chem. Phys.* 2007, *126*, 084504.

(80) Harder, E.; Eaves, J. D.; Tokmakoff, A.; Berne, B. J. *Proc. Nat. Acad. Sci.* 2005, *102*, 11611.

(81) Hayashi, T.; la Cour Jansen, T.; Zhuang, W.; Mukamel, S. *J. Phys. Chem. A* 2005, *109*, 64.

(82) la Cour Jansen, T.; Knoester, J. *J. Chem. Phys.* 2006, *124*, 044502.

(83) Moilanen, D. E.; Levinger, N. E.; Spry, D. B.; Fayer, M. D. *J. Am. Chem. Soc.* 2007, *129*, 14311.

(84) Tokmakoff, A. *Science* 2007, *317*, 54.

(85) Cowan, M. L.; Bruner, B. D.; Huse, N.; Dwyer, J. R.; Chugh, B.; Nibbering, E. T. J.; Elsaesser, T.; Miller, R. J. D. *Nature* 2005, *434*, 199.

(86) Farrow, D. A.; Smith, E. R.; Qian, W.; Jonas, D. M. *J. Chem. Phys.* 2008, *129*, 174509.

(87) Wynne, K.; Hochstrasser, R. M. *Chem. Phys.* 1993, *171*, 179.

(88) Nagarajan, V.; Johnson, E. T.; Williams, J. C.; Parson, W. W. *J. Phys. Chem. B* 1999, *103*, 2297.

(89) Parson, W. W. *Modern Optical Spectroscopy*; Springer-Verlag: Berlin, 2007.

(90) Qian, W.; Jonas, D. M. *J. Chem. Phys.* 2003, *119*, 1611.

(91) Zhang, J. M.; Shiu, Y. J.; Hayashi, M.; Liang, K. K.; Chang, C. H.; Gulbinas, V.; Yang, C. M.; Yang, T.-S.; Wang, H. Z.; Chen, Y.-T.; Lin, S. H. *J. Phys. Chem. A* 2001, *105*, 8878.

(92) Read, E. L.; Schlau-Cohen, G. S.; Engel, G. S.; Georgiou, T.; Papiz, M. Z.; Fleming, G. R. *J. Phys. Chem. B* 2009, *113*, 6495.

(93) Kukura, P.; McCamant, D. W.; Yoon, S.; Wandschneider, D. B.; Mathies, R. A. *Science* 2005, *310*, 1006.

(94) Hochstrasser, R. M. *Chem. Phys.* 2001, *266*, 273.

(95) Dreyer, J.; Moran, A. M.; Mukamel, S. *Bull. Korean Chem. Soc.* 2003, *24*, 1091.

CHAPTER 6. TOWARDS THE ORIGIN OF EXCITON ELECTRONIC STRUCTURE IN PHYCOBILIPROTEINS

6.1. INTRODUCTION

The phycobiliproteins, Allophycocyanin (APC) and C-Phycocyanin (CPC), are an energy donor-acceptor pair who, often together with phycoerythrin and phycoerythrocyanin, comprise the phycobilisome antenna of cyanobacteria.[1-3] APC and CPC, which are the subjects of this chapter, possess the nearly identical structures shown in Figure 6.1. Both proteins form three pairs of α84-ß84 phycocyanobilin dimers at the interfaces between adjacent peptide units, whereas three ß155 pigments are found only in CPC.[4-8] Estimates vary, however, it is generally agreed that the 2.1 nm separation and relative orientation of the α84 and ß84 pigments supports a coupling strength of 110-165 cm^{-1}.[9-16] It is not clear whether the electronic structure of the α84-ß84 dimer should be viewed in the exciton or local basis *a priori* because the coupling strength is comparable to the magnitudes of energy level fluctuations produced by motion of the environment. That is, electronic wavefunctions contract to the individual pigment sites when the (Coulombic) intermolecular coupling is insufficient to overcome interactions with the solvent bath. The Förster resonance energy transfer mechanism holds in this limit.[17-24] However, when the intermolecular coupling is large, exciton electronic states delocalize within the dimers and electronic relaxation proceeds by way of internal conversion.[25-31]

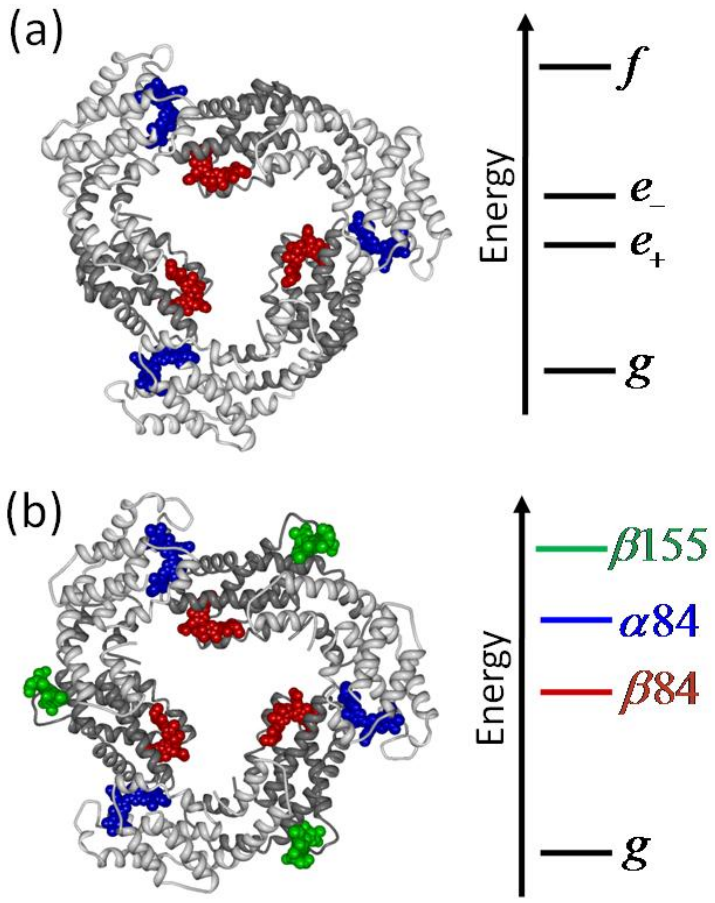

Figure 6.1. (a) Structure of APC trimer in which blue and red are respectively used to represent α84 and β84 pigments. Also shown is the energy level diagram discussed in Reference [32]. (b) Structure of CPC trimer in which red, blue and green are respectively used to represent the β84, α84, and β155 pigments. Also shown is the energy level diagram presented in Reference [33]. Structural representations for APC and CPC are generated using PDB files 1ALL[4] and 1GH0.[8] X-ray data for both systems are obtained using proteins isolated from *Spirulina platensis*.

We have recently investigated electronic relaxation mechanisms in APC and CPC, isolated from *Spirulina*, using a variety of nonlinear spectroscopies.[32,33] Analysis of these data using a Frenkel exciton model points to exciton electronic structure in APC but not CPC. Principal in reaching this conclusion is the careful analysis of allowed and forbidden nonlinearities consistent with the weak and strong coupling limits of electronic relaxation.

Two-dimensional photon echo and transient absorption anisotropy experiments for APC exhibit unambiguous signatures of a sub-100 fs internal conversion process between exciton states. The dominant internal conversion channel in APC is assigned to a promoting mode near 800 cm^{-1} involving hydrogen out-of-plane (HOOP) wagging motion similar to that observed in phytochrome and retinal proteins.[34-36] By contrast, the same experiments conducted for CPC do not find clear evidence of exciton formation. In fact, we are able to account for all experimental observations using a model in which energy transfer is incoherent and electronic wavefunctions are localized to the individual pigments. One particularly clear difference in experimental observations is that solvation dynamics cause photon echo line shapes in CPC to relax almost two times faster than those in APC, which suggests that environmental motion may be essential to understanding the electronic structures of the two proteins.

Overall, our interpretation of experiments for APC is consistent with earlier investigations by Beck and co-workers, who found clear evidence of exciton electronic structure in APC isolated from *Synechococcus*.[12,13,16,37] Indeed, much of the insights into the spectroscopic line shapes and the assignment of relaxation time constants are owed to this seminal work. Additionally, the >7-fold improvement in time resolution achieved in our study of APC enabled the attainment of new information.[32] For example, an 800 cm^{-1} nuclear coherence (i.e., HOOP mode) was detected in the transient absorption anisotropy. Broad laser bandwidth was also essential to the observation of an inter-exciton cross-peak in the 2D photon echo spectrum. It is interesting that the above conclusions and observations are inconsistent with a study by Sharkov et al. in which signatures of localized electronic states were found in APC isolated from *Mastigocladus laminosus*.[38] Studies of CPCs (isolated

from different organisms) have reached different conclusions regarding electronic relaxation mechanisms. For example, transient absorption anisotropy experiments have argued both for and against exciton electronic structure in *Synechococcus*[11] and *Mastigocladus laminosus*,[14] respectively. Sauer and co-workers obtained a 1.2 ps energy transfer time constant using time-resolved fluorescence experiments for CPC in *Synechococcus*, which agrees well with the Förster energy transfer time constant.[10] Because the 970 fs time constant found in our investigation of CPC is close to the Förster value, we are inclined to interpret the dynamics in the localized basis. Our present view is that no experiment we have conducted for CPC is better interpreted in the exciton basis.[33]

In this chapter, the nature of excited states and relaxation processes in APC and CPC are further investigated with new experiments. Transient grating (TG) spectroscopy employing quasi-continuum probe pulses establishes clear differences in the electronic and nuclear relaxation dynamics of the two proteins. To better understand the wavefunction compositions in APC and CPC, we also apply a specialized intraband electronic coherence spectroscopy (IECS) designed to enhance spectroscopic signatures of photoexcited coherences between pairs of exciton states. Signal contributions arising from impulsively excited vibrations also contribute under the IECS pulse configuration and provide information on vibronic couplings. The present measurements strengthen our earlier conclusion that energy level fluctuations at the α84 and ß84 pigments in both proteins are uncorrelated (or weakly uncorrelated). The role of such spatial correlations in promoting exciton coherence has been discussed in several recent theoretical[39-44] and experimental[45-49] investigations. This finding leads us to propose that exciton electronic structure in APC is

most appropriately viewed as wavefunction delocalization in the vibronic basis of the ß84 and α84 pigments (i.e., vibronic excitons).

Theoretical models commonly view molecular aggregates as coupled two-level systems without explicit consideration of quantized nuclear coordinates.[25-27,50] One reason for the success of these models is the suppression of vibronic couplings in large aggregates, which concentrates the transition moments of individual molecules onto the electronic origins of the ground and excited states.[51] Interaction between a pair of molecules may then be computed as the coupling between a single pair of purely electronic transition dipoles. However, the transition moment of a molecular site generally partitions as a Franck-Condon progression in small aggregates such as those found in many biological light harvesting antennae.[3,19,52] For these situations, the picture of coupled two-level systems is no longer a good approximation and the Hamiltonian should be written in a vibronic basis. The effect of vibronic couplings is clearly defined by vibronic exciton models applied to polypeptides,[53,54] the antenna of purple bacteria,[55] molecular aggregates,[56,57] and molecular solids.[58-63] It should be emphasized that the choice of basis generally has a significant impact on predicted exciton sizes and relaxation rates. That is, systems can be envisioned for which a vibronic model predicts internal conversion between exciton states, whereas the use of a purely electronic basis set points to incoherent energy transfer between pigments sites (i.e., APC is near this regime). Below we discuss the importance of vibronic couplings to the understanding of the electronic structures and relaxation rates in APC and CPC.

6.2. INTRABAND ELECTRONIC COHERENCE SPECTROSCOPY (IECS)

This Section discusses the information content of IECS with consideration of specific terms in the nonlinear polarization. We define the coherent signal components of interest

and examine issues involved in the suppression of undesired contributions from electronic populations. It should first be recognized that IECS selects a subset of the terms that contribute to conventional four-wave mixing spectroscopies (e.g., pump-probe, photon echo).[27,28,31,50,64] The unique information content of IECS originates in its use of a pair of pulses with little spectral overlap to initiate dynamics in T. Figure 6.2 defines the experimentally controlled delays between laser pulses in addition to intervals between field-matter interactions. As in pump-probe spectroscopy, the IECS polarization evolves in optical (interband) coherences during t_1 and t_3. The unique aspect of IECS is that the t_2 interval restricts dynamics to (intraband) electronic and nuclear coherences.

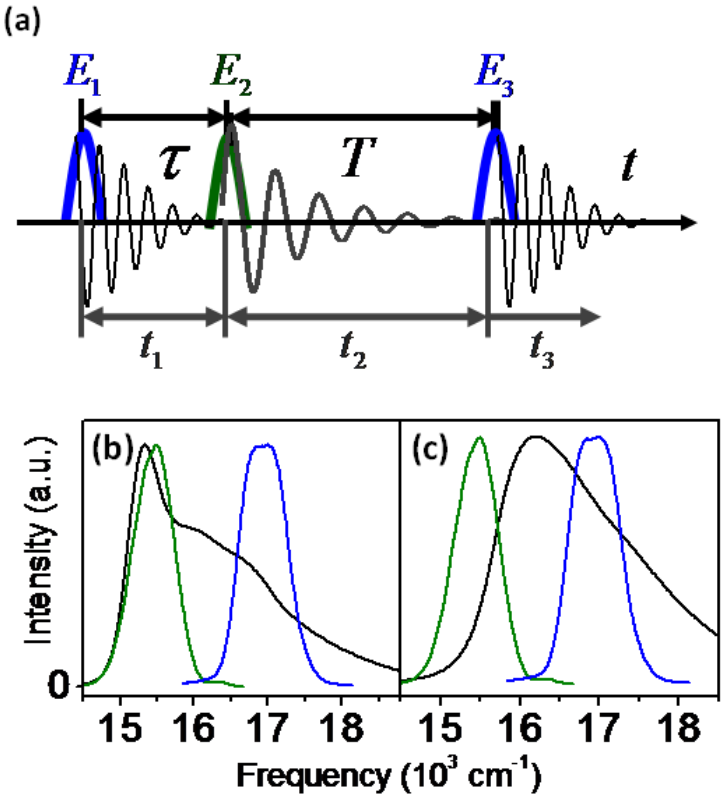

Figure 6.2. (a) Pulse sequence for intraband electronic coherence spectroscopy (IECS). Experimentally controlled delays are denoted by τ and T, where τ =0 for all measurements in this chapter. High (blue) and low (green) frequency laser pulses initiate electronic and

nuclear coherences in the delay, T. The polarization evolves in interband coherences in t_1 and t_3. Experimental laser spectra overlaid on absorbance spectra of (b) APC and (c) CPC.

The third-order polarization radiating the IECS signal field is written as[32]

$$\begin{aligned} P^{(3)}(t) = \int_0^\infty dt_1 \int_0^\infty dt_2 \int_0^\infty dt_3 \Big[S_D^{NRP}(t_1,t_2,t_3) + S_{OD}^{NRP}(t_1,t_2,t_3) \Big] \\ \times E_3(t-t_3) E_1^*(t+T-t_3-t_2) E_2(t+T-t_3-t_2-t_1) \\ + \Big[S_D^{RP}(t_1,t_2,t_3) + S_{OD}^{RP}(t_1,t_2,t_3) \Big] E_3(t-t_3) \\ \times E_2(t+T-t_3-t_2) E_1^*(t+T-t_3-t_2-t_1) \end{aligned} \tag{6.1}$$

where the S_D^{RP}, and S_D^{NRP} are expressed as

$$S_D^{NRP}(t_1,t_2,t_3) = R_1(t_1,t_2,t_3) + R_4(t_1,t_2,t_3) - R_2^*(t_1,t_2,t_3) \tag{6.2}$$

$$S_D^{RP}(t_1,t_2,t_3) = R_2(t_1,t_2,t_3) + R_3(t_1,t_2,t_3) - R_1^*(t_1,t_2,t_3) \tag{6.3}$$

Figure 6.3 presents Feynman diagrams corresponding to individual terms in the response function. The subscripts *D* and *OD* respectively denote fluctuations of the diagonal and off-diagonal elements of the Hamiltonian.[50] Diagonal fluctuations incorporate line broadening at the level of the cumulant expansion of Gaussian fluctuations, whereas off-diagonal fluctuations enable exciton transport. The incoherent signal components, S_{OD}^{RP} and S_{OD}^{NRP}, combine terms directly related to the diagrams in the third row of Figure 6.3 with functions that enforce conservation of electronic population. S_{OD}^{RP} and S_{OD}^{NRP} do not evolve as coherences during t_2 and therefore contribute little to the IECS polarization response.

The complex time-dependent part of the electric field relevant to the experimental phase-matching condition, $\mathbf{k_S} = -\mathbf{k}_1 + \mathbf{k}_2 + \mathbf{k}_3$, can be written as

$$E_j(t) = \varepsilon(t) \exp\left(-i\omega_j t\right) \tag{6.4}$$

where $\varepsilon(t)$ is the field envelope and ω_j is the carrier frequency. With Equation (6.4), we examine the sensitivity of IECS to photoexcited coherences by rewriting $P^{(3)}(t)$ as the sum of rephasing and non-rephasing components

$$P^{(3)}(t) = P^{(3)}_{NRP}(t) + P^{(3)}_{RP}(t) \tag{6.5}$$

where

$$\begin{aligned} P^{(3)}_{NRP}(t) = \exp\left[i(\omega_1 - \omega_2)T - i\omega_2 t \right] \int_0^\infty dt_1 \int_0^\infty dt_2 \int_0^\infty dt_3 \left[S_D^{NRP}(t_1,t_2,t_3) + S_{OD}^{NRP}(t_1,t_2,t_3) \right] \\ \times \varepsilon_3(t-t_3)\varepsilon_1(t+T-t_3-t_2)\varepsilon_2(t+T-t_3-t_2-t_1)\exp\left[i(\omega_2-\omega_1)t_2 - i\omega_2(t-t_3-t_1) \right] \end{aligned}$$

(6.6)

and

$$\begin{aligned} P^{(3)}_{RP}(t) = \exp\left[i(\omega_1 - \omega_2)T - i\omega_2 t \right] \int_0^\infty dt_1 \int_0^\infty dt_2 \int_0^\infty dt_3 \left[S_D^{RP}(t_1,t_2,t_3) + S_{OD}^{RP}(t_1,t_2,t_3) \right] \\ \times \varepsilon_3(t-t_3)\varepsilon_2(t+T-t_3-t_2)\varepsilon_1(t+T-t_3-t_2-t_1)\exp\left[i(\omega_2-\omega_1)t_2 + i\omega_2 t_3 - i\omega_1 t_1 \right] \end{aligned} \tag{6.7}$$

$P^{(3)}_{NRP}(t)$ and $P^{(3)}_{RP}(t)$ are obtained by setting the carrier frequencies of E_1 and E_3 equal ($\omega_1 = \omega_3$), while allowing E_2 to possess a unique carrier frequency, ω_2. Both polarization components, $P^{(3)}_{NRP}(t)$ and $P^{(3)}_{RP}(t)$, integrate over the convolution of a material response function with a complex exponential function whose argument increases linearly in t_2 at the rate $\omega_1 - \omega_2$. Therefore, the dominant terms in the material response function evolve as coherences in t_2 with frequencies near $\omega_1 - \omega_2$. Terms not evolving as coherences (i.e., populations) contribute little upon integration over t_2 because they oscillate between negative and positive values at the frequency $\omega_1 - \omega_2$.

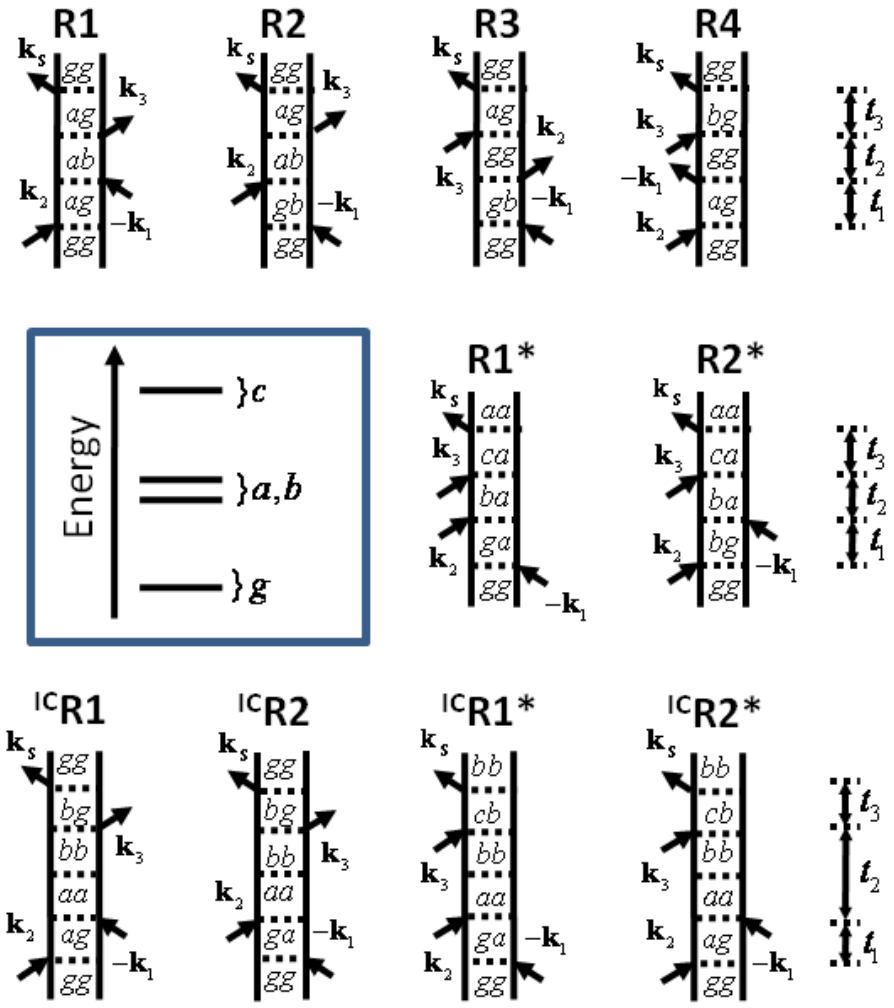

Figure 6.3. Feynman diagrams for dominant terms in transient grating and intraband electronic coherence spectroscopies. The dummy indices a and b are used for single exciton states, whereas c is reserved for the double exciton manifold. Terms in the first two rows yield the largest contributions in intraband electronic coherence spectroscopy. The superscript "IC" in the third row denotes incoherent population transfer. The excited state absorption terms, R_1^*, R_2^*, ${}^{IC}R_1^*$, and ${}^{IC}R_2^*$ do not enter the model response function for CPC.[33]

Observations of both electronic and nuclear coherences are enhanced by IECS. For example, consider the R_1 excited state emission term

$$R_1(t_1,t_2,t_3)=\sum_{ab}\left\langle \alpha_{gb}\beta_{ag}\gamma_{bg}\chi_{ga}\right\rangle Z^1_{ab}(t_1,t_2,t_3)\exp\Big(-i\omega_{ag}t_1-i\omega_{ab}t_2-i\omega_{ag}t_3 \\ -\frac{1}{2}f_1(t_1,t_1+t_2,t_1+t_2+t_3,0)\Big) \tag{6.8}$$

where

$$Z^1_{ab}(t_1,t_2,t_3)=F^{00}_a F^{00}_b+\sum_{\nu=1}^{2}F^{01}_{a\nu}F^{00}_b\exp\Big[-(i\omega_\nu+k_\nu)(t_1+t_2+t_3)\Big] \\ +F^{00}_a F^{01}_{b\nu}\exp\Big[(i\omega_\nu-k_\nu)t_2\Big] \\ +\delta_{ab}F^{01}_{a\nu}F^{00}_{b\nu}\exp\big(-i\omega_\nu t_1-k_\nu(t_1+t_2)\big)\Big[\exp(-i\omega_\nu t_3)+\big(\exp(k_\nu t_2)-1\big)\Big] \tag{6.9}$$

Equations (6.8) and (6.9) supplement the model of Reference [50] with the *ad hoc* vibronic coupling function $Z^1_{ab}(t_1,t_2,t_3)$ as explained in Reference [32]. The vibronic progressions of APC and CPC are dominated by the 0-0 transitions, so the first term in Equation (6.9), $F^{00}_a F^{00}_b$, is most significant. By setting $Z^1_{ab}(t_1,t_2,t_3)\approx F^{00}_a F^{00}_b$, we find that coherent enhancement of R_1 is achieved only when $\omega_2-\omega_1\approx\omega_{ab}$. Effective suppression of terms in which $a=b$ depends on the rate of growth of the real part of the line broadening function, f_1, with respect to t_2. To an approximation, electronic population terms, $a=b$, are well-suppressed when $\omega_1-\omega_2$ is larger than the inverse of the solvation time scale (i.e., dynamics of f_1 in t_2).

IECS also prepares nuclear coherences in the ground and excited states during t_2. For example, the R_4 ground state bleach term is given by

$$R_4(t_1,t_2,t_3)=\sum_{ab}\left\langle \alpha_{ag}\beta_{ga}\gamma_{bg}\chi_{gb}\right\rangle Z^4_{ab}(t_1,t_2,t_3)\exp\Big(-i\omega_{ag}t_1-i\omega_{bg}t_3 \\ -\frac{1}{2}f_1(t_1+t_2+t_3,t_1+t_2,t_1,0)\Big) \tag{6.10}$$

where

$$Z_{ab}^{4}\left(t_1,t_2,t_3\right)=F_a^{00}F_b^{00}+\sum_{\nu=1}^{2}F_{a\nu}^{01}F_b^{00}\exp\left[-\left(i\omega_\nu+k_\nu\right)t_1\right]+F_a^{00}F_{b\nu}^{01}\exp\left[-\left(i\omega_\nu+k_\nu\right)t_3\right] \\ +\delta_{ab}F_a^{00}F_{a\nu}^{01}\exp\left[-\left(i\omega_\nu+k_\nu\right)t_2\right] \tag{6.11}$$

The final term in $Z_{ab}^{4}\left(t_1,t_2,t_3\right)$ evolves as a vibrational coherence with frequency ω_ν. This term is enhanced when $\omega_\nu\approx\omega_1-\omega_2$, but scales as the products of Franck-Condon factors $F_a^{00}F_{a\nu}^{01}$, which for APC and CPC are approximately 10 times smaller than $F_a^{00}F_b^{00}$. Suppression of the term linear in $F_a^{00}F_b^{00}$ (i.e., ground state population response) depends on the same issues discussed above in the context of R_1. Again, we suggest a general rule that suppression is effective when the inverse of the solvation time scale is small compared to the difference frequency $\omega_1-\omega_2$.

The above analysis makes clear that electronic and nuclear coherences may be difficult to separate for some systems. In general, electric field polarizations can be utilized to distinguish these nonlinearities. Two polarization conditions are used in this chapter, *ZZZZ* and ZXZX. *ZZZZ* is a tensor element in which the polarizations of all three incident field and the signal are parallel. ZXZX assigns the Z polarization index to the two higher frequency incident fields and the X polarization index to the lower frequency incident field and signal. The ratio of these two tensor elements facilitates signal interpretation in APC because the transition dipoles connecting the ground state to the two single exciton excited states, $e+$ and $e-$, differ by approximately 52º. For example, the ratio of orientational factors, ZZZZ/ZXZX, yields 1.1 and 3.0 for R_1 pathways evolving as electronic and nuclear coherences, respectively.[65,66]

Experiments with motivation similar to IECS have been reported in recent literature.[49,67-70] For example, we used a mixed narrowband-broadband IECS pulse sequence to isolate intraband exciton coherences in a cylindrical molecular aggregate.[67] Optical properties of the aggregate, most notably the narrow line width of its lowest energy transition, made it particularly amenable to the mixed bandwidth approach. By contrast, the broad line widths of APC and CPC suggest advantages to an experiment applying all-femtosecond pulses, which is generally more powerful in that it can resolve interband coherences in t_1 and t_3. In fact, Reference [49] examines correlations in the t_1 (interband) and t_2 (intraband) coherences. Ultimately, the most appropriate IECS pulse sequence depends both on scientific questions and the system under investigation.

6.3. EXPERIMENT

APC and CPC, isolated from *Spirulina*, were purchased from Prozyme as suspensions in 60% ammonium sulfate. Solutions of APC and CPC in 50 mM and 100 mM were prepared in potassium phosphate buffer at pH 7.0. All experiments were performed within 12 hours of solution preparation. Solutions are circulated at a rate of 4 mL/s in flow system using a peristaltic pump with reservoir of 10 mL. The flow rate was set at the maximum value for which turbulence in the flow cell did not appreciably degrade the signal-to-noise ratio. In 0.5 mm path length, the absorbances of the APC and CPC solutions were 0.15 at 15300 cm^{-1} and 16200 cm^{-1}, respectively. Absorbance spectra were measured before and after experiments to confirm the absence of sample degradation.

Transient grating (TG) measurements utilize a diffractive optic-based interferometer resembling those reported in several earlier publications.[71-79] As in Reference [33], the $E_1 \& E_2$

pulse-pair (i.e., pump) and E_3 probe pulse are derived from separate home-built noncollinear optical parametric amplifiers (NOPAs).[80-82] The 16200 cm^{-1} pump pulses are nearly transform limited at 20 fs in duration, whereas the spectrum of the E_3 "probe" pulse spans the full 500-750 nm range. TG experiments are conducted with orthogonal pump ($E_1 \& E_2$) and probe ($E_3 \& E_4$) polarizations to suppress scattered pump light (i.e., ZZXX tensor element). The frequency-dependent time overlap of E_3 with the compressed $E_1 \& E_2$ pulse-pair is taken into account numerically. TG signals obtained with the transparent buffer solution are used as a reference to numerically correct the dependence of "time-zero" on the signal emission frequency. We obtain a full-width half maximum instrument response of <60 fs at signal emission frequencies in the range 14500-18500 cm^{-1} using a prism compressor configured to minimize dispersion at 16800 cm^{-1}.

Intraband electronic coherence spectroscopy (IECS) is conducted with the same interferometer used for TG experiments. The $E_1 \& E_3$ and $E_2 \& E_4$ pulse pairs are obtained as the +/-1 diffraction orders of the diffractive optic at the entrance to the interferometer. E_1 is a replica of E_3; E_4, which is a replica of E_2, is the reference field used for interferometric signal detection. Laser spectra are overlaid on the absorption spectra of APC and CPC in Figure 6.2 to clarify the configuration. The indices 1-3 account for the phase matching direction, $\mathbf{k}_S = -\mathbf{k}_1 + \mathbf{k}_2 + \mathbf{k}_3$, and the order of field-matter interactions (see Figure 6.2). E_1 and E_2 arrive simultaneously to initiate electronic and nuclear coherences in the sample (i.e., τ=0). The delay, T, is scanned with a step size of 0.75 fs and the data shown below represent an average of 15 scans.

For both TG and IECS, the combined pulse energies are 15 nJ and the FWHM spot size at the sample is 120 μm. The total laser fluence (i.e., 4.14×10^{14} photons/cm^2) is sufficient to photoexcite approximately 0.7 molecules and 3.0 molecules in APC and CPC, where an optical carrier frequency of 16200 cm^{-1} has been assumed and we take into account that CPC exists as a hexamer in solution (i.e., total of 18 phycocyanobilin pigments). Increasing the pulse energies by a factor of four has no effect on the measured dynamics. We remark that the insensitivity of the dynamics to this range of laser fluence may reflect the fact that the IECS pulse sequence is designed to suppression the initiation of electronic populations in the delay, T. Signals are detected by spectral interferometry using a back-illuminated CCD array (Princeton Instruments PIXIS 100B) mounted on a 0.3 meter spectrograph. Integration times are 100-200 ms. Signals are processed using a Fourier transform algorithm.[74,75,83-85] Total data acquisition times are less than 30 minutes.

6.4. RESULTS AND DISCUSSION

6.4.1. Transient Grating Spectroscopy with Broadband Probe

Our earlier photon echo experiments suggest that solvation is almost two times faster in CPC than in APC.[32,33] The present TG measurements view sub-100 fs dynamics from a different perspective. Both proteins are first excited with 20 fs pump pulses centered at 17000 cm^{-1} then probed with a broadband quasi-continuum laser pulse to examine the transient response in the full 500-750 nm range. In part, the motivation for the experiment is analogous to that of a "hole-burning" spectroscopy designed to detect dynamics in the position and width of a nuclear wavepacket. Similarly, fast electronic relaxation processes influence dynamics of the TG signal spectrum. The present data complement our previous measurements by viewing photoinitiated dynamics in a broader spectral window.

Experiments for APC and CPC are performed in immediate succession under identical experimental conditions to facilitate the comparison.

Figure 6.4 presents TG spectra obtained at various delay times, T. While the bulk of the spectra for both proteins red-shift with increasing delay, the magnitude of the shift is nearly two times larger in APC. Reference [32] shows that much of the red-shift of APC in the 16000-18000 cm^{-1} range is caused by interference between transient bleach and transient absorption signal components.[32] Furthermore, spectral relaxation in APC involves significant contributions from an inter-exciton internal conversion process.[33] By contrast, the present observations for CPC are attributed to solvation, which is consistent with our interpretation that the sub-100 fs dynamics do not reflect internal conversion between exciton states.[33] It should be emphasized that Figure 6.4 does not directly compare the solvation responses of APC and CPC because the spectral shift in APC is a signature of both electronic and nuclear relaxation.

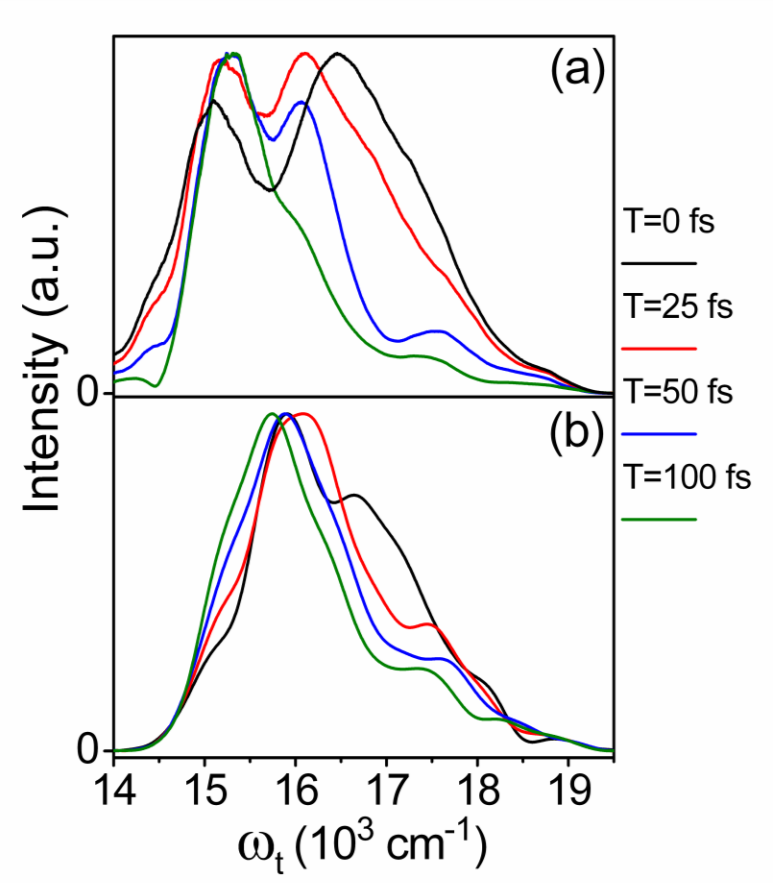

Figure 6.4. Absolute value of transient grating signal fields measured for (a) APC and (b) CPC under the ZZXX polarization condition in which the pump (E_1 & E_2) and probe (E_3 & E_4) pulses have orthogonal polarizations. Delay times, T, are given in the Figure legend. Excitation is achieved with 20 fs pump pulses centered at 17000 cm^{-1}.

Dynamics in the low energy portions of the signal spectra enable the clearest comparison of nuclear relaxation in the two systems. The low energy "wing" of the spectrum in APC actually blue-shifts as the electronic population concentrates at the electronic origin of $e+$. This blue-shift reflects the contribution of the dispersive signal component, which can be approximated as the Kramers-Kronig transform of the real part of the signal field.[86-88] That is, the dispersive tail of the signal for APC contracts as the real (absorptive) signal spectrum narrows due to internal conversion.[37] In comparison, the low energy wing of the

spectrum in CPC red-shifts by more than 400 cm^{-1} in the delay range T =0-100 fs. The dynamics in the spectrum are consistent the larger solvent reorganization energies of CPC obtained in our earlier studies; the solvent reorganization energy can be estimated using the line broadening parameter Δ (e.g., Equation (8.52c) of Reference [89]). In agreement with our interpretation of photon echo experiments, the data indicate that much of the energy dissipation involved in the Stokes shift of CPC occurs in less than 100 fs.

6.4.2. Intraband Electronic Coherence Spectroscopy

Experimental IECS signals obtained for APC and CPC are shown in Figure 6.5. Contour plots display the absolute value of the signal spectrum in ω_t as a function of the delay, T, following initiation of electronic and nuclear coherences with the $E_1 \& E_2$ pulse pair (see Figure 6.2). The signals consist of two distinct features: a sub-25 fs decay of signal amplitude followed by recurrence in the signal strength near T =45 fs. Both APC and CPC possess an 800 cm^{-1} vibrational mode with a large Franck-Condon factor whose 42 fs period partly explains the time scale of the recurrence.[32,33] The fact that the signal recurs only once suggests that a broad distribution of vibrational frequencies is initiated at T =0 due to the use of short laser pulses. The resulting superposition of incommensurate frequencies in the polarization is manifest as fast damping of the signal in T. Because of fast dephasing, Fourier transformation of the complex signal field with respect to T yields features too broad for interpretation of vibrational mode-specific contributions. Therefore, the present time domain representation is most appropriate for these data.

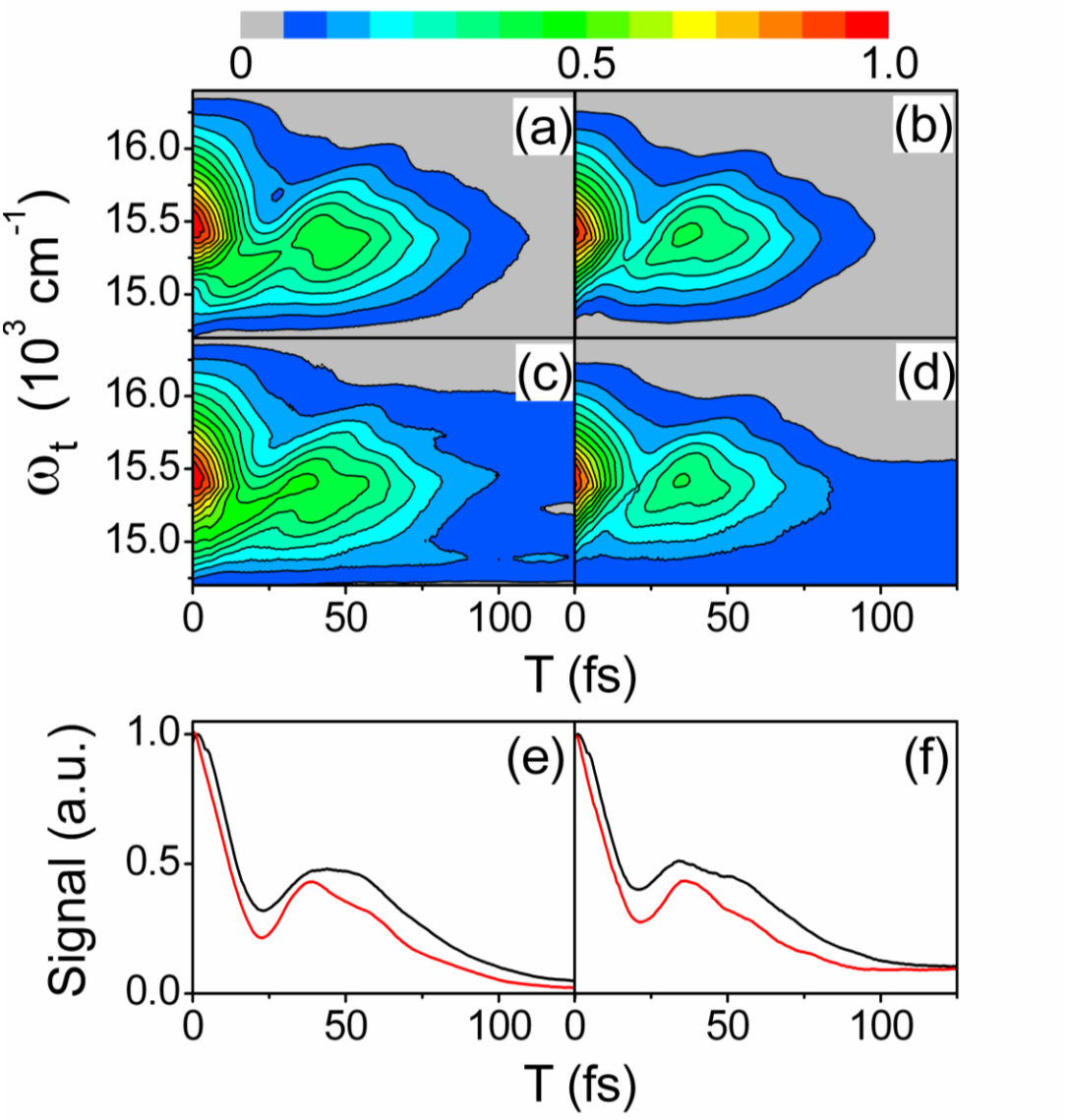

Figure 6.5. Absolute value IECS signals measured for (a), (c) APC; (b), (d) CPC. Panels (a) and (b) use the ZZZZ polarization condition, whereas (c) and (d) are ZXZX (see Section 6.2). Signals in all panels are normalized to 1.0. Absolute value of IECS signals at ω_t =15400 cm^{-1} for (black) APC and (red) CPC. Panels (e) and (f) respectively represent the ZZZZ and ZXZX tensor elements. Contour lines in panels (a)-(d) are linearly spaced.

One-dimensional slices of the signals obtained for APC and CPC at ω_t = 15400 cm^{-1} are overlaid in Figures 6.5e and 6.5f to examine signatures of electronic coherence between the $e+$ and $e-$ states of APC. The signals for APC decay more slowly at T <25 fs and recur with greater amplitude near T =45 fs. We suggest that these differences partly represent

contributions of electronic coherence in APC. First, the vibronic responses of APC and CPC observed by IECS should be quite similar because both proteins have only phycocyanobilin pigments. Second, electronic coherences between excited states are not initiated in CPC, where Reference [33] explains that nonlinearities involving coherent sequences of interactions on the donor and acceptor pigments do not contribute to the optical response in the weak-coupling limit. Another source of contrast in IECS signals for APC and CPC may be the difference in the line widths, which are slightly broader in CPC.[32,33]

Signals calculated with our Hamiltonians for APC and CPC are presented in Figure 6.6.[32,33] Here we have modified only the vibrational cooling parameters by setting them all equal to 35 fs to ensure that the calculated response is dominated by only a single amplitude recurrence. Agreement between the experiments and calculations is generally very good. The calculated signals exhibit a sub-25 fs decay in amplitude followed by a recurrence near T =45 fs. It is likely that deviations between experiment and theory originate in the *ad hoc* treatment of vibronic structure. The model effectively concentrates all intramolecular reorganization energy onto two coordinates at 800 cm^{-1} and 1500 cm^{-1}, whereas resonance Raman spectra of phycocyanobilins detect several Franck-Condon active vibrations.[90-92] Because the Hamiltonians were parameterized to fit a different set of experiments, it is quite remarkable that the calculated IECS signals capture the slightly slower decay of signal amplitude of APC at T <25 fs in addition to the larger amplitude of the recurrence. We emphasize that these calculations fully take into account the overlap between spectral line shapes and the laser spectra by integrating the nonlinear polarization numerically (Equation (6.5)). Indeed, without the numerical model, APC and CPC could not be compared objectively.

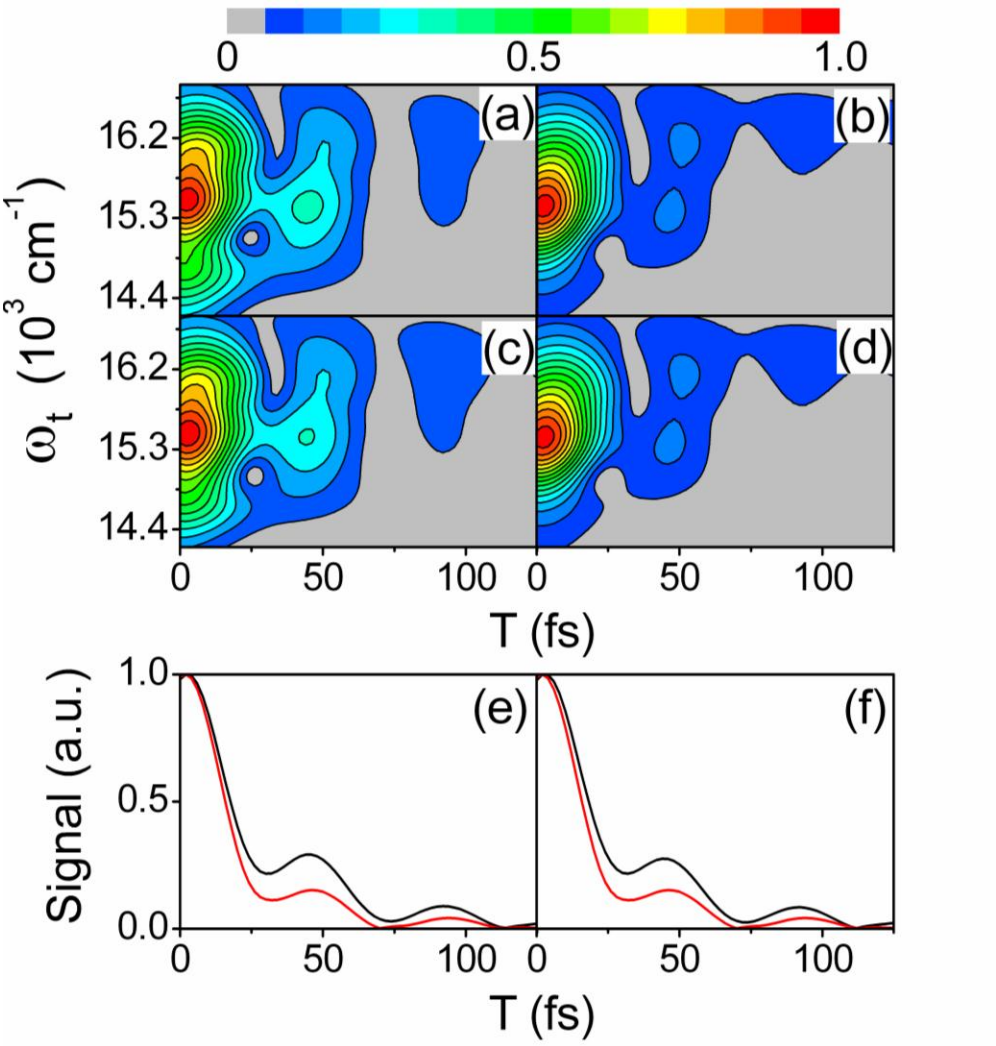

Figure 6.6. Absolute value IECS signals calculated for (a), (c) APC; (b), (d) CPC using Equation (6.1). Panels (a) and (b) use the ZZZZ polarization condition, whereas (c) and (d) are ZXZX. Signals in all panels are normalized to 1.0. Absolute value of IECS signals at ω_t =15400 cm^{-1} for (black) APC and (red) CPC. Panels (e) and (f) respectively represent the ZZZZ and ZXZX tensor elements. Contour lines in panels (a)-(d) are linearly spaced.

Figure 6.7 evaluates the utility of electric field polarizations for sensing contributions of coherent cross terms indicative of exciton electronic structure. The calculated signals show that the ratio ZZZZ/ZXZX= 3.0 is expected for all T using the Hamiltonian for CPC, whereas the ratio varies with T for APC. For CPC at T <40 fs, deviation between the experimental and theoretical ratio can be attributed to experimental error, which we estimate

at +/- 0.2. The model is less successful in capturing the polarization dependence of APC. For example, a minimum in the ratio, ZZZZ/ZXZX, is measured at T =30 fs but calculated at T =23 fs. Moreover, the discrepancy between the experiment and model is greater than experimental error at T <20 fs. Still, the model calculations capture the fact that the measured ratios for APC are less than CPC. Improperly ordered field matter interactions in the region of pulse overlap and/or the *ad hoc* treatment of vibronic structure may limit the calculation of accurate ZZZZ/ZXZX ratios. However, taken together, we believe that Figures 6.5-6.7 give strong support to our earlier conclusion of weakly correlated α84 and ß84 pigment fluctuations in APC (i.e., η <0.5).[32] Most importantly, the measurements show no sign of long-lived electronic coherence expected with correlated line broadening dynamics.[93] For illustration, Figure 6.7 presents the IECS signals radiated by the subset of terms evolving as electronic coherences in t_2 (i.e., R_1 and R_2 with $a \neq b$).

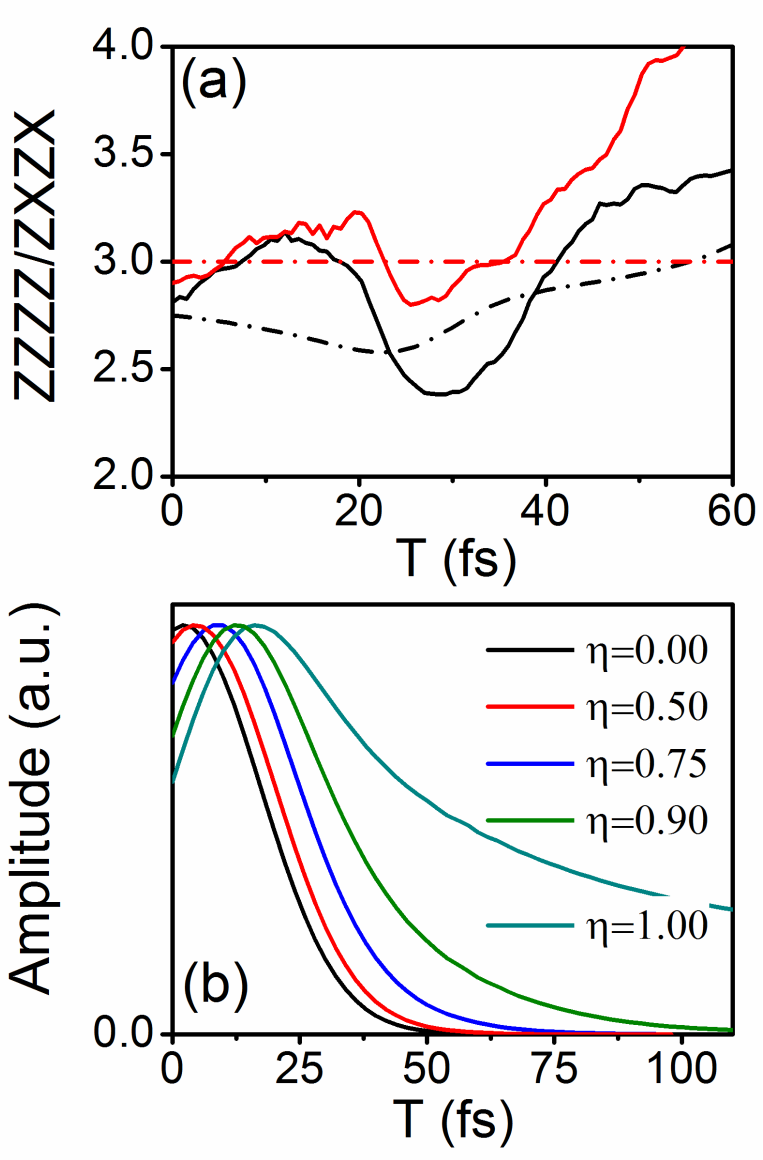

Figure 6.7. (a) Experimental (solid) and calculated (dash-dot) ZZZZ/ZXZX ratios of absolute value IECS signals emitted at ω_t =15400 cm^{-1}. Black and red lines respectively correspond to APC and CPC. (b) Calculated absolute value IECS signals for APC radiated at ω_t =15400 cm^{-1}. The parameter, η, tunes the amount of correlation characteristic of fluctuations at the α84 and ß84 pigment sites; uncorrelated and fully correlated fluctuations are found at η =0.0 and η =1.0, respectively. These calculations remove all nuclear coherences in t_2 from the response function to isolate effects of intraband exciton dephasing between $e+$ and $e-$.

6.5. CONCLUSIONS

The experiments presented in this chapter improve insight into the electronic structures of APC and CPC. TG experiments observe a sub-100 fs red-shift in the signal spectrum for APC, which is almost twice that of CPC. This observation is consistent with our view that the fastest dynamics in APC and CPC are respectively dominated by electronic and nuclear relaxation. IECS experiments find that dephasing of the intraband electronic coherence between $e+$ and $e-$ in APC occurs in less than 25 fs, which suggests weakly correlated (or fully uncorrelated) α84 and ß84 pigment fluctuations. Thus, IECS argues against correlated pigment fluctuations as the mechanism enabling exciton formation in APC. Still, we suggest that APC must be specially "tuned" in some way for wavefunction delocalization to occur. Otherwise, clear signatures of exciton electronic structure should also be present in CPC where the energy gap between α84 and ß84 pigment excitation energies is less than half of that found in APC.[33] Indeed, by the usual rule that wavefunctions more readily delocalize as a basis approaches degeneracy, exciton electronic structure is more likely in CPC. This is particularly true given the nearly identical structure of the dimers in both systems. Both the intermolecular distances and relative orientations of the α84 and ß84 pigments are quite similar and it is not clear by simple inspection of the X-ray structure why purely electronic (i.e., not vibronic) exciton formation is more readily achieved in APC. We are now using electronic structure calculations to examine subtler differences between the two systems.[4,8]

We suggest an alternative mechanism of exciton formation in APC that originates in its strong vibronic couplings. We previously parameterized off-diagonal elements of the Hamiltonian with couplings between purely electronic transition dipoles localized at the α84 and ß84 sites. In fact, these are the same transition dipoles defining the optical oscillator

strength, which generally decomposes as a vibronic progression. Thus, the wavefunction delocalization in the vibronic basis of the α84 and ß84 pigments is realized when the transition moment is similarly partitioned into specific vibronic channels. For example, two vibronic states likely to mix in APC are the electronic origin of α84 and the vibronic state of ß84 possessing 1 quantum of energy in its 800 cm^{-1} mode. According to our model, these two levels are separated by an energy gap of only 40 cm^{-1}. Using a conservative estimate for the dimensionless displacement in the 800 cm^{-1} mode at each site (Δ=0.5), we compute the magnitude of the coupling using

$$V = J_{12}\langle 0|0\rangle_{\alpha}\langle 0|1\rangle_{\beta} = \frac{J_{12}\Delta}{\sqrt{2}}\exp\left(-\frac{\Delta^2}{2}\right) = -51\mathrm{cm}^{-1} \tag{6.12}$$

where $\langle 0|n\rangle_j$ is the overlap in nuclear wavefunctions for the 0 to n vibronic transition on site j. The fact that the coupling is larger than the energy gap between states suggests that wavefunction delocalization is a feasible prospect. This viewpoint is consistent with the weak-coupling limit of energy transfer in CPC where the 350 cm^{-1} energy gap between α84 and ß84 pigments is not well-compensated for by Franck-Condon active modes. For example, Figure 6.7 in Reference [33] shows that the mode with the closest frequency at 270 cm^{-1} still leaves an 80 cm^{-1} gap, which is larger than the coupling between vibronic states. Ultimately, a rigorous analysis utilizing mode-specific Huang-Rhys factors obtained with resonance Raman spectroscopy will be needed to establish a robust explanation for the electronic structures of APC and CPC. The present analysis confirms that a model treating exciton formation in the vibronic basis is plausible and consistent with experimental data.

REFERENCES

(1) MacColl, R.; Guard-Friar, D. *Phycobiliproteins*; CRC Press: Boca Raton, 1987.

(2) MacColl, R. *J. Struct. Biol.* 1998, *124*, 311.

(3) Blankenship, R. E. *Molecular Mechanisms of Photosynthesis*; Blackwell Science Ltd.: Oxford, 2002.

(4) Brejc, K.; Ficner, R.; Huber, R.; Steinbacher, S. *J. Mol. Biol.* 1995, *249*, 424.

(5) Schirmer, T.; Bode, W.; Huber, R.; Sidler, W.; Zuber, H. *J. Mol. Biol.* 1985, *184*, 257.

(6) Schirmer, T.; Huber, R.; Schneider, M.; Bode, W.; Miller, M.; Hackert, M. L. *J. Mol. Biol.* 1986, *188*, 651.

(7) Schirmer, T.; Bode, W.; Huber, R. *J. Mol. Biol.* 1987, *196*, 677.

(8) Wang, X. Q.; Li, L. N.; Chang, W. R.; Zhang, J. P.; Gui, L. L.; Guo, B. J.; Liang, D. C. *Acta Crystallogr. D* 2001, *57*, 784.

(9) Debreczeny, M. P.; Sauer, K.; Zhou, J.; Bryant, D. A. *J. Phys. Chem.* 1995, *99*, 8412.

(10) Debreczeny, M. P.; Sauer, K.; Zhou, J.; Bryant, D. A. *J. Phys. Chem.* 1995, *99*, 8420.

(11) Riter, R. E.; Edington, M. D.; Beck, W. F. *J. Phys. Chem. B*` 1997, *101*, 2366.

(12) Edington, M. D.; Riter, R. E.; Beck, W. F. *J. Phys. Chem.* 1995, *99*, 15699.

(13) Edington, M. D.; Riter, R. E.; Beck, W. F. *J. Phys. Chem B* 1996, *100*, 14206.

(14) Gillbro, T.; Sharkov, A. V.; Kryukov, I. V.; Khoroshilov, E. V.; Kryukov, P. G.; Fischer, R.; Scheer, H. *Biochimica et Biophysica Acta* 1993, *1140*, 321.

(15) Zhang, J. M.; Zhao, F. L.; Zheng, X. G.; Wang, H. Z.; Yang, T.-S.; Hayashi, M.; Lin, S. H. *J. Photochem. Photobiol. B: Biol.* 1999, *53*, 128.

(16) Homoelle, B. J.; Edington, M. D.; Diffey, W. M.; Beck, W. F. *102* 1998, 3044.

(17) *Resonance Energy Transfer*; Andrews, D. L.; Demidov, A. A., Eds.; Wiley: Chichester, 1999.

(18) Andrews, D. L. *Chem. Phys.* 1989, *135*, 195.

(19) van Amerongen, H.; Valkunas, L.; van Grondelle, R. *Photosynthetic Excitons*; World Scientific: Singapore, 2000.

(20) Scholes, G. D. *Annu. Rev. Phys. Chem.* 2003, *54*, 57.

(21) Beljonne, D.; Curutchet, C.; Scholes, G. D.; Silbey, R. J. *J. Phys. Chem. B* 2009, *113*, 6583.

(22) Sumi, H. *J. Phys. Chem. B* 1999, *103*, 252.

(23) Jang, S.; Newton, M. D.; Silbey, R. J. *Phys. Rev. Lett.* 2004, *92*, 218301:1.

(24) Scholes, G. D.; Jordanides, X. J.; Fleming, G. R. *J. Phys. Chem. B* 2001, *105*, 1640.

(25) Davydov, A. *Theory of Molecular Excitons*; Plenum: New York, 1971.

(26) Capek, V.; Silinish, E. *Organic Molecular Crystals: Interaction, Localization, and Transport Phenomena*; AIP: New York, 1994.

(27) Abramavicius, D.; Palmieri, B.; Voronine, D. V.; Sanda, F.; Mukamel, S. *Chem. Rev.* 2009, *109*, 2350.

(28) Mukamel, S.; Abramavicius, D.; Yang, L.; Zhuang, W.; Schweigert, I. V.; Voronine, D. V. *Acc. Chem. Res.* 2009, *42*, 553.

(29) Zhuang, W.; Hayashi, T.; Mukamel, S. *Angew. Chemie.* 2009, *48*, 3750.

(30) Fleming, G. R.; Scholes, G. D. *Nature* 2004, *431*, 256.

(31) Cho, M. *Chem. Rev.* 2008, *108*, 1331.

(32) Womick, J. M.; Moran, A. M. *J. Phys. Chem. B* 2009, *113*, 15747.

(33) Womick, J. M.; Moran, A. M. *J. Phys. Chem. B* 2009, *113*, 15771.

(34) Lin, S. W.; Groesbeek, M.; van der Hoef, I.; Verdegem, P.; Lugtenburg, J.; Mathies, R. A. *Biochemistry* 1998, *28*, 1498.

(35) Andel III, F.; Murphy, J. T.; Haas, J. A.; McDowell, M. T.; van der Hoef, I.; Lugtenburg, J.; Lagarias, J. C.; Mathies, R. A. *Biochemistry* 2000, *39*, 2667.

(36) Fodor, S. P.; Lagarias, J. C.; Mathies, R. A. *Biochemistry* 1990, *29*, 11141.

(37) Edington, M. D.; Riter, R. E.; Beck, W. F. *J. Phys. Chem. B* 1997, *101*, 4473.

(38) Sharkov, A. V.; Kryukov, I. V.; Khoroshilov, E. V.; Kryukov, P. G.; Fischer, R.; Scheer, H.; Gillbro, T. *Chem. Phys. Lett.* 1992, *191*, 633.

(39) Jang, S. *J. Chem. Phys.* 2009, *131*, 164101.

(40) Jang, S.; Cheng, Y. C.; Reichman, D. R.; Eaves, J. *J. Chem. Phys.* 2008, *129*, 101104.

(41) Nazir, A. *Phys. Rev. Lett.* 2009, *103*, 146404:1.

(42) Rebentrost, P.; Mohseni, M.; Aspuru-Guzik, A. *J. Phys. Chem B* 2009, *113*, 9942.

(43) Chen, X.; Silbey, R. J. *J. Chem. Phys.* 2010, *132*, 204503.

(44) Olaya-Castro, A.; Lee, C. F.; Olsen, F. F.; Johnson, N. F. *Phys. Rev. B* 2008, *78*, 085115:1.

(45) Calhoun, T. R.; Ginsberg, N. S.; Schlau-Cohen, G. S.; Cheng, Y.-C.; Ballottari, M.; Bassi, R.; Fleming, G. R. *J. Phys. Chem. B* 2009, *xx*, dd.

(46) Womick, J. M.; Miller, S. A.; Moran, A. M. *J. Phys. Chem. B* 2009, *113*, 6630.

(47) Collini, E.; Scholes, G. D. *Science* 2009, *323*, 369.

(48) Collini, E.; Wong, C. Y.; Wilk, K. E.; Curmi, P. M.; Brumer, P.; Scholes, G. D. *Nature* 2010, *463*, 644.

(49) Lee, H.; Cheng, Y.-C.; Fleming, G. R. *Science* 2007, *316*, 1462.

(50) Abramavicius, D.; Mukamel, S. *Chem. Rev.* 2004, *104*, 2073.

(51) Cherepy, N. J.; Du, M.; Holzwarth, A. R.; Mathies, R. A. *J. Phys. Chem.* 1996, *100*, 4662.

(52) Sundström, V.; Pullerits, T.; van Grondelle, R. *J. Phys. Chem. B* 1999, *103*, 2327.

(53) Sanematu, T.; Mizuno, Y. *J. Phys. Soc. Jpn.* 1976, *40*, 1733.

(54) Sanematu, T. *J. Phys. Soc. Jpn.* 1976, *43*, 600.

(55) Linnanto, J. M.; Korppi-Tommola, J. E. I. *Chem. Phys.* 2009, *357*, 171.

(56) Spano, F. C.; Silvestri, L.; Spearman, P.; Raimondo, L.; Tavazzi, S. *J. Chem. Phys.* 2007, *127*, 184703:1.

(57) Spano, F. C.; Meskers, S. C. J.; Hennebicq, E.; Beljonne, D. *J. Am. Chem. Soc.* 2007, *129*, 7044.

(58) Franck, J.; Teller, E. *J. Chem. Phys.* 1938, *6*, 861.

(59) Philpott, M. R. *J. Chem. Phys.* 1967, *47*, 4437.

(60) McRae, E. G.; Siebrand, W. *J. Chem. Phys.* 1964, *41*, 905.

(61) Simpson, W. T.; Peterson, D. L. *J. Chem. Phys.* 1957, *26*, 588.

(62) West, B. A.; Womick, J. M.; Moran, A. M. *J. Phys. Chem. C* 2010, DOI: 10.1021/jp101621v.

(63) Spano, F. C. *Acc. Chem. Res.* 2010, *43*, 429.

(64) Fleming, G. R. *Chemical Applications of Ultrafast Spectroscopy*; University Press: New York, 1986.

(65) Hochstrasser, R. M. *Chem. Phys.* 2001, *266*, 273.

(66) Dreyer, J.; Moran, A. M.; Mukamel, S. *Bull. Korean Chem. Soc.* 2003, *24*, 1091.

(67) Womick, J. M.; Miller, S. A.; Moran, A. M. *J. Phys. Chem. A* 2009, *113*, 6587.

(68) Pakoulev, A. V.; Rickard, M. A.; Meyer, K. A.; Kornau, K. M.; Mathew, N. A.; Thompson, D. E.; Wright, J. C. *J. Phys. Chem. A* 2006, *110*, 3352.

(69) Pakoulev, A. V.; Rickard, M. A.; Mathew, N. A.; Kornau, K. M.; Wright, J. C. *J. Phys. Chem A* 2007, *111*, 6999.

(70) Mathew, N. A.; Yurs, L. A.; Block, S. B.; Pakoulev, A. V.; Kornau, K. M.; Wright, J. C. *J. Phys. Chem. A* 2009, *113*, 9261.

(71) Cowan, M. L.; Ogilvie, J. P.; Miller, R. J. D. *Chem. Phys. Lett.* 2004, *386*, 184.

(72) Goodno, G. D.; Dadusc, G.; Miller, R. J. D. *J. Opt. Soc. Am. B* 1998, *15*, 1791.

(73) Maznev, A. A.; Nelson, K. A.; Rogers, J. A. *Opt. Lett.* 1998, *23*, 1319.

(74) Moran, A. M.; Maddox, J. B.; Hong, J. W.; Kim, J.; Nome, R. A.; Bazan, G. C.; Scherer, N. F. *J. Chem. Phys.* 2006, *124*, 194904:1.

(75) Brixner, T.; Mancal, T.; Stiopkin, I. V.; Fleming, G. R. *J. Chem. Phys.* 2004, *121*, 4221.

(76) Khurmi, C.; Berg, M. A. *J. Phys. Chem. A* 2008, *112*, 3364.

(77) Underwood, D. F.; Blank, D. A. *J. Phys. Chem. A* 2003, *107*, 956.

(78) Gundogdu, K.; Stone, K. W.; Turner, D. B.; Nelson, K. A. *Chem. Phys.* 2007, *341*, 89.

(79) Kim, J.; Wong, C. Y.; Nair, P. S.; Fritz, K. P.; Kumar, S.; Scholes, G. D. *J. Phys. Chem. B* 2006, *110*, 25371.

(80) Kobayashi, T.; Baltuska, A. *Meas. Sci. Technol.* 2002, *13*, 1671.

(81) Cerullo, G.; Nisoli, M.; De Silvestri, S. *Appl. Phys. Lett.* 1997, *71*, 3616.

(82) Riedle, E.; Beutter, M.; Lochbrunner, S.; Piel, J.; Schenkl, S.; Spörlein, S.; Zinth, W. *Appl. Phys. B* 2000, *71*, 457.

(83) Lepetit, L.; Chériaux, G.; Joffre, M. *J. Opt. Soc. Am. B* 1995, *12*, 2467.

(84) Gallagher, S. M.; Albrecht, A. W.; Hybl, J. D.; Landin, B. L.; Rajaram, B.; Jonas, D. M. *J. Opt. Soc. Am. B* 1998, *15*, 2338.

(85) Hybl, J. D.; Albrecht Ferro, A.; Jonas, D. M. *J. Chem. Phys.* 2001, *115*, 6606.

(86) Nelson, K. A.; Casalegno, R.; Miller, R. J. D.; Fayer, M. D. *J. Chem. Phys.* 1982, *77*, 1144.

(87) Hybl, J. D.; Yu, A.; Farrow, D. A.; Jonas, D. M. *J. Phys. Chem A* 2002, *106*, 7651.

(88) Moran, A. M.; Park, S.; Scherer, N. F. *J. Phys. Chem. B* 2006, *110*, 19771.

(89) Mukamel, S. *Principles of Nonlinear Optical Spectroscopy*; Oxford University Press: New York, 1995.

(90) Zhang, J. M.; Shiu, Y. J.; Hayashi, M.; Liang, K. K.; Chang, C. H.; Gulbinas, V.; Yang, C. M.; Yang, T.-S.; Wang, H. Z.; Chen, Y.-T.; Lin, S. H. *J. Phys. Chem. A* 2001, *105*, 8878.

(91) Szalontai, B.; Gombos, Z.; Csizmadia, V.; Csatorday, K.; Lutz, M. *Biochemistry* 1989, *28*, 6467.

(92) Szalontai, B.; Gombos, Z.; Csizmadia, V.; Bagyinka, C.; Lutz, M. *Biochemistry* 1994, *33*, 11823.

(93) Venkatramani, R.; Mukamel, S. *J. Chem. Phys.* 2002, *117*, 11089.

CHAPTER 7. VIBRONIC ENHANCEMENT OF EXCITON SIZES AND ENERGY TRANSPORT IN PHOTOSYNTHETIC COMPLEXES

7.1. INTRODUCTION

Spectroscopy and dynamics in molecular aggregates and light harvesting proteins are intimately connected to interactions between electronic and nuclear coordinates.[1-15] In these systems, low-frequency thermally driven nuclear motion generally constitutes a source of noise responsible for decoherence between molecular sites. Vibronic couplings in high-frequency quantized modes, while not thermally populated, also influence exciton localization by reducing the magnitudes of molecular transition dipoles at their electronic origins, which in turn suppresses interactions between sites. The treatment of high-frequency modes with large displacements (i.e., with large reorganization energies) generally differs in investigations of molecular aggregates and semiconductor organic crystals. Vibronic exciton models, for example, define electronic structure in a basis of vibronic levels in systems whose optical spectra exhibit extended Franck-Condon progressions (e.g., acene crystals).[16-20] Vibronic excitations are allowed to delocalize between sites and the relationship between intramolecular reorganization energy and intermolecular coupling is naturally accounted for. Alternative approaches use the spectral density of the system's phonon environment to handle quantized modes with moderate Huang-Rhys factors. Low-frequency motions are then seen to promote transitions between electronic states whose energy differences are small compared to $k_B T$, whereas the quantized modes enable energy conservation in fast

Adapted with permission from Womick, J.M.; Moran, A.M. *J. Phys. Chem. B* 2011, *115*, 1347-1356.

transitions between electronic states with large energy gaps. Examples of transitions assisted by quantized modes (i.e., promoting modes) are found in photosynthetic reaction centers.[21-23]

The present chapter is motivated by our ongoing efforts to understand the origin of the difference in electronic relaxation rates observed in the pigment dimers of Allophycocyanin (APC) and C-Phycocyanin (CPC).[24-26] Figure 7.1 shows the structures of the dimers in APC and CPC isolated from *Spirulina platensis*.[27,28] The intermolecular distances (2.05 nm) and relative molecular orientations are quite similar in the two systems; the angles between transition dipoles are approximately 55 degrees.[24,25,29,30] The geometries of the ß84 pigments are nearly indistinguishable, whereas slight differences are found at the α84 sites. As shown in Figure 7.1, the BD and CD inter-ring torsion angles are >25° larger in CPC, which may influence electronic structure by interrupting double bond conjugation. Despite these structural similarities, our transient absorption anisotropy experiments yield electronic population transfer time constants of 220 fs and 970 fs in APC and CPC, respectively. In addition, two-dimensional photon echo experiments provide clear evidence of sub-20 fs population transfer in APC; this non-radiative transition also imposes significant lifetime broadening in the linear absorption spectrum of APC.[24] The faster relaxation process in APC is surprising given that the difference in α84 and ß84 site energies (760 cm^{-1}) is over twice that found in CPC (350 cm^{-1}). We remark that our conclusions are, more or less, consistent with earlier experimental studies of these two proteins isolated from different organisms, which have proven essential to the interpretation of our experiments.[29-38]

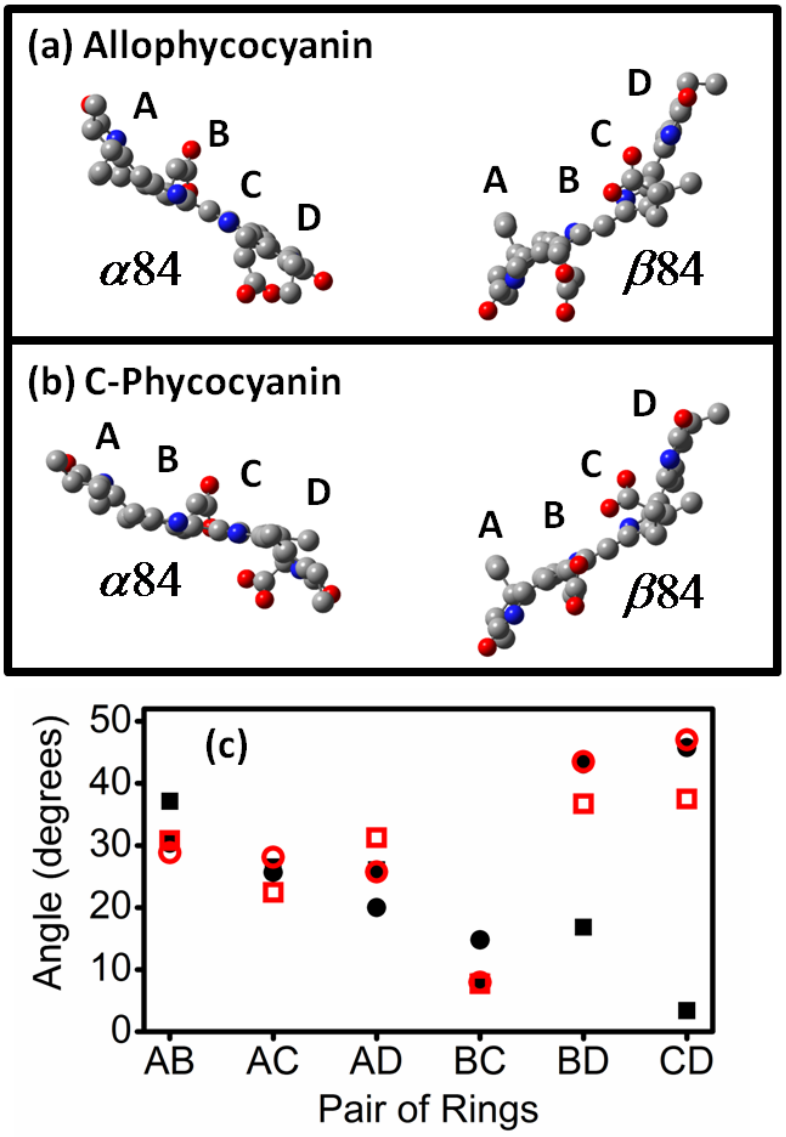

Figure 7.1. (a) Structure of APC dimer generated using PDB files 1ALL.[27] (b) Structure of CPC dimer generated using PDB files 1GH0.[28] X-ray data for both systems are obtained using proteins isolated from *Spirulina platensis*. The intermolecular distances are 2.06 and 2.01 nm for APC and CPC, respectively. (c) Inter-ring torsion angles for α84 in APC (filled black squares); ß84 in APC (filled black circles); α84 in CPC (open red squares); ß84 in CPC (open red circles). In this convention, ring A is covalently bonded to a cysteine residue.

In this contribution, we investigate electronic relaxation mechanisms in APC and CPC using modified Redfield theory with the goal of understanding the dynamics in both systems on a common footing.[39,40] Modified Redfield theory is appropriate for this task

because of its ability to interpolate between the limits of weak electron-phonon coupling (i.e., Redfield limit)[41] and weak donor-acceptor interactions (i.e., Förster limit).[42] Our fitting of spectroscopic line widths in APC and CPC yields site reorganization energies ranging from 235-417 cm^{-1}, whereas the intermolecular couplings in both systems are approximately -150 cm^{-1}. The comparable magnitudes of these two quantities make clear the need for a model capable of handling the intermediate coupling regime. The main focus of this work is the exploration of kinetic effects associated with a strongly coupled hydrogen out-of-plane (HOOP) wagging vibration, which gives rise to pronounced recurrences in the transient absorption anisotropies of both systems.[24,25] The HOOP mode is of particular interest because its 800 cm^{-1} frequency closely matches the energy gap between electronic states in APC but not in CPC. We suggested that the HOOP vibration functions in APC as the promoting mode responsible for extremely rapid relaxation between exciton states.[24] By contrast, the relaxation rate of CPC agrees well with the predictions of Förster theory.[30] In addition, the localized basis is adequate for the interpretation of spectroscopic signals in CPC.[25,26] Below it is shown that the behavior of both systems can be understood in a consistent manner by explicitly treating vibronic excitations of the HOOP mode as part of the system rather than the bath.

7.2. MODEL HAMILTONIANS USED IN RATE CALCULATIONS

This Section presents the two classes of Frenkel exciton models employed in this work. Background on these models and the latest developments can be found in recent literature.[5,18,40,43-45] In the first model, population transfer dynamics are computed in a basis of purely electronic two-level systems whose spectral densities possess all information on vibronic couplings. The second model incorporates vibronic levels in the system

Hamiltonian instead of the bath. Vibronic exciton models are often used to describe electronic structure in molecular crystals such as tetracene, where the individual sites exhibit well-resolved Franck-Condon progressions.[46,47] Applications have also been made to polypeptides,[48,49] the antenna of purple bacteria,[50] and molecular aggregates.[51,52]

In both models considered here, the Hamiltonian of the pigment complex is partitioned into three components as

$$H = H_{Sys} + H_{Bath} + H_{Sys-Bath} \tag{7.1}$$

Sections 7.2.1 and 7.2.2 present two different partitioning schemes, which differ in whether the intramolecular HOOP mode is treated as part of the system or bath. The bath is described within the well-known Brownian oscillator (BO) framework for which the key equations are summarized in Appendix G.[43,53] The BO model views both intramolecular and intermolecular modes as displaced harmonic oscillators. The two types of coordinates are distinguished only in the rates at which they dissipate energy following electronic excitation of the system. It is shown below that the partitioning scheme has non-trivial consequences on both transport kinetics and the predicted exciton sizes.

7.2.1. Purely Electronic Exciton Model

The model presented in this Section (and in Section 7.2.2.) is specific to the pigment dimers found in APC and CPC. However, the formulas are written using restricted summations to allow straightforward generalization to systems possessing additional pigments and/or larger Huang-Rhys factors. With all nuclear modes kept as part of the bath, the system Hamiltonian is given by[5,43]

$$H_{Sys}^{el} = \sum_{m=1}^{2} E_m B_m^{\dagger} B_m + \sum_{m=1}^{2} \sum_{n \neq m}^{2} J_{mn} B_m^{\dagger} B_n \tag{7.2}$$

where the basis is composed of purely electronic two-level systems. Here E_m is the thermally averaged energy gap of pigment m at the ground state equilibrium geometry (i.e., Franck-Condon geometry) and J_{mn} is the electrostatic coupling between molecules m and n. The Heitler-London approximation has been made in writing H_{Sys}^{El}, which contains only interactions between states with the same number of excitations. Quartic resonant interactions between chromophores are neglected because they are generally small compared to the quadratic coupling, J_{mn}. Moreover, the off-resonant terms found in the generalized Frenkel exciton Hamiltonian are neglected in H_{Sys}^{El} because $J_{mn} << E_m$ in both APC and CPC.[43]

The bath possesses two primary BO coordinates in the present purely electronic exciton model. First, interactions with low-frequency motions of the environment at site m are accounted for with an overdamped BO coordinate for which the odd component of the spectral density is written as[53]

$$C_m^{OD}(\omega) = 2\lambda_m \frac{\omega\Lambda_m}{\omega^2 + \Lambda_m^2} \tag{7.3}$$

For APC and CPC, $C_m^{OD}(\omega)$ peaks at frequencies smaller than $k_B T$ because the site reorganization energy, λ_m, is large compared to the relaxation rate, Λ_m. In this slow modulation regime, the standard deviation of fluctuations in E_m is (approximately) given by $\sqrt{2\lambda_m k_B T}$.[53] The second primary oscillator represents the underdamped intramolecular HOOP mode using the spectral density[53]

$$C_m^{UD}(\omega) = S_m \Omega_m^2 \left[\delta(\omega - \Omega_m) - \delta(\omega + \Omega_m) \right] \tag{7.4}$$

where S_m and $S_m\Omega_m$ are respectively the Huang-Rhys factor and reorganization energy at site m. It is adequate to write $C_m^{UD}(\omega)$ using delta functions instead of functions with finite widths because the solvent reorganization energy is large compared to the line widths of intramolecular modes. In all simulations conducted below, the mode frequency and displacement is taken to be equivalent on both pigment sites in the dimer. The total odd component of the spectral density at site m is given by the sum of these two contributions

$$C_m(\omega) = C_m^{OD}(\omega) + C_m^{UD}(\omega) \tag{7.5}$$

The line broadening function at site m is then computed using[53]

$$g_m(t) = \frac{1}{2\pi}\int_{-\infty}^{\infty} d\omega \frac{1-\cos(\omega t)}{\omega^2}\coth(\beta\hbar\omega/2)C_m(\omega) + \frac{i}{2\pi}\int_{-\infty}^{\infty} d\omega \frac{\sin(\omega t)-\omega t}{\omega^2}C_m(\omega) \tag{7.6}$$

Because of the $\coth(\beta\hbar\omega/2)$ function in Equation (7.6), the low-frequency portion of $C_m^{OD}(\omega)$ dominates the real part of $g_m(t)$ and is therefore primarily responsible for spectroscopic line broadening. By contrast, $C_m^{UD}(\omega)$ contributes mainly to the imaginary part of $g_m(t)$ because the frequency of the HOOP is over three times larger than k_BT. Overall, optical spectra computed with $g_m(t)$ appear as vibronic progressions in which the individual transitions exhibit identical line widths determined by $C_m^{OD}(\omega)$. Assuming that each site possesses an uncorrelated bath, the transformation of the local line broadening functions into the single exciton basis is given by

$$g_{abcd}(t) = \sum_{n=1}^{2} \phi_{am}\phi_{bm}\phi_{cm}\phi_{dm} g_m(t) \tag{7.7}$$

where the eigenvector of exciton state a is written as

$$|a\rangle = \sum_{m=1}^{2} \phi_{am} |m\rangle \tag{7.8}$$

7.2.2. Vibronic Exciton Model

As an alternative to the above approach, vibronic interactions may be incorporated explicitly using the Holstein-like Hamiltonian[17,18,54]

$$H_{Sys}^{vb} = \sum_{m=1}^{2}\sum_{\nu=0}^{1}\left(E_m + \nu\hbar\omega_\nu\right)B_{m\nu}^{\dagger}B_{m\nu} + \sum_{m=1}^{2}\sum_{n\neq m}^{2}\sum_{\nu=0}^{1}\sum_{\sigma=0}^{1}J_{mn}B_{m\nu}^{\dagger}B_{n\sigma}\langle 0|\nu\rangle\langle 0|\sigma\rangle \tag{7.9}$$

where the indices m and n represent molecular sites, ν and σ are vibronic levels at sites m and n, and ω_ν is the frequency of an intramolecular mode. In this notation, the operator $B_{m\nu}^{\dagger}$ ($B_{m\nu}$) creates (annihilates) an excitation at molecule m in vibronic level ν. H_{Sys}^{vb} treats only the intramolecular HOOP mode of APC and CPC explicitly. The product of overlap integrals between nuclear wavefunctions, $\langle 0|\nu\rangle\langle 0|\sigma\rangle$, distributes the inter-site electrostatic coupling, J_{mn}, in the vibronic basis; these integrals are computed in a harmonic basis with no Duchinsky rotation.[55] The expansion in vibronic levels is truncated at $\nu = 1$ because the overlap integrals, $\langle 0|\nu\rangle$, become negligible for higher excitation quanta, ν, due to the modest Huang-Rhys factors of APC and CPC.[24,25]

In this vibronic exciton model, each pigment site is coupled to a single overdamped BO coordinate under the assumption that all vibronic levels associated with a particular pigment site experience the same bath induced fluctuations. The total spectral density at site m is then equal to $C_m^{OD}(\omega)$. The single exciton block of the Hamiltonian matrix is constructed in a basis of vibronic excitations denoted as $|m,\nu\rangle$, which upon diagonalization yields

$$|a\rangle = \sum_{m=1}^{2}\sum_{\nu=0}^{1}\phi_{a,m\nu}|m,\nu\rangle \tag{7.10}$$

Transformation of the line broadening functions from the local to exciton basis is achieved with

$$g_{abcd}(t) = \sum_{n=1}^{2}\sum_{\nu=0}^{1}\phi_{a,m\nu}\phi_{b,m\nu}\phi_{c,m\nu}\phi_{d,m\nu}g_m(t) \tag{7.11}$$

where $g_m(t)$ is defined in Equation (7.6). Figure 7.2 summarizes the key ideas involved in the partitioning schemes utilized in the purely electronic and vibronic exciton Hamiltonians.

The coherent exciton scattering (CES) formalism is a powerful Green function approach, which has been used to simulate the optical response and delocalization of excitons in molecular aggregates.[13,56,57] The physical picture adopted by the present model is quite similar to CES. As in CES, the $g_m(t)$, which account for thermally driven motion, impart identical fluctuations in all vibronic levels, ν, of the individual pigments. The purely electronic exciton model differs in that intramolecular modes can also influence the line widths through the real part of $g_m(t)$, where the importance of this contribution increases with decreasing mode frequency. We also remark that both our vibronic exciton model and CES account for only the ground vibrational level in the electronic ground state.[57] For this reason, E_m represents the electronic origin (i.e., 0-0 transition) in H_{Sys}^{Vb}.

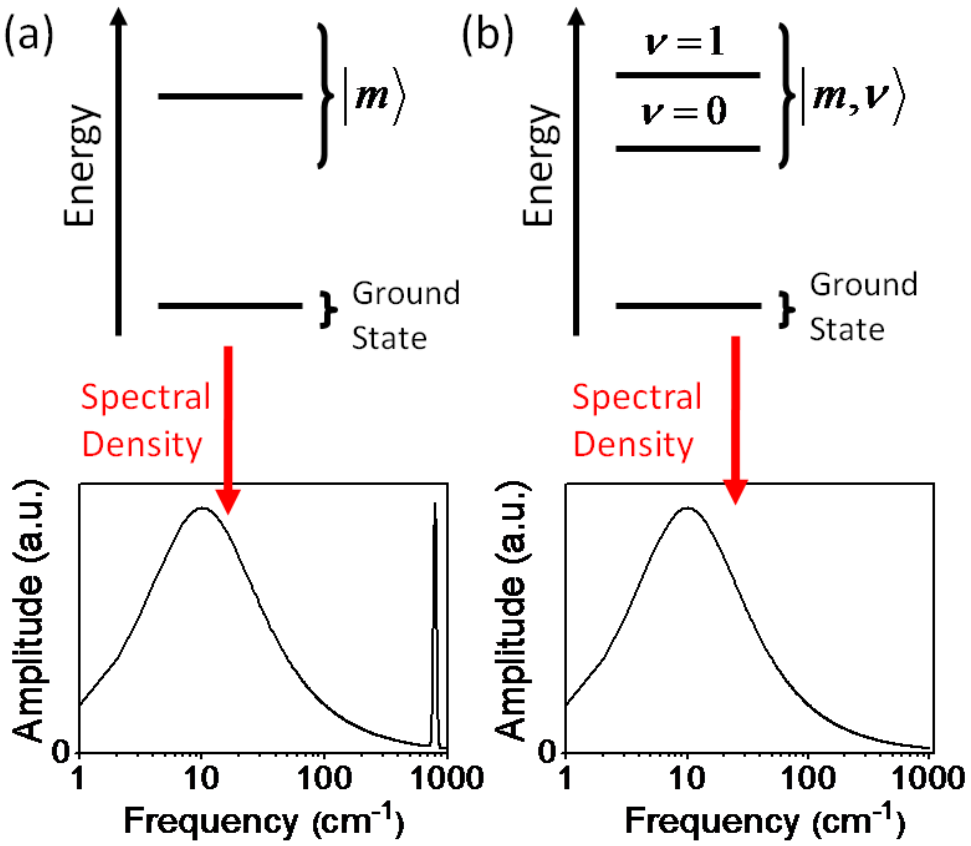

Figure 7.2. Key ideas involved in the Frenkel exciton models presented in Section 7.2. (a) Exciton model corresponding to H_{Sys}^{el}. The system Hamiltonian is diagonalized in a basis of two-level systems and underdamped modes are incorporated in the spectral density using $C_m^{UD}(\omega)$. The resonance at 800 cm^{-1} has been given a finite spectral width for illustration. (b) The vibronic exciton Hamiltonian, H_{Sys}^{vb}, explicitly treats intramolecular modes with large Franck-Condon factors. The spectral density possesses contributions from only the overdamped nuclear motion described by $C_m^{OD}(\omega)$.

7.2.3. Modified Redfield Rate Constants

The modified Redfield rate constants corresponding to a transition initiating in exciton a and terminating in exciton b is computed using[39]

$$K_{ba} = 2\,\mathrm{Re}\int_0^\infty dt F_{ba}(t) \times \exp\left[-i(\omega_b-\omega_a)t - g_{bbbb}(t) - g_{aaaa}^*(t) + 2\left\{g_{bbaa}(t) + i(\lambda_{bbaa}-\lambda_{aaaa})t\right\}\right] \tag{7.12}$$

where

$$F_{ba}(t)=\left[\ddot{g}_{baab}(t)-\left\{\dot{g}_{abaa}(t)-\dot{g}_{abbb}(t)+2i\lambda_{abaa}\right\}\left\{\dot{g}_{aaba}(t)-\dot{g}_{bbba}(t)+2i\lambda_{baaa}\right\}\right] \tag{7.13}$$

General physical insights associated with modified Redfield theory have been discussed in recent reviews.[5,40,43] Reference [40] demonstrates the ability of modified Redfield theory to interpolate between the limits of weak (Redfield) and strong (Förster) system-bath interactions. In addition, modified Redfield theory is capable of capturing rate enhancements involving the exchange of multiple excitation quanta with the bath. By contrast, traditional Redfield theory accounts only for transitions through vibronic channels in which the initial and final phonon states differ by single excitation quanta.

7.3. RESULTS AND DISCUSSION

Electronic population transfer rates in APC and CPC are computed below using the two classes of system Hamiltonians presented in Section 7.2. This comparison of models focuses on the appropriate treatment of the strongly coupled HOOP mode at 800 cm^{-1}. As suggested by Figure 7.2, H_{Sys}^{el} keeps the HOOP coordinate as part of the spectral density, which allows it to function as a traditional promoting mode in an internal conversion process. By contrast, H_{Sys}^{vb} handles explicitly the partitioning of the transition dipole in the vibronic progression of the HOOP mode, thereby supporting a mechanism of inter-site wavefunction delocalization not present in H_{Sys}^{el}. Figure 7.3, for example, explains that four vibronic excitons will be found in a dimer where each site possesses two vibronic levels (i.e., ν=0 and 1). The size of the Huang-Rhys factor is the key parameter governing the appropriate view of electronic structure. If the Huang-Rhys factor is small, then only the inter-site coupling between the ν=0 states will be significant and H_{Sys}^{el} is a good approximation.

However, H_{Sys}^{vb} is more appropriate when large mode displacements give rise to significant interactions between higher energy vibronic states ($\nu > 0$). Clearly the two Hamiltonians differ fundamentally in their views of electronic structure. The central issue examined here is the possibility that one Hamiltonian is better able to explain the relaxation rates of both APC and CPC in a consistent way.

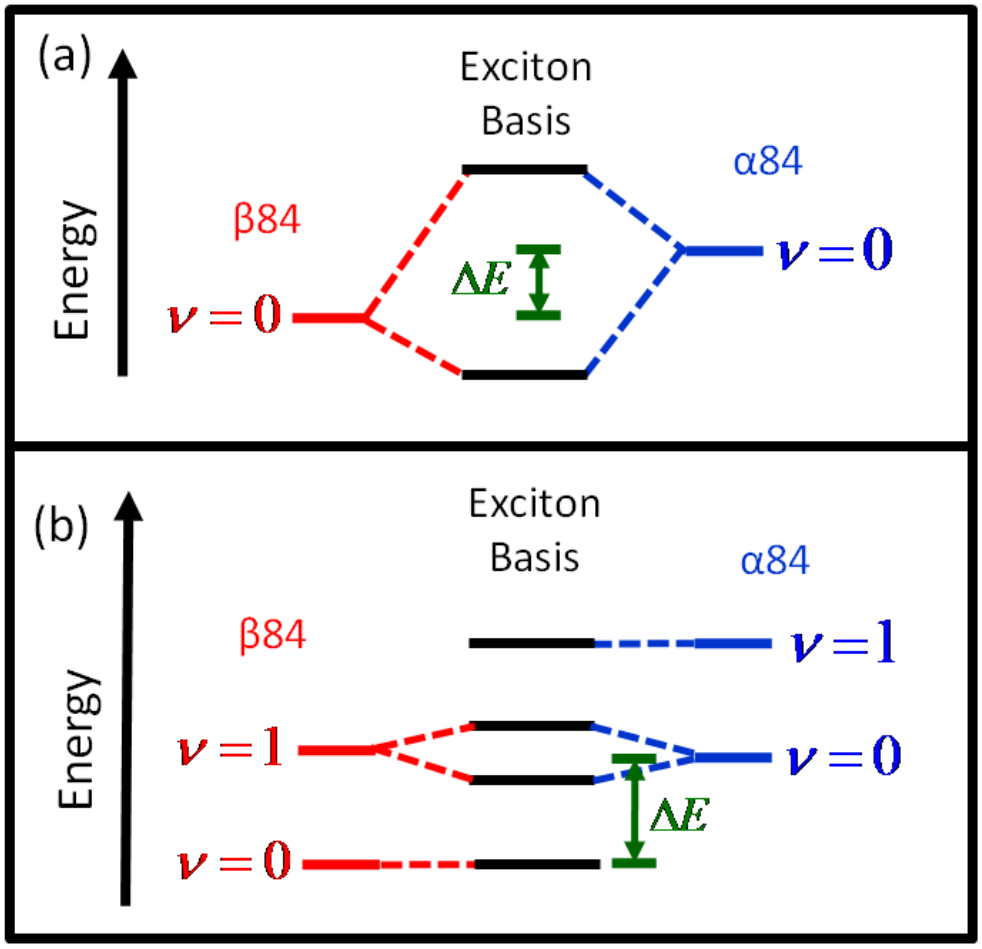

Figure 7.3. Schematics illustrating the electronic structures associated with (a) H_{Sys}^{el} and (b) H_{Sys}^{vb} for the molecular dimers in APC and CPC. Only the excited states of the system are shown because both Hamiltonians have block diagonal form. The difference in site energies is $\Delta E = E(\alpha 84) - E(\beta 84)$. (a) For H_{Sys}^{el}, the inter-site coupling, $J_{\alpha 84,\beta 84}$, reflects only the transition dipoles for the electronic origins. (b) Each site has two vibronic levels through

which exciton delocalization can occur. Dashed lines signify the basis states that contribute most to the respective excitons when $\Delta E \approx \omega$ and $J_{\alpha 84,\beta 84} < \Delta E$.

In the present analysis, the difference in site energies is viewed as the primary physical quantity distinguishing relaxation processes in APC and CPC. Of course, there may also be minor differences in the time scales of the bath and/or the reorganization energies in these two systems. However, the calculations presented below suggest it unlikely that differences in these characteristics of the bath justify the large disparity in kinetics. The parameters given in Table 7.1 are based on our earlier analysis of spectroscopic measurements.[24,25] It is true that the values of Λ_m and λ_m obtained by fitting spectroscopic signals will generally depend on the model employed. Therefore, effort is made to establish that the insights obtained below are robust within a physically reasonable range of parameter space.

7.3.1. Purely Electronic Excitons

Modified Redfield rate constants are displayed with respect to the site reorganization energies, λ, and the difference in site energies, $E_{\alpha 84} - E_{\beta 84}$, in Figure 7.4. In the interest of obtaining general physical insights, the reorganization energies are constrained to be the same for both pigments. The calculation reveals significant differences in the relaxation processes computed at small and large values of the reorganization energy. At λ <100 cm^{-1}, the calculation finds well-defined rate enhancements when $E_{\alpha 84} - E_{\beta 84}$ is equal to 775 cm^{-1} and 1600 cm^{-1}, which reflects participation of the HOOP coordinate as a promoting mode. The rate enhancement computed near 1600 cm^{-1} underscores the aforementioned ability of modifield Redfield theory to describe non-radiative transitions involving the exchange of

multiple excitation quanta with the bath. The well-defined rate enhancements calculated at λ<100 cm^{-1} broaden and eventually disappear as the reorganization energy increases. Effectively, the reorganization energy inflates the "bandwidth" of the vibronic relaxation channel until it is no longer well-localized at particular values of $E_{\alpha 84} - E_{\beta 84}$. The calculation in Figure 7.4 is repeated with different bath correlation times to make clear that this physical insight holds under reasonable variation of the parameters. To be consistent with our experiments,[24,25] both calculations are conducted in the slow modulation regime where (approximately) Gaussian line shapes are obtained.[53] The spectral density, $C_m^{OD}(\omega)$, concentrates more of its amplitude at ω<k_BT with Λ^{-1}=283fs than with Λ^{-1}=100fs. For this reason, large rate constants are predicted in Figure 7.4a even when λ<200cm^{-1} (i.e., with weak system-bath coupling). In the range of $E_{\alpha 84} - E_{\beta 84}$ relevant to APC and CPC, similar results are obtained for both values of Λ, which suggests that the interpretation of these physics is robust.

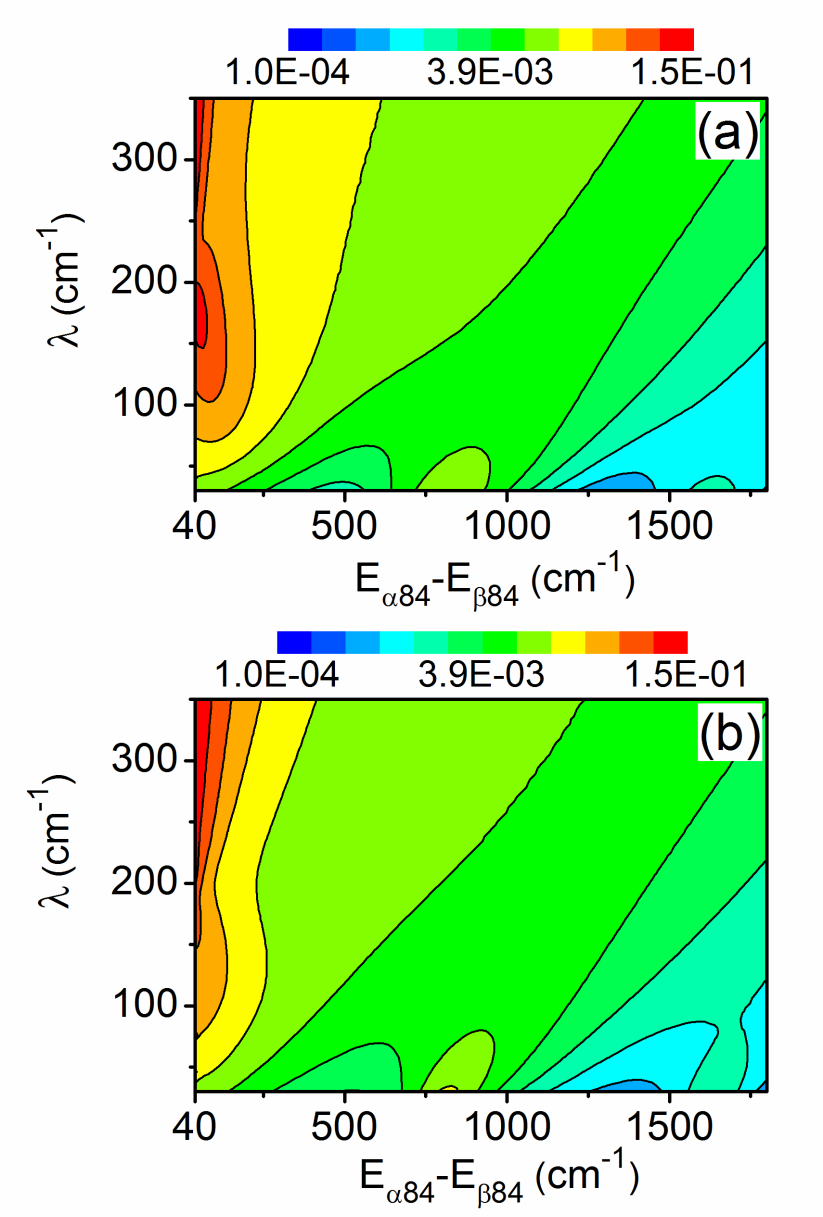

Figure 7.4. Modified Redfield rate constants, K_{12}, computed using H_{Sys}^{el}. The time scale of the bath, which is equivalent at each site, is (a) 283 fs and (b) 100 fs. The intermolecular coupling and Huang-Rhys factor for the HOOP mode are given in Table 7.2. At λ <100 cm^{-1}, the 800 cm^{-1} mode promotes well-defined rate enhancements when the difference in site energies, $E_{\alpha 84} - E_{\beta 84}$, is near 775 and 1600 cm^{-1}. Panels (a) and (b) display the logarithm (base 10) of K_{12}.

Figure 7.5 presents one-dimensional slices through the contour plot in Figure 7.4. This representation makes clear that the rate enhancement associated with the HOOP

coordinate is insensitive to the value of $E_{\alpha 84} - E_{\beta 84}$ when the reorganization energy is near that found experimentally. Most importantly, the rate decreases monotonically with $E_{\alpha 84} - E_{\beta 84}$ at realistic values of the site reorganization energies, which are most assuredly greater than 100 cm^{-1} because the measured spectroscopic line widths are at least 500 cm^{-1}. For example, in contrast with the observed kinetics, the calculation predicts that the relaxation rate is 1.5 times faster in CPC than it is in APC with λ =329 cm^{-1}. Insight into this behavior is obtained using the participation ratio[5]

$$PR_a = \frac{1}{\sum_{m=1}^{N} \phi_{am}^4} \tag{7.14}$$

PR_a is equal to 1 and 2 in the limit of fully localized and delocalized states, respectively. As should be expected, Figure 7.5 predicts that the excitons become more localized as $E_{\alpha 84} - E_{\beta 84}$ increases. The 1.07 value of PR_a computed at $E_{\alpha 84} - E_{\beta 84}$=760 cm^{-1} suggests that the Förster energy transfer mechanism should be a good approximation for APC. In fact, the Förster energy transfer mechanism is known to provide an accurate description of the dynamics in CPC where, according to H_{Sys}^{el}, the tendency for wavefunction delocalization is even greater (PR_a =1.27).[30]

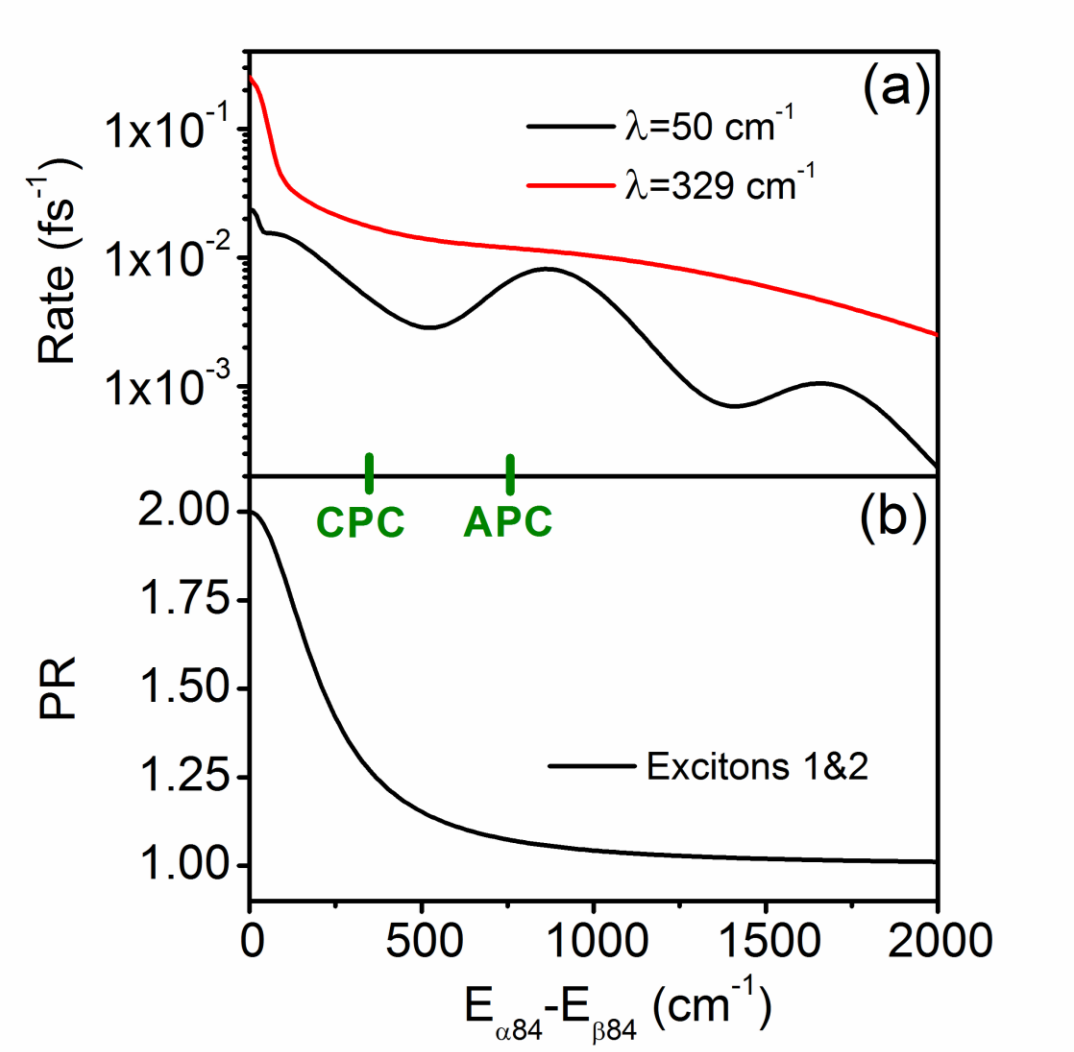

Figure 7.5. (a) Modified Redfield rate constant, K_{12}, computed using H_{Sys}^{el} and the parameters in Table 7.2. The value of the reorganization energy, which is equivalent at the two sites, is given in the figure legend. (b) Participation ratio computed using Equation (7.14). Also indicated are the empirically obtained differences in the site energies for APC and CPC (see Table 7.1).

Overall, the simulations presented in this Section are inconsistent with dynamics measured in APC and CPC.[24,25] Most important in reaching this conclusion is the model's prediction that, contrary to experimental observations, electronic relaxation is faster in CPC than in APC at realistic values of the reorganization energy (c.f., Figure 7.5). The

calculations show that the transition loses sensitivity to the energy difference between the initial and final states when λ increases because of growth in the "bandwidth" of the vibronic relaxation channel, which is similar in magnitude to the spectroscopic line width. The calculated exciton sizes are also inconsistent with experiments. The calculations presented in Figure 7.5 suggest that the excited states of CPC are more delocalized than those of APC, whereas the opposite behavior is found experimentally.[24,25]

It should be emphasized that the insights obtained here are based on a physically motivated correlation function, $C_m^{UD}(\omega)$, which treats only the intramolecular HOOP mode explicitly. Higher frequency bond stretching modes are observed in the resonance Raman spectra of phycocyanobilin.[58-60] However, modes with frequencies greater than the exciton splitting will have little influence on the dynamics because such vibronic relaxation channels would be energetically "uphill". In principle, the underdamped modes detected near 250 cm^{-1} in both APC and CPC can serve as promoting modes.[24,37] However, the non-radiative transition in APC would then deposit roughly three quanta of energy (i.e., total of 750 cm^{-1}) in the acceptor state. In this scenario, the coordinate would require an exceptionally large displacement in order for it to constitute the dominant relaxation channel. More importantly, a relaxation mechanism involving modes near 250 cm^{-1} would suggest that CPC possesses a faster relaxation rate than APC because of its smaller exciton splitting (i.e., only two quanta of energy would be deposited in the acceptor state).

7.3.2. Vibronic Excitons

In this Section, rate constants are computed with H_{Sys}^{vb} to address inconsistencies found when H_{Sys}^{el} is employed. The vibronic exciton Hamiltonian matrix is given by

$$H_{Sys}^{vb} = \begin{pmatrix} E_{\alpha 84} & 0 & V_{00} & V_{01} \\ 0 & E_{\alpha 84} + \hbar\omega & V_{10} & V_{11} \\ V_{00} & V_{10} & E_{\beta 84} & 0 \\ V_{01} & V_{11} & 0 & E_{\beta 84} + \hbar\omega \end{pmatrix} \tag{15}$$

where $V_{mn} = J_{\alpha 84,\beta 84} \langle 0|m\rangle_{\alpha 84} \langle 0|n\rangle_{\beta 84}$. The expansion of vibronic states, $|m,\nu\rangle$, in the HOOP mode is truncated at ν=1 because the electronic origin dominates the vibronic progressions in APC and CPC (i.e., relatively small Huang-Rhys factors).[24,25] This choice of basis is additionally well-suited for interpretation of our experiments because the laser pulses utilized in these studies primarily excited electronic states with resonances on the lower energy portion of the linear absorption spectra. Off-diagonal elements corresponding to different vibronic levels at a particular site are set equal to zero in H_{Sys}^{vb}. A more sophisticated treatment of these elements, which is beyond the scope of the present work, would capture the effects of intramolecular vibrational energy redistribution (IVR). As in Section 7.3.1, the dimensionless displacement of the HOOP coordinate is set equal to 0.5. However, vibronic coupling now directly controls the magnitudes of intermolecular interactions through the couplings in H_{Sys}^{vb}.

Figure 7.6 displays the rate constants K_{12}, K_{13}, and K_{23} as functions of $E_{\alpha 84} - E_{\beta 84}$ and the site reorganization energies, which are taken to be equivalent for both pigments. The rate, K_{12}, decreases monotonically as the difference in site energies increases, which is similar to the behavior shown in Figure 7.4. This similarity should be expected because the two lowest energy excitons have small contributions from excited vibronic levels when $E_{\alpha 84} - E_{\beta 84} < \hbar\omega$ (c.f., Figure 7.3). By contrast, K_{13} exhibits a steep rate increase when the nature of the non-radiative transition changes from intra-site to inter-site at $E_{\alpha 84} - E_{\beta 84} = \hbar\omega$;

inter-site transitions are obtained at $E_{\alpha 84} - E_{\beta 84} > \hbar\omega$. As mentioned above, the intra-site transitions are slow because H_{Sys}^{vb} neglects IVR processes on the individual pigments. Finally, K_{23} possesses a marked enhancement in the electronic population transfer rate at $E_{\alpha 84} - E_{\beta 84} = \hbar\omega$. At this value of $E_{\alpha 84} - E_{\beta 84}$, the excited vibronic level of the $\beta 84$ pigment is degenerate with the electronic origin of the $\alpha 84$ pigment, thereby promoting exciton delocalization through the V_{01} elements in H_{Sys}^{vb}. The behavior of K_{23} is distinct from that shown in Figure 7.4, where the HOOP mode is regarded as part of the bath, in that a well-defined enhancement is found near $E_{\alpha 84} - E_{\beta 84} = \hbar\omega$ even at large values of the site reorganization energies. Profiles of these three rate constants at realistic values of λ are shown in Figure 7.7. To ensure that these physical insights are robust, Figure 7.6 presents rate constants calculated with a shorter bath timescale, Λ^{-1}=100fs, and smaller Huang-Rhys factor, S=0.05. The shorter bath correlation time has little effect on K_{12} and K_{13}, whereas K_{23} is slightly smaller and does not peak as sharply at $E_{\alpha 84} - E_{\beta 84} = \hbar\omega$. The decrease in S also has a minor influence on the calculated rate constants; the pronounced rate enhancement in K_{23} persists when $E_{\alpha 84} - E_{\beta 84} = \hbar\omega$.

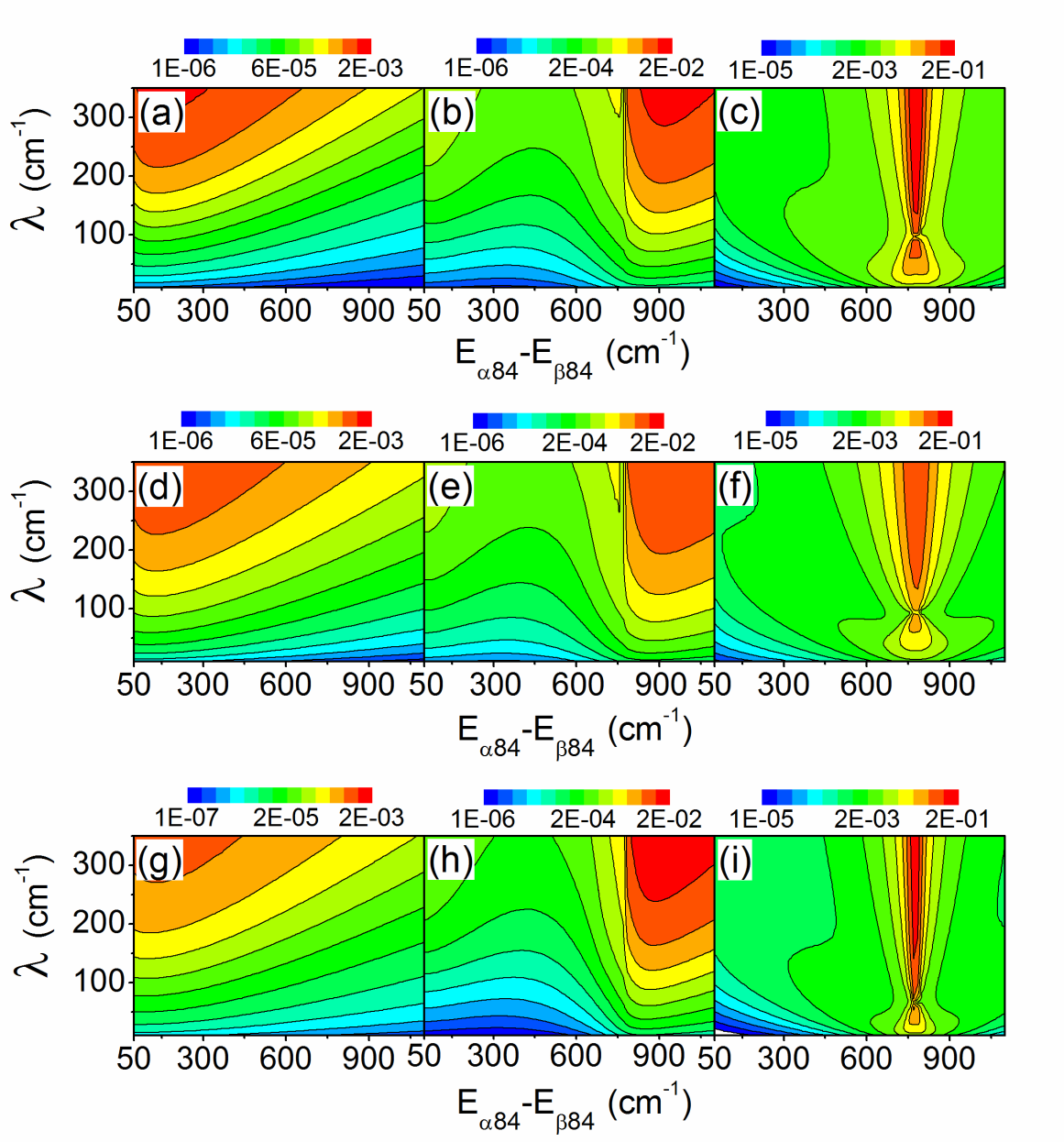

Figure 7.6. Modified Redfield rate constants computed using H_{Sys}^{vb}. Calculated rate constants include K_{12} (left column); K_{13} (middle column); K_{23} (right column). In panels (a)-(c), all parameters of Table 7.2 are used; (d)-(f) all parameters of Table 7.2 are used except that Λ^{-1} is set equal to 100 fs; (g)-(i) all parameters of Table 7.2 are used except that S = 0.05. In contrast with calculations based on H_{Sys}^{el}, well-defined rate enhancements are predicted near $E_{\alpha 84} - E_{\beta 84} = \hbar\omega$ at realistic values of the reorganization energy (λ >100 cm^{-1}). All panels display the logarithm (base 10) of the rate constants.

Spatial overlap in excitons 2 and 3 is at the root of the rate enhancement predicted in APC. Exciton sizes are quantified using a participation ratio valid for vibronic excitons

$$PR_a = \frac{1}{\sum_{m=1}^{N}\left(\sum_{\nu=0}\phi_{a,m\nu}^2\right)^2} \tag{7.16}$$

As in Equation (7.14), PR_a is respectively equal to 1 and 2 for fully localized and delocalized states. Figure 7.7b shows that PR_a maximizes near $E_{\alpha 84} - E_{\beta 84} = \hbar\omega$ when the excited vibronic level at the $\beta 84$ pigment comes into degeneracy with the electronic origin of $\alpha 84$. This delocalization mechanism contrasts with the common view that heterogeneity in molecular sites (i.e., diagonal disorder) can only suppress exciton delocalization. The present calculations show that special circumstances may arise in which large vibronic couplings actually promote delocalization. As illustrated in Figure 7.3b, the key to this delocalization mechanism is the resonance in (staggered) vibronic transitions with large Franck-Condon factors made possible by heterogeneity in the site energies.

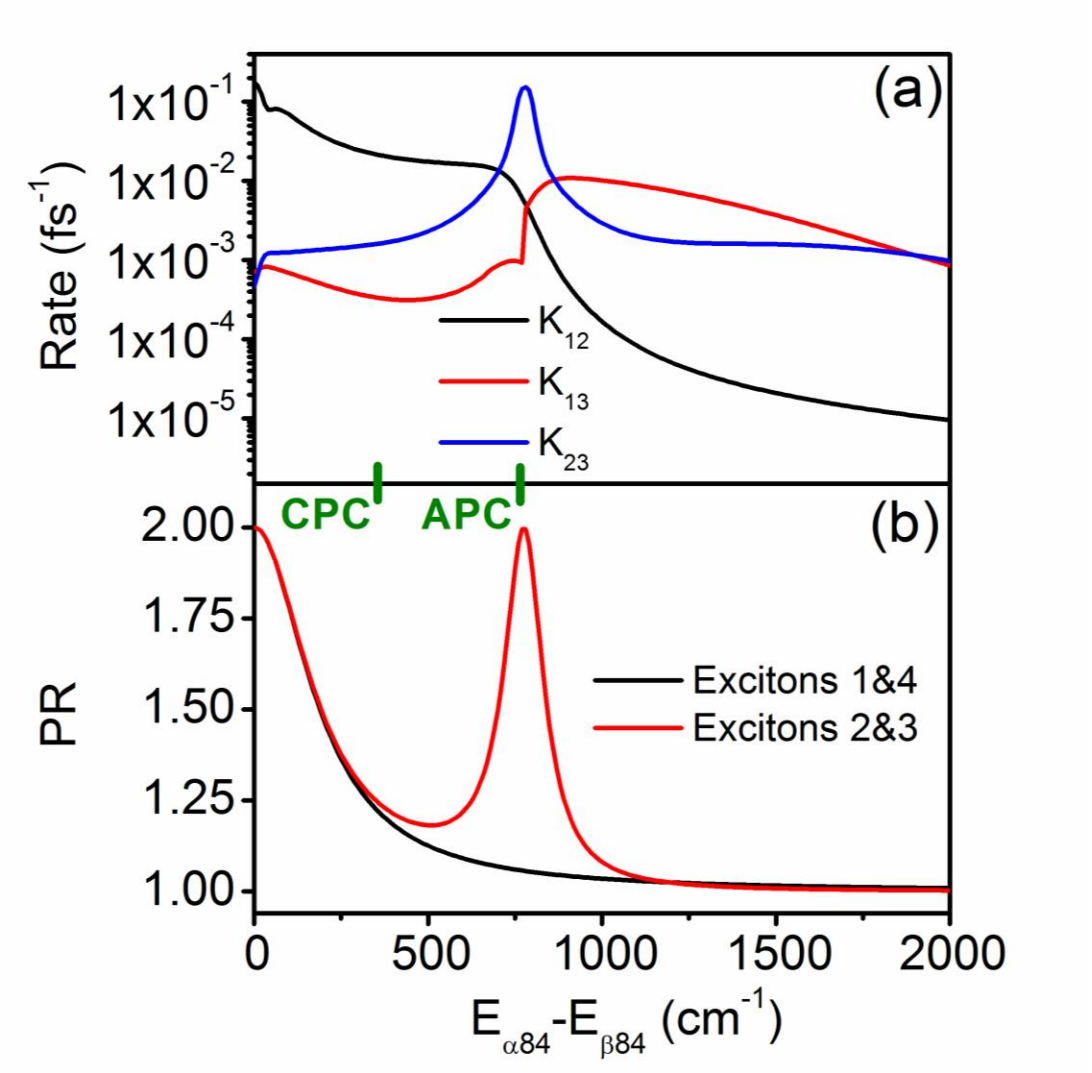

Figure 7.7. (a) Modified Redfield rate constants computed using H_{Sys}^{vb} and the parameters in Table 7.2. Color coding for the K_{12}, K_{13}, and K_{23} rate constants is defined in the figure legend. (b) Participation ratios calculated using Equation (7.16). Also indicated are the empirically obtained differences in the site energies for APC and CPC (see Table 7.1).

The most important aspect of these calculations is that a clear enhancement in the K_{23} of APC is predicted by invoking its experimentally established difference in site energies. Moreover, unlike the prediction of the purely electronic exciton model, the present rate enhancement persists at realistic site reorganization energies. We therefore suggest the H_{Sys}^{vb} successfully pinpoints the mechanism responsible for ultrafast population flow in APC,

while simultaneously justifying slower electronic relaxation in CPC. In addition to explaining the difference in kinetics, the vibronic exciton model yields exciton sizes consistent with the transient absorption anisotropies observed in both systems, which indicate greater wavefunction delocalization in APC. We envision that exciton delocalization in APC will be fairly delicate because the intermolecular couplings are (slightly) smaller than the site reorganization energies (e.g., V_{01}=-60 cm^{-1} when S=0. 5). One possibility is that the vibronic exciton delocalization mechanism operates for only a short amount of time following photoexcitation before solvation processes break the degeneracy depicted in Figure 7.3b and trap the excitation on the lower energy β84 site. Simulations conducted using a model capable of capturing self-trapping dynamics will be need to address this issue.[6,61]

7.4. CONCLUSION

The main conclusion of this chapter is that the behavior predicted by the vibronic exciton model is more consistent with experimental results for APC and CPC than that obtained when the HOOP mode is regarded as part of the spectral density. Most important to this conclusion is the result that well-defined rate enhancements persist near $E_{\alpha 84} - E_{\beta 84} = \hbar\omega$ at realistic values of the site reorganization energies (λ >100 cm^{-1}). As shown in Figures 7.5 and 7.7, only with the vibronic exciton model are faster electronic relaxation processes predicted in APC when λ >100 cm^{-1}. These rate enhancements originate in a vibronic exciton delocalization mechanism, which takes hold primarily in APC (c.f., Figure 7.3). Extensions of the model presented here should develop strategies for simulating the IVR processes taking place subsequent to electronic population transfer. The role of fast, solvation-driven exciton self-trapping should also be investigated. It is hoped that our experiments and the interpretation offered here will motivate rigorous theoretical studies of

these systems. APC and CPC are excellent models for studying vibronic effects on exciton sizes and energy transport, which are generally quite difficult to pinpoint experimentally.

An important broader implication of this work is that vibronic coupling may be more intimately connected to energy transfer in photosynthetic complexes than it is usually given credit for. Vibronic effects similar to those investigated here may indeed promote exciton delocalization in a wider variety of systems. As discussed in Section 7.3.2, the key ingredient underlying this mechanism of wavefunction delocalization is a degeneracy in staggered vibronic levels at different pigments made possible by diagonal disorder. In these situations, purely electronic exciton models underestimate exciton sizes because they see heterogeneity among sites as only a localizing influence. Exciting new research applies measures of entanglement developed in the field of quantum information to light harvesting proteins.[61-65] In this context, it will be interesting to investigate the role of the vibronic effects on quantum entanglement in these and other systems.

Table 7.1. Empirical Parameters Obtained from Fitting of Spectroscopic Signals

Parameter	APC	CPC
$E(\alpha 84)$	16060 cm^{-1}	16240 cm^{-1}
$E(\beta 84)$	15300 cm^{-1}	15890 cm^{-1}
$\Lambda^{-1}(\alpha 84)$	296 fs	278 fs
$\Lambda^{-1}(\beta 84)$	238 fs	327 fs
$\lambda(\alpha 84)$	360 cm^{-1}	417 cm^{-1}
$\lambda(\beta 84)$	235 cm^{-1}	304 cm^{-1}

Table 7.2. Parameters Used in Calculations

Parameter	Value
$E(\alpha 84)$	Varied
$E(\beta 84)$	15595 cm^{-1}
[(a)] $J_{\alpha 84,\beta 84}$	-150 cm^{-1}
[(b)] $\Lambda^{-1}(\alpha 84) = \Lambda^{-1}(\beta 84)$	283 fs
[(b)] $\lambda(\alpha 84) = \lambda(\beta 84)$	329 cm^{-1}
[(c)] ω	800 cm^{-1}
[(c)] S	0.125

[(a)] Parameter of Equations (7.2) and (7.9).

[(b)] Parameter of Equation (7.3) obtained as averages of the empirical values given in Table 7.1.

[(c)] Parameter of Equations (7.4) and (7.9).

REFERENCES

(1) van Amerongen, H.; Valkunas, L.; van Grondelle, R. *Photosynthetic Excitons*; World Scientific: Singapore, 2000.

(2) Grover, M.; Silbey, R. J. *J. Chem. Phys.* 1971, *54*, 4843.

(3) De Boer, S.; Wiersma, D. A. *Chem. Phys.* 1989, *131*, 135.

(4) Rebentrost, P.; Mohseni, M.; Kassal, I.; Lloyd, S.; Aspuru-Guzik, A. *New. J. Phys.* 2009, *11*, 033003:1.

(5) Abramavicius, D.; Palmieri, B.; Voronine, D. V.; Sanda, F.; Mukamel, S. *Chem. Rev.* 2009, *109*, 2350.

(6) Tanimura, Y. *J. Phys. Soc. Jpn.* 2006, *75*, 082001.

(7) Ishizaki, A.; Fleming, G. R. *J. Chem. Phys.* 2009, *130*, 234110.

(8) Fassioli, F.; Nazir, A.; Olaya-Castro, A. *J. Phys. Chem. Lett.* 2010, *1*, 2139.

(9) Cina, J. A.; Fleming, G. R. *J. Phys. Chem. A* 2004, *108*, 11196.

(10) Mancal, T.; Nemeth, A.; Milota, F.; Lukes, V.; Kauffmann, H. F. *J. Chem. Phys.* 2010, *132*, 184515.

(11) Reineker, P.; Supritz, C.; Warns, C.; Barvik, I. *J. Lumin.* 2004, *108*, 149.

(12) Renger, T. *Photosynth. Res.* 2009, *102*, 471.

(13) Eisfeld, A.; Briggs, J. S. *Chem. Phys.* 2002, *281*, 61.

(14) Seibt, J.; Marquetand, P.; Engel, V.; Chen, Z.; Dehm, V.; Würthner, F. *Chem. Phys.* 2006, *328*, 354.

(15) Roden, J.; Schulz, G.; Eisfeld, A.; Briggs, J. *J. Chem. Phys.* 2009, *131*, 044909.

(16) McRae, E. G.; Siebrand, W. *J. Chem. Phys.* 1964, *41*, 905.

(17) Philpott, M. R. *J. Chem. Phys.* 1967, *47*, 4437.

(18) Spano, F. C. *Acc. Chem. Res.* 2010, *43*, 429.

(19) Ahn, T.-S.; Müller, A. M.; Al-Kaysi, R. O.; Spano, F. C.; Norton, J. E.; Beljonne, D.; Brédas, J.-L.; Bardeen, C. J. *J. Chem. Phys.* 2008, *128*, 054505.

(20) Schwoerer, M.; Wolf, H. C. *Organic Molecular Solids*; Wiley-VCH: Weinheim, 2007.

(21) Jonas, D. M.; Lang, M. J.; Nagasawa, Y.; Joo, T.; Fleming, G. R. *J. Phys. Chem* 1996, *100*, 12660.

(22) Arnett, D. C.; Moser, C. C.; Dutton, P. L.; Scherer, N. F. *J. Phys. Chem. B* 1999, *103*, 2014.

(23) Wynne, K.; Haran, G.; Reid, G. D.; Moser, C. C.; Dutton, P. L.; Hochstrasser, R. M. *J. Phys. Chem* 1996, *100*, 5140.

(24) Womick, J. M.; Moran, A. M. *J. Phys. Chem. B* 2009, *113*, 15747.

(25) Womick, J. M.; Moran, A. M. *J. Phys. Chem. B* 2009, *113*, 15771.

(26) Womick, J. M.; Miller, S. A.; Moran, A. M. *J. Chem. Phys.* 2010, *133*, 024507.

(27) Brejc, K.; Ficner, R.; Huber, R.; Steinbacher, S. *J. Mol. Biol.* 1995, *249*, 424.

(28) Wang, X.-Q.; Li, L.-N.; Chang, W.-R.; Zhang, J.-P.; Gui, L.-L.; Guo, B.-J.; Liang, D.-C. *Acta Cryst.* 2001, *D57*, 784.

(29) Gillbro, T.; Sharkov, A. V.; Kryukov, I. V.; Khoroshilov, E. V.; Kryukov, P. G.; Fischer, R.; Scheer, H. *Biochimica et Biophysica Acta* 1993, *1140*, 321.

(30) Debreczeny, M. P.; Sauer, K.; Zhou, J.; Bryant, D. A. *J. Phys. Chem.* 1995, *99*, 8420.

(31) Sharkov, A. V.; Kryukov, I. V.; Khoroshilov, E. V.; Kryukov, P. G.; Fischer, R.; Scheer, H.; Gillbro, T. *Chem. Phys. Lett.* 1992, *191*, 633.

(32) Edington, M. D.; Riter, R. E.; Beck, W. F. *J. Phys. Chem.* 1996, *100*, 14206.

(33) Riter, R. E.; Edington, M. D.; Beck, W. F. *J. Phys. Chem. B* 1997, *101*, 2366.

(34) Edington, M. D.; Riter, R. E.; Beck, W. F. *J. Phys. Chem.* 1995, *99*, 15699.

(35) Edington, M. D.; Riter, R. E.; Beck, W. F. *J. Phys. Chem. B* 1997, *101*, 4473.

(36) Riter, R. R.; Edington, M. D.; Beck, W. F. *J. Phys. Chem.* 1996, *100*, 14198.

(37) Zhang, J. M.; Shiu, Y. J.; Hayashi, M.; Liang, K. K.; Chang, C. H.; Gulbinas, V.; Yang, C. M.; Yang, T.-S.; Wang, H. Z.; Chen, Y.-T.; Lin, S. H. *J. Phys. Chem. A* 2001, *105*, 8878.

(38) Zhang, J. M.; Zhao, F. L.; Zheng, X. G.; Wang, H. Z.; Yang, T.-S.; Hayashi, M.; Lin, S. H. *J. Photochem. Photobiol. B: Biol.* 1999, *53*, 128.

(39) Zhang, W. M.; Meier, T.; Chernyak, V.; Mukamel, S. *J. Chem. Phys.* 1998, *108*, 7763.

(40) Yang, M.; Fleming, G. R. *Chem. Phys.* 2002, *282*, 163.

(41) Redfield, A. G. *Adv. Magn. Res.* 1965, *1*, 1.

(42) Förster, T. *Ann. Physik* 1948, *437*, 55.

(43) Abramavicius, D.; Mukamel, S. *Chem. Rev.* 2004, *104*, 2073.

(44) Spano, F. C. *Annu. Rev. Phys. Chem.* 2006, *57*, 217.

(45) Zhuang, W.; Hayashi, T.; Mukamel, S. *Angew. Chemie.* 2009, *48*, 3750.

(46) Lim, S.-H.; Bjorklund, T. G.; Spano, F. C.; Bardeen, C. J. *Phys. Rev. Lett.* 2004, *92*, 107402:1.

(47) West, B. A.; Womick, J. M.; McNeil, L. E.; Tan, K. J.; Moran, A. M. *J. Phys. Chem. C* 2010, *114*, 10580.

(48) Sanematu, T. *J. Phys. Soc. Jpn.* 1976, *43*, 600.

(49) Sanematu, T.; Mizuno, Y. *J. Phys. Soc. Jpn.* 1976, *40*, 1733.

(50) Linnanto, J. M.; Korppi-Tommola, J. E. I. *Chem. Phys.* 2009, *357*, 171.

(51) Spano, F. C.; Meskers, S. C. J.; Hennebicq, E.; Beljonne, D. *J. Am. Chem. Soc.* 2007, *129*, 7044.

(52) Spano, F. C.; Silvestri, L.; Spearman, P.; Raimondo, L.; Tavazzi, S. *J. Chem. Phys.* 2007, *127*, 184703:1.

(53) Mukamel, S. *Principles of Nonlinear Optical Spectroscopy*; Oxford University Press: New York, 1995.

(54) Holstein, T. *Ann. Phys.* 1959, *8*, 325.

(55) Myers, A. B.; Mathies, R. A. *J. Chem. Phys.* 1984, *81*, 1552.

(56) Eisfeld, A.; Briggs, J. S. *Chem. Phys.* 2006, *324*, 376.

(57) Roden, J.; Eisfeld, A.; Briggs, J. S. *Chem. Phys.* 2008, *352*, 258.

(58) Szalontai, B.; Gombos, Z.; Csizmadia, V.; Csatorday, K.; Lutz, M. *Biochemistry* 1989, *28*, 6467.

(59) Szalontai, B.; Gombos, Z.; Csizmadia, V.; Bagyinka, C.; Lutz, M. *Biochemistry* 1994, *33*, 11823.

(60) Andel III, F.; Murphy, J. T.; Haas, J. A.; McDowell, M. T.; van der Hoef, I.; Lugtenburg, J.; Lagarias, J. C.; Mathies, R. A. *Biochemistry* 2000, *39*, 2667.

(61) Ishizaki, A.; Fleming, G. R. *New J. Phys.* 2010, *12*, 055004.

(62) Sarovar, M.; Ishizaki, A.; Fleming, G. R.; Whaley, K. B. *Nature Physics* 2010, *6*, 462.

(63) Mukamel, S. *J. Chem. Phys.* 2010, *132*, 241105.

(64) Thorwart, M.; Eckel, J.; Reina, J. H.; Nalbach, P.; Weiss, S. *Chem. Phys. Lett.* 2009, *478*, 234.

(65) Hossein-Nejad, H.; Scholes, G. D. *New J. Phys.* 2010, *12*, 065045.

(66) Homoelle, B. J.; Edington, M. D.; Diffey, W. M.; Beck, W. F. *J. Phys. Chem. B* 1998, *102*, 3044.

CHAPTER 8. EXCITON DELOCALIZATION AND ENERGY TRANSPORT MECHANISMS IN R-PHYCOERYTHRIN

8.1. INTRODUCTION

Recent years have seen significant advances in the understanding of electronic relaxation processes in molecular aggregates and photosynthetic antennae.[1-9] Most notably, transformative new experimental studies find that some light harvesting complexes utilize coherent energy transfer mechanisms, wherein electronic excitations undergo wave-like motion before concentrating on particular pigment sites.[10-13] Advanced quantum dynamical models show that non-Markovian effects and non-secular transitions explain some aspects of the experimental observations.[14-19] Theories incorporating spatially correlated nuclear motion in the environments surrounding the pigments are also under development.[20-24] Even in cases where conventional dynamical models hold, realistic descriptions of relaxation rates may require a more sophisticated description of vibronic couplings than is usually employed. Interactions between the system and bath are commonly taken into account by characterizing the statistics of thermal fluctuations in the system's energy levels.[2,25-28] A treatment of energy transport incorporating only thermally driven motions is often sufficient for modeling transitions between exciton states whose energies differ by less than $k_B T$. However, in some systems intramolecular modes facilitate rapid "energetically downhill" transitions across large energy gaps.[29-32] A more detailed description of the bath is needed to properly account for such dynamics. Modified Redfield theory (MRT), for example, is specially equipped to

Adapted with permission from Womick, J.M.; Liu, H.; Moran, A.M. *J. Phys. Chem. A* 2011, *115*, 2471-2482.

handle rate enhancements associated with intramolecular modes because it captures transitions in which multiple vibrational quanta are exchanged with the bath.[33,34]

In this chapter, we investigate the electronic structure and energy transport mechanisms in R-Phycoerythrin (RPE), a light harvesting protein found in red algae, using multiple nonlinear spectroscopies in conjunction with a Frenkel exciton model. We are particularly interested in the influence of exciton delocalization on photoinduced relaxation processes. RPE is well-suited to the purpose of this investigation because the shortest distances between pigments are approximately 2 nm, which is well within the range where wavefunction delocalization between bilin pigments is known to take hold.[11,32,35-39] In addition to the effect on the overall relaxation rate, we examine the influence of exciton electronic structure on the real-space paths traversed by electronic excitations as they relax toward equilibrium by comparing simulations conducted with MRT (delocalized) and Förster (localized) rate constants. While is it usually the case that kinetics speed up in the delocalized basis, the impact on the specific relaxation pathways in a complex network of pigments, such as that found in RPE, is less clear. Knowledge of the trajectories taken by photoexcitations is not only of fundamental interest but may also give insight into the strategies taken to avoid energy traps in RPE.

Two types of bilin pigments are found in RPE, phycoerythrobilin (PEB) and phycourobilin (PUB), whose molecular structures are displayed in Figure 8.1 along with their locations in the crystal structure.[40] PEB possesses a lower electronic resonance frequency because double-bond conjugation is maintained across three pyrrole rings (as opposed to only two in PUB). At the root of the hierarchical structure of RPE are pairs of α and β peptides (i.e., dimers), which both covalently bond two PEB pigments; a single PUB pigment is also

bonded to the β peptide.[40,41] Three α-β dimers self assemble into a trimer unit with C_3 symmetry. The final hexamer structure found in solution is composed of a pair of trimers self-assembled in a co-facial geometry. Figure 8.1 displaces the two trimers in the hexamer to make clear their relative orientations.

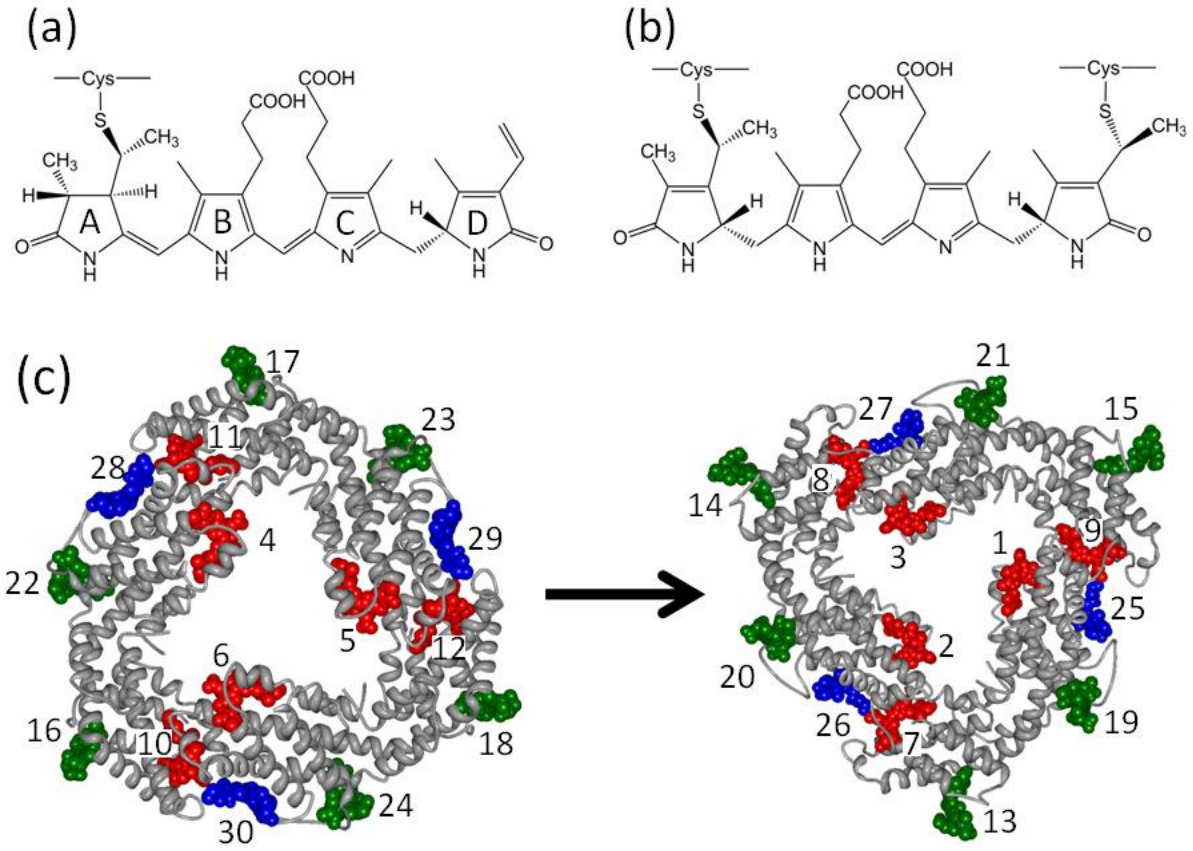

Figure 8.1. Molecular structure of (a) PEB and (b) doubly-linked PUB. (c) Structure of RPE trimer in which pigments are color-coded according to their molecular structures and conformations. All PUB pigments are blue. PEB pigments with A-B inter-ring torsion angles of 20° (inner PEB) and 50° (outer PEB) are shown in red and green, respectively. The upper and low trimers comprising the hexamer are respectively shown on the left and right, where the lower trimer is displaced in the direction of the arrow for clarity. Indices 1 to 6 represent PEB β82; 7 to 12 are PEB α82; 13 to 18 are PEB α139; 19 to 24 are PEB β158; 25 to 30 are PUB β50/61. This structural representation of the RPE trimer, isolated from Griffithsia monilis (red algae), is generated using PDB file 1B8D.[40]

Previous work by Gaigalas et al. established connections between particular pigments and spectroscopic properties in RPE, which constitute the foundation for the model employed here.[42] First, a peak in the linear absorbance spectrum near 20400 cm^{-1} primarily represents the PUB chromophores. Understanding the origin of two additional peaks in the absorbance spectrum at 17860 and 18870 cm^{-1} requires close inspection of the molecular conformations because RPE possesses only one other type of pigment, PEB. The PEB pigments can be assigned to one of two classes; the 18870 cm^{-1} peak in the absorbance spectrum is assigned to pigments whose A and B rings deviate from co-planarity by ~50°, whereas the group of PEB absorbing at 17860 cm^{-1} have smaller inter-ring torsion angles (~20°). To distinguish these two types of PEBs, pigments with inter-ring (A and B) torsion angles 20° and 50° will hereafter be referred to as the "inner PEB" and "outer PEB" (c.f., Figure 8.1c). The electronic resonance frequencies make clear that the overall structure of RPE is designed to funnel energy toward the center of the hexamer. This aspect of RPE is similar to other phycobiliproteins such as allophycocyanin and c-phycocyanin, which are also configured to transfer energy towards the center of their trimer and/or hexamer structures.[43-47]

In related work, our group recently examined the influence of vibronic couplings on the electronic structures and energy transport in cyanobacterial allophycocyanin and c-phycocyanin.[32,48-50] These studies confirmed earlier suggestions that the pigment dimers in allophycocyanin support wavefunction delocalization, thereby enabling sub-ps electronic relaxation between exciton states.[35,36,51-53] By contrast, it was found that the nearly identical dimers found in c-phycocyanin (apparently) possess localized electronic states and relax by way of the Förster mechanism.[54,55] With inspiration taken from theoretical treatment of electronic structure in organic semiconductors (i.e., vibronic exciton model),[56-58] we

proposed that electronic structures and relaxation processes in allophycocyanin and c-phycocyanin can be understood on the same footing only when the Franck-Condon progressions in their intramolecular modes are properly taken into account.[49,50] While a compelling case can be made for invoking a vibronic exciton model in allophycocyanin and c-phycocyanin, it may be that the exciton model outlined in Section 8.2, where vibronic couplings are kept as part of the bath, is more appropriate for applications to photosynthetic complexes possessing modest Huang-Rhys factors.

8.2. MODELING THE OPTICAL RESPONSE AND ELECTRONIC RELAXATION

This Section presents two models used to simulate the linear absorbance and energy transport kinetics of RPE. The first model employs a Frenkel exciton Hamiltonian in which delocalized electronic states govern both the spectroscopy and dynamics of the complex. Wavefunctions are localized to individual pigments and electronic relaxation proceeds through the Förster energy transfer mechanism in the second model. In both cases, interactions between the electronic excitations and nuclear modes are handled with a correlation function approach. These formulas are parameterized with constraints imposed by spectroscopic measurements. Ultimately, the goal will be to compare physical insights obtained with these two views of electronic structure.

8.2.1. Frenkel Exciton Hamiltonian

In the two models considered here, the Hamiltonian is partitioned into three components as

$$H = H_{Sys} + H_{Bath} + H_{Sys-Bath} \tag{8.1}$$

The first model employs a Frenkel exciton system Hamiltonian given by

$$H_{Sys}^{ex} = \sum_{m=1}^{N} E_m B_m^{\dagger} B_m + \sum_{m=1}^{N} \sum_{n \neq m}^{N} J_{mn} B_m^{\dagger} B_n \tag{8.2}$$

Here E_m is the energy gap of pigment molecule m at the ground state equilibrium geometry (i.e., Franck-Condon geometry), J_{mn} is the Coulombic coupling between molecular sites m and n, and N is the number of pigments in the complex. Diagonalization of the system Hamiltonian yields the single exciton eigenvectors

$$|a\rangle = \sum_{m=1}^{N} \phi_{am} |m\rangle \tag{8.3}$$

where the indices m and n (a, b, c, and d) are reserved for the local (exciton) bases throughout this chapter. Alternatively, if the Coulombic couplings are sufficiently weak, the system Hamiltonian can be written as

$$H_{Sys}^{loc} = \sum_{m=1}^{N} E_m B_m^{\dagger} B_m \tag{8.4}$$

When H_{Sys}^{loc} is utilized, energy transport occurs by way of the Förster mechanism and the fields applied in spectroscopic experiments interact with individual chromophores. It is worth noting that certain optical nonlinearities allowed in a system described by H_{Sys}^{ex} are forbidden with H_{Sys}^{loc} (c.f., Figure 8.3 in Reference [48]), which is potentially useful in detailed investigations of electronic structure.

Constraints must be imposed to minimize the number of adjustable parameters in this model because of the large number of pigments in RPE. With inspiration from the work of Gaigalas et al,[42] only three (physically motivated) energy gap parameters are used. All PUB pigments are taken to possess the same value of E_m, whereas the two remaining energy gap parameters are reserved for the inner and outer PEB pigments. The inter-pigment

interactions, J_{mn}, in H_{Sys}^{ex} are computed as couplings between transition dipoles. Locations of the dipoles are generated using the centers of mass of each pigment. The dipole orientations for each of the 5 unique pigments in RPE are obtained using electronic structure calculations conducted at the B3LYP/6-31G level. It is well-established that bath-induced fluctuations in the system's energy levels suppress the delocalization of excitons between sites with small transition dipole couplings (i.e., small compared to the fluctuation amplitude). To capture this effect, all $|J_{mn}|$<38 cm^{-1} are set equal to zero to obtain realistic exciton sizes and reorganization energies. Similarly motivated approaches have been used to parameterize the Hamiltonians of other photosynthetic complexes.[59] This threshold for treating intermolecular couplings is not equivalent to sampling over Gaussian distributions in site energies. The correlation functions introduced in the following Section encode all information about bath-induced fluctuations in the site energies. A single set of exciton eigenvectors (Equation (8.3)), obtained with the thermally averaged system Hamiltonian, is used to transform these correlation functions from the local to exciton basis.

8.2.2. Spectral Densities

The spectral density utilized in this work incorporates nuclear modes subject to two limiting cases of the Brownian oscillator (BO) model.[60] Solvation effects and low-frequency intramolecular motion are modeled by coupling a single overdamped BO mode to each pigment site. The spectral density of the bath in the overdamped BO model is given by[60]

$$C_m^{OD}(\omega) = 2\lambda_m \frac{\omega\Lambda_m}{\omega^2 + \Lambda_m^2} \tag{8.5}$$

where Λ_m^{-1} and λ_m are respectively the time scale and magnitude of fluctuations in the site energy E_m. Higher-frequency underdamped intramolecular modes are taken into account with the spectral density[60]

$$C_m^{UD}(\omega) = \sum_j S_{j,m}\omega_{j,m}^2\left[\delta(\omega-\omega_j)+\delta(\omega+\omega_j)\right] \tag{8.6}$$

where $S_{j,m}$ and $\omega_j S_{j,m}$ are respectively the Huang-Rhys factor and reorganization energy of mode j. The total spectral density at pigment site m is the sum of these two contributions

$$C_m(\omega) = C_m^{OD}(\omega) + C_m^{UD}(\omega) \tag{8.7}$$

With the total spectral density in hand, the line broadening function can be computed in the local basis using[60]

$$g_m(t) = \frac{1}{2\pi}\int_{-\infty}^{\infty} d\omega \frac{1-\cos(\omega t)}{\omega^2}\coth(\beta\hbar\omega/2)C_m(\omega) + \frac{i}{2\pi}\int_{-\infty}^{\infty} d\omega \frac{\sin(\omega t)-\omega t}{\omega^2}C_m(\omega) \tag{8.8}$$

Assuming that each site possesses an uncorrelated bath, the transformation of the local line broadening functions into the single exciton basis is written as

$$g_{abcd}(t) = \sum_{m=1}^{N}\phi_{am}\phi_{bm}\phi_{cm}\phi_{dm}g_m(t) \tag{8.9}$$

where the single exciton eigenvectors are defined in Equation (8.3).

Equation (8.8) makes clear that $C_m^{OD}(\omega)$ and $C_m^{UD}(\omega)$ influence the optical response and exciton transport in different ways. For systems in solution at room temperature, the spectral densities associated with the overdamped modes possess significant amplitudes at frequencies lower than k_BT because the magnitudes of fluctuations, λ_m, are generally large compared to the relaxation rates, Λ_m. Consequently, the overdamped modes broaden spectroscopic line widths in addition to exchanging energy with the system in non-radiative

electronic relaxation processes. By contrast, the underdamped intramolecular modes in the present model contribute little to the real part of $g_m(t)$ because their frequencies are larger than k_BT (i.e., frequencies ≥ 380 cm^{-1} here). Therefore, while our $C_m^{UD}(\omega)$ has only a minor impact on spectroscopic line broadening, its contribution to the imaginary part of $g_m(t)$ gives rise to a realistic Franck-Condon progression in the calculated absorption spectrum. Moreover, when the Frenkel exciton Hamiltonian, H_{Sys}^{ex}, is employed, the higher frequency modes in $C_m^{UD}(\omega)$ can significantly enhance the rates of electronic relaxation processes in which the frequencies of the modes closely match the energy gaps between exciton states. Such vibronic relaxation channels are analogous to promoting mode-assisted internal conversion processes.[61,62]

8.2.3. Linear absorption

Sections 8.2.1 and 8.2.2 establish all quantities needed to simulate the optical response. The linear absorption spectrum corresponding to H_{Sys}^{ex} is given by

$$\sigma_A^{ex}(\omega) = \sum_{a=1}^{N} \left|\vec{\mu}_a\right|^2 \int_0^\infty dt \exp\left[i(\omega-\omega_a)t - g_{aaaa}(t)\right] \tag{8.10}$$

where $\hbar\omega_a$ are the energy eigenvalues of H_{Sys}^{ex} and the transition dipoles are transformed from the local to exciton basis using

$$\vec{\mu}_a = \sum_{m=1}^{N} \phi_{am}\vec{\mu}_m \tag{8.11}$$

Similarly, the absorption spectrum associated with H_{Sys}^{loc} is computed with

$$\sigma_A^{loc}(\omega) = \sum_{m=1}^{N} \left|\vec{\mu}_m\right|^2 \int_0^\infty dt \exp\left[i(\omega-\omega_m)t - g_m(t)\right] \tag{8.12}$$

where $\omega_m = E_m / \hbar$ and $g_m(t)$ is defined in Equation (8.8). The transient grating and photon echo experiments applied below can also, in principle, be simulated using the same model Hamiltonians. These nonlinear optical experiments are not modeled here because the desired information is readily extracted by fitting the signals to simple phenomenological equations (i.e., sum of exponentials).

8.2.4. Electronic relaxation

As mentioned above, the choice of system Hamiltonian, H_{Sys}^{ex} or H_{Sys}^{loc}, governs the electronic relaxation mechanism. When H_{Sys}^{ex} is employed, the MRT rate constant corresponding to a transition initiating in exciton a and terminating in exciton b is computed using[2,33]

$$K_{ba} = 2\,\mathrm{Re}\int_0^\infty dt F_{ba}(t)\exp\left[-i(\omega_b-\omega_a)t - g_{bbbb}(t) - g_{aaaa}^{*}(t) + 2\left\{g_{bbaa}(t) + i(\lambda_{bbaa}-\lambda_{aaaa})t\right\}\right] \tag{8.13}$$

where

$$F_{ba}(t) = \left[\ddot{g}_{baab}(t) - \left\{\dot{g}_{abaa}(t) - \dot{g}_{abbb}(t) + 2i\lambda_{abaa}\right\}\left\{\dot{g}_{aaba}(t) - \dot{g}_{bbba}(t) + 2i\lambda_{baaa}\right\}\right] \tag{8.14}$$

Alternatively, when H_{Sys}^{loc} is used, the Förster rate constant associated with energy transfer from pigment m to pigment n is calculated with

$$K_{nm} = 2\pi \frac{J_{mn}^2 W_{mn}}{\hbar} \tag{8.15}$$

where J_{mn} is a transition dipole coupling and W_{mn} quantifies the overlap between the fluorescence and absorbance spectra at sites m and n, respectively. This spectral overlap factor is given by

$$W_{mn} = \frac{\mathrm{Re}\int_0^\infty dt \exp\left[-i\left(\omega_n - \omega_m + 2\lambda_m\right)t - g_n\left(t\right) - g_m^*\left(t\right)\right]}{\left\{\mathrm{Re}\int_0^\infty dt \exp\left[-i\omega_n t - g_n\left(t\right)\right]\right\}\left\{\mathrm{Re}\int_0^\infty dt \exp\left[-i\omega_m t + i2\lambda_m t - g_m^*\left(t\right)\right]\right\}} \tag{8.16}$$

The rate constants, K_{ba} or K_{nm}, parameterize a master equation for population transfer dynamics

$$\frac{d}{dt}\rho_{ij}\left(t\right) = -\sum_{i\neq j} K_{ji}\rho_{ii}\left(t\right) + \sum_{j\neq i} K_{ij}\rho_{jj}\left(t\right) \tag{8.17}$$

A principal advantage to MRT is its ability to interpolate between the limits of weak (traditional Redfield) and strong (Förster) system-bath interactions. MRT also captures rate enhancements involving the exchange of multiple vibrational excitation quanta with the bath, whereas traditional Redfield theory accounts only for transitions through vibronic channels in which the initial and final phonon states differ by single excitation quanta.[34] One potential drawback to MRT is its use of the secular approximation, which breaks down when population transfer and electronic dephasing occur on similar time scales. In these cases, couplings between populations and coherences can give rise to non-secular transitions with significant implications for light harvesting efficiencies.[10] Because K_{ba} is time-independent, MRT also misses local nuclear reorganization processes, which are capable of preserving electronic coherences on short time-scales.[14,15] It is always, of course, important to choose the appropriate dynamical model for the system under consideration. MRT is well-suited for RPE because its energy transport dynamics are >500 fs.

8.3. EXPERIMENTAL METHODS

RPE isolated from red algae was purchased from Prozyme as a suspension in 60% ammonium sulfate. Pulsed laser spectroscopies used solutions of RPE in 50 mM potassium phosphate buffer at pH 7.0. All experiments were performed within one week of solution

preparation. Solutions were circulated at a rate of 4 mL/s using a peristaltic pump with reservoir of 10 mL. The flow rate was set at the maximum value for which turbulence in the flow cell did not appreciably degrade the signal-to-noise ratio. In 0.5 mm path length, the absorbance of the RPE solution was 0.25 at 17700 cm^{-1}. Absorbance spectra were measured before and after all experiments to confirm the absence of sample degradation.

Transient grating (TG) experiments utilize a diffractive optic-based interferometer described elsewhere.[63] The measurements are conducted in either a one-color or two-color configuration with the phase matching geometry, $\mathbf{k}_S = -\mathbf{k}_1 + \mathbf{k}_2 + \mathbf{k}_3$. In the one-color configuration, a single home-built noncollinear optical parametric amplifier (NOPA) supplies the three applied fields (E_1, E_2, and E_3) that induce the nonlinear polarization in addition to the laser pulse used for interferometric signal detection, E_4. One-color experiments employ the three carrier frequencies: 17700, 18870, or 20400 cm^{-1}. In all cases, the four pulses are compressed to approximately 20 fs. Anisotropy measurements acquire the ZZZZ and ZZXX tensor elements in successive experiments. The total data acquisition time associated with the measurement of both tensor elements is 45 minutes. Each tensor element represents the average of 12 scans of the delay stage. Figure 8.2 defines the experimentally controlled delay, T, varied in TG (τ =0 in the TG technique).

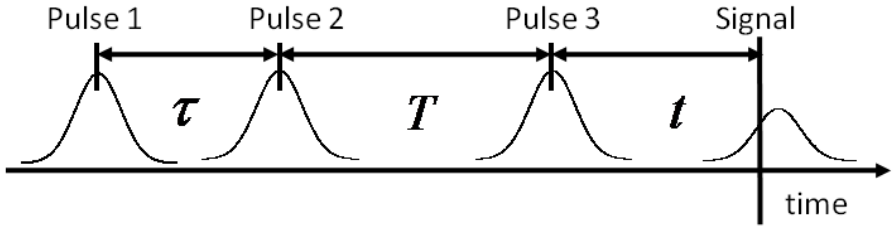

Figure 8.2. Pulse sequence used for TG and PE spectroscopies. The delays, τ and T, are experimentally controlled. TG and PE signals are radiated in the emission time, t.

The present two-color TG experiments are performed in a configuration identical to that described in Reference [48]. Briefly, the $E_1 \& E_2$ "pump" and $E_3 \& E_4$ "probe" pulses are derived from separate NOPAs.[64-66] The pump pulses, which have 20 fs durations, are applied with frequencies of 17700, 18850, or 20400 cm^{-1}. The spectra of the $E_3 \& E_4$ "probe" pulses span the full 13300-19000 cm^{-1} range. Because we are unable to compensate for dispersion over this broad spectral range, the frequency-dependent time overlap of E_3 with the compressed $E_1 \& E_2$ pulse-pair is taken into account numerically as described in Reference [49]. The dependence of "time-zero" on the signal emission frequency is corrected using TG signals measured in the transparent buffer solution as a reference. A full-width half maximum instrument response of <60 fs is obtained at signal emission frequencies in the 15890-17890 cm^{-1} range using a prism compressor configured to minimize dispersion at 16890 cm^{-1}.

Three separate one-color photon echo (PE) experiments are conducted with 20fs pulses at frequencies of 17700, 18850, or 20400 cm^{-1}. As described in Reference [67], the times at which the E_1 and E_2 pulses arrive at the sample are varied by inserting independent prism wedges in the beam paths, whereas a conventional optical delay line controls the arrival of the E_3 and E_4 pulses. The E_3 and E_4 pulses pass through an identical pair of prism wedges to ensure that all four pulses possess the same dispersion. The delay between E_1 and E_2, τ, is varied from -150 fs to 150 fs (c.f., Figure 8.2). Rephasing and non-rephasing PE signals are superposed to obtain absorptive spectra.[68,69] Scans of photon echo

spectra at a series of population times are repeated 5 times and averaged for a total data acquisition time of 5 hours.

The laser fluence used in TG and PE experiments is approximately 1×10^{14} photons/cm^2. Increasing or decreasing the pulse energies by a factor of two has no effect on the measured dynamics. Neither bleaching nor degradation of the samples are observed when the solutions are flowed at 4 mL/s. In all experiments, signals are detected by spectral interferometry using a back-illuminated CCD array (Princeton Instruments PIXIS 100B) mounted on a 0.3 meter spectrograph. Integration times are 100-200 ms. Signals are processed using a Fourier transform algorithm.[67,69-72]

8.4. RESULTS AND DISCUSSION

8.4.1. Parameterization of the Hamiltonian by Fitting of the Linear Absorption Spectrum

The linear absorption spectra shown in Figures 8.3a and 8.3b are fit using the H_{Sys}^{ex} and H_{Sys}^{loc} system Hamiltonians, respectively. The calculated spectra are decomposed into contributions from the three types of pigments (PUB, inner and outer PEB), where the same color code is employed in Figure 8.1c. Our calculated spectra resemble those reported by Gaigalas et al, whose view of electronic structure motivated the present parameterization scheme.[42] The parameters found with both the localized and delocalized basis sets generally give similar insights (c.f., Tables 8.1 and 8.2). In both models, the outer and inner PEB respectively possess the largest and smallest reorganization energies, λ_m; the site energies, E_m, differ by less than 100cm^{-1}; the PUB possess the smallest Huang-Rhys factors. One notable difference between models is that Huang-Rhys factors of all modes must be larger in

the exciton basis to compensate for line narrowing caused by exciton delocalization (i.e., exchange narrowing); the same is true for the λ_m associated with the PUB and inner PEB.

Attainment of realistic line shapes (i.e., skewed towards high frequencies) requires incorporation of the Franck-Condon progressions in the intramolecular modes. Resonance Raman spectra of RPE reveal a number of coupled vibrations in the fingerprint region, where the most intense transitions are found at 445, 957, 1271, and 1597 cm^{-1}.[73] It is not possible to constrain Huang-Rhys factors, $S_{j,m}$ in Equation (8.6), for modes with closely spaced frequencies because the individual vibronic transitions are unresolved due to broad line widths. Instead, five effective modes spanning the fingerprint frequency range are incorporated.

The transition dipole magnitudes reported in Tables 8.1 and 8.2 are adjustable, but kept near 11 Debye as determined in earlier investigations of other phycobiliproteins.[37-39] The transition dipole coupling with the largest magnitude (-99 cm^{-1}) is found between inner PEB pigments located on the adjacent α and β subunits (α82 and β82). Particularly because RPE is a symmetric system, the calculated exciton sizes become unrealistically large if all inter-pigment couplings, J_{mn}, are incorporated. As discussed in Section 8.2.1, the present model addresses this issue by including only off-diagonal elements, $|J_{mn}|$>38 cm^{-1}, in the Hamiltonian. Physically reasonable parameters are found at this threshold. By contrast, if all J_{mn} are included, site reorganization energies, λ_m, in excess of 2000 cm^{-1} are needed to fit the linear absorbance spectrum because of significant exchange narrowing (i.e., the line widths decrease as the exciton sizes increase). Reorganization energies similar to those reported here have been found in the phycobiliproteins, allophycocyanin and c-phycocyanin.[50]

To quantify the exciton sizes when the H_{Sys}^{ex} system Hamiltonian is employed, participation ratios are computed using

$$PR_a = \frac{1}{\sum_{m=1}^{N} \phi_{am}^4} \tag{8.18}$$

The PR_a calculated for all exciton states are displayed in Figure 8.4. The PR_a associated with all 12 inner PEB exciton states are near 2. These excitons delocalize primarily between pairs of inner PEB pigments located on adjacent α and β subunits (α82 and β82). Of the 12 outer PEB excitons, six are almost fully localized to the α139 PEB pigments (PR_a are close to 1) because these chromophores interact weakly with other PEBs; the other six delocalize between β158 PEB pigments bound to separate trimers (e.g., pigments 21 and 23 in Figure 8.1c). Finally, the 6 PUB excitons also possess PR_a close to 2. For this set of excitons, delocalization also occurs primarily between pairs of PUB pigments located in separate trimers (e.g., pigments 25 and 30 in Figure 8.1c).

8.4.2. Probing Electronic and Nuclear Relaxation With Transient Grating Spectroscopy

With guidance from the decomposition of the total absorption spectrum presented in Figure 8.3, TG experiments are performed with excitation frequencies (ω_1 and ω_2) tuned into resonance with the PUB in addition to both the outer and inner PEB. In these three configurations, the state of the system at T=0 is fairly well-defined. Of course, photoexcitation initiates both electronic and nuclear relaxation processes, which must be distinguished in the measurements. Based on comparisons to related photosynthetic pigment complexes, relaxation in nuclear coordinates (i.e., solvation) is expected to occur on the sub-picosecond time scale.[74,75] By contrast, electronic relaxation spans a broad range of time

scales depending on the proximity of the initial and final states involved in a particular transition. Here we focus on the relatively fast dynamics associated with pigments possessing short intermolecular distances.

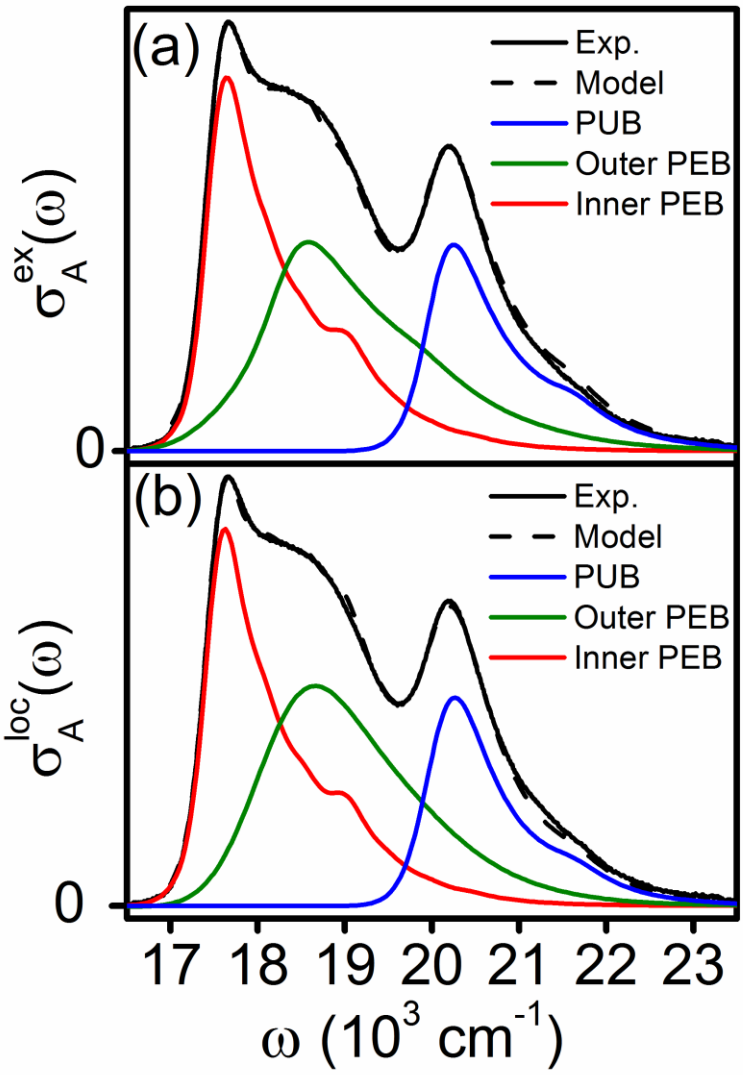

Figure 8.3. Linear absorption spectra calculated using (a) Equation (8.10) and (b) Equation (8.12) are overlaid on measured spectra of RPE (solid black). The calculated spectra are separated into contributions from each of the three classes of pigments discussed in Section 8.2.1, where the same color code is employed in Figure 8.1. This decomposition is achieved by restricting the summations in Equations (8.10) and (8.12) to only the states of interest. In order of increasing energy, the red line represents states 1-12; green is 13-24; blue is 25-30.

TG experiments conducted with color tunable excitation pulses and broadband probing pulses covering the spectral range associated with the inner and outer PEB are presented in Figure 8.5. These signals provide three key pieces of information: (i) significant red-shifting in the signal spectra occurs when the PUB and outer PEB states are photoexcited; (ii) most of the red-shifting in the signal spectra is complete by T =1 ps; (iii) essentially no evolution in the signal spectrum is observed when the inner PEB states are photoexcited. Together, these three observations suggest that rapid electronic relaxation must play a role in the sub-ps dynamics. Of course, red-shifting in the signal spectra is also a signature of nuclear relaxation. However, if only nuclear relaxation is at the root of the dynamics, a larger spectral shift should be found when the inner PEB are photoexcited. A large discrepancy in the Stokes-shifts of the various pigments is not expected because the line widths shown in Figure 8.3 are similar.[60]

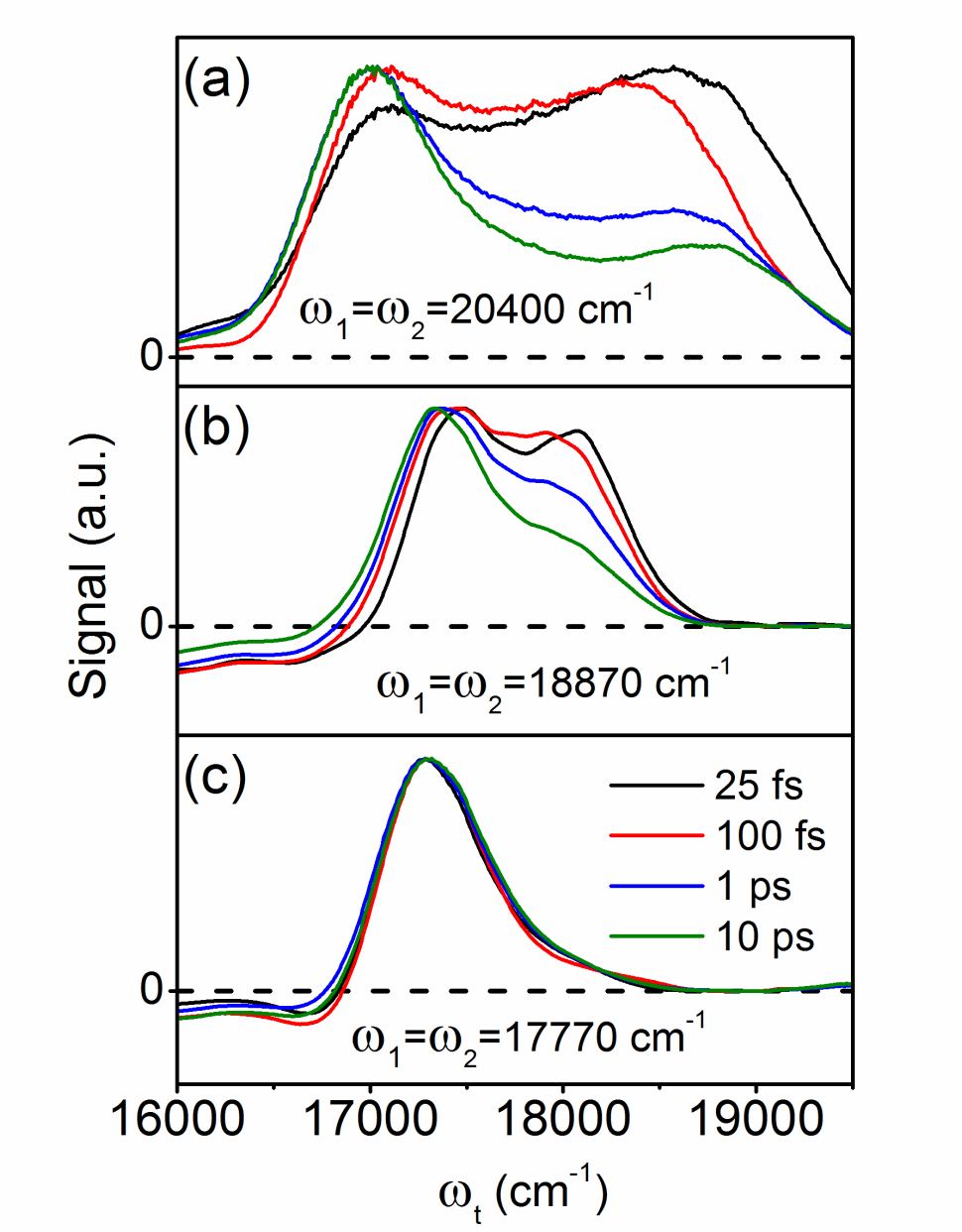

Figure 8.5. Real part of transient grating signal field acquired with excitation at the "pump" frequency $\omega_1 = \omega_2$ (i.e., carrier frequency of E_1 and E_2) indicated in the respective panel. In all panels, the pulse delay, T, is color-coded as: T =25fs (black) ; T =100fs (red); T =1ps (blue); T =10ps (green). Signals with a positive and negative signs respectively correspond to an increase and decrease in transmission of a probe pulse in a conventional transient absorption experiment.

In Figure 8.6, dynamics in the TG signal spectra are examined with the higher time resolution achieved in one-color laser pulse configurations. Because the signal spectra are

not always well-fit using Gaussian functions, the signal emission frequencies are quantified using

$$\Omega_s(T) = \frac{\int_{-\infty}^{\infty} \omega_t \left| E_s(\omega_t, T) \right| d\omega_t}{\int_{-\infty}^{\infty} \left| E_s(\omega_t, T) \right| d\omega_t} \tag{8.19}$$

Interestingly, the sub-150fs dynamics mirror the slower processes studied in Figure 8.5. Again, significant red-shifting is found only when the PUB and outer PEB are photoexcited, which points to contributions from electronic relaxation. We suggest that these red-shifts in the signal spectra may, in part, reflect rapid exciton localization driven by solvation processes (i.e., exciton self-trapping). That is, while the equivalent site energies promote exciton delocalization at the ground state equilibrium geometry, rapid excited state solvation may break these degeneracies, thereby localizing the wavefunctions. Interestingly, a slight blue-shift is even found using laser pulses resonant with the inner PEB. It is tempting to assign this blue-shift to energetically uphill exciton transport and/or equilibration of electronic population within the manifold of inner PEB exciton states. However, Figure 8.5 shows that excited state absorption occurs ω_t <16700 cm^{-1}. Therefore, it is also possible that interferences between optical nonlinearities (e.g., excited state emission and excited state absorption) contribute to the dynamics in the signal spectra in the frequency range corresponding to the inner PEB.

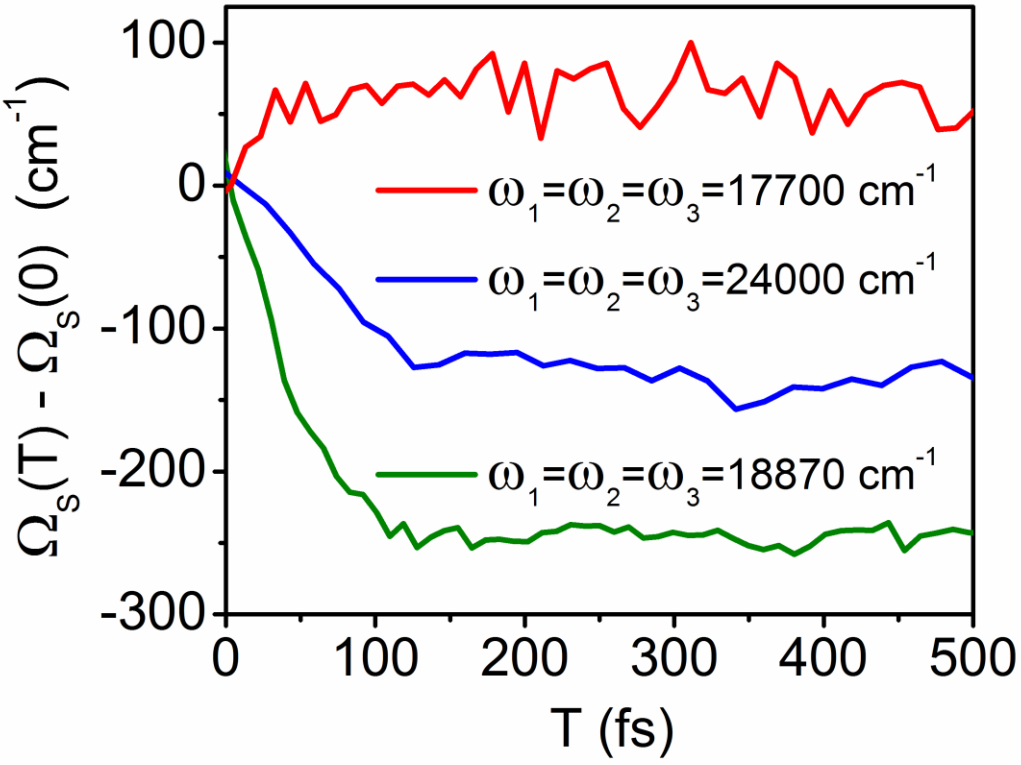

Figure 8.6. Evolution of TG signal frequency obtained in one-color experiments employing 20 fs laser pulses at the carrier frequencies indicated in the figure legend. The signal frequency is calculated using Equation (8.19).

Anisotropies are measured in one-color laser pulse configurations to isolate energy transport dynamics. The real parts of the measured TG signals, $S_{ZZZZ}(T)$ and $S_{ZZXX}(T)$, are used to generate the anisotropies, $r(T)$, using

$$r(T) = \frac{S_{ZZZZ}(T) - S_{ZZXX}(T)}{S_{ZZZZ}(T) + 2S_{ZZXX}(T)} \tag{8.20}$$

In this notation, the $S_{ZZZZ}(T)$ tensor element involves all-parallel electric fields, whereas in $S_{ZZXX}(T)$ the E_1 and E_2 fields have polarizations orthogonal to E_3 and the signal pulse. The anisotropies shown in Figure 8.7 are obtained with laser pulses tuned into resonance

with the PUB, outer PEB, and inner PEB pigment states. Although signatures of ~100 fs electronic relaxation are observed in Figure 8.6, we do not detect similar temporal components in the anisotropy, possibly due to the limited sensitivity associated with sequential (rather than simultaneous) measurements of $S_{ZZZZ}(T)$ and $S_{ZZXX}(T)$. The initial value of the anisotropy (~0.4) found with excitation of the PUB states is consistent with localized electronic states in a two-level system. The decrease in the initial values of the anisotropies measured at lower frequencies may reflect increasing contributions from the inner PEB excitons, whose wavefunction delocalization is most robust because of large coupling strengths, J_{mn}=-99 cm^{-1}. We have discussed, for example, how particular terms in the ground state bleach nonlinearities influence the initial value of the anisotropy in c-phycocyanin, which is also less than 0.4.[48] Finally, although the signs of signals correspond to a net "bleach", we remark that the anisotropies should be interpreted with caution because interferences with excited state absorption nonlinearities may have a significant influence. Therefore, the main conclusion drawn here is that the time constants given in Table 8.3 most certainly reflect energy transport.

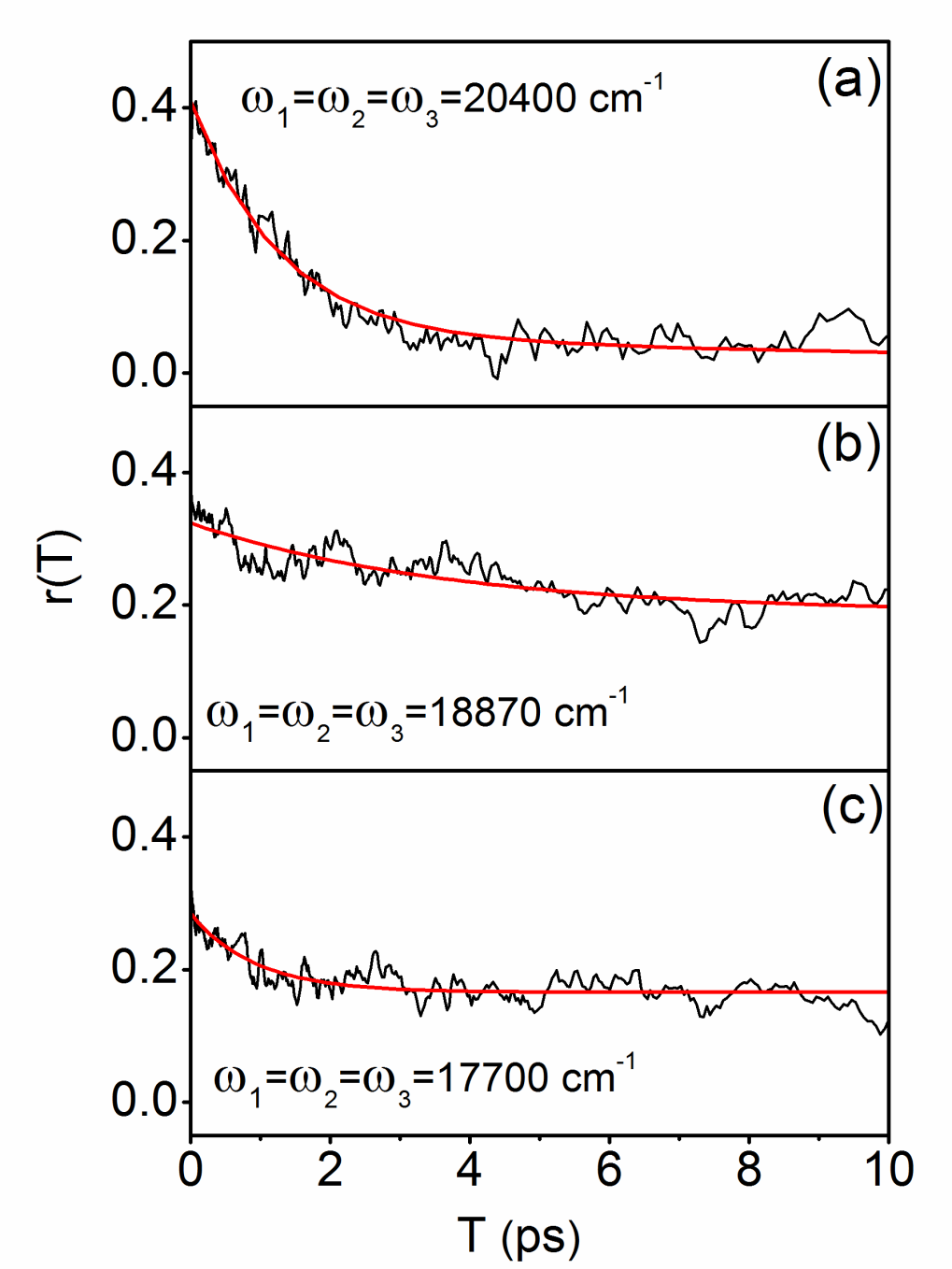

Figure 8.7. Anisotropy computed with the real part of measured transient grating signals using Equation (8.20). Experiments are conducted in a one-color configuration, where the carrier frequencies are given in the figure legend. Fitting parameters used to generate the red lines are presented in Table 8.3.

In summary, the measurements presented in this Section reveal electronic and nuclear relaxation processes taking place on time scales ranging from less than 100fs to several

picoseconds. TG experiments find a red-shift in the signal spectrum only with photoexcitation of the PUB and outer PEB pigments. We suggest that these dynamics in the spectra, in part, reflect electronic relaxation processes because the fastest energetically "downhill" transitions originate in the PUB and outer PEB exciton states, whereas transitions initiating in the inner PEB states are necessarily slower because of detailed balance. Anisotropies in the TG signals make clear that energy transport proceeds on the picosecond time scale following excitation of all three classes of pigments. To be consistent with the interpretation of the signals presented in Figures 8.5 and 8.6, we suggest that photoexcitation of the inner PEB primarily promotes electronic transitions within the manifold of inner PEB exciton states. That is, a non-Boltzmann distribution of electronic populations in the inner PEB states is present at $T=0$ because the distribution is dominated by the excited states possessing the largest transition dipoles. In this interpretation, the dynamics in the anisotropy shown in Figure 8.7c are governed by the equilibration of population within this manifold of inner PEB states, which in turn only weakly influences the signal frequency.

8.4.3. Photon Echo Signatures of Ultrafast Solvation

PE spectroscopy has clear utility in photosynthetic complexes and molecular aggregates where individual transitions are well-resolved in linear absorption spectra.[76,77] Exciton correlations are then readily derived from two-dimensional spectra through the dynamics of cross-peaks. Although the broad line shapes found in room temperature systems tend to obscure information content, it has been demonstrated that coherent dynamics in some complexes can be pinpointed by careful analysis of the line shapes, amplitudes, and phases of two-dimensional spectra.[11,78] Ideally, we would investigate RPE with a laser spectrum covering all three peaks in the linear absorbance spectrum. However, this is

presently not possible because of technical limitations. Therefore, the dynamics in the PE line shapes are instead examined at frequencies resonant with the PUB, outer PEB, and inner PEB.

Figure 8.8 presents absorptive PE spectra acquired with laser pulses tuned into resonance with each of the three classes of pigments. Notably, at T =0 the PE spectra do not exhibit elongated line shapes indicative of inhomogeneous line broadening.[69,79] By contrast, we observed elongated PE line shapes in the related systems, allophycocyanin and c-phycocyanin, at short pulse delays.[32,48] One possibility is that rigidity of the RPE hexamer suppresses disorder in the site energies, however, the origin of the line shape in RPE is presently unclear. Experiments conducted with broader laser bandwidths will be needed to resolve homogeneous and inhomogeneous contributions to the line width. While the changes in the PE line shapes at T <100fs are subtle, we find that the ratio in the diagonal, Γ_{diag}, and anti-diagonal, $\Gamma_{anti-diag}$, line widths changes systematically with T. For example, the ratio, $\Gamma_{anti-diag}/\Gamma_{diag}$, rapidly decreases for the PUB, whereas essentially no change in line shape is measured for the outer PEB. The dynamics in the PE line shape of the PUB are likely a signature of solvation dynamics. It is not clear why the ratio, $\Gamma_{anti-diag}/\Gamma_{diag}$, is essentially independent of T for the outer PEB. It may be that the overlapping resonances of the inner and outer PEB obscures the dynamics. Interestingly, the PE measurements associated with the inner PEB reveal more than one full cycle of a coherence with a period of 51 fs (i.e., frequency of 650 cm^{-1}). It is not yet clear how these dynamics should be interpreted. One option is to assign the recurrence to a 617 cm^{-1} nuclear mode observed in Resonance Raman spectra of PEB. However, it would then be difficult to explain why only a single mode would influence dynamics in the PE line shape. Although long-lived electronic coherences

in phycobiliproteins are not unprecedented,[11] the 617 cm^{-1} frequency cannot be justified by any of the energy gaps between electronic states in Table 8.1 (i.e., 890cm^{-1} is the smallest gap).

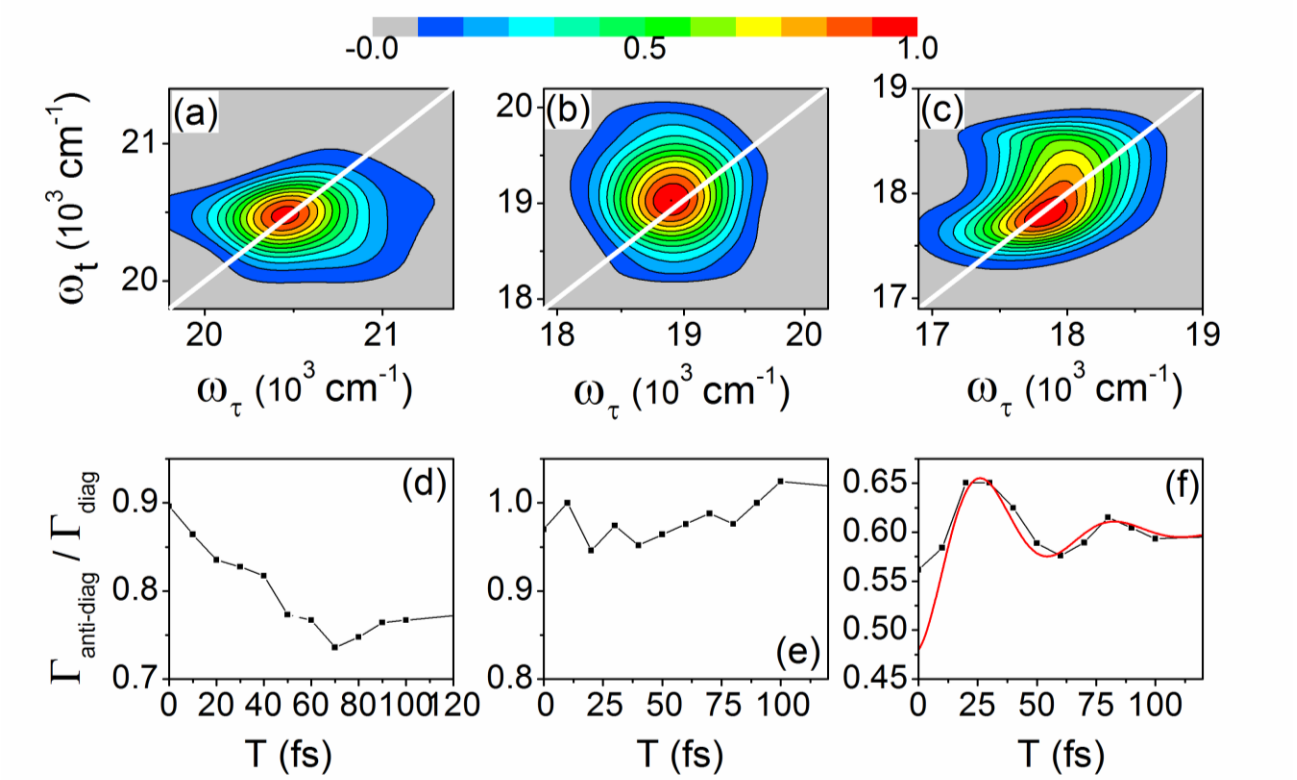

Figure 8.8. The first row displays absorptive PE spectra normalized to 1.0 and plotted on a linear scale. The ratio of the anti-diagonal, $\Gamma_{anti-diag}$, and diagonal, Γ_{diag}, line widths are obtained at various pulse delays, T, and plotted in the second row. Signals corresponding to particular applied field frequencies are given in separate columns: (a),(d) 20400 cm^{-1}; (b),(e) 18870 cm^{-1}; (c),(f) 17700 cm^{-1}. The measurement in panel (f) is fit to an exponentially damped cosine function with a recurrence frequency of 650 cm^{-1} and a (damping) time constant of 35 fs.

8.4.4. Simulations of Electronic Relaxation

MRT and Förster rate constants calculated using the empirical parameters in Tables 8.1 and 8.2 are displayed in Figure 8.9. The largest MRT rate constants involve transport

between excitons within the same class (e.g., PUB, outer PEB, inner PEB), where the fastest transitions connect exciton states delocalized between the same pair of pigments (i.e., excitons in Figure 8.4 with PR_a ~2.0). This behavior should be expected because both energy conservation and the spatial overlap in exciton states govern the magnitude of K_{ba} in Equation (8.13); sensitivity to the spatial overlap of excitons enters through the transformation of line broadening functions given in Equation (8.9). For the interpretation of experiments, it is also important to note that MRT predicts rapid transport from the PUB to PEB excitons (both inner and outer) located in the same region of the hexamer structure. By contrast with MRT, Förster theory finds a smaller distribution in rates. The largest Förster rate constants involve the six inner PEB pigment dimers (i.e., α82 and β82). As in MRT, rapid energy transport is also predicted between the PUB and both types of PEB (inner and outer). Specifically, large Förster rate constants are associated with: (i) the PUB (β50/61) and an outer PEB at the β158 position within the same β subunit; (ii) the PUB (β50/61) and an inner PEB at the β82 position within the same β subunit.

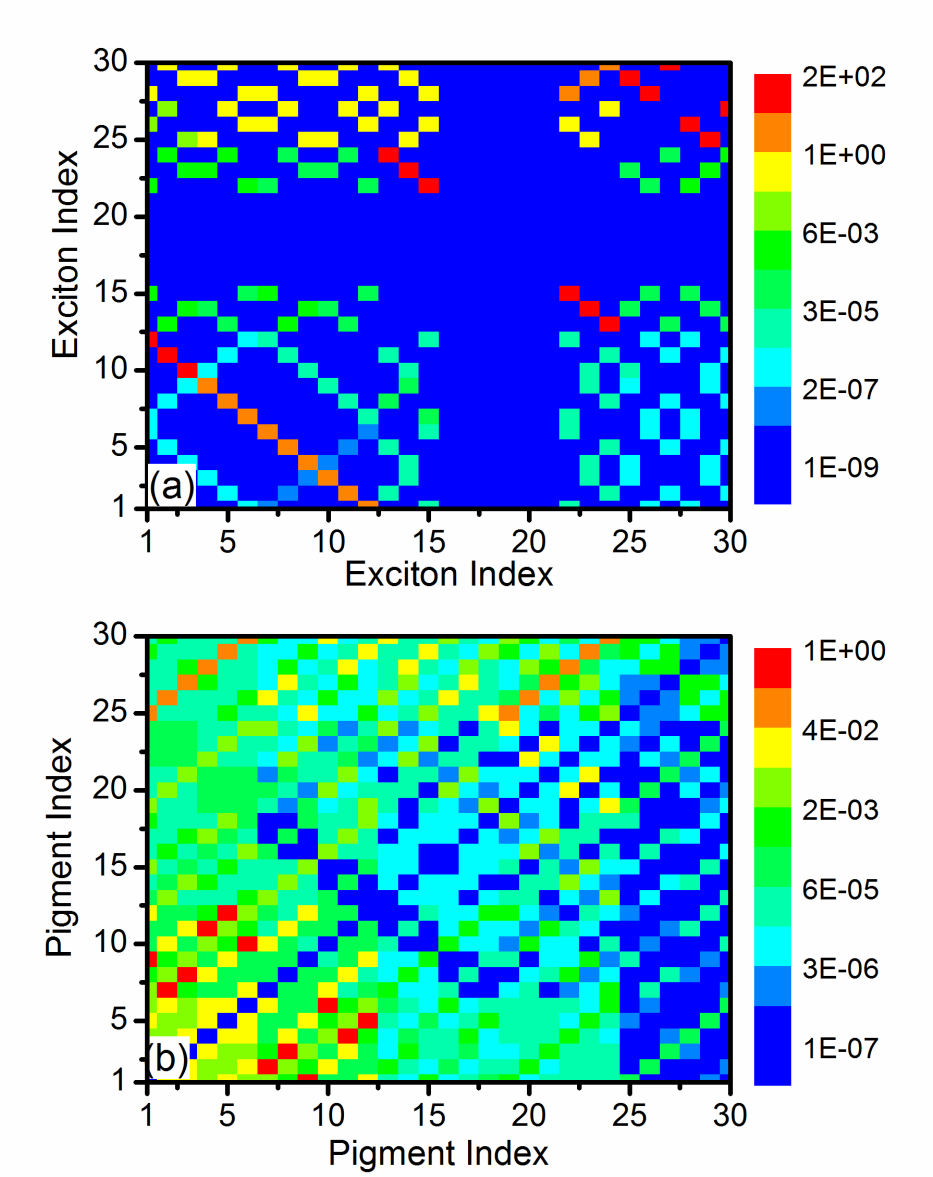

Figure 8.9. (a) Modified Redfield rate constants computed with Equation (8.13). (b) Förster rate constants computed with Equation (8.15). In both panels, the indices are arranged in order of increasing energy: excitons 1-12 are the inner PEB; 13-24 are the outer PEB; 25-30 are the PUB. Both plots utilize a log scale with units of 1/ps. Energetically downhill rate constants are shown above the diagonal.

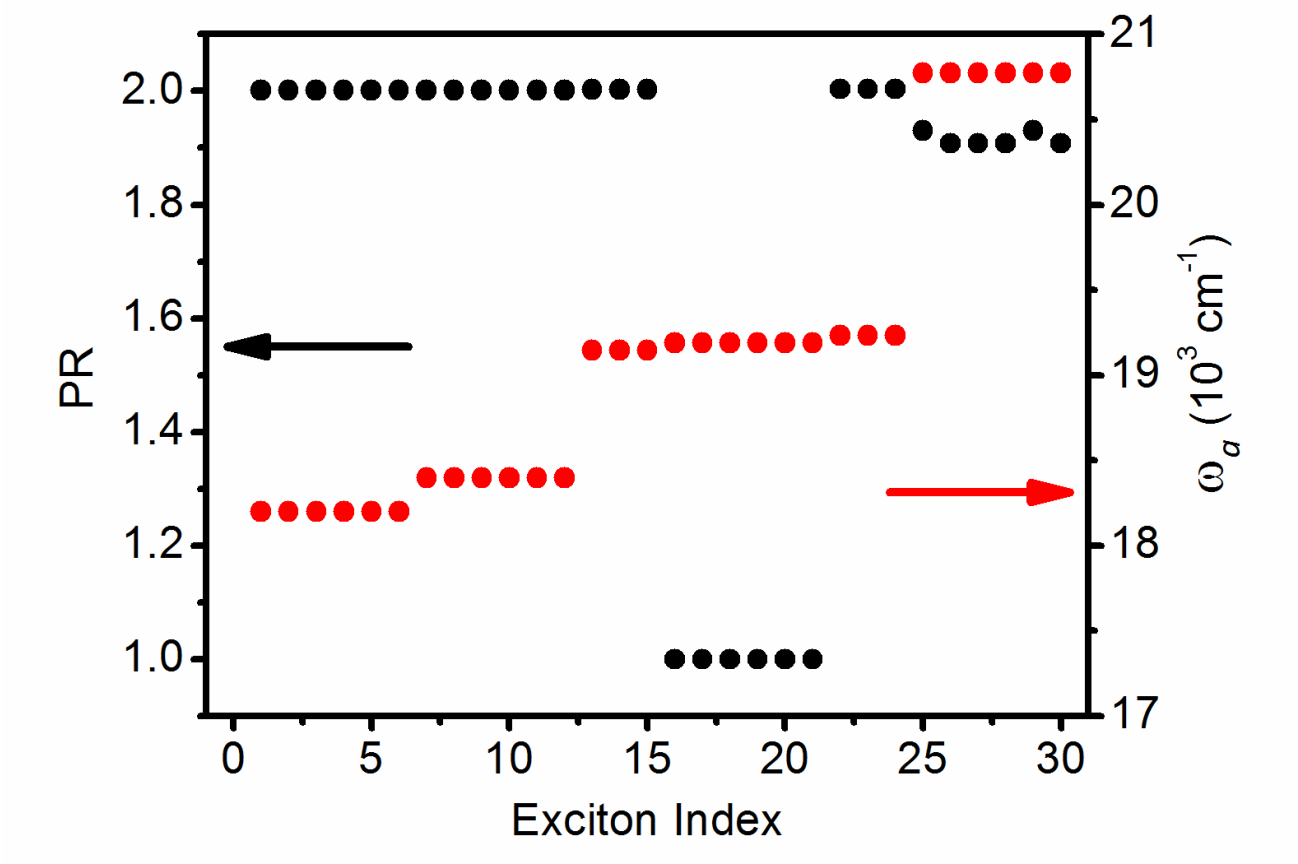

Figure 8.4. Participation ratios (black circles, left) and single exciton transition frequencies (red circles, right) calculated for the 30 exciton states in RPE. Exciton indices 1-12 correspond to the inner PEB; 13-24 are the outer PEB; 25-30 are the PUB.

To aid in the interpretation of complex kinetics, we define the three following quantities sensitive to the flow of population in and out of the three classes of electronic states

$$\rho_{PUB}(T) = \sum_{j=25}^{30} \rho_{jj}(T) \tag{8.21}$$

$$\rho_{PEB}^{Outer}(T) = \sum_{j=13}^{24} \rho_{jj}(T) \tag{8.22}$$

$$\rho_{PEB}^{Inner}(T) = \sum_{j=1}^{12} \rho_{jj}(T) \tag{8.23}$$

Here we write the arguments of the populations as T to be consistent with the "population time" defined in Figure 8.2. Figure 8.10 compares dynamics for the two sets of rate constants, where it is assumed that the six highest energy excited states possess equal populations at T=0. Both MRT and Förster theory predict that $\rho_{PUB}(T)$ decays rapidly due to population flow into both the inner and outer PEB states. MRT yields ~0.8ps dynamics that are roughly 10 times faster than those found with the Förster rate constants. The >10ps dynamics in $\rho_{PEB}^{Inner}(T)$ and $\rho_{PEB}^{Outer}(T)$ obtained with the two models also reflects differences in the electronic structures generated with H_{Sys}^{ex} and H_{Sys}^{loc}; the experiments conducted in this chapter probe faster processes and are unable to distinguish between these two predictions. Although MRT is in better agreement with the 1.26 ps time constant found with photoexcitation of the PUB (c.f., Figure 8.7a), the prediction of Förster theory does not differ substantially from MRT. Therefore, strong conclusions regarding the nature of PUB excited states (i.e., localized versus delocalized) cannot be drawn based on the present experiments and simulations.

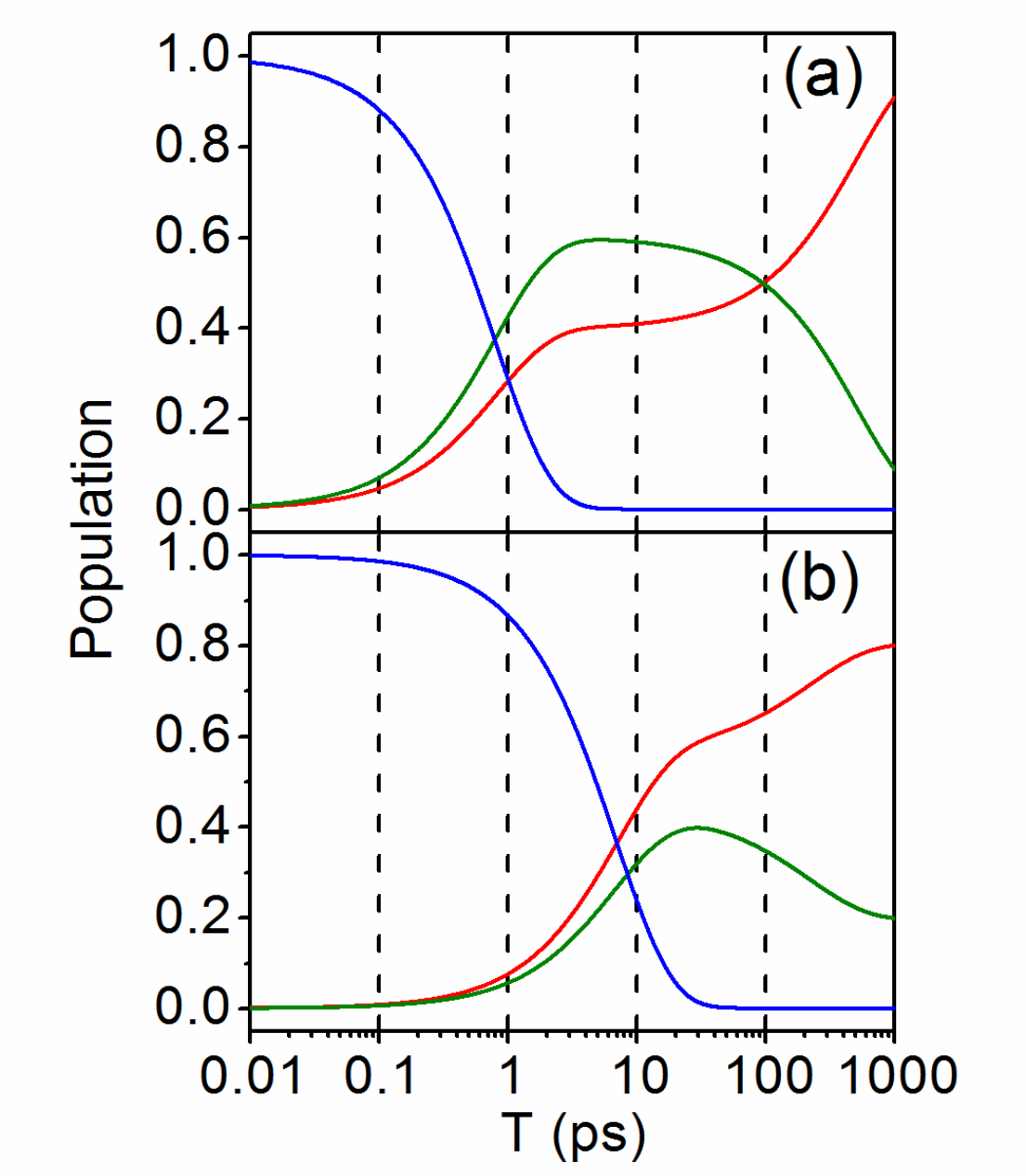

Figure 8.10. Dynamics in $\rho_{PUB}(T)$ (blue), $\rho_{PEB}^{Outer}(T)$ (green), and $\rho_{PEB}^{Inner}(T)$ (red) computed using Equation (8.17) with (a) MRT and (b) Förster rate constants. It is assumed that the six highest energy excited states (i.e., the PUB electronic states) possess equal populations at T =0.

In comparison to energy transport originating in the PUB, the dynamics in $\rho_{PEB}^{Inner}(T)$ and $\rho_{PEB}^{Outer}(T)$ slow down significantly when the outer and inner PEB are initially populated.

Figure 8.11 shows that both MRT and Förster theory predict population flow from the outer to inner PEB on a time scale >100ps. In both models, fairly large distances between the inner and outer PEB pigments, which range from 3.5-10nm, are at the root of these slow kinetics. Weak interactions between pigments, J_{mn}, directly impact the Förster kinetics through the magnitudes of the K_{nm}, whereas these small couplings manifest as poor spatial overlap of excitons in MRT. Figure 8.12 also finds slow (>100ps) energy transport when the inner PEB are initially populated. MRT predicts negligible "energetically uphill" population flow from the inner PEB into the outer PEB, whereas Förster theory finds significant redistribution in the electronic populations. At the origin of the dynamics in the Förster model are the broad absorption line shapes of the outer PEB, which enhance their overlap with the fluorescence spectra of the inner PEB despite the 890cm^{-1} gap in the site energies for these two classes of pigments.

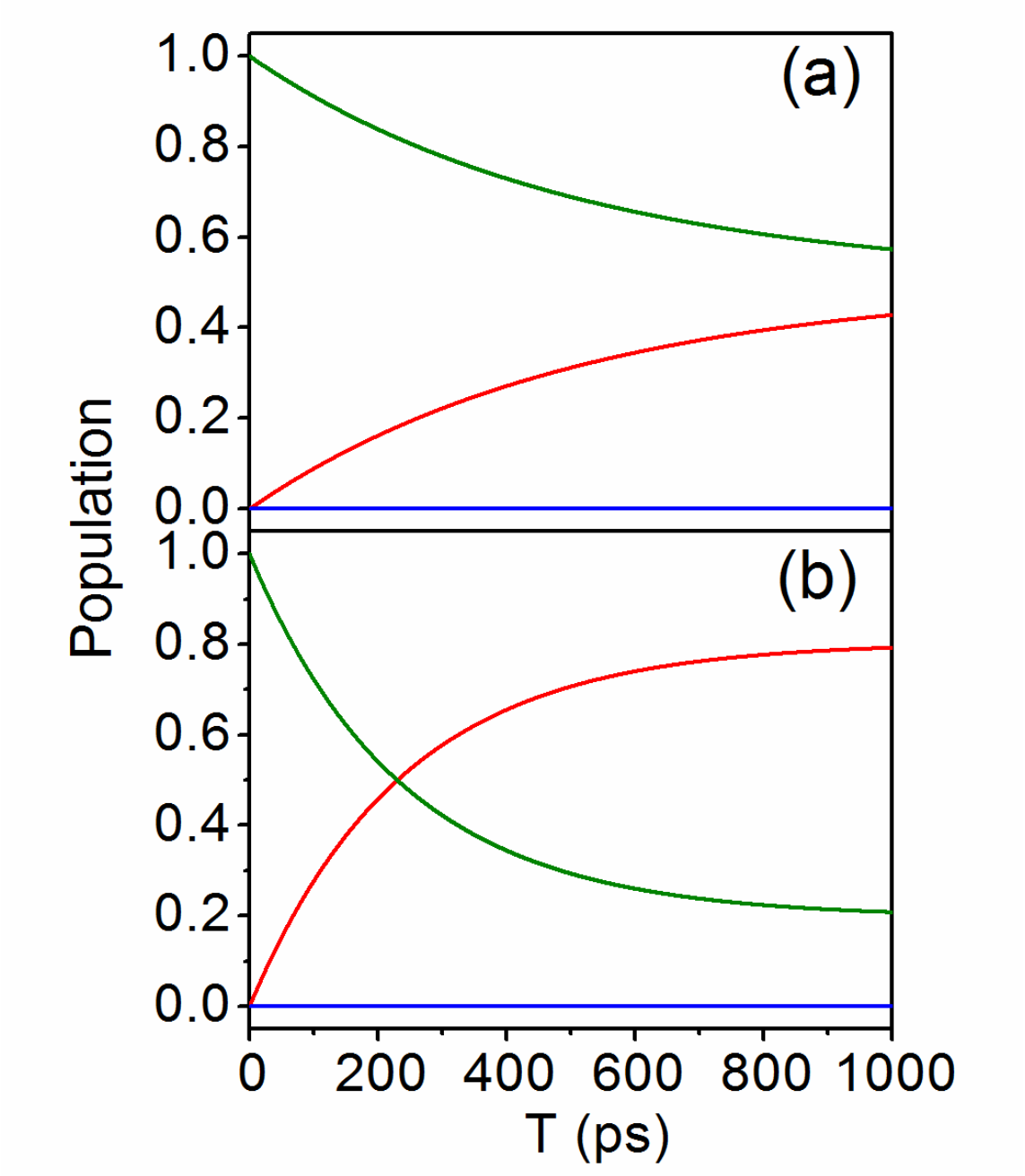

Figure 8.11. Dynamics in $\rho_{PUB}(T)$ (blue), $\rho_{PEB}^{Outer}(T)$ (green), and $\rho_{PEB}^{Inner}(T)$ (red) computed using Equation (8.17) with (a) MRT and (b) Förster rate constants. It is assumed that excited states associated with the outer PEB (i.e., indices 13-24) possess equal populations at T =0.

While Figures 8.11 and 8.12 are useful for understanding kinetics on the 100ps time scale, these data do not explain the much faster relaxation processes apparent in the transient

absorption anisotropies shown in Figure 8.7. Dynamics in the populations of excitons 13 and 22 are examined in Figure 8.13 to pinpoint the origin of these processes. First, it is shown that MRT predicts sub-100fs electronic relaxation involving the 6 outer PEB excitons whose PR_a are near 2.0 (c.f., Figure 8.4). These populations are forced to rapidly equilibrate because the excitons possess different energies (i.e., splitting of 45cm^{-1} between excitons 13-15 and 22-24). Similar physics explains electronic relaxation within the inner PEB manifold of exciton states. Here MRT yields picosecond dynamics in the populations of excitons 1 and 7, where the 197cm^{-1} exciton splitting associated with the inner PEB dimers is the aspect of the system driving rapid transport. Notably, these picosecond dynamics are in good agreement with the time constants found in the anisotropy when 17700cm^{-1} laser pulses are used to excite the inner PEB. By contrast, Förster theory predicts that the >100ps population flow between the outer and inner PEB pigments is faster than transport between PEB pigments of the same class. For this reason, insight into the picosecond dynamics present in the experimental anisotropy decays is not obtained by examination of the populations of individual pigments with Förster theory.

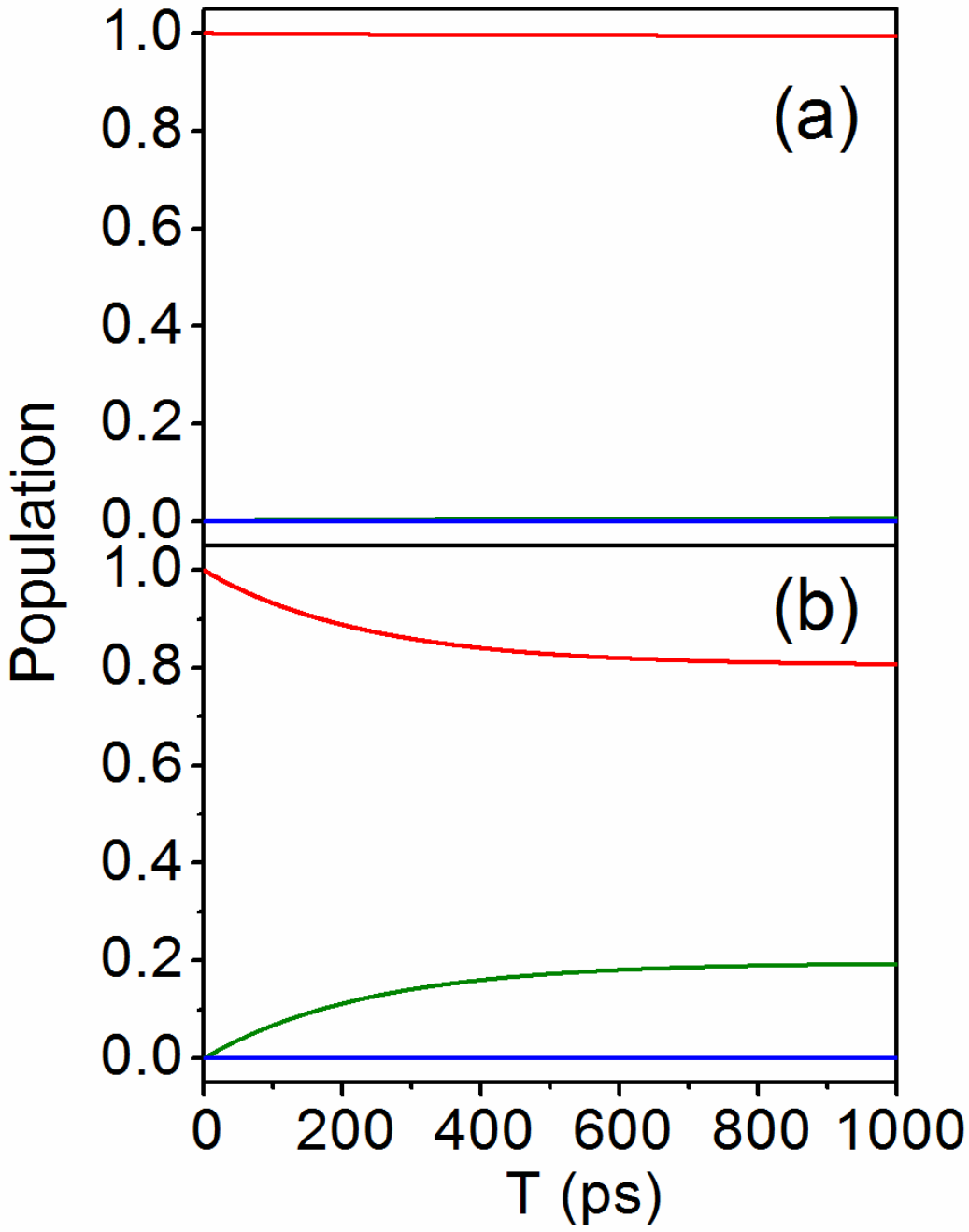

Figure 8.12. Dynamics in $\rho_{PUB}(T)$ (blue), $\rho_{PEB}^{Outer}(T)$ (green), and $\rho_{PEB}^{Inner}(T)$ (red) computed using Equation (8.17) with (a) MRT and (b) Förster rate constants. It is assumed that excited states associated with the inner PEB (i.e., indices 1-12) possess equal populations at T =0.

The calculations presented in this Section address the electronic structures and energy transport mechanisms for all three classes of pigments in RPE. First, MRT predicts ~0.8ps

relaxation in the populations of the PUB, which is roughly 10 times faster than that found with Förster theory. A strong conclusion regarding the most appropriate description of the PUB electronic states cannot be reached based on the present measurements and simulations alone because both models are in reasonable agreement with the 1.26ps time constant obtained from the data Figure 8.7a. Experiments conducted at lower temperatures are one approach to investigating the electronic structure of the PUB states with greater sensitivity; narrower line widths would resolve contributions from particular pigments. Second, MRT predicts sub-ps electronic relaxation within both the outer and inner PEB manifolds of exciton states. This prediction suggests that the decays in the anisotropies obtained with photoexcitation of the inner and outer PEB (c.f., Figures 8.7b and 8.7c) does not originate in energy transport between excitons associated with different classes of pigments. Finally, we remark that caution must be taken in comparing the measurements employing 18870cm^{-1} excitation pulses and the calculated dynamics in the outer PEB. While electronic relaxation involving the outer PEB is certain to contribute to the measured signals, transport involving the inner PEB is also likely to play a role because the vibronic progression of the inner PEB extends beyond 18870cm^{-1}.

8.5. CONCLUSION

In summary, we have investigated the electronic structure and energy transport mechanisms in RPE using femtosecond laser spectroscopies in conjunction with theoretical models employing localized and delocalized basis sets. The linear absorption spectrum of RPE imposes constraints on the parameters of both models, which yield similar insights into the reorganization energies and electronic resonance frequencies of the three classes of pigments found in RPE (i.e., PUB, outer and inner PEB). TG experiments detect electronic

and nuclear relaxation processes occurring on time scales ranging from less than 100fs to 10ps. Transient absorption anisotropies indicate that the fastest energy transport dynamics are close to 1ps. However, sub-100fs evolution in the TG signal spectra suggests that excited state solvation may also drive rapid exciton localization (i.e., exciton self-trapping). PE line shapes of the PUB reflect solvation processes, whereas excitation of the inner PEB reveal a recurrence in an underdamped nuclear mode at 650cm^{-1} (i.e., this is a tentative assignment). The extent of wavefunction delocalization is evaluated by comparing dynamics detected in the time-resolved experiments with simulations conducted using MRT (delocalized) and Förster (localized) models.

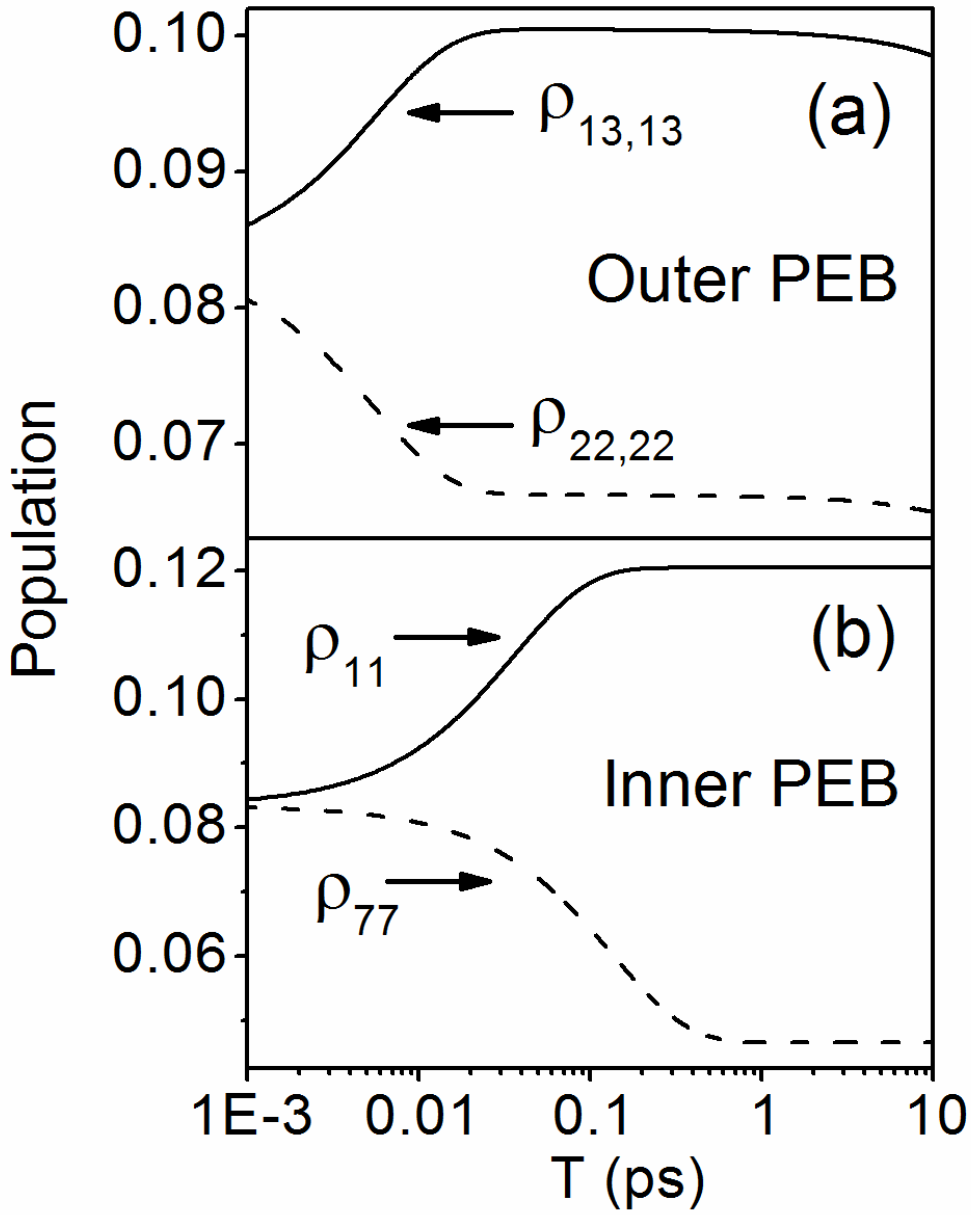

Figure 8.13. (a) Time-dependent exciton populations, $\rho_{13,13}(T)$ and $\rho_{22,22}(T)$, generated using Equation (8.17) and the MRT rate constants. Dynamics identical to $\rho_{13,13}(T)$ and $\rho_{22,22}(T)$ are found for excitons 14-15 and 23-24, respectively. (b) Time-dependent exciton populations, $\rho_{11}(T)$ and $\rho_{77}(T)$, generated using Equation (8.17) and the MRT rate constants. Dynamics identical to $\rho_{11}(T)$ and $\rho_{77}(T)$ are found for excitons 2-6 and 8-12, respectively. Förster theory does not predict the evolution of populations within the manifolds of outer and inner PEB electronic states (see text).

Based on this work, we conclude that the electronic structures of the inner PEB dimers are most appropriately viewed in the exciton basis. Evidence for this includes the large inter-pigment coupling, J_{mn}=-99cm^{-1}, and the fast relaxation processes found both experimentally (Figure 8.7a) and theoretically (Figure 8.13b). This conclusion is consistent with the exciton electronic structure found in the phycocyanobilin pigment dimers, which are bound at analogous locations (i.e., interface between α and β subunits), of cyanobacterial allophycocyanin and c-phycocyanin.[35,36,44,45,80] A strong case either for or against exciton delocalization in the PUB and outer PEB cannot be made based on the present experiments and simulations. The similar kinetics predicted by both MRT and Förster theories (Figure 8.10) suggests that caution should be taken in reaching a conclusion regarding the electronic structure of the PUB states. In addition, although relatively fast (3.75ps) dynamics are measured following (nominal) excitation of the outer PEB at 18870cm^{-1}, it is possible that electronic relaxation on the inner PEB dimers contributes to these TG signals because vibronic transitions of the inner PEB absorb at this frequency. Measurements conducted at lower temperatures with broader laser bandwidths will be needed to probe the electronic structure of the PUB and outer PEB with greater sensitivity.

Table 8.1. Fitting Parameters for Exciton Model

Parameter	PUB	Outer PEB	Inner PEB
[a] E_m	20770 cm^{-1}	19190 cm^{-1}	18300 cm^{-1}
[b] Λ_m^{-1}	300 fs	300 fs	300 fs
[b] λ_m	450 cm^{-1}	600 cm^{-1}	230 cm^{-1}
[c] ω_1, S_1	380 cm^{-1}, 0.26	380 cm^{-1}, 0.32	380 cm^{-1}, 0.32
[c] ω_2, S_2	445 cm^{-1}, 0.26	445 cm^{-1}, 0.32	445 cm^{-1}, 0.32
[c] ω_3, S_3	617 cm^{-1}, 0.26	617 cm^{-1}, 0.32	617 cm^{-1}, 0.32
[c] ω_4, S_4	957 cm^{-1}, 0.26	957 cm^{-1}, 0.32	957 cm^{-1}, 0.32
[c] ω_5, S_5	1430 cm^{-1}, 0.26	1430 cm^{-1}, 0.32	1430 cm^{-1}, 0.32
[d] μ_m	12.5 D	11.0 D	11.0 D

[a] Parameter of Equation (8.2).

[b] Parameter of Equation (8.5).

[c] Parameter of Equation (8.6).

[d] Transition dipole magnitude is used to compute J_{mn} in Equation (8.2).

Table 8.2. Fitting Parameters for Förster Model

Parameter	PUB	Outer PEB	Inner PEB
[a] E_m	20700 cm^{-1}	19120 cm^{-1}	18230 cm^{-1}
[b] Λ_m^{-1}	300 fs	300 fs	300 fs
[b] λ_m	260 cm^{-1}	770 cm^{-1}	150 cm^{-1}

[c] ω_1, S_1	380 cm^{-1}, 0.11	380 cm^{-1}, 0.15	380 cm^{-1}, 0.15
[c] ω_2, S_2	445 cm^{-1}, 0.11	445 cm^{-1}, 0.15	445 cm^{-1}, 0.15
[c] ω_3, S_3	617 cm^{-1}, 0.11	617 cm^{-1}, 0.15	617 cm^{-1}, 0.15
[c] ω_4, S_4	957 cm^{-1}, 0.11	957 cm^{-1}, 0.15	957 cm^{-1}, 0.15
[c] ω_5, S_5	1430 cm^{-1}, 0.11	1430 cm^{-1}, 0.15	1430 cm^{-1}, 0.15
[d] μ_m	12.5 D	11.0 D	11.0 D

[a] Parameter of Equation (8.4).

[b] Parameter of Equation (8.5).

[c] Parameter of Equation (8.6).

[d] Parameter of Equation (8.12).

Table 8.3. Transient Absorption Anisotropy Fitting Parameters

[a]Parameter	[b]PUB	[c]Outer PEB	[d]Inner PEB
r_0	0.06 +/-0.03	0.19 +/-0.01	0.17 +/-0.01
r_1	0.36 +/- 0.01	0.16 +/-0.01	0.12 +/-0.01
τ_1 (ps)	1.26 +/-0.05	3.75 +/-0.42	0.93 +/-0.07

[a] Fit to Equation $r(T) = r_0 + r_1 \exp(-T/\tau_1)$

[b] All laser pulses tuned to 20400 cm^{-1}

[c] All laser pulses tuned to 18870 cm^{-1}

[d] All laser pulses tuned to 17700 cm^{-1}

REFERENCES

(1) van Amerongen, H.; Valkunas, L.; van Grondelle, R. *Photosynthetic Excitons*; World Scientific: Singapore, 2000.

(2) Abramavicius, D.; Palmieri, B.; Voronine, D. V.; Sanda, F.; Mukamel, S. *Chem. Rev.* 2009, *109*, 2350.

(3) Milota, F.; Sperling, J.; Nemeth, A.; Mancal, T.; Kauffmann, H. F. *Acc. Chem. Res.* 2009, *42*, 1364.

(4) Spano, F. C.; Yamagata, H. *J. Phys. Chem. B* 2010, DOI:10.1021/jp104752k.

(5) Cho, M. *Chem. Rev.* 2008, *108*, 1331.

(6) Ishizaki, A.; Calhoun, T. R.; Schlau-Cohen, G. S.; Fleming, G. R. *Phys. Chem. Chem. Phys.* 2010, *12*, 7319.

(7) Novoderezhkin, V. I.; van Grondelle, R. *Phys. Chem. Chem. Phys.* 2010, *12*, 7352.

(8) Myers, J. A.; Lewis, K. L. M.; Fuller, F. D.; Tekavec, P. F.; Yocum, C. F.; Ogilvie, J. P. *J. Phys. Chem. Lett.* 2010, *1*, 2774.

(9) Madjet, M. E. A.; Muh, F.; Renger, T. *J. Phys. Chem. B* 2009, *113*, 12603.

(10) Engel, G. S.; Calhoun, T. R.; Read, E. L.; Ahn, T. K.; Mancal, T.; Cheng, Y. C.; Blankenship, R. E.; Fleming, G. R. *Nature* 2007, *446*, 782.

(11) Collini, E.; Wong, C. Y.; Wilk, K. E.; Curmi, P. M. G.; Brumer, P.; Scholes, G. D. *Nature* 2010, *463*, 644.

(12) Panitchayangkoon, G.; Hayes, D.; Fransted, K. A.; Caram, J. R.; Harel, E.; Wen, J.; Blankenship, R. E.; Engel, G. S. *Proc. Natl. Acad. Sci.* 2010, *107*, 12766.

(13) Calhoun, T. R.; Ginsberg, N. S.; Schlau-Cohen, G. S.; Cheng, Y.-C.; Ballottari, M.; Bassi, R.; Fleming, G. R. *J. Phys. Chem. B* 2009, *113*, 16291.

(14) Ishizaki, A.; Fleming, G. R. *J. Chem. Phys.* 2009, *130*, 234110.

(15) Ishizaki, A.; Fleming, G. R. *J. Chem. Phys.* 2009, *130*, 234111.

(16) Mancal, T.; Valkunas, L.; Read, E. L.; Engel, G. S.; Calhoun, T. R.; Fleming, G. R. *Spectroscopy* 2008, *22*, 199.

(17) Thorwart, M.; Eckel, J.; Reina, J. H.; Nalbach, P.; Weiss, S. *Chem. Phys. Lett.* 2009, *478*, 234.

(18) Nalbach, P.; Eckel, J.; Thorwart, M. *New. J. Phys.* 2010, *12*, 065043.

(19) Rebentrost, P.; Mohseni, M.; Aspuru-Guzik, A. *J. Phys. Chem B* 2009, *113*, 9942.

(20) Nazir, A. *Phys. Rev. Lett.* 2009, *103*, 146404:1.

(21) Fassioli, F.; Nazir, A.; Olaya-Castro, A. *J. Phys. Chem. Lett.* 2010, *1*, 2139.

(22) Hennebicq, E.; Beljonne, D.; Curutchet, C.; Scholes, G. D.; Silbey, R. J. *J. Chem. Phys.* 2009, *130*, 214505:1.

(23) Beljonne, D.; Curutchet, C.; Scholes, G. D.; Silbey, R. J. *J. Phys. Chem. B* 2009, *113*, 6583.

(24) Jang, S. *J. Chem. Phys.* 2009, *131*, 164101.

(25) Grover, M.; Silbey, R. J. *J. Chem. Phys.* 1971, *54*, 4843.

(26) Kubo, R. *Adv. Chem. Phys.* 1969, *15*, 101.

(27) Tanimura, Y. *J. Phys. Soc. Jpn.* 2006, *75*, 082001.

(28) Renger, T. *Photosynth. Res.* 2009, *102*, 471.

(29) Arnett, D. C.; Moser, C. C.; Dutton, P. L.; Scherer, N. F. *J. Phys. Chem. B* 1999, *103*, 2014.

(30) Jonas, D. M.; Lang, M. J.; Nagasawa, Y.; Joo, T.; Fleming, G. R. *J. Phys. Chem* 1996, *100*, 12660.

(31) Zhang, J. M.; Shiu, Y. J.; Hayashi, M.; Liang, K. K.; Chang, C. H.; Gulbinas, V.; Yang, C. M.; Yang, T.-S.; Wang, H. Z.; Chen, Y.-T.; Lin, S. H. *J. Phys. Chem. A* 2001, *105*, 8878.

(32) Womick, J. M.; Moran, A. M. *J. Phys. Chem. B* 2009, *113*, 15747.

(33) Zhang, W. M.; Meier, T.; Chernyak, V.; Mukamel, S. *J. Chem. Phys.* 1998, *108*, 7763.

(34) Yang, M.; Fleming, G. R. *Chem. Phys.* 2002, *282*, 163.

(35) Edington, M. D.; Riter, R. E.; Beck, W. F. *J. Phys. Chem.* 1995, *99*, 15699.

(36) Edington, M. D.; Riter, R. E.; Beck, W. F. *J. Phys. Chem.* 1996, *100*, 14206.

(37) Doust, A. B.; Marai, C. N. J.; Harrop, S. J.; Wilk, K. E.; Curmi, P. M. G.; Scholes, G. D. *J. Mol. Biol.* 2004, *344*, 135.

(38) Doust, A. B.; Wilk, K. E.; Curmi, P. M. G.; Scholes, G. D. *J. Photochem. Photobiol. A* 2006, *184*, 1.

(39) Doust, A. B.; van Stokkum, I. H. M.; Larsen, D. S.; Wilk, K. E.; Curmi, P. M. G.; van Grondelle, R.; Scholes, G. D. *J. Phys. Chem. B* 2005, *109*, 14219.

(40) Ritter, S.; Hiller, R. G.; Wrench, P. M.; Welte, W.; Diederichs, K. *J. Struct. Biol.* 1999, *126*, 86.

(41) Jiang, T.; Zhang, J.-P.; Liang, D.-C. *Proteins* 1999, *34*, 224.

(42) Gaigalas, A.; Gallagher, T.; Cole, K. D.; Singh, T.; Wang, L.; Zhang, Y.-Z. *Photochem. Photobiol.* 2006, *82*, 635.

(43) Schirmer, T.; Huber, R.; Schneider, M.; Bode, W.; Miller, M.; Hackert, M. L. *J. Mol. Biol.* 1986, *188*, 651.

(44) Schirmer, T.; Bode, W.; Huber, R. *J. Mol. Biol.* 1987, *196*, 677.

(45) Brejc, K.; Ficner, R.; Huber, R.; Steinbacher, S. *J. Mol. Biol.* 1995, *249*, 424.

(46) MacColl, R.; Guard-Friar, D. *Phycobiliproteins*; CRC Press: Boca Raton, 1987.

(47) MacColl, R. *J. Struct. Biol.* 1998, *124*, 311.

(48) Womick, J. M.; Moran, A. M. *J. Phys. Chem. B* 2009, *113*, 15771.

(49) Womick, J. M.; Miller, S. A.; Moran, A. M. *J. Chem. Phys.* 2010, *133*, 024507.

(50) Womick, J. M.; Moran, A. M. *J. Phys. Chem. B* 2011, DOI: 10.1021/jp106713q.

(51) Matro, A.; Cina, J. A. *J. Phys. Chem* 1995, *99*, 2568.

(52) Xie, S.; Du, M.; Mets, L.; Fleming, G. R. "Femtosecond Fluorescence Depolarization Study of Photosynthetic Antenna Proteins: Observation of Ultrafast Energy Transfer in Trimeric C-phycocyanin and Allophycocyanin"; SPIE Symposium, 1992.

(53) Edington, M. D.; Riter, R. E.; Beck, W. F. *J. Phys. Chem. B* 1997, *101*, 4473.

(54) Debreczeny, M. P.; Sauer, K.; Zhou, J.; Bryant, D. A. *J. Phys. Chem.* 1995, *99*, 8412.

(55) Debreczeny, M. P.; Sauer, K.; Zhou, J.; Bryant, D. A. *J. Phys. Chem.* 1995, *99*, 8420.

(56) Schwoerer, M.; Wolf, H. C. *Organic Molecular Solids*; Wiley-VCH: Weinheim, 2007.

(57) Spano, F. C. *Annu. Rev. Phys. Chem.* 2006, *57*, 217.

(58) Spano, F. C. *Acc. Chem. Res.* 2010, *43*, 429.

(59) Cho, M.; Vaswani, H. M.; Brixner, T.; Stenger, J.; Fleming, G. R. *J. Phys. Chem. B* 2005, *109*, 10542.

(60) Mukamel, S. *Principles of Nonlinear Optical Spectroscopy*; Oxford University Press: New York, 1995.

(61) Freed, K. F. *Top. Appl. Phys.* 1976, *15*, 23.

(62) Morse, M. D.; Puiu, A. C.; Smalley, R. E. *J. Chem. Phys.* 1983, *78*, 3435.

(63) Womick, J. M.; Miller, S. A.; Moran, A. M. *J. Phys. Chem. B* 2009, *113*, 6630.

(64) Kobayashi, T.; Baltuska, A. *Meas. Sci. Technol.* 2002, *13*, 1671.

(65) Cerullo, G.; Nisoli, M.; De Silvestri, S. *Appl. Phys. Lett.* 1997, *71*, 3616.

(66) Riedle, E.; Beutter, M.; Lochbrunner, S.; Piel, J.; Schenkl, S.; Spörlein, S.; Zinth, W. *Appl. Phys. B* 2000, *71*, 457.

(67) Brixner, T.; Mancal, T.; Stiopkin, I. V.; Fleming, G. R. *J. Chem. Phys.* 2004, *121*, 4221.

(68) Khalil, M.; Demirdöven, N.; Tokmakoff, A. *J. Phys. Chem. A* 2003, *107*, 5258.

(69) Hybl, J. D.; Albrecht Ferro, A.; Jonas, D. M. *J. Chem. Phys.* 2001, *115*, 6606.

(70) Lepetit, L.; Chériaux, G.; Joffre, M. *J. Opt. Soc. Am. B* 1995, *12*, 2467.

(71) Gallagher, S. M.; Albrecht, A. W.; Hybl, J. D.; Landin, B. L.; Rajaram, B.; Jonas, D. M. *J. Opt. Soc. Am. B* 1998, *15*, 2338.

(72) Moran, A. M.; Maddox, J. B.; Hong, J. W.; Kim, J.; Nome, R. A.; Bazan, G. C.; Mukamel, S.; Scherer, N. F. *J. Chem. Phys.* 2006, *124*, 194904:1.

(73) Andel III, F.; Murphy, J. T.; Haas, J. A.; McDowell, M. T.; van der Hoef, I.; Lugtenburg, J.; Lagarias, J. C.; Mathies, R. A. *Biochemistry* 2000, *39*, 2667.

(74) Riter, R. R.; Edington, M. D.; Beck, W. F. *J. Phys. Chem.* 1996, *100*, 14198.

(75) Homoelle, B. J.; Edington, M. D.; Diffey, W. M.; Beck, W. F. *J. Phys. Chem. B* 1998, *102*, 3044.

(76) Brixner, T.; Stenger, J.; Vaswani, H. M.; Cho, M.; Blankenship, R. E.; Fleming, G. R. *Nature* 2005, *434*, 625.

(77) Milota, F.; Sperling, J.; Nemeth, A.; Kauffman, L. J. *Chem. Phys.* 2009, *357*, 45.

(78) Collini, E.; Scholes, G. D. *Science* 2009, *323*, 369.

(79) Gallagher Faeder, S. M.; Jonas, D. M. *J. Phys. Chem. A* 1999, *103*, 10489.

(80) Riter, R. E.; Edington, M. D.; Beck, W. F. *J. Phys. Chem. B* 1997, *101*, 2366.

CHAPTER 9. CORRELATED EXCITON FLUCTUATIONS IN CYLINDRICAL MOLECULAR AGGREGATES

9.1. INTRODUCTION

Natural photosynthetic systems transport energy from the site of light absorption in an antenna complex to a reaction center where biosynthesis occurs.[1-3] Light harvesting proteins located in the antenna generally absorb light with exciton excited states delocalized over multiple pigments. Weak interactions between these excited states and the solvent bath sustain electronic coherences for significant length and time scales.[4-9] Underlying these coherences are fluctuations of the individual pigments induced by local environmental motion. Individual pigments in close proximity can undergo correlated, uncorrelated, or anti-correlated fluctuations, which transform into similar correlations for the exciton energy levels.[10-13] Positively correlated exciton fluctuations preserve phase relationships in electronic coherence and impact electronic relaxation rates.[14] The importance of correlated fluctuations and their manifestation in the dynamics of a wider variety of systems are topics of much current interest, largely because these dynamics can now be experimentally probed with new pulsed laser spectroscopies.[15-21]

The investigation of molecular level fluctuations is of fundamental interest but also projects on the development of materials useful for harnessing solar energy. New experimental access to these correlations and the underlying microscopic motion has important implications even under conventional rate theories such as Förster energy transfer. We discuss below how the nuclear line shape factors entering the Förster rate formula reflect

Adapted with permission from Womick, J.M.; Miller, S.A.; Moran, A.M. *J. Phys. Chem. B* 2009, *113*, 6630-6639.

molecular-level correlations. In addition, recent experiments have revealed the importance of relaxation dynamics not accounted for by conventional rate theories. For example, non-secular terms (i.e. coherence transfer) in Redfield's equations were found to be important for the light-harvesting efficiency of green bacteria.[6] Also remarkable is the persistence of phase coherence between exciton states for durations longer than the population transfer times, which contrasts with conventional limitations on dephasing rates. These initial observations raised the possibility that coherence in energy transfer requires biological fine tuning. However, it is quite astonishing that similar dynamics were recently detected in a conjugated polymer at room temperature.[22]

The molecular aggregate studied in this chapter (see Figure 9.1) self-assembles cyanine dye molecules into a double-walled cylindrical structure.[23,24] Dispersion forces related to its double bond network promote aggregation, whereas the hydrophobic aliphatic chains govern the morphology. It is thought that the aliphatic groups bundle in the region between the walls of the cylinder.[23] The single exciton manifold of optically allowed transitions is understood with consideration of four excited states corresponding to peaks labeled in the linear absorption spectrum shown in Figure 9.2.[25,26] Transition #1 at 16670 cm^{-1} is localized on the inner cylinder.[23,27] Measurements of linear dichroism find this transition to be polarized parallel to the long axis of the cylinder.[28] Transition #2 at 17150 cm^{-1} is also polarized parallel to the long axis of the cylinder and corresponds to an excited state localized on the outer cylinder as indicated by its solvent sensitivity.[27,28] The 17330 cm^{-1} transition #3 is polarized perpendicular to the other three transitions; this excited state is correlated with the 16670 cm^{-1} transition wavelength but its real-space localization is not as well-defined as those of the other three excitons. Pump-probe experiments find that

excitation of the 17860 cm^{-1} band (transition #4) induces bleaching of the lower energy transitions localized on the inner and outer cylinders.[29] We interpret this exciton as delocalized between the inner and outer cylinder walls. It has been suggested that the 17860 cm^{-1} peak is highly sensitive to details of molecular packing into the self-assembled structure.[28]

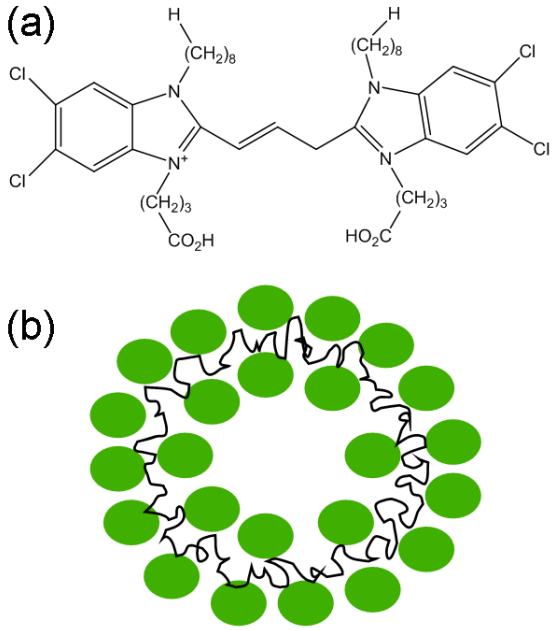

Figure 9.1. (a) Monomer building block for the cylindrical aggregate, 5,5',6,6'-tetrachlorobenzimidacarbocyanine. (b) Cross section of double-walled cylindrical structure of the aggregate in which the molecular sites are represented by the green circles and the hydrophobic chains (black lines) are bundled between the cylinder walls.

This chapter investigates correlated exciton energy level fluctuations of the C8O3 cylindrical aggregate with transient grating (TG) and photon echo (PE) spectroscopies. TG spectra acquired under different polarization conditions reveal a complex series of resonances reflecting the electronic structure of the single and double exciton bands. In addition, recurrences in the PE peaks measured as a function of the time following photoexcitation represent an electronic coherence between the exciton localized on the inner

cylinder and the exciton delocalized between the cylinder walls. Signatures of correlated fluctuations are found in the PE cross peak corresponding to these two exciton states. It is important to establish the role these correlations play in non-radiative relaxation. As a straightforward illustration, we present a model showing how correlated fluctuations directly impact the Förster energy transfer efficiency of a composite system in which the cylindrical aggregate functions as an energy donor.

Pugzlys and co-workers have applied linear and nonlinear spectroscopies for insight into the electronic structure and relaxation dynamics of the present cylindrical aggregate and related systems.[29] Linear dichroism measurements determined how the single exciton transition dipoles project on the orientation of the cylinder.[28] Femtosecond pump-probe experiments investigated the multi-level electronic structure and were further complemented with anisotropy measurements.[29] Understanding of the real-space excited state localization described above is owed to these measurements and related theoretical work.[25,26,30] These previous experiments examined relaxation dynamics occurring on the time scales longer than 100 fs, where the shortest measured time constant of 275 fs was assigned to energy transfer from the outer to inner cylinder.[29] This chapter differs from these earlier studies in that we investigate dynamics occurring on the sub-100 fs time scale which are only accessible by PE spectroscopy.

In a related experimental study, Milota et al. examined the dynamics of C8O3 in a mixture of water and octanol, where the aggregate self-assembles into a double-walled cylinder with a linear absorption spectrum dominated by two single exciton transitions.[31] Quantum beats were observed in the cross peak corresponding to the two single exciton states during the first 100 fs after excitation, whereas population transfer from the higher to

lower energy state was found at longer times. The present chapter investigates a different self-assembled morphology of C8O3 exhibiting the four spectrally resolved single exciton transitions seen in the linear absorption spectrum of Figure 9.1. Comparing observations for these two related systems yields important physical insight. For example, our observation of quantum beats persisting on the 100 fs time scale (see Section 9.3.4) suggests similar wavefunction delocalization and bath induced exciton fluctuations to the system examined by Milota et al.[31]

9.2. EXPERIMENT

The C8O3 dye molecule was purchased from FEW Chemicals and used without further purification. Solutions were prepared following the instructions of Reference [23] in which the formation of double-walled cylindrical molecular aggregates in 10 mM NaOH solutions was confirmed by cryogenic transmission electron microscopy. The linear absorption spectrum shown in Figure 9.2 reproduces Figure 9.4 of Reference [23]. The concentration was adjusted to obtain an absorbance of 0.3 at 16670 cm^{-1} in a 1 mm path sample cell.

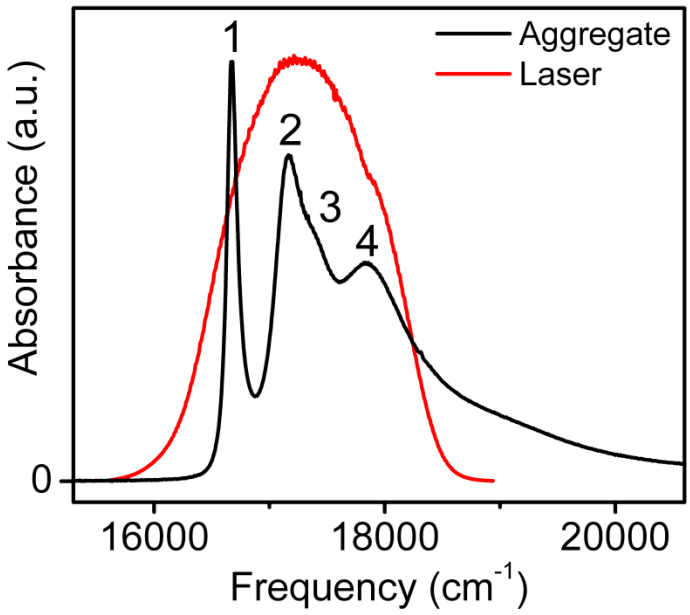

Figure 9.2. Linear absorption spectra measured for the aggregate (black) overlayed with the spectrum of the laser pulse used in transient grating and photon echo experiments (red). Single exciton transitions are labeled.

Femtosecond optical experiments utilize a Quantronix Integra C Titanium Sapphire amplifier generating 130 fs, 800 nm, 2.0 mJ laser pulses at 1 kHz. The laser system pumps a home-built noncollinear optical parametric amplifier (NOPA) producing laser pulses spanning the 500-750 nm wavelength range.[32,33] A 45 nm full width half-maximum portion of the NOPA spectrum centered at 580 nm is filtered in a fused silica prism compressor for use in four-wave mixing experiments. Pulses are compressed to 15 fs with a time-bandwidth product of 0.6 where residual third-order dispersion prevents compression to the 11 fs Fourier transform limit. Figure 9.2 overlays the spectrum of the laser pulse with the absorption spectrum of the cylindrical molecular aggregate.

Transient grating (TG) and photon echo (PE) experiments are performed with two similar interferometers based on the schematic in Figure 9.3. The interferometers resemble

earlier nonlinear spectroscopy experiments in that the laser beam geometries are generated with diffractive-optics (DO) for passively phase-stabilized interferometric signal detection.[34-42] Phase fluctuations measured for these interferometers have standard deviations of 0.2 radians over a 3 hour period. The local oscillator (pulse 4) is attenuated by a factor of approximately 1000 times with a 2 mm thick reflective fused silica neutral density filter (ND, Thorlabs) and arrives at the sample 800 fs before the pulse 3, which is delayed with a 2 mm thick fused silica window (W, Edmund) and two 175 micron thick microscope cover slips (CS, Fisher). The signal is collinear with the local oscillator after the sample by the $\mathbf{k}_S = -\mathbf{k}_1 + \mathbf{k}_2 + \mathbf{k}_3$ phase matching geometry. The signal and local oscillator are dispersed in a 0.3 m spectrograph and detected with a back-illuminated CCD (Princeton Instruments PIXIS 100B) in line-binning mode with an integration time of 200 ms.

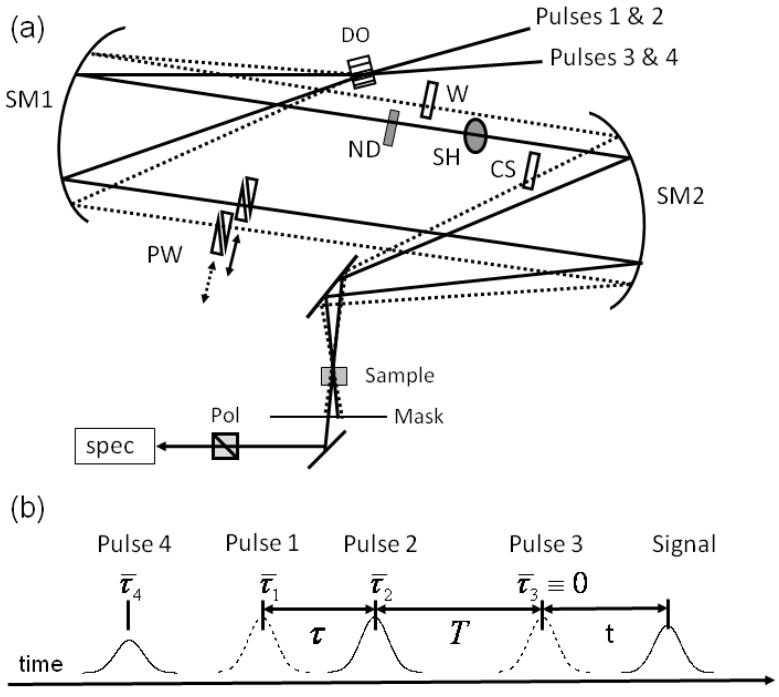

Figure 9.3. (a) Design of diffractive optic based interferometers used for TG and PE experiments. For TG, SM1and SM2 are respectively 15 and 20 cm focal lengths; no prisms wedges (PW) are present; ND is a fused silica reflective neutral density filter; W is a fused

silica window; SH is a mechanical shutter used to subtract scattered light associated with pulses 1 and 2. The PE setup differs in that SM1 and SM2 are respectively 50 cm and 20 cm focal length mirrors; prism wedges control the delays of pulses 1 and 2. (b) Pulse sequence defining experimentally controlled delays, $\tau = \bar{\tau}_2 - \bar{\tau}_1$ and $T = \bar{\tau}_3 - \bar{\tau}_2$. The local oscillator, pulse 4, arrives 800 fs before pulse 3, $\bar{\tau}_4$ =800fs.

The TG interferometer uses a DO (Holoeye) producing an angle of 4.65 degrees between the +/-1 diffraction orders at 590 nm. The pump (pulses 1 and 2) and probe (pulses 3 and 4) beams are crossed at angle of approximately 4.6 degrees in the DO. Pulses 1 and 2 arrive at the sample at the same time, whereas pulse 3 is delayed with a motorized translation stage (Newport GTS150).

The PE interferometer splits the pump and probe beams at the entrance to the interferometer with an 80 g/mm transmission grating (Edmund) optimized for 25% diffraction efficiency into the +/-1 diffraction orders (i.e. total of 50%). The pump and probe beams are crossed in the transmission grating at approximately 5.4º. Delays of the grating forming beams are introduced using prism wedges (Edmund, 1º wedge angle) mounted on translation stages (Thorlabs CR1-Z6). The pulse delay varies linearly over the range of the translation stage used in the experiments, where 1 mm translation of the prism wedge imparts 30 fs pulse delay. The repeatability of the delay was measured by placing a second 80 g/mm transmission grating at the sample position and determining the delay between pulses 1 and 2 with spectral interferometry.[43-45] Standard deviations of 65 attoseconds in the arrival times of the pulses were found for 10 scans in which the stages were translated by 1.5 mm, sent back to the initial positions, then again translated over the same 1.5 mm ranges.

For both the TG and PE experiments, 0.4 mL sample volumes are contained in a 1 mm path quartz cell with an open slit top (Starna Cells). To minimize the sample volume required for a single experiment, a thin piece of plastic was mounted on an electric

toothbrush motor and used to gently stir the sample during data acquisition. In the absence of stirring, sample bleaching is observed in less than one minute with 1 nJ laser pulses. Sample degradation was further avoided by keeping data acquisition times to less than 10 minutes per 0.4 mL volume of the solution held by the sample cell. Pulses with 250-750 pJ energies were focused to a 120 micron diameter spot size at the sample for a fluence of $2.7x10^{13}$ photons/cm^2. Under these conditions, changes in the absorption spectrum of the sample were not observed during data acquisition.

The optimal sample concentration minimizes both contributions from solvent emission at low solute concentrations[46-48] and propagation effects associated with high optical densities.[49,50] We find that C8O3 solute emission dominates over that of the solvent for optical densities greater than 0.2 at 16670 cm^{-1}. At lower C8O3 concentrations, the quasi-instantaneous nonlinearity of the transparent solvent gives rise to significant signal emission when the pulses are overlapped in the sample.[47,48] This quasi-instantaneous response manifests as a gating effect on the signal emission time (i.e. linear spectral phase),[46] and is the same nonlinearity underlying the pulse characterization technique of frequency resolved optical gating.[51] Suppression of the solvent response is particularly important for the present study because the dynamics of interest occur at less than 110 fs after excitation when the solvent emission is most significant (e.g. quasi-instantaneous nonlinearity and Raman response).

9.3. RESULTS

9.3.1. Polarization Sensitivity of Transient Grating Signals

Transient grating (TG) signals measured for C8O3 are presented in Figure 9.4. These data are processed following earlier published procedures.[37] These real (i.e. absorptive)

signals are formally equivalent to those obtained using conventional pump-probe spectroscopy in which the differential transmission of a probe pulse is detected.[15,52] Positive and negative signals respectively represent the transient bleach and absorption of the sample caused by interaction with pulses 1 and 2 (i.e. pump pulses). Figures 9.4(a) and 9.4(b) differ in that pulses 1 and 2 have parallel and perpendicular polarizations with respect to the pulses 3 and 4, respectively. We will hereafter refer to these polarization conditions as the ZZZZ and ZZXX tensor elements.[53] In principal, the anisotropy in the material response can be computed with the data in Figure 9.4.[54] Here, the differences in the two tensor components are emphasized for interpretation of the photon echo spectra presented in the following section.

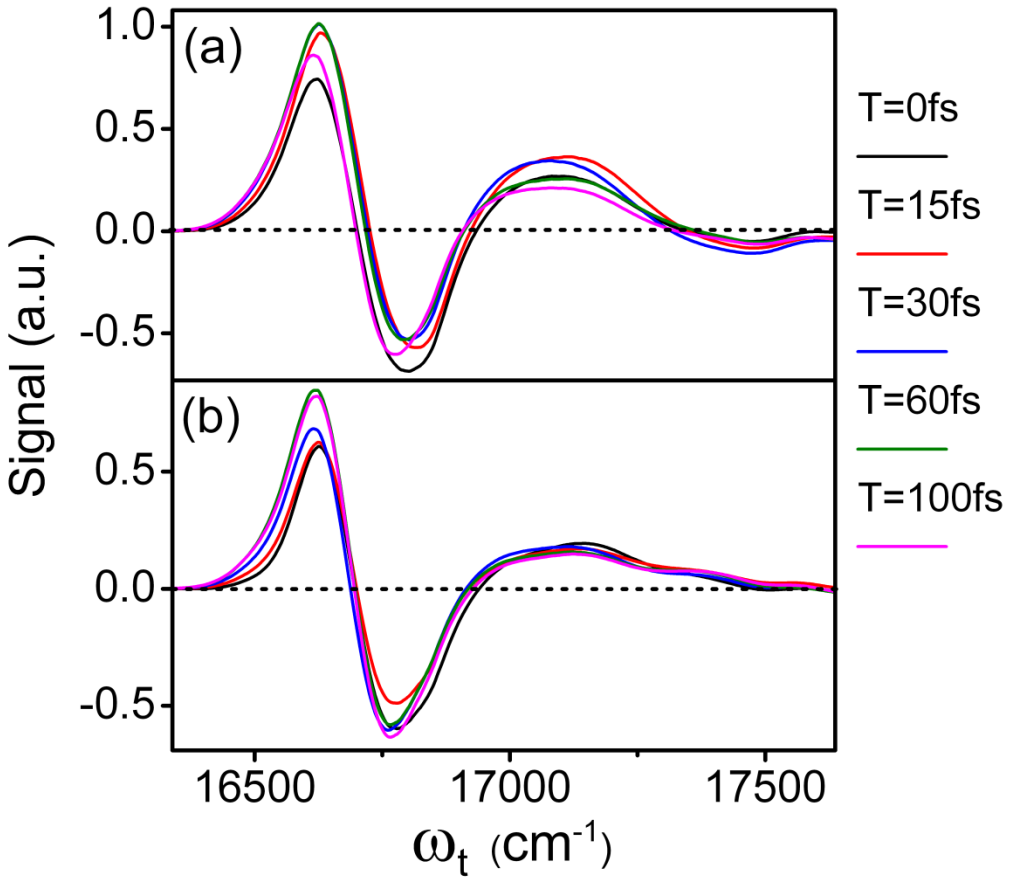

Figure 9.4. Real (absorptive) components of transient grating signals measured for (a) ZZZZ and (b) ZZXX tensor elements. Signals with positive and negative signs respectively represent transient bleach and absorptive signal components. The signal strengths for the two tensor elements can be directly compared.

Signals acquired under both the ZZZZ and ZZXX polarization conditions show bleached resonances at 17090 and 16670 cm^{-1}, whereas absorption between the single and double exciton manifolds of excited states is measured at 17450 and 16810 cm^{-1}. This pattern of signal components with alternating positive and negative signs is consistent with earlier observations for j-aggregates.[55] At the origin of the response is the quasi-fermionic nature of the aggregates defined by the rule that not more than one excitation can reside on an individual dye molecule.[52,56] Essentially, the second photo-excited exciton is confined in a smaller segment length of the aggregate than the first exciton, which causes a blue-shift in the energy of the double exciton resonance with respect to that of the single exciton. This description of Frenkel excitons is valid for molecular aggregates interacting through weak electrostatic interactions[57,58] but breaks down as the interacting sites become closer in proximity and the effects of wavefunction overlap take over.[59] In this regard, it is interesting that carbon nanotubes, which consist of closely spaced atom sites, behave in the opposite sense. Stabilization of bi-excitons gives rise to transient absorption features red-shifted with respect to the corresponding bleach of the ground state.[60,61]

The ZZZZ polarized data in Figure 9.4(a) show an increase in the signal amplitude at both 17090 (outer cylinder) and 16670 cm^{-1} (inner cylinder) within the first 30 fs following excitation, whereas the signal amplitudes decrease in the delay range T =30-100 fs. The dynamics at 16810 cm^{-1} are more complicated because this resonance represents multiple radiative transitions between the single and double exciton manifolds.[29] A fairly weak

transient absorption (i.e. negative) signal component is measured at 17450 cm^{-1}. The dynamics of this multi-level system are difficult to intrepret on the basis of the TG experiments alone. TG signals spectrally resolve the dipoles radiating the signal but leave correlations to the absorbing (i.e. pumped) dipoles undetermined because a broadband laser pulse is used for excitation. This limitation of TG motivates the use of photon echo experiments in Section 9.3.2 for correlation of the "pumped" and "probed" transition dipoles.

By contrast with the ZZZZ experiments, the ZZXX polarization condition yields signals with only minor changes in amplitude at frequencies greater than 16950 cm^{-1} as a function of T [see Figure 9.4(b)]. This difference is further discussed in the context of photon echo measurements in Section 9.3.2. Another difference between the two tensor elements is the presence of a negative signal component at 17400 cm^{-1} for the ZZZZ tensor element, which is absent in ZZXX. This observation suggests the absorptive signal component at 17400 cm^{-1} arises through pump and probe interactions with nearly parallel transition dipoles, whereas that at 16810 cm^{-1} corresponds to a pair of transition dipoles differing by an angle of close to 45º.

It should be noted that essentially no signal emission is measured at frequencies greater than 17700 cm^{-1} for either tensor element even though this spectral region is within the laser bandwidth (see Figure 9.2). This observation is consistent with those of earlier pump-probe studies.[29] It may be that signal components possessing opposite signs (e.g. ground state bleach vs. excited state absorption) destructively interfere at frequencies greater than 17700 cm^{-1}.

9.3.2. Two-Dimensional Photon Echo Spectra

The real (absorptive) photon echo (PE) spectrum acquired for the ZZZZ tensor element at T=30 fs is shown in Figure 9.5. The horizontal and vertical axes represent Fourier transforms of the time intervals defined in Figure 9.3(b), τ and t.[62,63] The spectrum is dominated by four signal contributions with labeled peak positions: (i) a bleach component correlating τ and t time evolution in an electronic coherence between the ground state and the excited state localized on the inner cylinder; (ii) a bleach component similar to peak (i) but corresponding to the excited state localized on the outer cylinder; (iii) an excited state absorption component correlating multiple single exciton coherences in τ to coherences between the single and double exciton manifolds in t; (iv) a "cross peak" correlating coherence in τ for the ground state and the exciton delocalized between the cylinder walls to coherence in t between the ground state and the exciton localized on the inner cylinder. As mentioned above, signal emission is quite weak at emission frequencies, ω_t, greater than 17700 cm^{-1}. Our analysis focuses on these four dominant peaks.

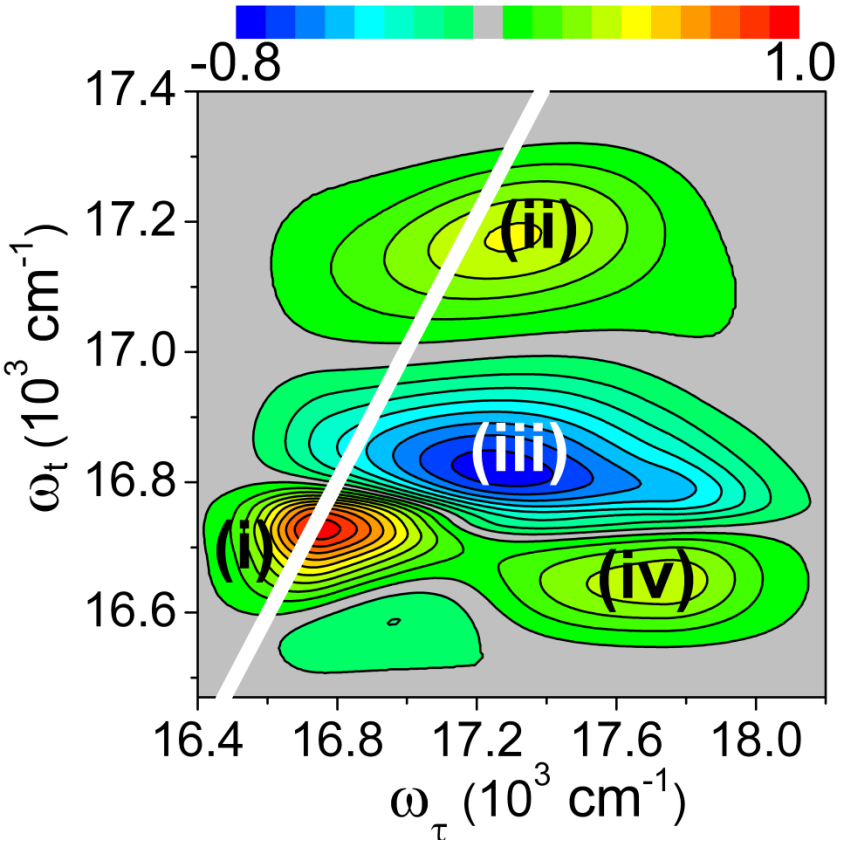

Figure 9.5. Real (absorptive) photon echo spectrum measured for the ZZZZ tensor element at T =30 fs. Signals with positive and negative signs respectively represent bleaches and absorptions. The axes are the frequency domain conjugates to the τ and t intervals defined in Figure 9.3(b). Peak indices given in this spectrum are referred to in the text. The white line is the diagonal of the photon echo spectrum, $\omega_\tau = \omega_t$.

Figure 9.6 presents evolution of the PE spectra for the ZZZZ tensor element during the time interval T =0-90 fs. Peaks (i) and (ii) correspond to the double-sided Feynman diagrams shown in Figure 9.7(a). Signal emission is a superposition of ground state bleach (two diagrams on left in Figure 9.7(a)) and excited state emission (two diagrams on right in Figure 9.7(a)) terms in the response function. These signal components spectrally overlap in the radiated signal because weak system-bath interactions lead to an extremely small Stokes shift.[64] The amplitude of the ground state bleach does not change in T. However, the magnitude of the stimulated emission response varies with the size of the excited state

population and is therefore sensitive to non-radiative processes causing population flow.[63] All signal components show changes in their line shapes with increasing T; the peaks shapes have slight diagonal tilts at T=0, then relax with increasing T towards more symmetric shapes. This line shape evolution reflects relaxation of the inhomogeneous distribution of transition frequencies.[44]

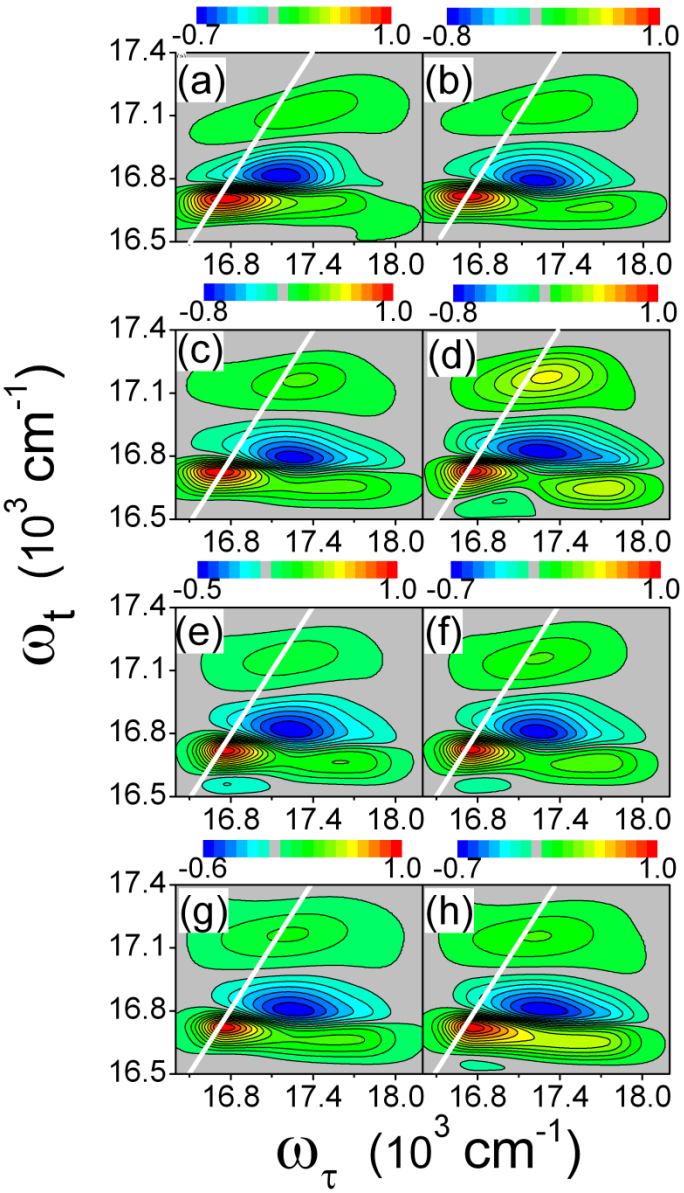

Figure 9.6. Real (absorptive) component of photon echo signal measured for the ZZZZ tensor element at the delay times T : (a) 0 fs; (b) 10 fs; (c) 20 fs; (d) 30 fs; (e) 40 fs; (f) 50 fs; (g) 70 fs; (h) 90 fs. The spectra are normalized at each delay T , so the scales at different values of T should not be compared. The white line is the diagonal of the photon echo spectrum, $\omega_\tau = \omega_t$.

An interesting aspect of peak (iii) is its width with respect to the ω_τ axis. By the quasi-fermionic interpretation of excitons in a j-aggregate, this peak should be most closely associated with pump interaction at 16670 cm^{-1} (i.e. excited state absorption should be blue-shifted with respect to the corresponding single exciton bleach).[52,55,56] However, peak (iii) correlates excited state absorption into the double exciton band with pump interactions for all single exciton levels accessible from the ground state (i.e. transitions 1-4 in Figure 9.2). The corresponding Feynman diagrams are shown in Figure 9.7(c). Similar insight was obtained with pump-probe experiments utilizing a tunable pump pulse.[29] However, the PE spectra additionally show a shift in the peak to greater excitation frequencies, ω_τ , as T increases.

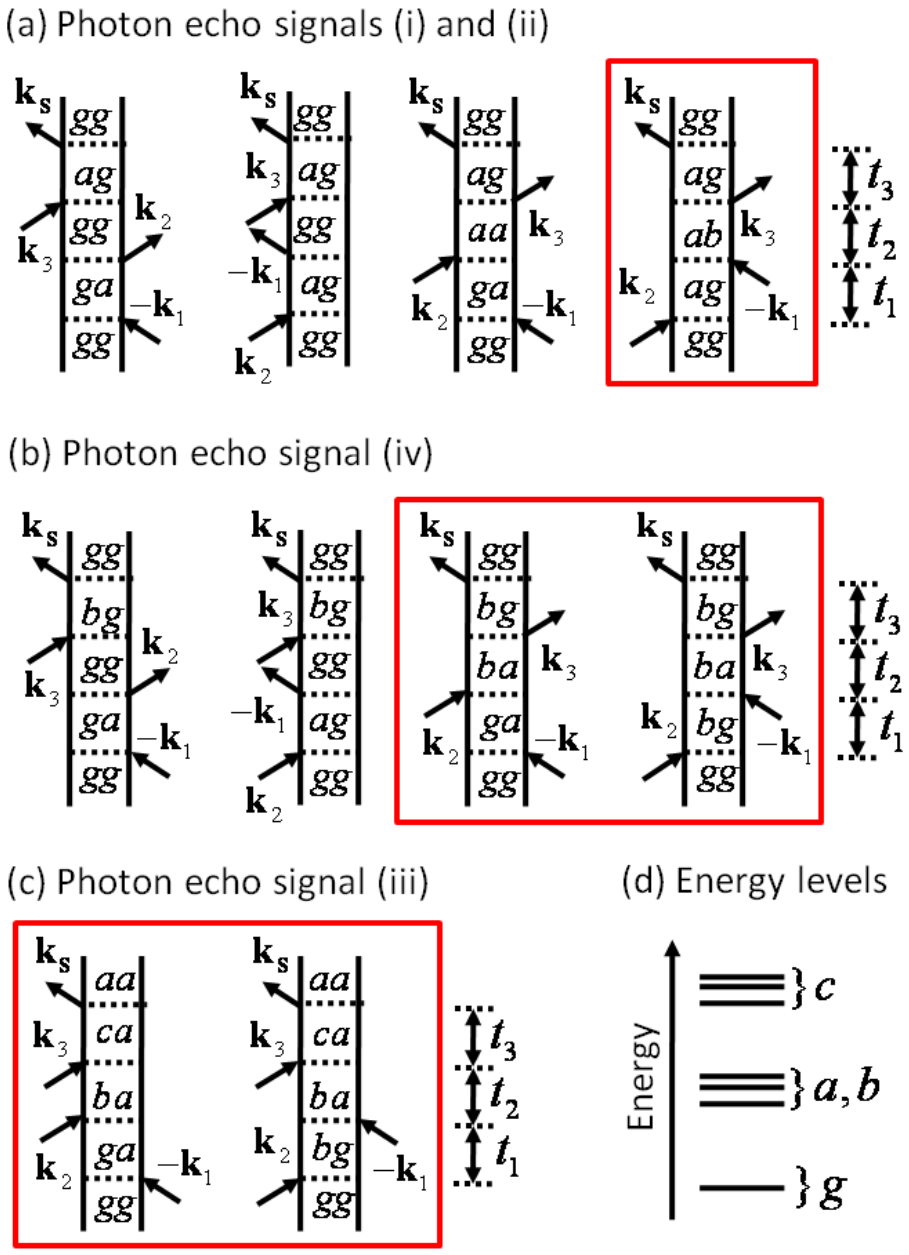

Figure 9.7. Feynman diagrams corresponding to dominant peaks in photon echo spectra labeled in Figure 9.5. (a) For signals (i) and (ii) index a corresponds to excited states localized on the outer and inner cylinders, respectively. (b) Cross-peak (iv) associates the index a with the excited state delocalized between walls of the cylinder and index b with the excited state localized on the inner cylinder. (c) Signal (iii) represents excited state absorption into the double exciton manifold where index a can represent any single exciton state. (d) Energy level scheme in which index g is the ground state, indices a and b are single exciton states, and index c is a double exciton state. Diagrams enclosed in red boxes undergo coherent amplitude modulation in the pulse delay, T, for $a \neq b$.

The PE cross peak (iv) involves two field matter interactions with the transition dipole of the exciton delocalized between the cylinder walls (transition #4 in Figure 9.2) and two field matter interactions with the transition dipole associated with the inner cylinder (peak #1 in Figure 9.2). Feynman diagrams leading to this signal contribution are shown in Figure 9.7(b). Figure 9.6 shows that the relative amplitude of peak (iv) is small at T =0 compared to the other features in the PE spectrum, but increases and maximizes at T =30 fs. For delay times longer than T =30 fs, the amplitude ratios of peak (iv) with respect to peaks (i)-(iii) remains essentially constant. The evolution of the PE peak amplitudes in T is further discussed in Section 9.3.4.

PE spectra acquired under the ZZXX polarization condition are shown in Figure 9.8 and exhibit features similar to those in Figure 9.6. However, two differences immediately clear are the suppression of peak (i) and the enhancement of peak (iii). Diagonal tilt in the peaks is again observed at short T and relaxes within a few tens of femtoseconds. Enhancement of the response in the region near ω_τ =17240 cm^{-1}, ω_t =16670 cm^{-1} is also observed. We interpret this enhancement as a cross peak associated with transitions 1 and 3 in Figure 9.2. Transition 3 has a dipole oriented orthogonal to those of the other three single exciton transitions, which explains its prominence in the ZZXX tensor element. The amplitude recurrence in peak (iv) measured for the ZZZZ tensor element is not observed for ZZXX. The ZZXX polarization condition apparently suppresses this cross peak because it involves interaction with all-parallel transition dipoles (transitions #1 and #4 in Figure 9.2).

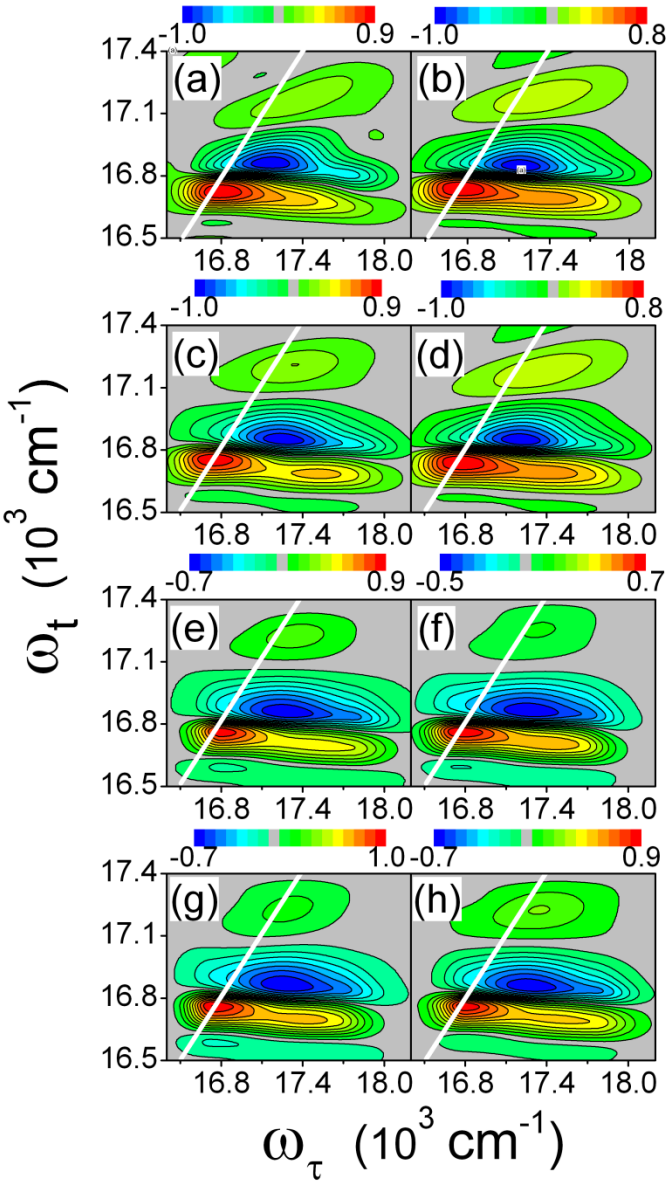

Figure 9.8. Real (absorptive) component of photon echo signal measured for the ZZXX tensor element at the delays T : (a) 0 fs; (b) 10 fs; (c) 20 fs; (d) 30 fs; (e) 40 fs; (f) 50 fs; (g) 70 fs; (h) 90 fs. The spectra are normalized at each delay time, T , so the scales at different values of T should not be compared. The white line is the diagonal of the photon echo spectrum, $\omega_\tau = \omega_t$.

9.3.3. Photon Echo Signatures of Correlated Exciton Fluctuations

Fluctuations induced by system-bath interactions at the individual molecular sites manifest in linear absorption line shapes of the exciton states by the same transformation that

diagonalizes the Hamiltonian of the aggregate.[11] Similarly, c*orrelation* in the fluctuations at the molecular sites transforms onto the exciton basis to produce spectroscopic signatures encoded in photon echo line shapes. Theoretical investigations have shown that the PE cross peaks possess diagonal orientations for correlated exciton fluctuations, anti-diagonal orientations for anti-correlated fluctuations, and neither diagonal or anti-diagonal orientation for uncorrelated fluctuations.[10-13]

Figure 9.9 magnifies cross peak (iv) measured for the ZZZZ tensor element at T =0-30 fs. The line shape exhibits a clear diagonal tilt, which is most pronounced at T =10 fs. Diagonal tilt in the line shape suggests correlated energy level fluctuations for the excited state delocalized between the cylinder walls and excited state localized on the inner cylinder. It is important to recognize that the presence of nearby peaks can influence photon echo line shapes. For this reason, the narrow spectroscopic line widths of C8O3 make it a particularly appropriate system for the investigation of correlation effects. Correlated line broadening can also be detected indirectly by its effects on the dynamics of electronic coherences.[14,22] The material in Section 9.3.4 gives further support to this conclusion.

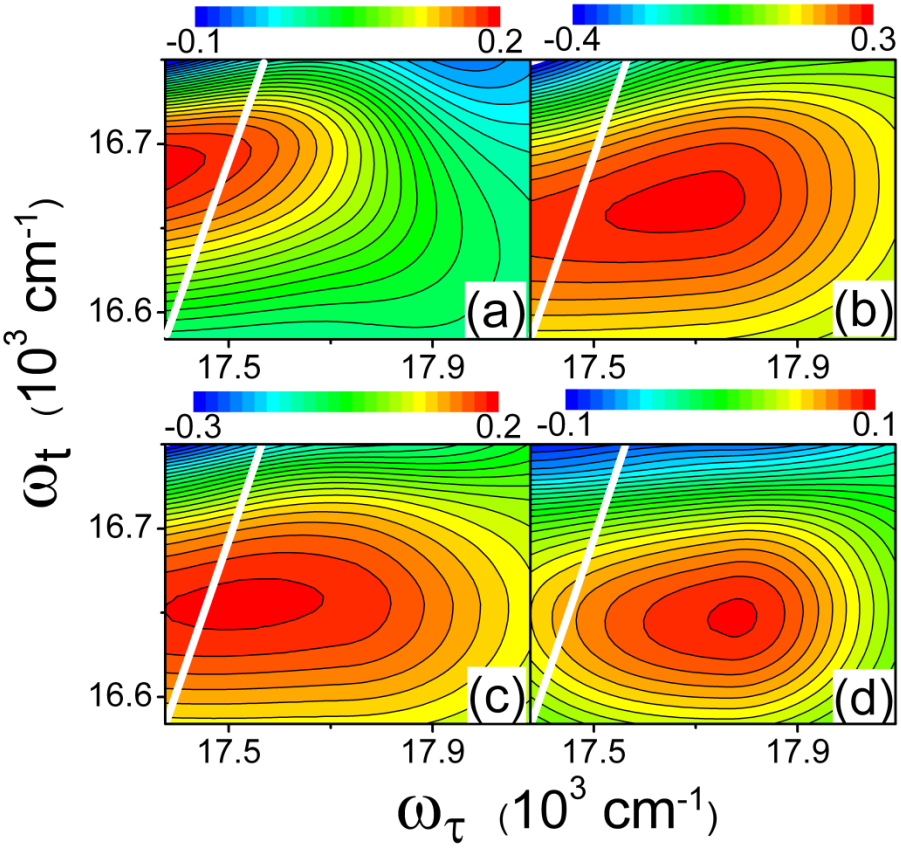

Figure 9.9. Real (absorptive) photon echo spectra acquired for the ZZZZ tensor element at the delay times, T : (a) 0 fs; (b) 10 fs; (c) 20 fs; (d) 30 fs. These are magnified views of the measurements in Figure 9.6. The white line is parallel to the diagonal of the photon echo spectrum, $\omega_\tau = \omega_t$.

9.3.4. Electronic Coherence in the Single Exciton Manifold

The finding of correlated line broadening for PE cross peak (iv) suggests that the the corresponding excited states are specially equipped for long-lasting electronic coherence.[8,14] Figure 9.10 plots the PE peak volumes with respect to T . PE peaks (i), (iii), (iv) and show oscillations with periods of approximately 25 fs, whereas peak (ii) exhibits a lower amplitude modulation with a period of 45 fs. Peaks (i) and (iii) undergo amplitude changes commensurate with peak (iv) but exhibit different sensitivity to the delay, T . That is,

amplitude changes of 60-80% are measured for peaks (i) and (iii) between T =0 fs and T =25 fs, whereas that of peak (iv) increases by 10%.

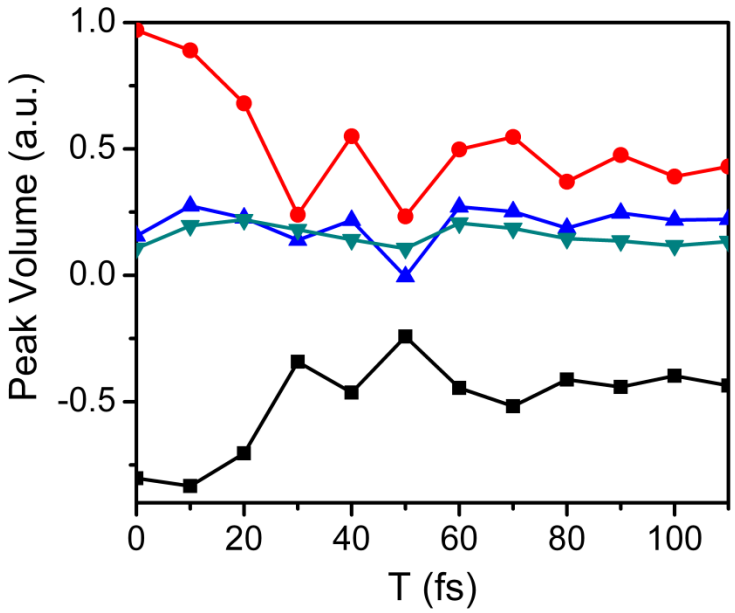

Figure 9.10. Real ZZZZ photon echo signals integrated over a 70 cm^{-1} radius centered on: peak (i), red circles; peak (ii), cyan triangles; peak (iii), blue triangles; peak (iv), black squares. These signals are magnified views of those shown in Figure 9.6.

The Feynman diagrams describing recurrence in peaks (i) and (ii) are enclosed in the red box in Figure 9.7(a) under the special case that $a \neq b$; the diagrams associated with peak (iii) are given by Figure 9.7(c) with $a \neq b$; the diagrams corresponding to peak (iv) are enclosed in the red box in Figure 9.7(b) also with $a \neq b$. PE peaks (i), (iii), (iv) have the same recurrence frequency and therefore represent field-matter interaction sequences evolving in the same electronic coherence during the t_2. The lowest and highest energy single exciton states (see transitions #1 and #4 in Figure 9.2) have an energy gap of 1190 cm^{-1}, so the coherence between these states has a period of 28 fs. The oscillations in Figure 9.10 agree with this period. However, the 45 fs period of the oscillations for peak (ii) agrees well

with the 710 cm^{-1} energy gap between peaks #2 and #4 in the linear spectrum of Figure 9.2 (i.e. period of 47 fs). *Therefore, the recurrences in peaks (i), (iii), (iv) are assigned to an electronic coherence between the exciton localized on the inner cylinder and the exciton delocalized between the cylinder walls. Similarly, the recurrence in peak (ii) is assigned to an electronic coherence between the exciton localized on the outer cylinder and the exciton delocalized between the cylinder walls.*

Physical insight into these dynamics is challenged by fast dephasing and the short temporal period of the coherence, which is comparable to the experimental time resolution of 18 fs. It is possible that a complicated beating pattern is present but not fully resolved. Electronic coherences are not detected for the ZZXX tensor element. We interpret suppression of coherence in the ZZXX tensor element as reflecting the all-parallel transition dipoles associated with the field-matter interaction sequence discussed in the previous paragraph. However, it may also be that for ZZXX multiple coherences produce a complicated beating pattern not detected due to insufficient time resolution. New spectroscopies are under development to address this issue for C8O3.[65]

Relating the peak volume changes occurring in T to dynamics at the molecular level is a challenging problem. Ultimately, we would like to understand how fluctuations of the exciton states transform onto fluctuations at the individual molecular sites. The transformation is readily defined for a dimer but is extremely complicated for a system composed of many molecules. New experiments capable of selectively probing individual electronic coherences will be essential for obtaining deeper information content. Models providing insight into earlier spectroscopic experiments will be used as a starting point for data interpretation.[25,26]

9.4. DISCUSSION

9.4.1. The importance of correlated fluctuations for Förster energy transfer

The importance of coherent quantum dynamics for the function of natural light-harvesting systems has been addressed in recent experimental[6,66] and theoretical[67-70] work. The role of coherence transfer in light harvesting systems is one area of investigation.[6,22] Signatures of coherence transfer dynamics in linear and four-wave mixing spectroscopies have been clearly defined and experiments are revealing deeper insight into this phenomenon.[70-74] Clear evidence for coherence transfer was not obtained in the present measurements. However, the finding of correlated exciton fluctuations still has important consequences for the aggregate's light harvesting function. Experimental access to these dynamics is fairly new and clear connections to conventional rate processes should be firmly established. This Section shows one way that correlated fluctuations impact energy transfer under conventional Förster rate theories.

The Förster energy transfer rate, K_{FET}, is proportional to the overlap between the fluorescence spectrum of the energy donor, $f_D(\omega)$, and absorption spectrum of the acceptor, $\varepsilon_A(\omega)$,

$$K_{FET} \propto \int \varepsilon_A(\omega) f_D(\omega) \omega^{-4} d\omega \tag{9.1}$$

This integral enforces energy conservation in the non-radiative transition. Fluctuations in the molecular basis are readily transformed onto the line shapes of the donor and acceptor spectra by

$$\left\langle \Omega_\alpha(t) \Omega_\beta(0) \right\rangle = \sum_{mnkl} \phi_{\alpha m} \phi^*_{\alpha n} \phi_{\beta k} \phi^*_{\beta l} \left\langle q_{mn}(t) q_{kl}(0) \right\rangle \tag{9.2}$$

where the coefficient, $\phi_{\alpha m}$, is the eigenvector component of exciton state, α, corresponding to molecule, m, and $\langle q_{mn}(t) q_{kl}(0) \rangle$ is a correlation function corresponding to fluctuations in either diagonal ($m = n$, $k = l$) or off-diagonal ($m \neq n$, $k \neq l$) elements of the Hamiltonian (see Appendix H for further background). Cross-correlation functions for the molecular energy gaps can be related to the corresponding auto-correlation functions using

$$\langle q_{mm}(t) q_{kk}(0) \rangle = \eta_{mk} \sqrt{\langle q_{mm}(t) q_{mm}(0) \rangle \langle q_{kk}(t) q_{kk}(0) \rangle} \tag{9.3}$$

where η_{mk} is a correlation parameter interpolating between the fully correlated, $\eta_{mk} > 1$, and anti-correlated limits, $\eta_{mk} < 1$. Using Eq. (9.3), Eq. (9.2) can be rewritten as

$$\langle \Omega_\alpha(t) \Omega_\beta(0) \rangle = \sum_{mnkl} \phi_{\alpha m} \phi^*_{\alpha n} \phi_{\beta k} \phi^*_{\beta l} \langle q_{mn}(t) q_{kl}(0) \rangle \left[1 - \eta_{mk} \delta_{mn} \delta_{kl} (1 - \delta_{mk}) \right] \tag{9.4}$$

Equations (9.1)-(9.4) establish a relationship between correlated molecular fluctuations and Förster energy transfer efficiency. This connection most readily shown under the slow modulation limit of spectroscopic line broadening, which is usually a fair approximation for molecular systems in solution.[75] In this limit, the absorption and fluorescence spectra for the acceptor and donor have Gaussian shapes given by[52]

$$\varepsilon_A(\omega) \propto \exp\left[\frac{-(\omega - \omega_a)^2}{2\Delta_a^2} \right] \tag{9.5}$$

and

$$f_D(\omega) \propto \exp\left[\frac{-(\omega - \omega_b + 2\lambda_b)^2}{2\Delta_b^2} \right] \tag{9.6}$$

where the index a (b) represents an exciton localized on the acceptor (donor) and λ_α is the solvent reorganization energy associated with a transition from the ground state to exciton

state α. Parameters of the line shapes are expressed in terms of the correlation function at $t = 0$ as

$$\lambda_\alpha = \frac{\langle \Omega_\alpha(0)\Omega_\alpha(0)\rangle}{2k_B T} \tag{9.7}$$

and

$$\Delta_\alpha^2 = \langle \Omega_\alpha(0)\Omega_\alpha(0)\rangle \tag{9.8}$$

where k_B is Boltzmann's constant and T is temperature. Together, Eqs. (9.1)-(9.8) show that molecular site correlations, η_{mk}, control the energy transfer efficiency by tuning the line shapes of the donor and acceptor spectra entering Eq. (9.1). Equations (9.5)-(9.8) hold under the slow modulation limit. However, this conclusion generalizes to the intermediate line broadening regime.

Figure 9.11 illustrates the argument presented in this Section. We assume a donor-acceptor system in which the cylindrical aggregate functions as the energy donor, whereas the energy acceptor possesses the fixed absorption spectrum, $\varepsilon_A(\omega)$. The molecular site correlations governing the line shape of $f_D(\omega)$ directly controls the energy transfer efficiency [Eq. (9.1)]; the highest efficiency is found when $\varepsilon_A(\omega)$ and $f_D(\omega)$ possess equal line widths. The development of an energy donor/acceptor composite system utilizing the cylindrical aggregate is the emphasis of on-going work. Artificial light harvesting systems utilizing cylindrical aggregates are relevant to modern solar energy conversion technology.[76,77] Such systems are inspired by the cylindrical aggregate of chlorophyll c pigments (i.e. the chlorsome) found in green sulfur bacteria.[78,79]

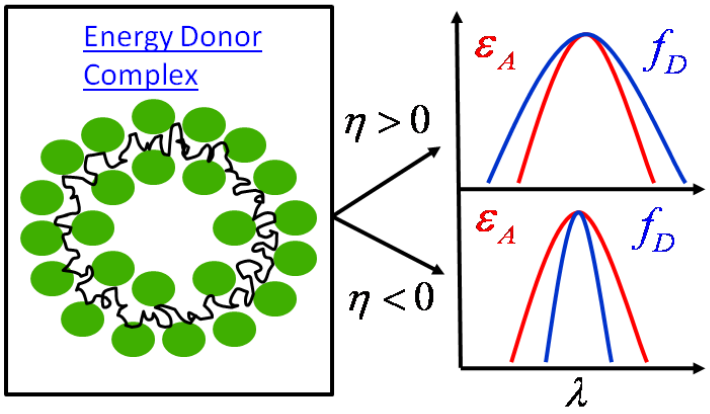

Figure 9.11. This Figure illustrates how correlations affect the energy donor function of the cylindrical aggregate in a composite system. With a fixed acceptor spectrum, ε_A, correlated ($\eta > 1$) and anti-correlated ($\eta < 1$) fluctuations respectively increase and decrease the width of the donor spectrum, thereby controlling its overlap with ε_A. The highest energy transfer efficiency is found when the widths of ε_A and f_D are equal [see Eq. (9.1)].

9.4.2. Length scale of bath fluctuations

The delocalization of exciton states over a large volume gives rise to small system-bath interaction strengths (i.e. electron-phonon couplings). The ability to correlate fluctuations at localized sites directly relates to the spatial extent of the excitons. Correlations between molecules in close proximity should dominate Eq. (9.4) because these molecular sites most readily interact with the same fluctuating coordinates in the environment. The shortest distance between molecules in the cylindrical aggregate is approximately 0.6 nm.[25] The nuclear coordinate in the solvent environment inducing molecular fluctuations must span a similar length scale.

It is possible that water fills the space inside the inner cylinder in addition to surrounding the outer cylinder. Experiments studying orientational relaxation of water observe signatures of a collective hydrogen bonded network at room temperature (i.e. the temperature at which the present data were obtained).[80] Perhaps the length scale of

correlated nuclear motion in water extends to 0.6 nm through bridging of hydrogen bonds. Confinement effects may additionally increase the length scale over which fluctuations persist in the inner cylinder.[81] It may also be that motion of the hydrophobic functional groups, which are thought to bundle in the interstitial region between the cylinder walls, drives the molecular fluctuations. These aliphatic chains extend over 8 bond lengths (~0.8 nm) and therefore readily satisfy the requirement that the environmental coordinate spans the 2 nm length scale.

9.5. CONCLUSION

The principal conclusion of this work is that correlated energy level fluctuations occur for the exciton localized on the inner cylinder and the exciton delocalized between the cylinder walls. Signatures of this correlation and their impact on an electronic coherence between the two states are revealed by two-dimensional photon echo spectroscopy. We have discussed how these correlations transform onto the fluctuations of the individual molecules comprising the aggregate. The shortest distance between molecules in the aggregate is estimated at 0.6 nm which means that the environmental nuclear coordinate modulating the energies at the molecular sites must also maintain correlation on this length scale. This environmental motion is most likely associated with the water confined inside the cylinder or with the aliphatic chains bundled between the cylinder walls. The importance of correlated exciton fluctuations for the function of a composite energy donor-acceptor system has been discussed and suggests important insights relevant to both biological and artificial systems based on this design principal. On-going work will incorporate the cylindrical aggregate into such a composite system with light-harvesting and charge separation processes.

The dynamics of the cylindrical aggregate may indeed be more complex than found here. Signal fields radiated by polarization components associated with electronic populations complicate the measurement of electronic coherence using photon echo spectroscopy. The present experiments represent a basis for forthcoming work applying new nonlinear spectroscopies to this molecular aggregate.[65] These new experiments isolate individual terms in the polarization, which are not readily separated by photon echo methods, for improved physical insight. Parameters essential to theoretical modeling and a deeper understanding of electronic relaxation dynamics in the cylindrical aggregate be obtained.

REFERENCES

(1) Blankenship, R. E. *Molecular Mechanisms of Photosynthesis*; Blackwell Science Ltd.: Oxford, 2002.

(2) Lawlor, D. *Photosynthesis, 3rd Edition*; Springer-Verlag: New York, 2001.

(3) Falkowski, P. G.; Raven, J. A. *Aquatic Photosynthesis*; Blackwell Science: Malden, MA, 1997.

(4) Pullerits, T.; Chachisvilis, M.; Sundström, V. *J. Phys. Chem.* 1996, *100*, 10787.

(5) Arnett, D. C.; Moser, C. C.; Dutton, P. L.; Scherer, N. F. *J. Phys. Chem. B* 1999, *103*, 2014.

(6) Engel, G. S.; Calhoun, T. R.; Read, E. L.; Ahn, T. K.; Mancal, T.; Cheng, Y. C.; Blankenship, R. E.; Fleming, G. R. *Nature* 2007, *446*, 782.

(7) Savikhin, S.; Buck, D. R.; Struve, W. S. *Chem. Phys.* 1997, *223*, 303.

(8) Parson, W. W. *Science* 2007, *316*, 1438.

(9) Book, L. D.; Ostafin, A. E.; Ponomarenko, N.; Norris, J. R.; Scherer, N. F. *J. Phys. Chem. B* 2000, *104*, 8295.

(10) Venkatramani, R.; Mukamel, S. *J. Chem. Phys.* 2002, *117*, 11089.

(11) Abramavicius, D.; Mukamel, S. *Chem. Rev.* 2004, *104*, 2073.

(12) Pisliakov, A. V.; Mancal, T.; Fleming, G. R. *J. Chem. Phys.* 2006, *124*, 234505.

(13) Demirdöven, N.; Khalil, M.; Tokmakoff, A. *J. Phys. Chem. A* 2001, *105*, 8025.

(14) Lee, H.; Cheng, Y.-C. *Science* 2007, *316*, 1462.

(15) Jonas, D. M. *Annu. Rev. Phys. Chem.* 2003, *54*, 425.

(16) Khalil, M.; Demirdöven, N.; Tokmakoff, A. *J. Phys. Chem. A* 2003, *107*, 5258.

(17) Piletic, I. R.; Moilanen, D. E.; Levinger, N. E.; Fayer, M. D. *J. Am. Chem. Soc.* 2006, *128*, 10366.

(18) Hochstrasser, R. M. *PNAS* 2007, *104*, 14189.

(19) Mukamel, S. *Annu. Rev. Phys. Chem.* 2000, *51*, 691.

(20) Shim, S.-H.; Strasfeld, D. B.; Ling, Y. L.; Zanni, M. T. *PNAS* 2007, *104*, 14197.

(21) Myers, J. A.; Lewis, K. L. M.; Tekavec, P. F.; Ogilvie, J. P. *Optics Express* 2008, *16*, 17420.

(22) Collini, E.; Scholes, G. D. *Science* 2009, *323*, 369.

(23) Kirstein, S.; Däehne, S. *Int. J. Photoener.* 2006, 1.

(24) von Berlepsch, H.; Böttcher, C.; Ouart, A.; Burger, C.; Däehne, S.; Kirstein, S. *J. Phys. Chem. B* 2000, *104*, 5255.

(25) Didraga, C.; Pugžlys, A.; Hania, R.; von Berlepsch, H.; Duppen, K.; Knoester, J. *J. Phys. Chem. B* 2004, *108*, 14976.

(26) Knoester, J. *Int. J. Photoener.* 2006, 1.

(27) von Berlepsch, H.; Kirstein, S.; Böttcher, C. *Langmuir* 2002, *18*, 7699.

(28) von Berlepsch, H.; Kirstein, S.; Hania, R.; Didraga, C.; Pugžlys, A.; Böttcher, C. *J. Phys. Chem. B* 2003, *107*, 14176.

(29) Pugžlys, A.; Hania, R.; Augulis, R.; Duppen, K.; van Loosdrecht, P. H. M. *Int. J. Photoener.* 2006, 1.

(30) Lampoura, S. S.; Spitz, C.; Däehne, S.; Knoester, J.; Duppen, K. *J. Phys. Chem. B* 2002, *106*, 3103.

(31) Milota, F.; Sperling, J.; Nemeth, A.; Kauffman, L. J. *Chem. Phys.* 2008, In Press.

(32) Riedle, E.; Beutter, M.; Lochbrunner, S.; Piel, J.; Schenkl, S.; Spörlein, S.; Zinth, W. *Appl. Phys. B* 2000, *71*, 457.

(33) Kobayashi, T.; Baltuska, A. *Meas. Sci. Technol.* 2002, *13*, 1671.

(34) Cowan, M. L.; Ogilvie, J. P.; Miller, R. J. D. *Chem. Phys. Lett.* 2004, *386*, 184.

(35) Goodno, G. D.; Dadusc, G.; Miller, R. J. D. *J. Opt. Soc. Am. B* 1998, *15*, 1791.

(36) Maznev, A. A.; Nelson, K. A.; Rogers, J. A. *Opt. Lett.* 1998, *23*, 1319.

(37) Moran, A. M.; Maddox, J. B.; Hong, J. W.; Kim, J.; Nome, R. A.; Bazan, G. C.; Scherer, N. F. *J. Chem. Phys.* 2006, *124*, 194904:1.

(38) Brixner, T.; Mancal, T.; Stiopkin, I. V.; Fleming, G. R. *J. Chem. Phys.* 2004, *121*, 4221.

(39) Khurmi, C.; Berg, M. A. *J. Phys. Chem. A* 2008, *112*, 3364.

(40) Underwood, D. F.; Blank, D. A. *J. Phys. Chem. A* 2003, *107*, 956.

(41) Gundogdu, K.; Stone, K. W.; Turner, D. B.; Nelson, K. A. *Chem. Phys.* 2007, *341*, 89.

(42) Kim, J.; Wong, C. Y.; Nair, P. S.; Fritz, K. P.; Kumar, S.; Scholes, G. D. *J. Phys. Chem. B* 2006, *110*, 25371.

(43) Lepetit, L.; Chériaux, G.; Joffre, M. *J. Opt. Soc. Am. B* 1995, *12*, 2467.

(44) Gallagher Faeder, S. M.; Jonas, D. M. *J. Phys. Chem. A* 1999, *103*, 10489.

(45) Tokunaga, E.; Terasaki, A.; Kobayashi, T. *J. Opt. Soc. Am. B* 1995, *12*, 753.

(46) Moran, A. M.; Nome, R. A.; Scherer, N. F. *J. Chem. Phys.* 2006, *125*, 031101:1.

(47) Christensson, N.; Dietzek, B.; Pascher, T.; Yartsev, A.; Pullerits, T. *Chem. Phys. Lett.* 2008, *457*, 106.

(48) Oskouei, A. A.; Bräm, O.; Cannizzo, A.; van Mourik, F.; Tortschanoff, A.; Chergui, M. *J. Mol. Liq.* 2008, *141*, 118.

(49) Keusters, D.; Warren, W. S. *J. Chem. Phys.* 2003, *119*, 4478.

(50) Yetzbacher, M. K.; Belebas, N.; Kitney, K. A.; Jonas, D. M. *J. Chem. Phys.* 2007, *126*, 044511:1.

(51) Trebino, R.; DeLong, K. W.; Fittinghoff, D. N.; Sweetser, J. N.; Krumbügel, M. A.; Richman, B. A. *Rev. Sci. Instrum.* 1997, *68*, 3277.

(52) Mukamel, S. *Principles of Nonlinear Optical Spectroscopy*; Oxford University Press: New York, 1995.

(53) Boyd, R. W. *Nonlinear Optics, Second Edition*; Academic Press: San Diego, 2003.

(54) Fleming, G. R. *Chemical Applications of Ultrafast Spectroscopy*; University Press: New York, 1986.

(55) Fidder, H.; Knoester, J.; Wiersma, D. A. *J. Chem. Phys.* 1993, *98*, 6564.

(56) Bednarz, M.; Knoester, J. *J. Phys. Chem. B* 2001, *105*, 12913.

(57) Davydov, A. S. *Theory of Molecular Excitons*; Plenum Press: New York, 1971.

(58) Capek, V.; Silinish, E. *Organic Molecular Crystals: Interaction, Localization, and Transport Phenomena*; AIP: New York, 1994.

(59) Scholes, G. D. *ACS Nano* 2008, *2*, 523.

(60) Styers-Barnett, D. J.; Ellison, S. P.; Park, C.; Wise, K. E.; Papanikolas, J. M. *J. Phys. Chem. A* 2005, *109*, 289.

(61) Styers-Barnett, D. J.; Ellison, S. P.; Mehl, B. P.; Westlake, B. C.; House, R. L.; Park, C.; Wise, K. E.; Papanikolas, J. M. *J. Phys. Chem. C* 2008, *112*, 4507.

(62) Hybl, J. D.; Albrecht Ferro, A.; Jonas, D. M. *J. Chem. Phys.* 2001, *115*, 6606.

(63) Cho, M. *Chem. Rev.* 2008, *108*, 1331.

(64) Pugžlys, A.; Augulis, R.; van Loosdrecht, P. H. M.; Didraga, C.; Malyshev, V. A.; Knoester, J. *J. Phys. Chem. B* 2006, *110*, 20268.

(65) Womick, J. M.; Miller, S. A.; Moran, A. M. *submitted to J. Phys. Chem. A* 2009.

(66) Sugisaki, M.; Fujiwara, M.; Yanagi, K.; Cogdell, R. J.; Hashimoto, H. *Photosynth. Res.* 2008, *95*, 299.

(67) Kleinekathöfer, U.; Schröder, M.; Schreiber, M. *J. Lumin.* 2005, *112*, 461.

(68) Cheng, Y. C.; Silbey, R. J. *Phys. Rev. Lett.* 2006, *96*, 028103:1.

(69) Olaya-Castro, A.; Lee, C. F.; Olsen, F. F.; Johnson, N. F. *Phys. Rev. B* 2008, *78*, 085115:1.

(70) Mancal, T.; Valkunas, L.; Read, E. L.; Engel, G. S.; Calhoun, T. R.; Fleming, G. R. *Spectroscopy* 2008, *22*, 199.

(71) Khalil, M.; Demirdöven, N.; Tokmakoff, A. *J. Chem. Phys.* 2004, *121*, 362.

(72) Nee, M. J.; Baiz, C. R.; Anna, J. M.; McCanne, R.; Kubarych, K. J. *J. Chem. Phys.* 2008, *129*, 084503:1.

(73) Rickard, M. A.; Pakoulev, A.; Mathew, N. A.; Kornau, K. M.; Wright, J. C. *J. Phys. Chem. A* 2007, *111*, 1163.

(74) Pakoulev, A.; Rickard, M. A.; Mathew, N. A.; Kornau, K. M.; Wright, J. C. *J. Phys. Chem. A* 2008, *112*, 6320.

(75) Moran, A. M.; Kelley, A. M. *J. Chem. Phys.* 2001, *115*, 912.

(76) Wang, Z.; Medforth, C. J.; Shelnutt, J. A. *J. Am. Chem. Soc.* 2004, *126*, 16720.

(77) Katterle, M.; Prokorenko, V. I.; Holzarth, A. R.; Jesorka, A. *Chem. Phys. Lett.* 2007, *447*, 284.

(78) Olson, J. M. *Photochem. Photobiol.* 1998, *67*, 61.

(79) Egawa, A.; Fujiwara, T.; Mizoguchi, T.; Kakitani, Y.; Koyama, Y.; Akutsu, H. *PNAS* 2007, *104*, 790.

(80) Moilanen, D. E.; Fenn, E. E.; Lin, Y.-S.; Skinner, J. L.; Bagchi, B.; Fayer, M. D. *PNAS* 2008, *105*, 5295.

(81) Moilanen, D. E.; Levinger, N. E.; Spry, D. B.; Fayer, M. D. *J. Am. Chem. Soc.* 2007, *129*, 14311.

CHAPTER 10. PROBING DYNAMICS OF INTRABAND ELECTRONIC COHERENCES IN MOLECULAR AGGREGATES

10.1. INTRODUCTION

Light harvesting proteins located in the photosynthetic antenna generally absorb light with exciton excited states delocalized over multiple pigments.[1-3] Weak interactions between these excited states and the surrounding solvent bath can sustain electronic coherences for significant length and time scales.[4-9] Recent experimental[6,10] and theoretical[11-14] work suggests the importance of these electronic coherences for energy transfer. However, the precise mechanism by which this "wave-like" energy transfer occurs is not yet well understood. Also remarkable is the persistence of phase coherence between exciton states for durations longer than population transfer times, which contrasts with conventional limitations on dephasing rates.[15-17] These initial observations raised the possibility that coherence in energy transfer requires biological fine tuning. However, it is quite astonishing that similar dynamics were recently detected in a conjugated polymer at room temperature.[18]

Experiments capable of probing electronic coherence are challenged by the attainment of adequate time resolution and the suppression of undesired population terms in the polarization response, which can dominate over those corresponding to electronic coherence. Pump-probe anisotropy experiments are one exception that has proven effective for probing coherence between excited states with large angles between their transition dipoles.[5,7,19] In addition, two-dimensional Fourier transform photon echo experiments detect

Adapted with permission from Womick, J.M.; Miller, S.A.; Moran, A.M. *J. Phys. Chem. A* 2009, *113*, 6587-6598.

electronic coherences as quantum beats in diagonal and cross peaks without special requirements regarding transition dipole orientations.[6,8,20-22] However, photon echo experiments investigating the dynamics of electronic coherences still must contend with undesired population terms in the nonlinear polarization. One recent experiment addresses this issue using a two-color laser pulse configuration to isolate signal components associated with electronic coherence.[23] The present work isolates these same signal components, but differs in that it utilizes lasers pulses possessing different colors and bandwidths.

This chapter describes the experimental and theoretical aspects of a specialized technique designed to examine intraband electronic coherences in molecular aggregates (i.e. coherences associated with pairs of single exciton states). The experiment uses multiplex array detection for one-step acquisition of intraband coherence spectra. In this way, it closely resembles multiplex coherent Raman spectroscopies applied to molecular vibrations, but additionally implements pulse delays to suppress signal contributions arising from improperly ordered field-matter interactions. Another important outcome of this pulse configuration is that the measured intraband coherence line widths are narrower than the inverse of the dephasing rates. This line narrowing effect is significant because it reduces spectral congestion and facilitates signal interpretation. Data acquisition times of a few seconds are obtained with use of interferometric signal detection and the generation of (synchronized) narrowband and broadband color tunable laser pulses. By contrast, the attainment of equivalent information by a time domain method would require approximately 30 minutes. Below we show that the ability of this experiment to quickly measure signals under various experimental conditions has already facilitated a deeper understanding of the C8O3 cylindrical aggregate composed of the monomer shown in Figure 10.1.

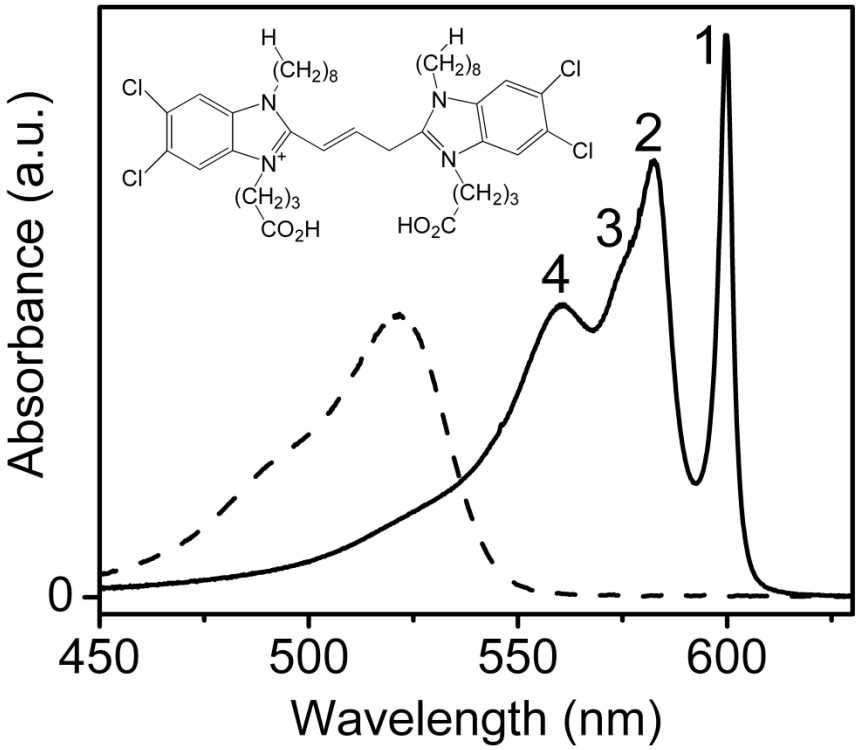

Figure 10.1. (Dashed) Absorption spectrum of monomer. (Solid) Absorption spectrum of cylindrical molecular aggregate in 0.01 M NaOH. The structure of the monomer is shown in the inset. The relative absorbances for the monomer and aggregate are unrelated.

Self-assembled aggregates of C8O3 have been the subject of several experimental[20,24-27] and theoretical studies.[28,29] The absorption spectrum for C8O3 in 0.01 M NaOH exhibits four peaks signifying the double-walled cylindrical structure (see Figure 10.1). The nature of the four electronic transitions has been investigated extensively[24-26] and is understood as follows: (1) the transition at 600 nm is localized on the inner cylinder; (2) the transition at 583 nm represents an exciton localized on the outer cylinder, (3) whereas the peak at 577 nm is more closely associated with the inner cylinder; (4) the highest energy transition at 560 nm represents an exciton delocalized between the inner and outer cylinder walls. Transitions 1, 2 and 4 are thought to have parallel transition dipoles, which are orthogonal to the dipole of transition 3.[30] We will hereafter refer to the single exciton excited

states corresponding to these transitions as states 1-4. Below we control the morphology of C8O3 by varying the concentration of methanol in an aqueous solution. The known correlation between methanol concentration and the aggregate morphology is owed to von Berlepsch et al. who characterized the structures using cryogenic transmission electron microscopy.[26] The aggregate retains its double-walled cylindrical structure at the methanol concentrations used here but increases its diameter to 11 nm, whereas a diameter of 10 nm is found in pure NaOH.

Recent applications of photon echo spectroscopy to C8O3 have discovered excited state electronic coherences persisting on the 100 fs time scale. Milota et al. investigated the dynamics of C8O3 in a mixture of water and octanol, where the aggregate self-assembles into a double-walled cylinder with a linear absorption spectrum dominated by two transitions.[20] Quantum beats were observed in the cross peak corresponding to the two single exciton states followed by population transfer from the higher to lower energy state at longer times. Another photon echo study by the same group examined C8O3 in pure NaOH solution, where the linear spectrum has four single exciton transitions (see Figure 10.1).[27] Incoherent non-radiative relaxation within the single exciton manifold was found to proceed with time constants between 109 and 833 fs. The authors observed no evidence of quantum beats in the photon echo measurements, which further motivates the development of techniques with greater sensitivity to these dynamics.

10.2. THEORY

10.2.1. Multiplexed Probing of Intraband Electronic Coherences

This Section develops a simplified model establishing the sensitivity of the present technique to intraband (i.e. single exciton band) electronic coherences in molecular

aggregates. It is shown that this sensitivity points to useful analogies with multiplexed coherent Raman spectroscopies applied to molecular vibrations.[31-34] Physical insight motivates the use of several approximations, which are later supported by numerical calculations in Section 10.2.3. In addition, the model identifies an interesting line narrowing effect, which enhances spectral resolution of the intraband electronic coherences beyond the conventional limitation imposed by the dephasing rates. That is, the experiment suppresses spectral congestion by measuring line widths narrower than homogeneous widths of the intraband resonances.

The fundamental observable in four-wave mixing spectroscopies is the signal field radiated by the sample, which under perfect phase-matching conditions is related to the third-order polarization by

$$E_S(t) = \frac{i2\pi l\omega_t}{n(\omega_t)c} P^{(3)}(t), \tag{10.1}$$

where $n(\omega_t)$ is the refractive index, l is the sample length, and c is the speed of light. The polarization, $P^{(3)}(t)$, is found by convoluting the material response function with three incoming fields as

$$\begin{aligned} P^{(3)}(t) = \int_0^\infty dt_1 \int_0^\infty dt_2 \int_0^\infty dt_3 \Big[R_1(t_1,t_2,t_3) - R_2^*(t_1,t_2,t_3) \Big] E_{NB2}(t-t_3) \\ \times E_{NB1}^*(t+T-t_3-t_2) E_{BB}(t+T-t_3-t_2-t_1) \\ + \Big[R_2(t_1,t_2,t_3) - R_1^*(t_1,t_2,t_3) \Big] E_{NB2}(t-t_3) E_{BB}(t+T-t_3-t_2) \\ \times E_{NB1}^*(t+T-t_3-t_2-t_1) \end{aligned} \tag{10.2}$$

where E_{NB1} and E_{NB2} are "narrowband" pulses, E_{BB} is the broadband pulse, T is the experimentally controlled delay defined in Figure 10.2(a), t_i are intervals between field-matter interactions. This Section focuses on the special case in which $R_i(t_1,t_2,t_3)$ neglects

coherence transfer transitions. Expressions for these terms, ${}^{0}R_i\left(t_1,t_2,t_3\right)$, terms valid in the homogeneous limit of line broadening are given in Appendix I; the superscript "0" [e.g. ${}^{0}R_i\left(t_1,t_2,t_3\right)$] signifies that coherence transfer transitions do not take place. Feynman diagrams corresponding to these four terms are shown in Figure 10.3(a). Additional terms accounting for coherence transfer will be discussed in the following section.

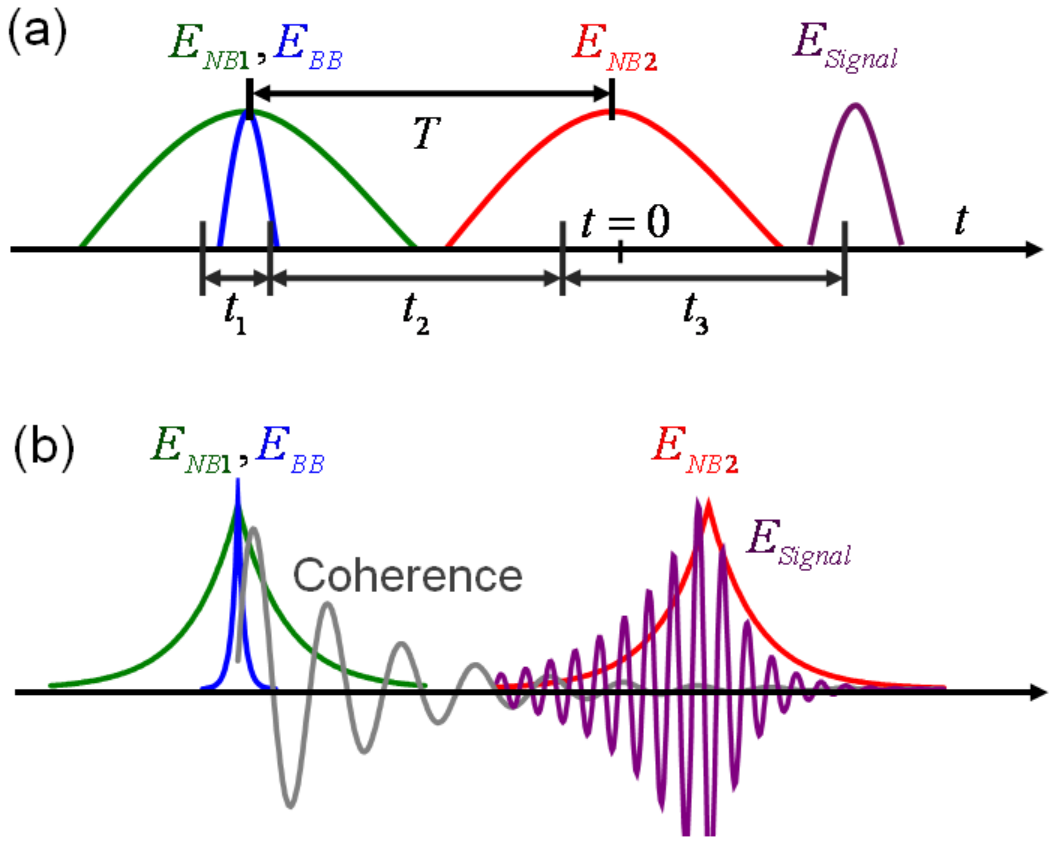

Figure 10.2. (a) Experimental pulse sequence. E_{NB1} (green) and E_{BB} (blue) are time-coincident, whereas E_{NB2} (red) arrives at the sample after an experimentally controlled delay, T. Intervals between field-matter interactions times are given as t_i. (b) Illustration of model outlined in Section 10.2.1. The narrowband (NB1, green) and broadband (BB, blue)

pulses interact with the material to produce an electronic coherence (gray) evolving at the frequency ω_{ab}. The signal field (purple) envelope is the product of the envelopes for the electronic coherence and E_{NB2} (red). The signal field frequency is given as the sum $\omega_{NB}+\omega_{ab}$ [Eq. (10.8)].

Evaluation of the integrals in Eq. (10.2) is simplified with three approximations. Approximation (1) removes the t_i intervals from the arguments of the two narrowband pulse envelopes. This approximation recognizes that the experimental implementation uses narrowband pulses with durations long compared to the dephasing times of the material coherences. Approximation (2) removes the t_1 and t_3 intervals from the argument of the broadband pulse envelope by the same argument as (1). This is generally not a strong approximation when using 20-30 fs broadband pulses but is reasonable here because the experiment is most sensitive to dynamics in t_2, whereas dynamics in t_1 and t_3 contribute indirectly. Approximation (3) assumes the spectral width of the broadband pulse is greater than the material line widths for individual exciton resonances, but not broad compared to the full manifold of single exciton transitions. The envelope of the broadband pulse is then written as a delta function but keep its imaginary frequency argument. Additional background on these approximations is given in Chapter 13 of Reference [16].

For illustration, we evaluate the polarization component associated with ${}^0R_1\left(t_1,t_2,t_3\right)$. For the purpose of integral evaluation, we assume applied fields with double-sided exponential envelopes (i.e. Lorentzian spectra)

$$E_j\left(t\right)=\exp\left(-i\omega_j t-\Lambda_j\left|t\right|\right) \tag{10.3}$$

This choice of field shape will facilitate the discussion line narrowing effects below. The ${}^0R_1\left(t_1,t_2,t_3\right)$ polarization component is given by

$$P_{{}^{0}R1}^{(3)}(t)=\int_0^\infty dt_1\int_0^\infty dt_2\int_0^\infty dt_3\ {}^{0}R_1(t_1,t_2,t_3)\,E_{NB2}(t)\,E_{NB1}^{*}(t+T)\exp\left[-i\omega_{St}(t+T-t_3-t_2-t_1)\right] \tag{10.4}$$

or with ${}^{0}R_1(t_1,t_2,t_3)$ from Appendix I as

$$\begin{aligned}P_{R1}^{(3)}(t)=&\left(\frac{i}{\hbar}\right)^3\mu_{gb}\mu_{ag}\mu_{bg}\mu_{ga}\exp\left[i\omega_{NB}T-i\omega_{BB}(t+T)-\Lambda_{NB}|t+T|-\Lambda_{NB}|t|\right]\\&\times\sum_{ab}\int_0^\infty dt_1\int_0^\infty dt_2\int_0^\infty dt_3\,\theta(t_1)\theta(t_2)\theta(t_3)\exp\left(-i\omega_{ag}t_1+i\omega_{BB}t_1-\Gamma_{ag}t_1\right)\\&\times\exp\left(i\omega_{ba}t_2-i\omega_{RS}t_2-\Gamma_{ab}t_2\right)\exp\left(-i\omega_{ag}t_3+i\omega_{BB}t_3-\Gamma_{ag}t_3\right)\\&\times\delta(t+T-t_2)\end{aligned} \tag{10.5}$$

where a and b are dummy indices, the summation involves all excited electronic states, and it is assumed that only the ground state, g, is populated at thermal equilibrium.[16,35] The integrals evaluate as

$$P_{R1}^{(3)}(t)=\left(\frac{i}{\hbar}\right)^3\mu_{gb}\mu_{ag}\mu_{bg}\mu_{ga}\sum_{ab}\sigma_{ag}^{2}(\omega_{St})\,\xi_{ab}(t) \tag{10.6}$$

where

$$\sigma_{ab}(\omega)=\left(\frac{1}{i\omega-i\omega_{ab}-\Gamma_{ab}}\right) \tag{10.7}$$

and

$$\xi_{ab}(t)=\theta(t+T)\exp\left[-i\omega_{ab}T-i(\omega_{NB}+\omega_{ab})t-\Gamma_{ab}(t+T)-\Lambda_{NB}|t|\right] \tag{10.8}$$

Equation (10.8) finds that the signal field shape primarily reflects dynamics occurring in the t_2 interval between field matter interactions. The signal frequency is shifted from that of the narrowband pulse, ω_{NB}, by an amount equal to the intraband coherence frequency, ω_{ab}; this is analogous to the Raman shift defined by coherent Raman spectroscopies probing vibrational resonances.[31-34] Furthermore, the signal field duration is governed by the

dephasing rate of the intraband coherence, Γ_{ab}. Figure 10.2(b) emphasizes the time-domain view of a line narrowing effect whose frequency domain interpretation is given below. The rising side of E^{*}_{NB2} (at negative t) convolutes with the decay of the $\rho_{ab}(t_2)$ electronic coherence when $T > \Lambda^{-1}_{NB}$. In this configuration, E^{*}_{NB2} is able to sustain the $\rho_{ab}(t_2)$ coherence for an amount of time greater than that imposed by the dephasing rate, Γ_{ab}.

The signal field shape is defined by the Fourier transform

$$\int_{-T}^{\infty} \xi_{ab}(t)\exp(i\omega_t t) = \frac{\exp\left[-(i\omega_{ab}+\Gamma_{ab})T\right]-\exp\left[\left(-i\omega_t+i\omega_{NB}-\Lambda_{NB}\right)T\right]}{i\omega_t - i\omega_{ab} - i\omega_{NB} - \Gamma_{ab} + \Lambda_{NB}} - \frac{\exp\left[-(i\omega_{ab}+\Gamma_{ab})T\right]}{i\omega_t - i\omega_{ab} - i\omega_{NB} - \Gamma_{ab} - \Lambda_{NB}} \tag{10.9}$$

The first and second terms on the right side of Eq. (10.9) predict the signal bandwidth to be narrower and broader than the pure homogeneous line width, Γ_{ab}, respectively. When the bandwidth of E_{NB} is much less than the line width of the coherence we have

$$\int_{-T}^{\infty} \xi_{ab}(t)\exp(i\omega_t t) \approx \frac{-\exp\left[\left(-i\omega_t+i\omega_{NB}-\Lambda_{NB}\right)T\right]}{-i\omega_t + i\omega_{ab} + i\omega_{NB} + \Gamma_{ab} - \Lambda_{NB}} \qquad \Gamma_{ab}/\Lambda_{NB} >> 1 \tag{10.10}$$

whereas when $\Gamma_{ab}/\Lambda_{RP} \approx 1$ and the pulse delay, T, is small

$$\int_{-T}^{\infty} \xi_{ab}(t)\exp(i\omega_t t) \approx -\frac{\exp\left[-(i\omega_{ab}+\Gamma_{ab})T\right]}{i\omega_t - i\omega_{ab} - i\omega_{NB} - \Gamma_{ab} - \Lambda_{NB}} \qquad \Gamma_{ab}/\Lambda_{NB} \approx 1,\ T \approx 0 \tag{10.11}$$

Equation (10.10) dominates under the experimental conditions defined in Section 10.3. The use of delays with $T > \Lambda^{-1}_{NB}$ reduces the spectral width of the signal because Γ_{ab} and Λ_{NB} enter the denominator with opposite signs. This is a key attribute to the present experiment because narrowing of the signal bandwidth reduces spectral congestion promotes resolution

of various intraband coherences in multi-level excitonic systems. This pulse configuration is readily adapted to coherent Raman spectroscopies probing vibrational resonances. Such an approach will be particularly useful for investigations of vibrations associated with excited electronic states, which are often broad and not easily separated from signals corresponding to electronic populations.[36]

10.2.2. Modeling Coherence Transfer in the Homogeneous Limit

This Section presents a model for the nonlinear spectroscopy introduced in Section 10.2.1 which accounts for coherence transfer processes in the homogeneous limit of line broadening. Expressions describing coherence transfer between density matrix elements are first presented. The model builds on Redfield theory[15] and an earlier treatment of collisional coherence transfer by Stenholm.[37] Wright and co-workers have captured the main features of their infrared coherence transfer spectroscopy with a similar model.[38,39] These formulas are then used to obtain response functions accounting for coherence transfer in the t_1, t_2 and t_3 intervals between field-matter interactions. Electric field polarization effects are also incorporated.

Coherence transfer dynamics between the density matrix elements, ρ_{ab} and ρ_{cd}, is described by a pair of coupled differential equations

$$\dot{\rho}_{ab}(t) = \left(-i\omega_{ab} - \Gamma_{ab} - \kappa_{ab,cd}\right)\rho_{ab}(t) + \kappa_{cd,ab}\rho_{cb}(t) \tag{10.12a}$$

$$\dot{\rho}_{cd}(t) = \left(-i\omega_{cd} - \Gamma_{cd} - \kappa_{cd,ab}\right)\rho_{cd}(t) + \kappa_{ab,cd}\rho_{ab}(t) \tag{10.12b}$$

where $\kappa_{ab,cd}$ is the coherence transfer rate corresponding to $\rho_{ab} \rightarrow \rho_{cd}$ and $\kappa_{cd,ab}$ is related to $\kappa_{ab,cd}$ by detailed balance. With the initial conditions, $\rho_{ab}(0) = \rho_{cd}(0)$, we obtain the solutions[37]

$$\rho_{ab}(t) \approx \eta_{cd,ab}\left[I_{cd}(t) - \left(1-\eta_{cd,ab}^{-1}\right) I_{ab}(t)\right] \tag{10.13a}$$

$$\rho_{cd}(t) \approx \eta_{ab,cd}\left[I_{ab}(t) - \left(1-\eta_{ab,cd}^{-1}\right) I_{cd}(t)\right] \tag{10.13b}$$

where

$$\eta_{ab,cd} = \frac{\kappa_{ab,cd}}{i\left(\omega_{cd}-\omega_{ab}\right)+\Gamma_{cd}-\Gamma_{ab}} \tag{10.14}$$

and the propagation function $I_{ab}(t)$ is given by Eq. (10.A5). Here it is assumed that only a single coherence transfer occurs (e.g. $\rho_{ab} \to \rho_{cd} \to \rho_{ef}$ is not allowed) because $\kappa_{ab,cd}, \kappa_{cd,ab} << \Gamma_{ab}, \Gamma_{cd}$.

Time evolution of $\rho_{cd}(t)$ is well-described by Eq. (10.13b) when $t << \left(\kappa_{ab,cd}+\Gamma_{ab}\right)^{-1}$. However, at longer times, the ρ_{ab} coherence may decay and no longer feed ρ_{cd} if $\Gamma_{ab} > \Gamma_{cd}$, which transforms the temporal beats at $\omega_{ab}-\omega_{cd}$ into evolution at the single frequency, ω_{cd}. That is,

$$\rho_{cd}(t) \approx \left(1-\eta_{ab,cd}\right) I_{cd}(t) \qquad t >> \left(\kappa_{ab,cd}+\Gamma_{ab}\right)^{-1} \tag{10.15}$$

A good approximation to the exact solution of Eq. (10.13b) is

$$\begin{aligned}\rho_{cd}(t) \approx \eta_{ab,cd} &\left\{\exp\left[-\left(\Gamma_{ab}+\kappa_{ab,cd}\right)t\right]\left[I_{ab}(t) - \left(1-\eta_{ab,cd}^{-1}\right) I_{cd}(t)\right]\right. \\ &\left.-\left(1-\exp\left[-\left(\Gamma_{ab}+\kappa_{ab,cd}\right)t\right]\right)\left(1-\eta_{ab,cd}^{-1}\right) I_{cd}(t)\right\} \\ \approx \eta_{ab,cd} &\left\{I_{ab}(t)\exp\left(-\Gamma_{ab}t-\kappa_{ab,cd}t\right) - \left(1-\eta_{ab,cd}^{-1}\right) I_{cd}(t)\right\}\end{aligned} \tag{10.16}$$

Equation (10.16) interpolates between solutions obtained at $t << \left(\kappa_{ab,cd}+\Gamma_{ab}\right)^{-1}$ and $t >> \left(\kappa_{ab,cd}+\Gamma_{ab}\right)^{-1}$. We have confirmed that Eq. (10.16) agrees with the converged numerical solution of Eq. (10.12). Similar equations can be written for $\rho_{ab}(t)$.

With Eq. (10.16), response functions accounting for coherence transfer dynamics can now be obtained. Each of the four diagrams in Figure 10.3(a) yields three additional terms corresponding to coherence transfer during each of the three time intervals between field-matter interactions. Feynman diagrams for all terms involving coherence transfer are shown in Figure 10.3(b). The response functions in Appendix J are obtained with Eq. (10.16) by defining a new propagation function for the t_i time interval in which coherence transfer occurs

$$K_{ab,cd}\left(t_i\right)=\eta_{ab,cd}\Phi_{ab,cd}\left\{-I_{cd}\left(t_i\right)+I_{ab}\left(t_i\right)\exp\left[-\left(\Gamma_{ab}+\kappa_{ab,cd}\right)t_i\right]\right\} \tag{10.17}$$

where the rule

$$\Phi_{ab,cd}=\left(1-\delta_{ab}\right)\left(1-\delta_{cd}\right)\left\{\delta_{ac}\left(1-\delta_{bd}\right)+\delta_{bd}\left(1-\delta_{ac}\right)+\left(1-\delta_{ac}\right)\left(1-\delta_{bd}\right)\right\} \tag{10.18}$$

restricts the summations over dummy indices to coherences (not populations) and also ensures that $\rho_{ab}\neq\rho_{cd}$ in the transition $\rho_{ab}\rightarrow\rho_{cd}$. To summarize, the ρ_{cd} density matrix element found by solution of Eq. (10.12) is written as the sum of two components

$$\rho_{cd}\left(t\right)=I_{cd}\left(t\right)+K_{ab,cd}\left(t\right) \tag{10.19}$$

(a) Feynman diagrams without coherence transfer

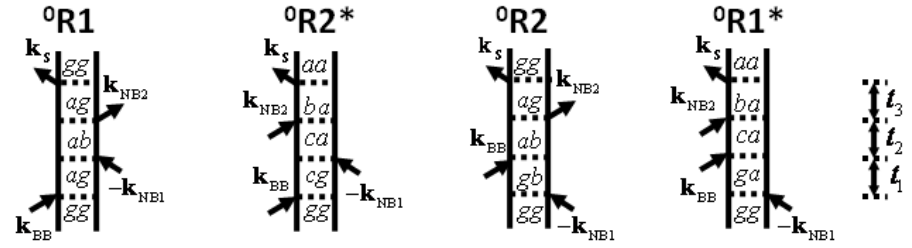

(b) Feynman diagrams with coherence transfer

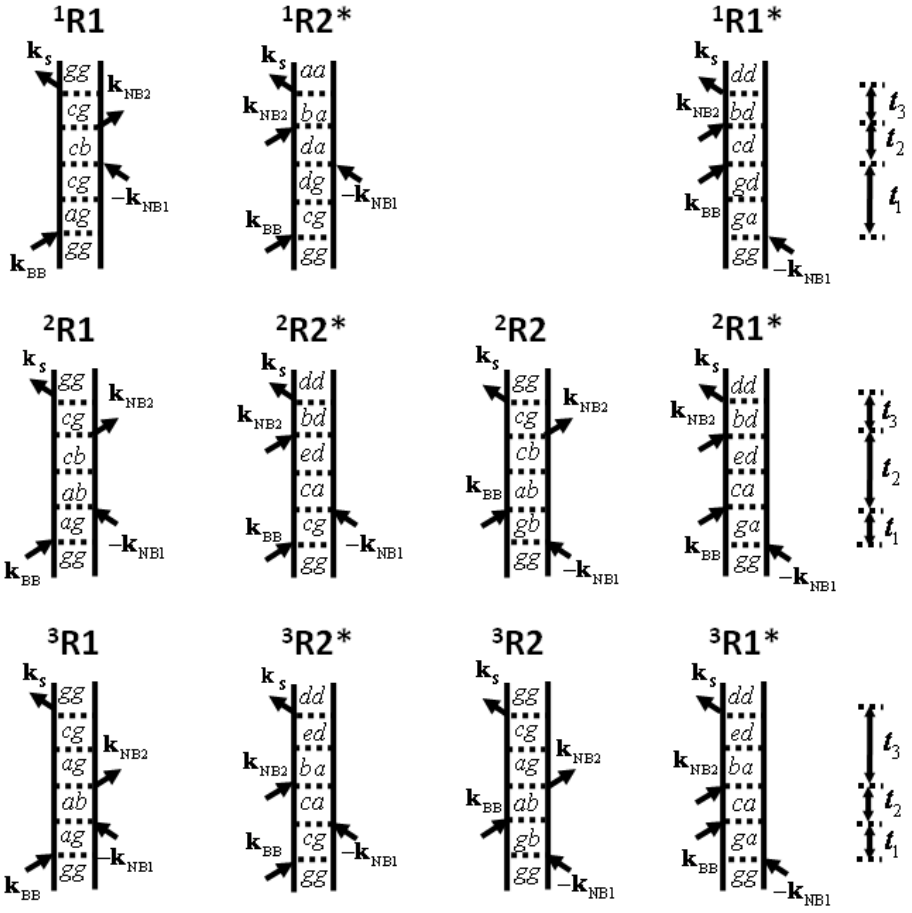

Figure 10.3. Feynman diagrams describing signal emission in the (a) absence and (b) presence of coherence transfer. The $^{0}\mathbf{R}$ terms in (a) do not involve coherence transfer. The response functions, $^{i}\mathbf{R}$, in (b) denote coherence transfer transitions in the time interval t_i. Index g represents the ground electronic state, whereas a, b, c, d and e are dummy indices running over all single and double exciton energy levels. Only resonant terms survive integration of Eq. (10.2).

Equation (10.19) shows that the full response function accounting for coherence transfer in t_i must superpose two terms. Appendix J addresses the component of the nonlinear response associated with the second term on the right side of Eq. (10.19). Essentially, the equations in Appendix J are obtained by substituting $K_{ab,cd}(t_i)$ of Eq. (10.17) for the corresponding $I_{ab}(t_i)$ function in Appendix I. This straightforward exchange of $I_{ab}(t_i)$ and $K_{ab,cd}(t_i)$ is possible in the limit of fast bath modulation (i.e. homogeneous limit of line broadening) because uncorrelated dynamics occur in the three time intervals.[16] For example, the $^{0}R_1$ term evolves according to $I_{ag}(t_1)$ in t_1, whereas $^{1}R_1$ [Eq. (10.B1)] describes coherence transfer in t_1 with substitution of $K_{ag,cg}(t_1)$. The $^{1}R_1$ Feynman diagram in Figure 10.3(b) shows that coherence transfers from $\rho_{ag}(t_1)$ to $\rho_{cg}(t_1)$ in t_1. The index a used for the t_2 and t_3 propagations functions in $^{0}R_1$ must then be replaced by index c for $^{1}R_1$. Thus, the products $I_{ag}(t_1)I_{ab}(t_2)I_{ag}(t_3)$ and $K_{ag,cg}(t_1)I_{cb}(t_2)I_{cg}(t_3)$ describe dynamics for the $^{0}R_1$ and $^{1}R_1$ terms, respectively.

Electric field polarization effects are readily accounted with bookkeeping of the material dipole with which each of the four fields interacts. Here the notation of Reference [40]

is used. For example, the tensor element for term ${}^0R_1$ is given as $\left\langle \alpha_{bg}\beta_{ga}\gamma_{gb}\phi_{ag} \right\rangle$, where the α, β, γ and ϕ indices respectively denote the polarizations of the fields, E_{NB1}, E_{BB}, E_{NB2} and E_S. We use this convention for all terms in the response function regardless of the order of field-matter interactions. Signal contributions by individual terms can then be discussed on the same footing given a particular lab frame tensor element (e.g. ZZXX or ZXZX). The ${}^1R_1$ term modifies the tensor notation of ${}^0R_1$ with the substitution $a \to c$ for all field-matter interactions following coherence transfer. The polarization tensor for ${}^1R_1$ is therefore written as $\left\langle \alpha_{bg}\beta_{ga}\gamma_{gb}\phi_{cg} \right\rangle$. Together with the $K_{ab,cd}(t_i)$ propagation function discussed in the previous paragraphs, the ${}^1R_1$ term in the response function is given by

$$ {}^1R_1(t_1,t_2,t_3) = \left(\frac{i}{\hbar}\right)^3 \sum_{abc} \left\langle \alpha_{bg}\beta_{ga}\gamma_{gb}\phi_{cg} \right\rangle K_{ag,cg}(t_1) I_{cb}(t_2) I_{cg}(t_3) \tag{10.20} $$

where a, b and c are dummy indices running over all excited electronic states. The other terms in Appendix J are found by the same procedure.

The full nonlinear response functions in Appendix K superpose all terms in Appendix J with those associated with the first term on the right side of Eq. (10.19). These additional terms radiate signals at times short compared to the inverse of the damping rate, which includes contributions from both dephasing and coherence transfer (i.e. these are the feeding coherences). For generalization to a multi-level system these feeding coherences must damp according the sum of all coherence transfer channels. Appendix K accounts for these parallel coherence transfer channels with an *ad hoc* damping rate, χ_{ab} [see Eq. (10.C6)], while still assuming $\kappa_{ab,cd}, \kappa_{cd,ab} << \Gamma_{ab}, \Gamma_{cd}$. A superior model will explicitly solve Redfield's

equations without restricting terms to a single coherence transfer within a particular time interval t_i. However, the present model captures the essential photophysics and establishes the information content of the experiment.

10.2.3. Model Calculations

Here Eq. (10.2) is numerically integrated to explore signatures of coherence transfer in a five level model system whose single exciton electronic structure resembles the C8O3 cylindrical aggregate. The line shapes and transitions dipoles of the model are parameterized for agreement with the spectroscopic measurements discussed in Section 10.4. Calculations will first examine the line narrowing effect predicted under several approximations in Section 10.2.1. We will then define general signatures of coherence transfer in the signal field amplitude, phase and polarization. Knowledge of these signatures will be used to interpret the measured signals in Section 10.4.

Figure 10.4(a) overlays the spectrum of E_{BB} and the E_{NB1} & E_{NB2} pulse pair on the linear absorption spectrum of a five level model system (see Appendix L). The narrowband pulses are tuned to the lowest energy single exciton transition at 16667 cm^{-1}, whereas the three higher energy transitions are in resonance with E_{BB}. The parameters of the model system, given in Table 10.1, are constrained by both the linear and nonlinear experimental measurements discussed in Section 10.4. Coherence transfer rate constants governing dynamics within a particular time interval are fixed to the same value for transitions in which the final coherence possesses a lower frequency than the initial coherence; the detailed balance condition is used to compute rate constants for the reverse processes. This constraint is applied to reduce the total parameter space. It is possible to achieve better agreement in

the experimental line shapes by freely varying all coherence transfer rates. However, the present model captures the essential physical insight needed to interpret the data below.

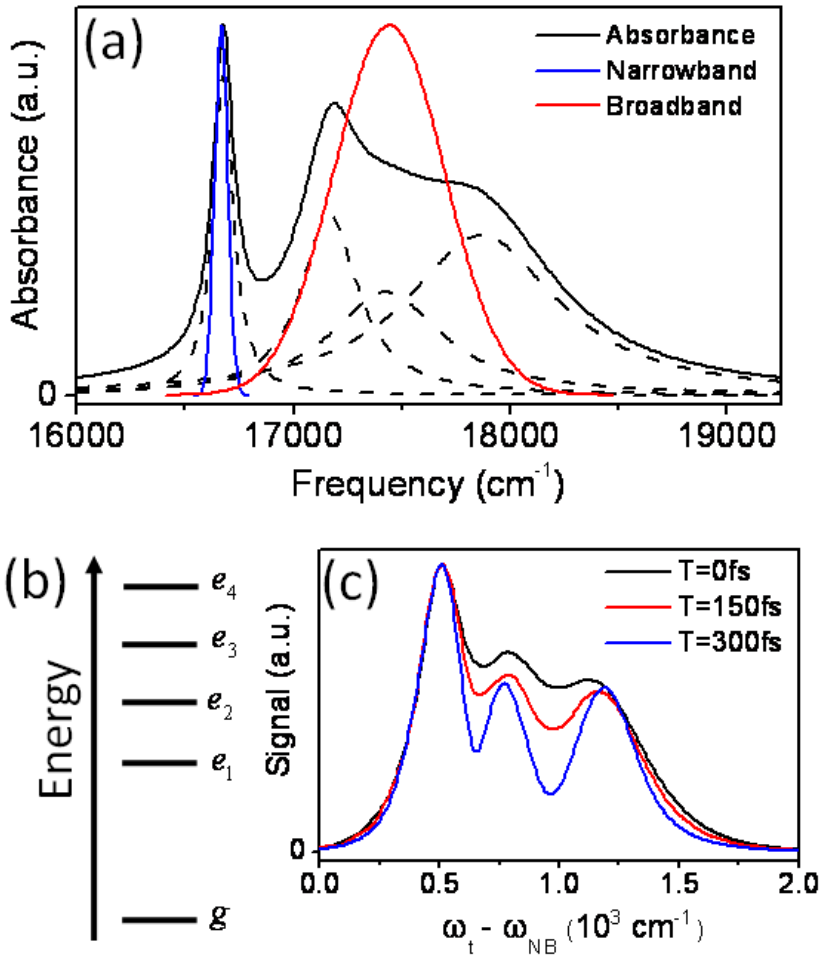

Figure 10.4. (a) Absorption spectrum (solid) of five-level model system computed with the parameters in Table 10.11. Dashed lines decompose the absorption spectrum into the sum of four electronic transitions. Overlayed are spectra of the narrowband (NB1 and NB2, blue) and broadband (BB, red) pulses. (b) Electronic structure of model system. (c) Nonlinear signal, $\left|P^{(3)}(\omega_t)\right|$, computed by numerical integration of Eq. (10.2) with the response function given in Appendix K. The frequency, $\omega_t - \omega_{NB}$, is the intraband coherence frequency (i.e. analogue of Raman shift).

Nonlinear signals computed by numerical integration of Eq. (10.2) are given in Figure 10.4(c) for laser pulses with all-parallel polarizations (i.e. ZZZZ tensor element). The signals

are computed with T=0, 150, and 300 fs. Comparison of the calculated signals reveals a clear narrowing of the line widths with increasing delay, T, as predicted by Section 10.2.1. Also significant is the presence of three peaks corresponding the three excited state electronic coherences in t_2; e_1 forms coherences with the higher energy electronic states, e_2, e_3, and e_4. This calculation supports the analogy of Section 10.2.1 between the present technique and a coherent Raman spectroscopy applied to vibrational resonances. That is, the dispersed signal reflects a Fourier transform of the dynamics occurring in t_2. The frequencies of the intraband coherences are given by $\omega_t - \omega_{NB}$.

Coherence transfer dynamics also manifest in the linear absorption spectrum. Figures 10.5(a) and 10.5(b) show that coherence transfer broadens the line widths of transitions in the linear spectra. For this reason, the linear spectra will represent a powerful constraint for the parameterization of nonlinear response functions. Spectral and temporal amplitudes of nonlinear signals are given in Figure 10.5(c) and 10.5(d) for the ZZZZ tensor element. These calculations compare three conditions: no coherence transfer; coherence transfer only in t_2; coherence transfer in t_1, t_2 and t_3. The neglect of coherence transfer in t_2 has a major effect on the spectral and temporal profiles. The spectral amplitudes skew towards smaller and larger frequencies, $\omega_t - \omega_{NB}$, in the presence and absence of coherence transfer. Essentially, these calculations reflect the dominance of terms transitioning into lower frequency coherences (i.e. $\rho_{e2,e1}$); the reverse processes contribute more weakly because of detailed balance. By contrast, the absence of coherence transfer in t_1 and t_3 has a relatively minor effect on the signals. In part, this reflects the fact these transitions are taken to be 20 times slower due to constraints imposed by the linear spectrum (see Section 10.4). The temporal

amplitudes in 5(e) give similar information. The presence of multiple spectral peaks manifests as quantum beats between coherences in the time domain, whereas the spectral line widths govern the signal pulse duration. The calculations in Figures 10.5(e) and 10.5(f) lead to the same insight for the ZXZX tensor element.

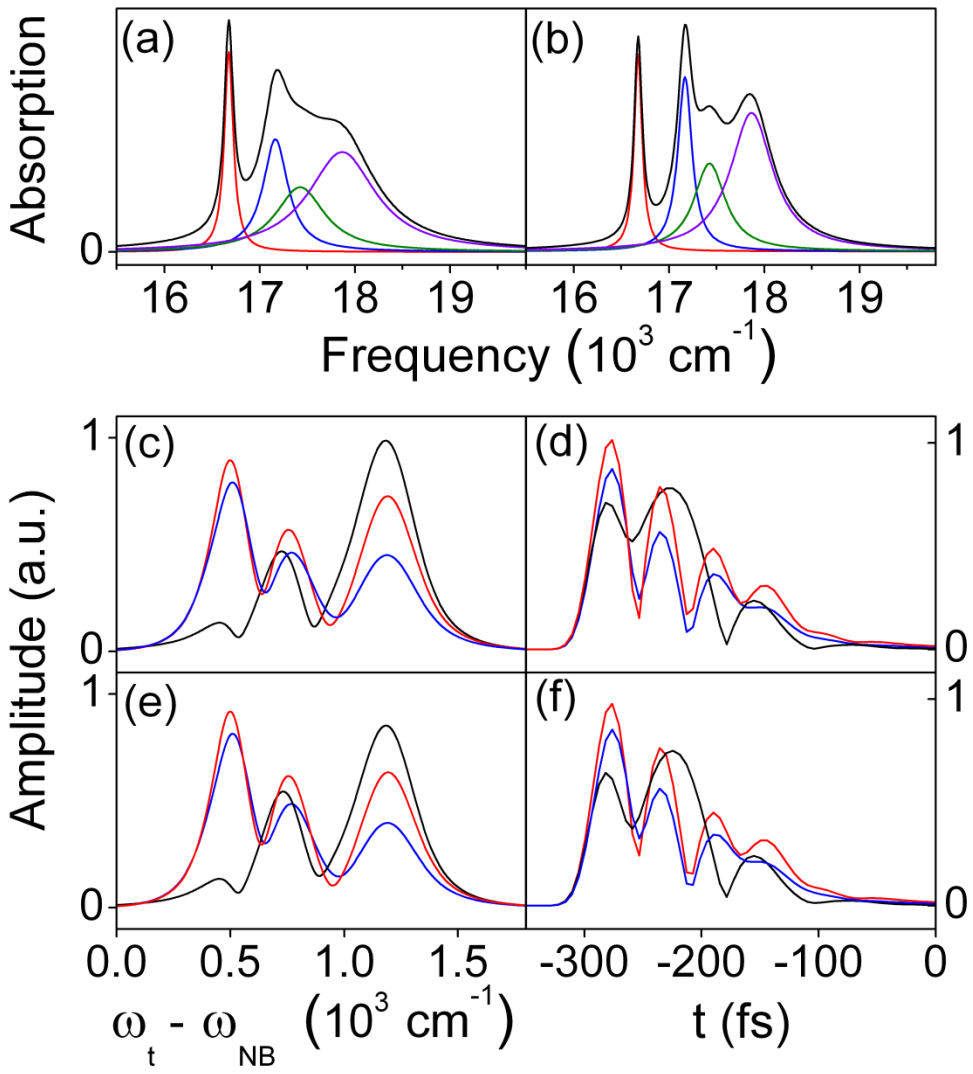

Figure 10.5. (a) Absorption spectrum (solid) of five-level model system computed with the parameters in Table 10.1. Dashed lines decompose the absorption spectrum into the sum of four electronic transitions. (b) Absorption spectrum (solid) of five-level model system computed with the parameters in Table 10.1, except that all interband coherence transfer rate constants, $\kappa_{eig,ejg}^{-1}$, are equal to zero. Nonlinear signals are computed by numerical integration

of Eq. (10.2) with the response function given in Appendix K: (c), (e) $\left|P^{(3)}\left(\omega_t\right)\right|$; (d), (f) $\left|P^{(3)}\left(t\right)\right|$. Panels (c)-(d) and (e)-(f) respectively represent the ZZZZ and ZXZX tensor elements. Calculations are performed with three sets of parameters: (black line) Table 10.1 except all coherence transfer rates are zero; (red line) Table 10.1 except all interband coherence transfer rate constants, $\kappa_{eig,ejg}^{-1}$, are equal to zero; (blue line) all parameters of Table 10.1 are used.

Figure 10.5 confirms that the signal closely reflects dynamics of the intraband coherences during the t_2 interval as suggested by Section 10.2.1. The signal field (i.e. amplitude and phase) possesses both temporal and spectral information on these dynamics with resolution governed by the line width of the narrowest resonance. Spectrograms are a useful representation for complex electric fields and can be calculated with[41-43]

$$S\left(t,\omega_t\right)=\left|\int_{-\infty}^{\infty}d\tau E_S\left(\tau\right)g\left(t-\tau\right)\exp\left(-i\omega_t\tau\right)\right| \tag{10.21}$$

where $g\left(t-\tau\right)$ is a gate function and $E_S\left(\tau\right)$ is the measured signal field. The right side of Eq. (10.21) is not squared for enhancement of the weakest features in the signal. The calculations below take $g\left(t-\tau\right)$ to be a Gaussian function with a width equal to that of the broadband pulse. $S\left(t,\omega_t\right)$ essentially decomposes the signal field, $E_S\left(\tau\right)$, into individual intraband coherences identified by the detection frequency ω_t (i.e. coherence frequency is $\omega_t-\omega_{NB}$). A slice of $S\left(t,\omega_t\right)$ at ω_t informs on the dynamics in t_2 which map onto t by the argument of Section 10.2.1.

Signal spectrograms computed with Eqs. (10.2) and (10.21) are given in Figure 10.6; these calculations use the same six sets of parameters as Figures 10.5(a)-5(d). The first row presents ZZZZ, ZXZX and ZZZZ-ZXZX tensor elements for a system with all coherence transfer rates set equal to zero; parameters are otherwise given by Table 10.1. The ZZZZ and

ZXZX time-frequency shapes appear quite similar, whereas the difference shows that the ZZZZ element dominates at greater coherence frequencies with a weak negative feature (<2.5% signal amplitude) near $\omega_t - \omega_{NB}$=300 cm^{-1}. The calculation in the second row additionally allows for coherence transfer in t_2 (not in t_1 or t_3). Signal emission at smaller coherence frequencies, $\omega_t - \omega_{NB}$, is greater than that calculated without coherence transfer due to the spectral skew found in Figures 10.5(c) and 10.5(d). The difference ZZZZ-ZXZX reveals dominance of the ZZZZ elements at shorter times and higher frequencies, whereas the negative feature reflects accumulation of coherence at lower frequencies. The "boomerang" shape of the positive feature reflects the change in the orientation of transition dipole radiating the signal field that occurs as coherence transfers to lower frequencies, $\omega_t - \omega_{NB}$, with increasing t_2; the Feynman diagrams in Figures 10.3(a) and 10.3(b) have different tensor elements. Calculations in the third row allow coherence transfer in all three time intervals. The individual tensor elements possess greater amplitude at smaller coherence frequencies than those in panels (d) and (e); this means that coherence transfer finds the lowest frequency coherence in t_1. The difference, ZZZZ-ZXZX, has a shape similar to that in panel (f), but exhibits less amplitude near t=185 fs and $\omega_t - \omega_{NB}$=600 cm^{-1}.

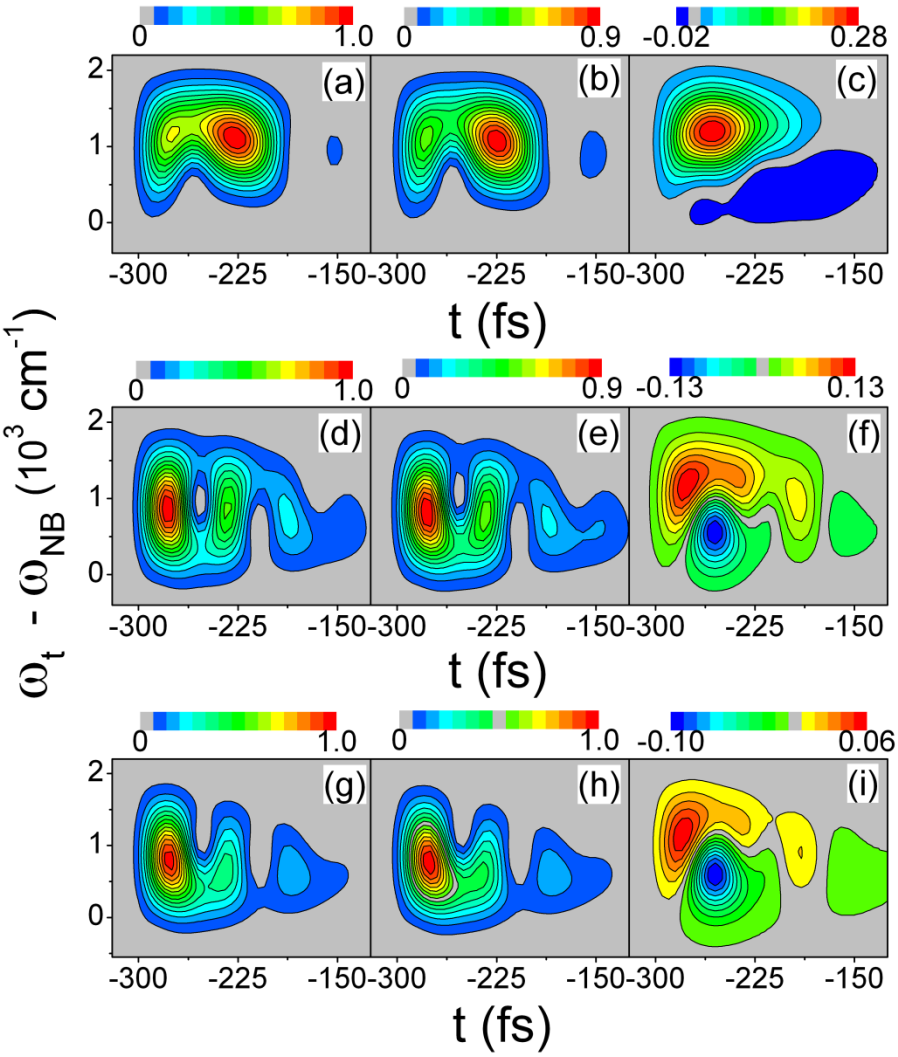

Figure 10.6. Equation (10.2) is integrated with the response function in Appendix K. Spectrograms are computed with Eq. (10.21), where the gate with is equal to the 25 fs. Calculations are performed with three sets of parameters: (a)-(c) Table 10.1 except all coherence transfer rates are zero; (d)-(f) Table 10.1 except all interband coherence transfer rate constants, $\kappa_{eig,ejg}^{-1}$, are equal to zero; (g)-(i) parameters of Table 10.1 are used. The first, second and third columns respectively correspond to the ZZZZ, ZXZX and ZZZZ-ZXZX tensor elements.

To summarize, the calculations presented in this section identify two general signatures of coherence transfer. First, simultaneous fitting of linear and nonlinear signals provides a powerful constraint on the parameters. For example, Figure 10.5 shows that

coherence transfer in t_2 skews the spectral amplitude towards smaller coherence frequencies; this effect is readily detectable by comparison with nonlinear signals computed using transition dipole magnitudes set by a fit to the linear spectrum. Pump-probe measurements will be useful for defining further constraints. We have also defined signatures of coherence transfer in the signal field shape for the difference in tensor elements, ZZZZ-ZXZX. In general, coherence transfer skews the time-frequency shape towards increasing t and decreasing $\omega_t - \omega_{NB}$. However, this effect may represent only a small fraction of the total signal. Changes in the tensor element should therefore be leveraged for increased sensitivity. The appearance of the ZZZZ-ZXZX spectrogram depends on the transition dipole orientations, which can be obtained by reproducing the ratio in spectral amplitudes for the two signal fields with constraint by the linear spectrum. For the present model system, which is motivated by the C8O3 cylindrical aggregate, a sign change in the signal is predicted with increasing t and decreasing $\omega_t - \omega_{NB}$.

10.3. EXPERIMENT

The C8O3 dye molecule shown in the inset of Figure 10.1 was purchased from FEW Chemicals and used without further purification. Solutions of C8O3 in 10 mM NaOH were diluted with methanol by use of a volumetric pipette to (vol %) concentrations of 0, 5, 10, 13 and 15. At methanol concentrations greater than 15%, absorption of the monomer at 520 nm becomes comparable to that associated with the aggregate.[26] All solutions were prepared with concentrations giving an absorbance of 0.3 at 600 nm in a 1 mm path length sample cell. The resulting absorbance spectra reproduce those shown in Figure 10.1 of Reference [26].

Experiments are based on a Quantronix Integra C Titanium Sapphire amplifier producing 120 fs, 800 nm, 2.0 mJ laser pulses at 1 kHz. This laser system pumps two

separate home-built optical parametric amplifiers (OPA) for generation of both broadband and narrowband laser pulses tunable between 500 and 750 nm. The broadband pulses are produced in a standard noncollinear OPA (NOPA)[44-46] in which the 400 nm pump pulses are stretched to 450 fs duration by transmission through a 20 cm fused silica glass block (ESCO Products). Figure 10.7(a) shows that the NOPA spectrum spans the 500-750 nm wavelength range. A portion of the full spectrum is filtered in a fused silica prism compressor for use in as the broadband pulse in experiments.

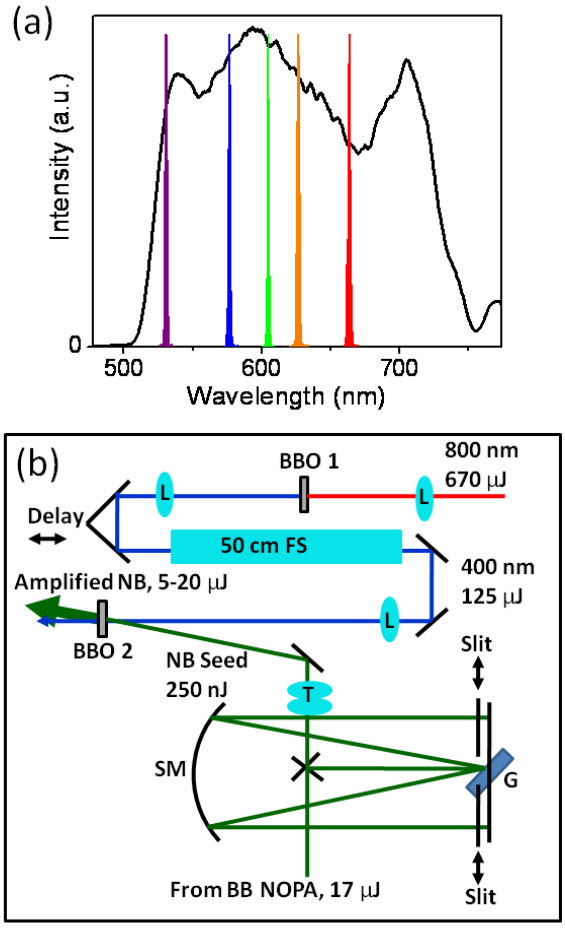

Figure 10.7. (a) Spectrum for broadband NOPA (black) used to seed NB OPA and typical spectra for tunable amplified NB pulses. (b) Schematic for NB-OPA showing 30 cm focal length lenses (L); telescope composed of 7.5 cm and -5.0 cm focal length lenses (T); 20 cm focal length spherical mirror (SM); 1200 g/mm grating (G); 50 cm of fused silica glass (50

cm FS); BBO1 is 0.7 mm thick, Type I, and θ=29.2º; BBO2 is 1.5 mm thick, Type I, and θ=31.5º.

The narrowband OPA (NB-OPA) used here is seeded with a portion of the broadband NOPA ouput (17 μJ), which is then spectrally filtered in an all-reflective, grating-based compressor aligned for zero dispersion (i.e. a 4F setup) as shown in Figure 10.7(b).[47,48] Translation of the slit position at the 2F plane selects portions of the broadband NOPA spectrum centered at different frequencies with bandwidths as narrow as 20 cm^{-1}. The slit width was set to filter 70 cm^{-1} pulses for the present measurements. Amplification of the (100-250 nJ) narrowband seed pulse without significant spectral broadening requires that the pump pulse duration is greater than or equal to that of the broadband seed.[49,50] Chirped pump pulses with 1 picosecond durations are obtained by first producing 125 microjoule, 400 nm pulses as the second harmonic of the compressed laser fundamental then stretching the 400 nm pulse by transmission through 50 cm of fused silica. The narrowband seed pulse is amplified in a BBO crystal with the chirped pump pulses using a collinear geometry.

The interferometer shown in Figure 10.8 resembles earlier nonlinear spectroscopy experiments in that the laser beam geometry is generated with a diffractive optic (DO) for passively phase-stabilized interferometric signal detection.[43,51-58] We use a 1 mm thick fused silica DO producing an angle of 4.5 degrees between the +/-1 diffraction orders at 575 nm (Holoeye). The broadband and narrowband laser pulses are spatially overlapped at the DO to produce two pulse pairs. A fused silica glass window and a pair of 175 μm thick microscope cover slips (Fisher Scientific) are placed in path of the broadband pulse to control its delay with respect to the local oscillator, which is a replica of the broadband pulse (i.e. a different diffraction order). The local oscillator pulse is attenuated with a 2 mm thick BK7 neutral

density filter (OD=3) and arrives at the sample 800 fs before the broadband pulse. Additional glass cover slips are placed in the E_{NB2} beam path to implement the delay, T =300 fs (see Figure 10.2). The signal is collinear with the local oscillator after the sample by the $\mathbf{k}_S = -\mathbf{k}_{NB1} + \mathbf{k}_{BB} + \mathbf{k}_{NB2}$ phase matching geometry. Pulse energies at the sample are 5 and 15 nJ for the broadband and narrowband pulses, respectively. Signals are detected in line-binning mode with a back-illuminated CCD array (Princeton Instruments PIXIS 100B) mounted on a 0.3 meter spectrograph (Princeton Instruments).

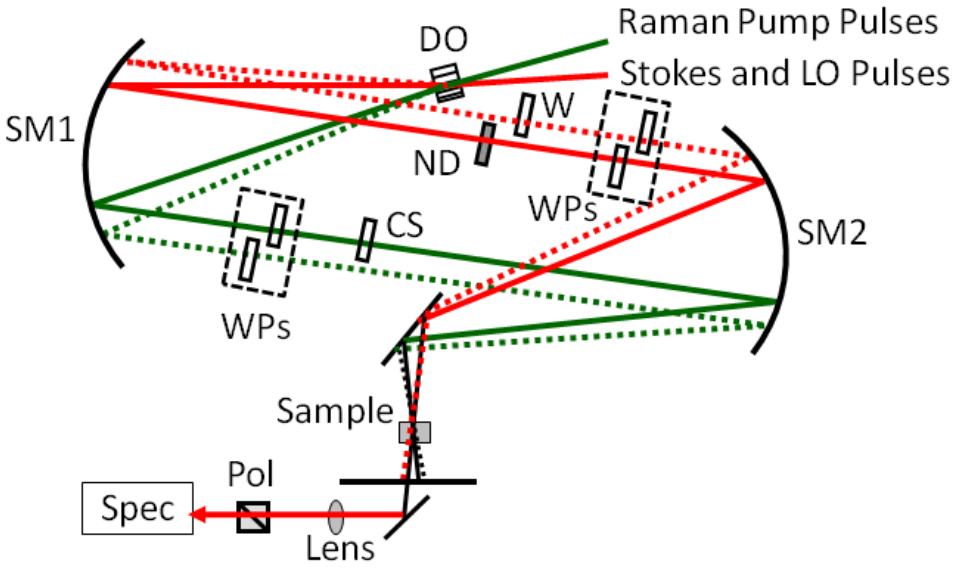

Figure 10.8. Diffractive optic (DO) based interferometer: 30 cm focal length spherical mirror (SM1); 20 cm focal length spherical mirror (SM2); 2 mm thick BK7 neutral density filter (ND); 2 mm thick fused silica window (W); half-waveplates (WPs); polarizer (Pol.); spectrometer (Spec).

Scattered light from the broadband laser pulse is subtracted by chopping the narrowband pulses with a mechanical shutter and calculating the difference, narrowband pulses on – narrowband pulses off. Each spectrum represents the average of 10 differences with 250 ms integrations times for a total data acquisition time of less than 5 seconds. The

short data acquisition time helps to avoid sample degradation, which is observed after approximately 5 minutes exposure to the laser pulses. The sample is held in a 1 mm thick cell (0.4 mL) with an open slit top and is gently stirred during the experiment with a piece of inert plastic mounted on an electric toothbrush motor. Under these conditions, we observe no changes in the linear absorption spectra during the course of the experiment.

Phase-resolved signals are obtained with signal detection by spectral interferometry.[42,59,60] This chapter detects and processes four-wave mixing signal by the same algorithm used in earlier photon echo[42,54,61] and transient grating experiments.[43] Attainment of passively phase-stabilized signal and local oscillator field with multiplex coherent Raman pulse configurations is discussed in Reference [62]; these same issues apply to the present experiment.

The quasi-instantaneous nonlinearity of the transparent solvent can give rise to significant signal emission in four-wave mixing spectroscopies when the laser pulses are overlapped in the sample.[63,64] The experiments in this chapter use a pulse delay, T =300 fs, with 210 fs narrowband and 25 fs broadband laser pulses. We measure no signal radiated by the quasi-instantaneous nonlinearity of the solvent under these conditions. Raman transitions of the aqueous solvent are not observed. However, this is not a general result. Raman transitions of solvents with stronger responses (e.g. toluene) are observed with these experimental conditions.

Calibration of the absolute phase is particularly difficult because the measurement of different tensor elements requires rotation of the waveplates (see Figure 10.8), which disrupts the signal phase. In principle, the signal phase for the solutions can be determined by comparison to Raman transitions of the pure solvent (i.e. an internal standard). However,

Raman transitions of the aqueous solutions used here are quite weak and broad which prohibits reliable characterization of the absolute phase. The measurements below define a sensitive probe of relaxation dynamics based on the comparison of higher order spectral phases measured under different polarization conditions. Knowledge of the absolute phase is not essential to the experimental information content.

10.4. RESULTS AND DISCUSSION

10.4.1. Effect of Methanol on Linear Absorption Spectra of C8O3

Linear absorption spectra of solutions containing various concentrations of methanol are shown in Figure 10.9. Significant changes in the absorption spectra are observed as the methanol concentration increases from 0%-15%: transition 1 (see Figure 10.1) shifts to longer wavelengths; transitions 2-4 are replaced with a single band centered at 575 nm. The morphologies associated with the solvent mixtures were investigated with cryo-transmission electron microscopy and circular dichroism measurements by von Berlepsch et al.[26] The authors found that methanol induces a 1 nm increase in the 10 nm cylinder diameter measured for the pure NaOH solution. It was concluded that methanol must cause significant reorganization of the molecules within the cylinder without inducing changes in the overall shape.

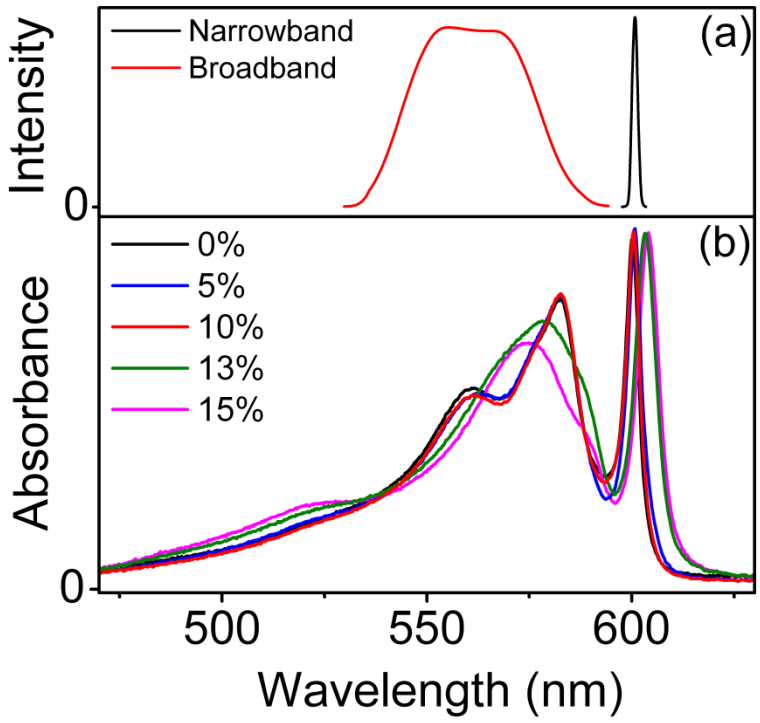

Figure 10.9. (a) Spectra of Raman pump (black) and Stokes (red) pulses. (b) Absorption spectra of 0.01 M NaOH solutions of cylindrical aggregates with various (vol%) concentrations of methanol.

10.4.2. Effect of Morphology on Nonlinear Response

Spectral and temporal amplitudes of signals measured for both the ZZZZ and ZXZX tensor elements are shown in Figure 10.10. The similar signal amplitudes found for both tensor elements indicates that the transition dipole connecting the ground state to the lowest energy single exciton level is nearly 55° relative to the other single exciton transition dipoles.[40] These transition dipole were already interpreted as being either parallel or perpendicular to that of the lowest energy transition[30] as require for an ideal cylinder.[29] One explanation for this discrepancy is the helical twisting of multiple tubules;[24] deviation from the straight tubular shape breaks the symmetry which causes the transition dipoles to align either parallel or perpendicular to the long axis of the tube.[29] In addition, the transition

dipole orientations were assigned based on experiments for a solution in a flow system, whereas the present measurements stir the solution. It may be that flowing the solution suppresses bundle formation and/or forces straightening of the tubes. We have confirmed that the absorption spectra are robust to sample stirring and that the absorption spectrum is independent of the electric field polarization (i.e. isotropic sample).

The spectral amplitudes in the first column of Figure 10.10 exhibit three peaks representing each of the three coherences between the exciton localized to the inner cylinder and those at higher energies. The lowest energy coherence exhibits the strongest response despite the relatively small spectral overlap of the broadband pulse with transition #2 in the linear spectrum (see Figure 10.9). Figure 10.10 also shows that increasing the methanol concentration reduces the signal strength for the ZZZZ tensor elements compared to ZXZX. One clear difference between the experimental and measured spectral amplitudes is that they possess resonances at frequencies, $\omega_t - \omega_{NB}$, of 800 and 900 cm^{-1}, respectively. Better agreement with the nonlinear measurement is readily achieved by increasing the value of the parameter ω_{e2g} (see Table 10.1). However, this worsens the fit to the linear spectrum. It is possible that the assumption of four exciton states is not adequate for describing the nonlinear measurement. That is, an exciton contributing weakly to the linear spectrum may be involved in particularly long-lived intraband coherences if thermal fluctuations in its energy are correlated with the other exciton states.[23] This issue is still under investigation.

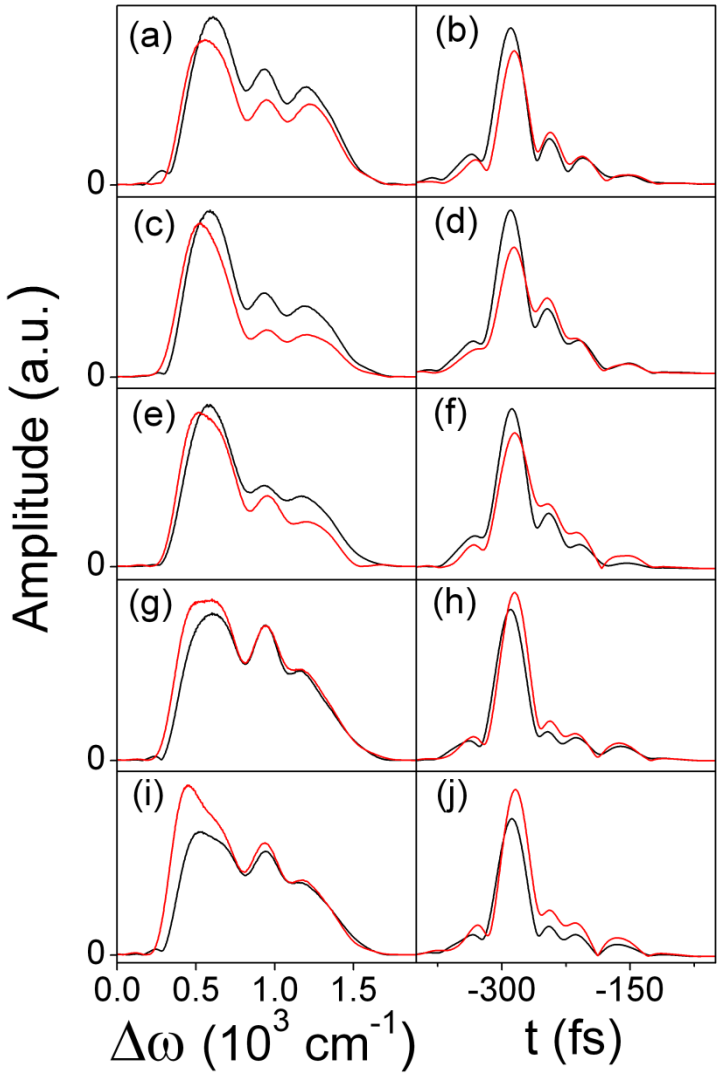

Figure 10.10. Measured spectral, $\left|E_S(\omega_t)\right|$, and temporal, $\left|E_S(t)\right|$, signal field amplitudes are shown in the left and right columns, respectively. The rows organize data by (vol%) concentrations of methanol: (a)-(b) 0%; (c)-(d) 5%; (e)-(f) 10%; (g)-(h) 13%; (i)-(j) 15%. The frequency axis for the left column is defined as $\Delta\omega = \omega_t - \omega_{NB}$.

The temporal amplitudes in the second column tell a story similar to the spectral amplitudes in the first column. The presence of multiple coherences gives rise to quantum beats in the signal field. These beats are most pronounced for 0% and 5% methanol

concentrations. Comparison of the temporal profiles for different tensor elements points to the t-dependent polarization effect discussed in Section 10.2.3. At low methanol concentrations, the ZZZZ amplitude dominates at t<-260 fs, whereas ZXZX is larger for t>-260 fs. The response to different tensor elements is changing due to dynamics in t_2. Further interpretation is made possible by the time-frequency representation.

Spectrograms corresponding to the ZZZZ and ZXZX tensor elements are shown in Figure 10.11, where each row represents a different methanol concentration. Differences in the spectrogram shapes are not readily seen by inspection. However, the experimental spectrograms with methanol concentrations <13% exhibit shapes most similar to the calculated spectrograms shown in Figures 10.6(g) and 10.6(h). Specifically, the experimental and calculated spectrograms both possess a "U-shaped" feature near t=-200 fs. By contrast, the calculated spectrograms in Figures 10.6(d) and 10.6(e) exhibit an upside down "U-shaped" feature. The parameters used to compute these signals identify this as a signature of coherence transfer in the t_1 time interval. That is, coherence transfer in the t_1 increases the strength of terms in which coherence is initiated at lower frequencies in t_2.

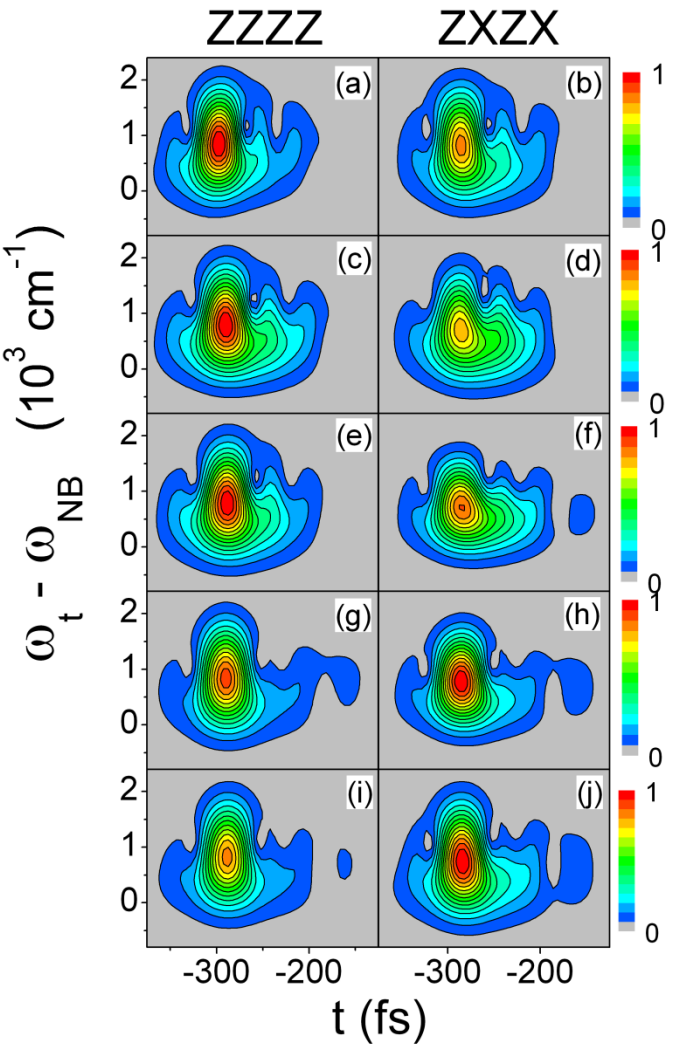

Figure 10.11. Signal field spectrograms, $S(t,\omega_t)$, measured under the ZZZZ (left) and ZXZX (right) polarization conditions for 0.01 M NaOH solutions of cylindrical aggregates with various (vol%) concentrations of methanol: (a)-(b) 0%; (c)-(d) 5%; (e)-(f) 10%; (g)-(h) 13%; (i)-(j) 15%.

Difference spectrograms are presented in Figure 10.12. At methanol concentrations less than 13%, the measured signals exhibit a sign change similar to that calculated in Figure 10.6(i), where the spectrogram measured for the 10% methanol solution is in best agreement with the calculation. We interpret these data as reflecting coherence transfer for solution

with less than 13% methanol concentration. The experiment does not necessarily rule out coherence transfer processes for methanol concentrations greater than 10%; fast dephasing may suppress the observation. Figure 10.9 shows that the four distinct single exciton transitions merge into two bands at methanol concentrations greater than 10%. Resolution of the individual single exciton transitions is lost, which may indicate fast dephasing dynamics for this morphology. It is interesting that the line narrowing capability of the nonlinear technique makes possible the observation of three coherences in Figures 10.10(g) and 10.10(i) even though the transitions are unresolved in the linear spectrum.

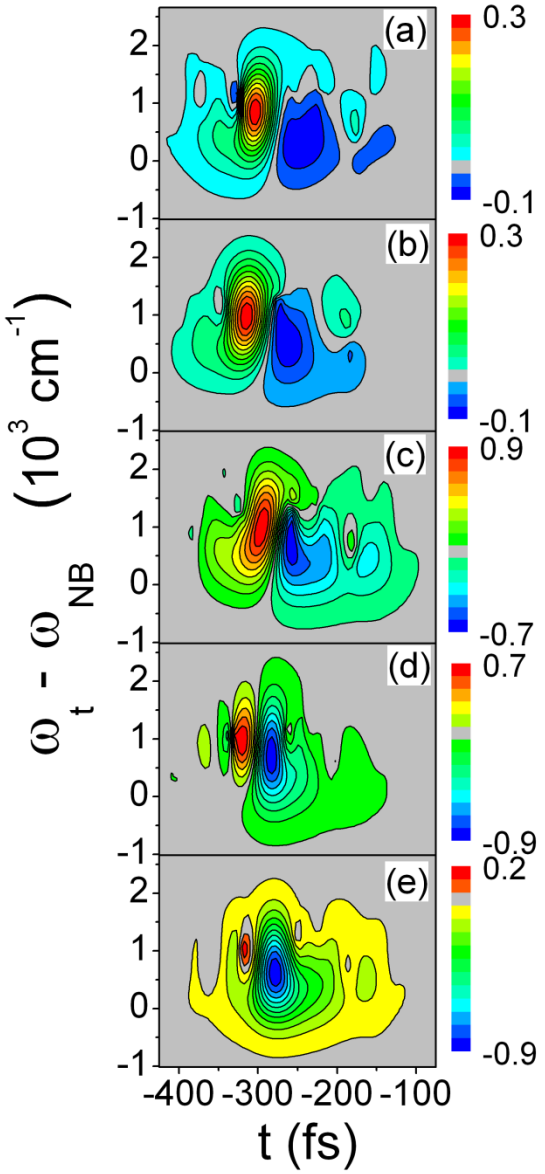

Figure 10.12. ZZZZ-ZXZX linear combination of signal field spectrograms for 0.01 M NaOH solutions of cylindrical aggregates with various (vol%) concentrations of methanol: (a) 0%; (b) 5%; (c) 10%; (d) 13%; (e) 15%.

Our assignment of coherence transfer in C8O3 is based on three criteria: (i) resemblance of the calculated and experimental linear spectrum shown in Figure 10.13(a); (ii) agreement between the calculated and experimental spectral amplitudes for the two tensor

elements in Figure 10.13(b) and 10.13(c); (iii) the similarity of the measured and calculated spectrogram shapes in Figures 10.6(i) and 10.9(a)-9(c). We believe that differences between the calculated and experimental data are mainly due to the model's assumption of homogeneous line broadening. For example, adding an inhomogeneous component to the line shape of the model system would yield in a nonlinear signal with a broader line width. The line narrowing effect predicted in Section 10.2.1 assumes only homogeneous dephasing in the three intervals between field-matter interactions. The cancellation between Γ_{ab} and Λ_{NB} in the denominator of Eq. (10.10) is not obtained when dynamics in the three time intervals are correlated by inhomogeneous line broadening.

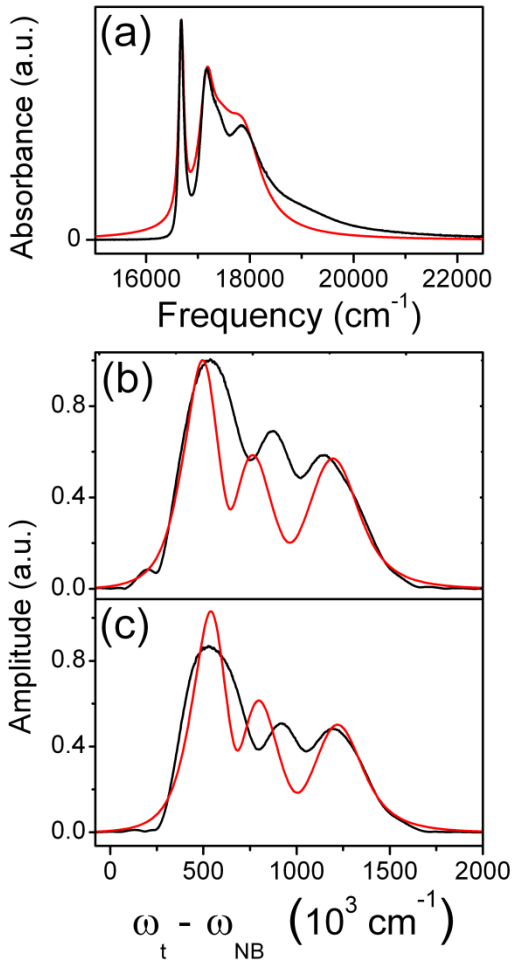

Figure 10.13. (a) Overlay of measured (black) and calculated (red) linear absorption spectra. Overlay of measured (black) and calculated (red) spectral amplitudes for the (a) ZZZZ and (b) ZXZX tensor elements. Calculated signals use the parameters of Table 10.1.

The neglect of vibronic coupling is a strong approximation for the C8O3 aggregate. Most importantly, we detect no vibrational resonances at Raman shifts of 200-3500 cm^{-1} when the narrowband pulse width is reduced to 30 cm^{-1}. Furthermore, weak vibronic coupling makes sense for C8O3. The exciton states are spatially delocalized such that their excitation produces only a minor change in the charge distribution surrounding localized nuclear modes (e.g. bond stretching vibrations). For the same reason, the chlorosome of green bacteria also possesses a weak Raman response (i.e. small Huang Rhys factors).[65] The extremely small Stokes shift of C8O3 is also consistent with the view that its delocalized excited states are associated with weak nuclear reorganization.[66]

10.5. CONCLUSION

This chapter establishes the utility of a specialized nonlinear spectroscopy for investigating the dynamics of intraband electronic coherences in molecular aggregates. The strength of this approach derives from the use of both narrowband and broadband laser pulses, which enables fast data acquisition rates and full suppression of the interfering population response present in conventional pump-probe and photon echo spectroscopies. We have shown this technique to be a viable method for the detection of coherence transfer processes, which are otherwise difficult to measure in complex systems. Methods applying all-femtosecond pulses can additionally resolve the t_1 and t_3 intervals between field-matter interactions, thereby obtaining information to which the present technique is insensitive.[23] However, the use of a narrowband laser pulse allows for superior selectivity of the

coherences prepared in t_2. For example, in this chapter, the bra side of the density operator is associated with only one excited state because the narrowband pulse overlaps with a single transition in the ground state absorption spectrum. The most appropriate experimental method (i.e. all femtosecond versus mixed narrow and broadband) is dictated by the particular system and information sought.

Five different morphologies of the C8O3 molecular aggregate produced by varying the concentration of methanol in an aqueous solvent have been investigated. Coherence transfer processes are detected for morphologies associated with methanol concentrations less than 13% (vol. %). All coherences probed in this chapter have in common an exciton localized on the inner cylinder wall as one component of the superposition of excited states. Future work will examine coherences between pairs of excitons not probed here and further explore the information provided by a wider variety of tensor elements. Ultimately, our goal is to establish a complete picture of the electronic structure and relaxation dynamics of the C8O3 molecular aggregate with the information provided by a variety of nonlinear spectroscopies. The present measurements represent an important step towards this goal.

Table 10.1. Parameters of calculated signals

Parameter	Value
$\omega_{NB1} = \omega_{NB2}$	16667 cm^{-1}
ω_{BB}	17442 cm^{-1}
[(a)] $\tau_{NB1} = \tau_{NB2}$	210 fs

[a] τ_{BB}	25 fs
ω_{e1g}	16667 cm^{-1}
ω_{e2g}	17167 cm^{-1}
ω_{e3g}	17427 cm^{-1}
ω_{e4g}	17867 cm^{-1}
Γ_{e1g}	50 cm^{-1}
Γ_{e2g}	90 cm^{-1}
Γ_{e3g}	200 cm^{-1}
$\Gamma_{e4g} = \Gamma_{e2e4}$	270 cm^{-1}
$\Gamma_{e2e3} = \Gamma_{e2e5}$	300 cm^{-1}
Γ_{e3g}	
$\kappa^{-1}_{e4g,e3g} = \kappa^{-1}_{e4g,e2g} = \kappa^{-1}_{e4g,e1g} = \kappa^{-1}_{e3g,e2g} = \kappa^{-1}_{e3g,e1g} = \kappa^{-1}_{e2g,e1g}$	628 fs
$\kappa^{-1}_{e4e1,e3e1} = \kappa^{-1}_{e4e2,e2e1} = \kappa^{-1}_{e3e1,e2e1}$	32 fs
$\vec{\mu}_{e1g}$	$2.02\hat{x} + 0\hat{y} + 0\hat{z}$
$\vec{\mu}_{e2g}$	$1.45\hat{x} + 2.10\hat{y} + 0\hat{z}$
$\vec{\mu}_{e3g}$	$1.35\hat{x} + 2.34\hat{y} + 0\hat{z}$
$\vec{\mu}_{e4g}$	$2.53\hat{x} + 3.02\hat{y} + 0\hat{z}$

T	300 fs

[a] Full width half maximum of Gaussian electric field envelope

REFERENCES

(1) Blankenship, R. E. *Molecular Mechanisms of Photosynthesis*; Blackwell Science Ltd.: Oxford, 2002.

(2) Lawlor, D. *Photosynthesis, 3rd Edition*; Springer-Verlag: New York, 2001.

(3) Falkowski, P. G.; Raven, J. A. *Aquatic Photosynthesis*; Blackwell Science: Malden, MA, 1997.

(4) Pullerits, T.; Chachisvilis, M.; Sundström, V. *J. Phys. Chem.* 1996, *100*, 10787.

(5) Arnett, D. C.; Moser, C. C.; Dutton, P. L.; Scherer, N. F. *J. Phys. Chem. B* 1999, *103*, 2014.

(6) Engel, G. S.; Calhoun, T. R.; Read, E. L.; Ahn, T. K.; Mancal, T.; Cheng, Y. C.; Blankenship, R. E.; Fleming, G. R. *Nature* 2007, *446*, 782.

(7) Savikhin, S.; Buck, D. R.; Struve, W. S. *Chem. Phys.* 1997, *223*, 303.

(8) Parson, W. W. *Science* 2007, *316*, 1438.

(9) Book, L. D.; Ostafin, A. E.; Ponomarenko, N.; Norris, J. R.; Scherer, N. F. *J. Phys. Chem. B* 2000, *104*, 8295.

(10) Sugisaki, M.; Fujiwara, M.; Yanagi, K.; Cogdell, R. J.; Hashimoto, H. *Photosynth. Res.* 2008, *95*, 299.

(11) Kleinekathöfer, U.; Schröder, M.; Schreiber, M. *J. Lumin.* 2005, *112*, 461.

(12) Cheng, Y. C.; Silbey, R. J. *Phys. Rev. Lett.* 2006, *96*, 028103:1.

(13) Olaya-Castro, A.; Lee, C. F.; Olsen, F. F.; Johnson, N. F. *Phys. Rev. B* 2008, *78*, 085115:1.

(14) Mancal, T.; Valkunas, L.; Read, E. L.; Engel, G. S.; Calhoun, T. R.; Fleming, G. R. *Spectroscopy* 2008, *22*, 199.

(15) Redfield, A. G. *Adv. Magn. Reson.* 1965, *1*, 1.

(16) Mukamel, S. *Principles of Nonlinear Optical Spectroscopy*; Oxford University Press: New York, 1995.

(17) Nitzan, A. *Chemical Dynamics in Condensed Phases*; Oxford University Press: New York, 2006.

(18) Collini, E.; Scholes, G. D. *Science* 2009, *323*, 369.

(19) Qian, W.; Jonas, D. M. *J. Chem. Phys.* 2003, *119*, 1611.

(20) Milota, F.; Sperling, J.; Nemeth, A.; Kauffman, L. J. *Chem. Phys.* 2008, In Press.

(21) Womick, J. M.; Miller, S. A.; Moran, A. M. *submitted to J. Phys. Chem. B* 2008.

(22) Cho, M. *Chem. Rev.* 2008, *108*, 1331.

(23) Lee, H.; Cheng, Y.-C.; Fleming, G. R. *Science* 2007, *316*, 1462.

(24) Kirstein, S.; Däehne, S. *Int. J. Photoener.* 2006, 1.

(25) von Berlepsch, H.; Böttcher, C.; Ouart, A.; Burger, C.; Däehne, S.; Kirstein, S. *J. Phys. Chem. B* 2000, *104*, 5255.

(26) von Berlepsch, H.; Kirstein, S.; Böttcher, C. *Langmuir* 2002, *18*, 7699.

(27) Nemeth, A.; Milota, F.; Sperling, J.; Abramavicius, D.; Mukamel, S.; Kauffman, L. J. *Chem. Phys. Lett.* 2009, *469*, 130.

(28) Didraga, C.; Pugžlys, A.; Hania, R.; von Berlepsch, H.; Duppen, K.; Knoester, J. *J. Phys. Chem. B* 2004, *108*, 14976.

(29) Knoester, J. *Int. J. Photoener.* 2006, 1.

(30) von Berlepsch, H.; Kirstein, S.; Hania, R.; Didraga, C.; Pugžlys, A.; Böttcher, C. *J. Phys. Chem. B* 2003, *107*, 14176.

(31) Cheng, J.-X.; Volkmer, A.; Book, L. D.; Xie, X. S. *J. Phys. Chem. B* 2002, *106*, 8493.

(32) Yoshizawa, M.; Kurosawa, M. *Phys. Rev. A* 1999, *61*, 013808: 1.

(33) Kukura, P.; McCamant, D. W.; Mathies, R. A. *Annu. Rev. Phys. Chem.* 2007, *58*, 461.

(34) Laimgruber, S.; Schachenmayer, H.; Schmidt, B.; Zinth, W.; Gilch, P. *Appl. Phys. B* 2006, *85*, 557.

(35) Abramavicius, D.; Mukamel, S. *Chem. Rev.* 2004, *104*, 2073.

(36) Kukura, P.; McCamant, D. W.; Mathies, R. A. *J. Phys. Chem. A* 2004, *108*, 5921.

(37) Stenholm, S. *J. Phys. B: Atom. Molec. Phys.* 1977, *10*, 761.

(38) Rickard, M. A.; Pakoulev, A.; Mathew, N. A.; Kornau, K. M.; Wright, J. C. *J. Phys. Chem. A* 2007, *111*, 1163.

(39) Pakoulev, A.; Rickard, M. A.; Mathew, N. A.; Kornau, K. M.; Wright, J. C. *J. Phys. Chem. A* 2008, *112*, 6320.

(40) Dreyer, J.; Moran, A. M.; Mukamel, S. *Bull. Korean Chem. Soc.* 2003, *24*, 1091.

(41) Mukamel, S. *J. Chem. Phys.* 1997, *107*, 4165.

(42) Gallagher, S. M.; Albrecht, A. W.; Hybl, J. D.; Landin, B. L.; Rajaram, B.; Jonas, D. M. *J. Opt. Soc. Am. B* 1998, *15*, 2338.

(43) Moran, A. M.; Maddox, J. B.; Hong, J. W.; Kim, J.; Nome, R. A.; Bazan, G. C.; Scherer, N. F. *J. Chem. Phys.* 2006, *124*, 194904:1.

(44) Cerullo, G.; Nisoli, M.; De Silvestri, S. *Appl. Phys. Lett.* 1997, *71*, 3616.

(45) Riedle, E.; Beutter, M.; Lochbrunner, S.; Piel, J.; Schenkl, S.; Spörlein, S.; Zinth, W. *Appl. Phys. B* 2000, *71*, 457.

(46) Kobayashi, T.; Baltuska, A. *Meas. Sci. Technol.* 2002, *13*, 1671.

(47) Martinez, O. E. *J. Opt. Soc. Am. B* 1986, *3*, 929.

(48) Goodman, J. W. *Introduction to Fourier Optics, Third Edition*; Roberts & Company: Greenwood Village, 2005.

(49) Ishibashi, T.; Onishi, H. *Appl. Phys. Lett.* 2002, *81*, 1338.

(50) Shim, S.; Mathies, R. A. *Appl. Phys. Lett.* 2006, *89*, 121124:1.

(51) Cowan, M. L.; Ogilvie, J. P.; Miller, R. J. D. *Chem. Phys. Lett.* 2004, *386*, 184.

(52) Goodno, G. D.; Dadusc, G.; Miller, R. J. D. *J. Opt. Soc. Am. B* 1998, *15*, 1791.

(53) Maznev, A. A.; Nelson, K. A.; Rogers, J. A. *Opt. Lett.* 1998, *23*, 1319.

(54) Brixner, T.; Mancal, T.; Stiopkin, I. V.; Fleming, G. R. *J. Chem. Phys.* 2004, *121*, 4221.

(55) Khurmi, C.; Berg, M. A. *J. Phys. Chem. A* 2008, *112*, 3364.

(56) Underwood, D. F.; Blank, D. A. *J. Phys. Chem. A* 2003, *107*, 956.

(57) Gundogdu, K.; Stone, K. W.; Turner, D. B.; Nelson, K. A. *Chem. Phys.* 2007, *341*, 89.

(58) Kim, J.; Wong, C. Y.; Nair, P. S.; Fritz, K. P.; Kumar, S.; Scholes, G. D. *J. Phys. Chem. B* 2006, *110*, 25371.

(59) Lepetit, L.; Chériaux, G.; Joffre, M. *J. Opt. Soc. Am. B* 1995, *12*, 2467.

(60) Tokunaga, E.; Terasaki, A.; Kobayashi, T. *J. Opt. Soc. Am. B* 1995, *12*, 753.

(61) Hybl, J. D.; Albrecht Ferro, A.; Jonas, D. M. *J. Chem. Phys.* 2001, *115*, 6606.

(62) Moran, A. M.; Nome, R. A.; Scherer, N. F. *J. Phys. Chem. A* 2006, *110*, 10925.

(63) Christensson, N.; Dietzek, B.; Pascher, T.; Yartsev, A.; Pullerits, T. *Chem. Phys. Lett.* 2008, *457*, 106.

(64) Oskouei, A. A.; Bräm, O.; Cannizzo, A.; van Mourik, F.; Tortschanoff, A.; Chergui, M. *J. Mol. Liq.* 2008, *141*, 118.

(65) Cherepy, N. J.; Du, M.; Holzwarth, A. R.; Mathies, R. A. *J. Phys. Chem.* 1996, *100*, 4662.

(66) Pugžlys, A.; Augulis, R.; van Loosdrecht, P. H. M.; Didraga, C.; Malyshev, V. A.; Knoester, J. *J. Phys. Chem. B* 2006, *110*, 20268.

APPENDICES

Appendix A. Tensor Elements for Electric Field Polarizations

This Appendix presents the orientational part of the nonlinear response functions. The indices α, β, γ, χ and respectively correspond to the fields E_1, E_2, E_3 and E_S. For convenience, this orientational factor absorbs the four transition dipole magnitudes as

$$\begin{aligned}
&\left\langle \chi_{gh}\gamma_{ef}\beta_{cd}\alpha_{ab}\right\rangle = \mu_{ab}\mu_{cd}\mu_{ef}\mu_{gh}\Big[\left\langle \cos\theta_{ab,cd}\cos\theta_{ef,gh}\right\rangle \\
&\times\left(4\cos\theta_{\alpha\beta}\cos\theta_{\gamma\chi}-\cos\theta_{\alpha\gamma}\cos\theta_{\beta\chi}-\cos\theta_{\alpha\chi}\cos\theta_{\beta\gamma}\right) \\
&+\left\langle \cos\theta_{ab,ef}\cos\theta_{cd,gh}\right\rangle\left(4\cos\theta_{\alpha\gamma}\cos\theta_{\beta\chi}-\cos\theta_{\alpha\beta}\cos\theta_{\gamma\chi}\right. \\
&\left.-\cos\theta_{\alpha\chi}\cos\theta_{\beta\gamma}\right)+\left\langle \cos\theta_{ab,gh}\cos\theta_{cd,ef}\right\rangle\left(4\cos\theta_{\alpha\chi}\cos\theta_{\beta\gamma}\right. \\
&\left.-\cos\theta_{\alpha\beta}\cos\theta_{\gamma\chi}-\cos\theta_{\alpha\gamma}\cos\theta_{\beta\chi}\right)\Big]
\end{aligned} \tag{A1}$$

Appendix B. Nonlinear Response Functions

This Appendix presents expressions for response functions corresponding to four of the six Feynman diagrams in Figure 4.3. Section 4.3.3 discusses the motivations for this model in the context of the $R_1(t_1,t_2,t_3)$ term. Response functions involving only the ground and single exciton electronic states are given by

$$R_2(t_1,t_2,t_3) = \sum_{ab} \left\langle \alpha_{gb}\beta_{ag}\gamma_{bg}\chi_{ga} \right\rangle Z_{ab}^2(t_1,t_2,t_3) \exp\Big(-i\omega_{gb}t_1 - i\omega_{ab}t_2 - i\omega_{ag}t_3 - \frac{1}{2} f_1(0, t_1+t_2, t_1+t_2+t_3, t_1)\Big) \tag{B1}$$

$$R_3(t_1,t_2,t_3) = \sum_{ab} \left\langle \alpha_{gb}\beta_{bg}\gamma_{ag}\chi_{ga} \right\rangle Z_{ab}^3(t_1,t_2,t_3) \exp\Big(-i\omega_{gb}t_1 - i\omega_{ag}t_3 - \frac{1}{2} f_1(0, t_1, t_1+t_2+t_3, t_1+t_2)\Big) \tag{B2}$$

$$R_4(t_1,t_2,t_3) = \sum_{ab} \left\langle \alpha_{ag}\beta_{ga}\gamma_{bg}\chi_{gb} \right\rangle Z_{ab}^4(t_1,t_2,t_3) \exp\Big(-i\omega_{ag}t_1 - i\omega_{bg}t_3 - \frac{1}{2} f_1(t_1+t_2+t_3, t_1+t_2, t_1, 0)\Big) \tag{B3}$$

where the line broadening functions, $f_1(t_4,t_3,t_2,t_1)$, are given in Reference [1] and vibronic coupling is described with

$$\begin{aligned} Z_{ab}^2(t_1,t_2,t_3) = {} & F_a^{00}F_b^{00} + \sum_{\nu=1}^{2} F_a^{00}F_{b\nu}^{01} \exp\left[\left(i\omega_\nu - k_\nu\right)\left(t_1+t_2\right)\right] \\ & + F_{a\nu}^{01}F_b^{00} \exp\left[-\left(i\omega_\nu + k_\nu\right)\left(t_2+t_3\right)\right] \\ & + \delta_{ab}F_{a\nu}^{01}F_{b\nu}^{00} \exp\left(i\omega_\nu t_1 - k_\nu\left(t_1+t_2\right)\right)\left[\exp\left(-i\omega_\nu t_3 - k_\nu t_3\right) + \left(\exp\left(k_\nu t_2\right) - 1\right)\right] \end{aligned} \tag{B4}$$

$$\begin{aligned} Z_{ab}^3(t_1,t_2,t_3) = {} & F_a^{00}F_b^{00} + \sum_{\nu=1}^{2} F_a^{00}F_{b\nu}^{01} \exp\left[i\left(\omega_\nu - k_\nu\right)t_1\right] \\ & + F_{a\nu}^{01}F_b^{00} \exp\left[-i\left(\omega_\nu + k_\nu\right)t_3\right] \\ & + \delta_{ab}F_a^{00}F_{a\nu}^{01} \exp\left[i\left(\omega_\nu - k_\nu\right)t_2\right] \end{aligned} \tag{B5}$$

$$
\begin{aligned}
Z_{ab}^{4}\left(t_1,t_2,t_3\right) = F_a^{00}F_b^{00} + \sum_{\nu=1}^{2} F_{a\nu}^{01}F_b^{00}\exp\left[-i\left(\omega_\nu + k_\nu\right)t_1\right] \\
+F_a^{00}F_{b\nu}^{01}\exp\left[-i\left(\omega_\nu + k_\nu\right)t_3\right] \\
+\delta_{ab}F_a^{00}F_{a\nu}^{01}\exp\left[-i\left(\omega_\nu + k_\nu\right)t_2\right]
\end{aligned}
\tag{B6}
$$

Vibronic coupling functions for the ground state bleach terms, $Z_{ab}^{3}\left(t_1,t_2,t_3\right)$ and $Z_{ab}^{4}\left(t_1,t_2,t_3\right)$, sum over three terms evolving in coherences in either the t_1, t_2 or t_3 intervals. This model restricts the summation to the dominant terms in which at least two field matter interactions couple the electronic origins of the ground and excited states. This treatment is appropriate for systems, such as APC, in which the 0-0 transitions possess the largest Franck-Condon factors.

The excited state absorption terms do not include vibronic structure due to limited experimental information. These terms

$$
\begin{aligned}
R_1^{*}\left(t_1,t_2,t_3\right) = \sum_{abc}\left\langle \alpha_{ga}\beta_{bg}\gamma_{cb}\chi_{ac}\right\rangle \\
\times\exp\left(-i\omega_{ga}t_1 - i\omega_{ba}t_2 - i\omega_{ca}t_3 - \frac{1}{2}f_2\left(t_1,t_1+t_2,t_1+t_2+t_3,0\right)\right)
\end{aligned}
\tag{B7}
$$

$$
\begin{aligned}
R_2^{*}\left(t_1,t_2,t_3\right) = \sum_{abc}\left\langle \alpha_{ga}\beta_{bg}\gamma_{cb}\chi_{ac}\right\rangle \\
\times\exp\left(-i\omega_{bg}t_1 - i\omega_{ba}t_2 - i\omega_{ca}t_3 - \frac{1}{2}f_2\left(0,t_1+t_2,t_1+t_2+t_3,t_1\right)\right)
\end{aligned}
\tag{B8}
$$

are taken directly from Section 5.1 of Reference [1]. Figure 4.3 reserves the indices a and b for single exciton states, whereas c is only used for double exciton states. Equation (5.28) in Reference [1] does not use this convention. The $f_2\left(t_4,t_3,t_2,t_1\right)$ function used in Equations (B7) and (B8) is given by

$$f_2(t_4,t_3,t_2,t_1) = g_{aa}(t_{21}) + g_{cc}(t_{32}) + g_{bb}(t_{43}) - g_{ac}(t_{21}) - g_{ac}(t_{32}) + g_{ac}(t_{31}) + g_{ab}(t_{32}) + g_{ab}(t_{41}) - g_{ab}(t_{31}) - g_{ab}(t_{42}) - g_{cb}(t_{32}) - g_{cb}(t_{43}) + g_{cb}(t_{42}) \quad \text{(B9)}$$

Appendix C. Calculation of Absorption and Fluorescence Spectra

Absorption and fluorescence spectra are calculated with

$$\sigma_A(\omega) = \sum_{a=1}^{N} \mu_{ag}^2 \int_0^\infty dt \left\{ F_a^{00} + \sum_{\nu=1}^{2} F_{a\nu}^{01} \exp(-i\omega_\nu t) \right\} \exp\left[i(\omega - \omega_{ag})t - \frac{1}{2} g_{aa}(t) \right] \Phi_a(t) \qquad \text{(C1)}$$

and

$$\sigma_F(\omega) = \sum_{a=1}^{N} \mu_{ag}^2 P_a \int_0^\infty dt \left\{ F_a^{00} + \sum_{\nu=1}^{2} F_{a\nu}^{01} \exp(i\omega_\nu t) \right\} \exp\left[i(\omega - \omega_{ag})t - \frac{1}{2} g_{aa}^*(t) \right] \Phi_a(t) \qquad \text{(C2)}$$

where N is the number of pigments, P_a is the Boltzmann factor representing the population of excited states, $\Phi_a(t)$ accounts for lifetime broadening and is obtained by summing the Green function, $G_{ba}(t)$, over all population transfer channels as

$$\Phi_a(t) = \sum_b G_{ba}(t) \qquad \text{(C3)}$$

Appendix D. Nonlinear Response Functions

This Section summarizes expressions used to calculate transient grating and photon echo signals. This model is based on that presented in Sections 5.1 and 5.2 of Reference [1]. In Reference [2], we modified the model for inclusion of vibronic structure. Here the equations are summarized to make clear how the parameters of Table 5.1 enter the calculation of nonlinear signals.

The six terms in the nonlinear response function are computed using

$$R_1(t_1,t_2,t_3) = \sum_{ab} \left\langle \alpha_{gb}\beta_{ag}\gamma_{bg}\chi_{ga} \right\rangle Z^1_{ab}(t_1,t_2,t_3) \exp\left(-i\omega_{ag}t_1 - i\omega_{ab}t_2 - i\omega_{ag}t_3 - \frac{1}{2} f_1(t_1, t_1+t_2, t_1+t_2+t_3, 0)\right) \tag{D1}$$

$$R_2(t_1,t_2,t_3) = \sum_{ab} \left\langle \alpha_{gb}\beta_{ag}\gamma_{bg}\chi_{ga} \right\rangle Z^2_{ab}(t_1,t_2,t_3) \exp\left(-i\omega_{gb}t_1 - i\omega_{ab}t_2 - i\omega_{ag}t_3 - \frac{1}{2} f_1(0, t_1+t_2, t_1+t_2+t_3, t_1)\right) \tag{D2}$$

$$R_3(t_1,t_2,t_3) = \sum_{ab} \left\langle \alpha_{gb}\beta_{bg}\gamma_{ag}\chi_{ga} \right\rangle Z^3_{ab}(t_1,t_2,t_3) \exp\left(-i\omega_{gb}t_1 - i\omega_{ag}t_3 - \frac{1}{2} f_1(0, t_1, t_1+t_2+t_3, t_1+t_2)\right) \tag{D3}$$

$$R_4(t_1,t_2,t_3) = \sum_{ab} \left\langle \alpha_{ag}\beta_{ga}\gamma_{bg}\chi_{gb} \right\rangle Z^4_{ab}(t_1,t_2,t_3) \exp\left(-i\omega_{ag}t_1 - i\omega_{bg}t_3 - \frac{1}{2} f_1(t_1+t_2+t_3, t_1+t_2, t_1, 0)\right) \tag{D4}$$

$$^{IC}R_1(t_1,t_2,t_3) = \sum_{ab} \left\langle \alpha_{ga}\beta_{ag}\gamma_{bg}\chi_{gb} \right\rangle \exp\left[-i\omega_{ag}t_1 - i\omega_{bg}t_3 - g_{aa}(t_1) - g_{bb}(t_1) + 2i\lambda_{bb}t_3\right] \times Z^{IC}_{ab}(t_1,t_3)\left[G_{ba}(t_2) - 1\right] - R_1(t_1,\infty,t_3) - R_4(t_1,\infty,t_3) \tag{D5}$$

$$^{IC}R_2(t_1,t_2,t_3) = \sum_{ab} \left\langle \alpha_{ga}\beta_{ag}\gamma_{bg}\chi_{gb} \right\rangle \exp\left[i\omega_{ag}t_1 - i\omega_{bg}t_3 - g^*_{aa}(t_1) - g^*_{bb}(t_1) + 2i\lambda_{bb}t_3\right] \times Z^{IC}_{ab}(-t_1,t_3)\left[G_{ba}(t_2) - 1\right] - R_2(t_1,\infty,t_3) - R_3(t_1,\infty,t_3) \tag{D6}$$

where the orientation part of the response function, $\left\langle \alpha_{ga}\beta_{ag}\gamma_{bg}\chi_{gb}\right\rangle$, is presented elsewhere.[2-4] The $f_1\left(t_4,t_3,t_2,t_1\right)$ function is expanded according to

$$f_1\left(t_4,t_3,t_2,t_1\right)=g_{aa}\left(t_{21}\right)+g_{bb}\left(t_{43}\right)+g_{ab}\left(t_{32}\right)+g_{ab}\left(t_{41}\right)-g_{ab}\left(t_{31}\right)-g_{ab}\left(t_{42}\right) \qquad \text{(D7)}$$

where $t_{ij}=t_i-t_j$ and the line broadening function is given by Equation (5.2). The *ad hoc* auxiliary functions used to described vibronic couplings are

$$\begin{aligned} Z^1_{ab}\left(t_1,t_2,t_3\right)=&F_a^{00}F_b^{00}+\sum_{\nu=1}^{2}F_{a\nu}^{01}F_b^{00}\exp\left[-\left(i\omega_\nu+k_\nu\right)\left(t_1+t_2+t_3\right)\right]\\ &+F_a^{00}F_{b\nu}^{01}\exp\left[\left(i\omega_\nu-k_\nu\right)t_2\right]\\ &+\delta_{ab}F_{a\nu}^{01}F_{b\nu}^{00}\exp\left(-i\omega_\nu t_1-k_\nu\left(t_1+t_2\right)\right)\left[\exp\left(-i\omega_\nu t_3\right)+\left(\exp\left(k_\nu t_2\right)-1\right)\right] \end{aligned} \qquad \text{(D8)}$$

$$\begin{aligned} Z^2_{ab}\left(t_1,t_2,t_3\right)=&F_a^{00}F_b^{00}+\sum_{\nu=1}^{2}F_a^{00}F_{b\nu}^{01}\exp\left[\left(i\omega_\nu-k_\nu\right)\left(t_1+t_2\right)\right]\\ &+F_{a\nu}^{01}F_b^{00}\exp\left[-\left(i\omega_\nu+k_\nu\right)\left(t_2+t_3\right)\right]\\ &+\delta_{ab}F_{a\nu}^{01}F_{b\nu}^{00}\exp\left(i\omega_\nu t_1-k_\nu\left(t_1+t_2\right)\right)\left[\exp\left(-i\omega_\nu t_3\right)+\left(\exp\left(k_\nu t_2\right)-1\right)\right] \end{aligned} \qquad \text{(D9)}$$

$$\begin{aligned} Z^3_{ab}\left(t_1,t_2,t_3\right)=&F_a^{00}F_b^{00}+\sum_{\nu=1}^{2}F_a^{00}F_{b\nu}^{01}\exp\left[i\left(\omega_\nu-k_\nu\right)t_1\right]\\ &+F_{a\nu}^{01}F_b^{00}\exp\left[-i\left(\omega_\nu+k_\nu\right)t_3\right]\\ &+\delta_{ab}F_a^{00}F_{a\nu}^{01}\exp\left[i\left(\omega_\nu-k_\nu\right)t_2\right] \end{aligned} \qquad \text{(D10)}$$

$$\begin{aligned} Z^4_{ab}\left(t_1,t_2,t_3\right)=&F_a^{00}F_b^{00}+\sum_{\nu=1}^{2}F_{a\nu}^{01}F_b^{00}\exp\left[-i\left(\omega_\nu+k_\nu\right)t_1\right]\\ &+F_a^{00}F_{b\nu}^{01}\exp\left[-i\left(\omega_\nu+k_\nu\right)t_3\right]\\ &+\delta_{ab}F_a^{00}F_{a\nu}^{01}\exp\left[-i\left(\omega_\nu+k_\nu\right)t_2\right] \end{aligned} \qquad \text{(D11)}$$

$$Z^{IC}_{ab}\left(t_1,t_3\right)=F_a^{00}F_b^{00}+F_b^{00}\sum_{\nu=1}^{2}F_{a\nu}^{01}\exp\left(-i\omega_\nu t_1-k_\nu\left|t_1\right|\right)+F_a^{00}\sum_{\nu=1}^{2}F_{b\nu}^{01}\exp\left(i\omega_\nu t_3-k_\nu t_3\right) \qquad \text{(D12)}$$

Appendix E. An Exciton Model For C-Phycocyanin

This Section presents details for the Hamiltonian used to compute the photon echo signals in Figure 5.10. This exciton model adds interaction between the α84 and β84 pigments to the zeroeth-order Hamiltonian of Equation (5.1), but neglects interactions between all other pairs of pigments. The neglect of couplings between pigments that are not members of the α84-β84 dimers can be motivated with the fluctuation amplitudes, Δ_{aa}, in Table 5.1. The assumption of localized electronic states holds when Δ_{aa} are large compared to intermolecular couplings which, with the exception of the dimer, are less than 75 cm^{-1}. Furthermore, the parameter, κ_a, indicates that the spectroscopic line widths are not motionally narrowed. Therefore, to a good approximation, we can regard heterogeneity in the site energies as the source of wavefunction localization in CPC. For example, the parameters of Table 5.1 indicate the three α84 (or β84) pigments in the trimer (Figure 5.1) do not form a band structure as would be expected in a degenerate basis.[5] The present treatment is also consistent with the tens of picoseconds time scale for energy transfer involving pigments that are not members of the same dimer.[6,7]

The single exciton part of the Hamiltonian, $H1$, block diagonalizes as

$$H1 = \begin{pmatrix} E_{\beta 84} & J & 0 \\ J & E_{\alpha 84} & 0 \\ 0 & 0 & E_{\beta 155} \end{pmatrix} \qquad \text{(E1)}$$

where subscripts are written on the diagonal elements to denote particular pigments and J represents coupling between the transition dipoles at the α84 and β84 sites. The energy level diagram in Figure 5.10a presents a notation for the three eigenstates obtained by diagonalization of $H1$: $e+$, $e-$ and $\beta 155$.

The $e+$ and $e-$ states superpose excitations at α84 and β84. By the usual treatment of coupled two-level systems, Figure 5.10a also shows a doubly excited state, f, whose energy is given by the sum of $E_{\beta 84}$ and $E_{\alpha 84}$ (i.e., the double exciton Hamiltonian possesses a single element).

The exciton model is parameterized by setting the coupling, J, equal to -141 cm^{-1} and increasing the value of $\Delta_{aa}(\beta 84)$ from 510 cm^{-1} to 610 cm^{-1}. The coupling strength, J, is consistent with earlier calculations based on the X-ray crystal structure of CPC.[6-8] Furthermore, we directly parameterize the exciton basis with the Franck-Condon factors in Table 5.1 by exchanging the $\beta 84$ and $\alpha 84$ indices for $e+$ and $e-$. For example, the $F_a^{00}(\beta 84)$ and $F_a^{00}(\alpha 84)$ Franck-Condon factors of Table 5.1 become $F_a^{00}(e+)$ and $F_a^{00}(e-)$ in the present exciton model. Our treatment of Allophycocyanin similarly parameterizes Franck-Condon factors in the exciton basis.[2] All other parameters of Table 5.1 are unchanged. The present set of parameters fit the absorption spectrum quite well (Figure 5.10b) and suggest no need for further modification.

Diagonalization of $H1$ defines the rules needed to transform the line broadening functions of the $\beta 84$ and $\alpha 84$ pigments (Equation (5.2)) from the local to exciton basis.[1,9,10] The nonlinear response functions given in Appendix B still apply when supplemented with ESA terms.[1,2,9] The nonlinear response is restricted by allowing only the $e+$ and $e-$ states to radiate as coherent cross terms in which $a \neq b$. That is, the electronic states of $\beta 155$ do not evolve in coherence with $e+$ and $e-$, which is again consistent with experimental work showing that its electronic relaxation occurs in the weak-coupling limit.[6,7] In other words,

the four-wave mixing response of the present model essentially superposes nonlinearities of two independent systems: a two-level pigment ($\beta 155$) and a four-level exciton dimer.

Appendix F. Electronic and Nuclear Coherence in Intraband Electronic Coherence Spectroscopy

This Section summarizes terms in the IECS response function not discussed in Section 6.2. Vibronic structure is not included in the R_1^* and R_2^* terms because the parameters are not well-constrained.[2] Terms in the third row of Figure 6.3, which are given elsewhere,[1] yield negligible contributions to IECS and are not written here. The four remaining terms in the IECS nonlinear response function are computed using

$$R_2(t_1,t_2,t_3) = \sum_{ab} \left\langle \alpha_{gb}\beta_{ag}\gamma_{bg}\chi_{ga} \right\rangle Z_{ab}^2(t_1,t_2,t_3) \exp\Big(-i\omega_{gb}t_1 - i\omega_{ab}t_2 - i\omega_{ag}t_3 - \frac{1}{2} f_1(0,t_1+t_2,t_1+t_2+t_3,t_1)\Big) \tag{F1}$$

$$R_3(t_1,t_2,t_3) = \sum_{ab} \left\langle \alpha_{gb}\beta_{bg}\gamma_{ag}\chi_{ga} \right\rangle Z_{ab}^3(t_1,t_2,t_3) \exp\Big(-i\omega_{gb}t_1 - i\omega_{ag}t_3 - \frac{1}{2} f_1(0,t_1,t_1+t_2+t_3,t_1+t_2)\Big) \tag{F2}$$

$$R_1^*(t_1,t_2,t_3) = \sum_{abc} \left\langle \alpha_{ga}\beta_{bg}\gamma_{cb}\chi_{ac} \right\rangle \exp\Big(-i\omega_{ga}t_1 - i\omega_{ba}t_2 - i\omega_{ca}t_3 - \frac{1}{2} f_2(t_1,t_1+t_2,t_1+t_2+t_3,0)\Big) \tag{F3}$$

$$R_2^*(t_1,t_2,t_3) = \sum_{abc} \left\langle \alpha_{ga}\beta_{bg}\gamma_{cb}\chi_{ac} \right\rangle \exp\Big(-i\omega_{bg}t_1 - i\omega_{ba}t_2 - i\omega_{ca}t_3 - \frac{1}{2} f_2(0,t_1+t_2,t_1+t_2+t_3,t_1)\Big) \tag{F4}$$

where

$$\begin{aligned} Z_{ab}^2(t_1,t_2,t_3) = {} & F_a^{00}F_b^{00} + \sum_{\nu=1}^{2} F_a^{00}F_{b\nu}^{01} \exp\left[(i\omega_\nu - k_\nu)(t_1+t_2)\right] \\ & + F_{a\nu}^{01}F_b^{00} \exp\left[-(i\omega_\nu + k_\nu)(t_2+t_3)\right] \\ & + \delta_{ab}F_{a\nu}^{01}F_{b\nu}^{00} \exp\left(i\omega_\nu t_1 - k_\nu(t_1+t_2)\right)\left[\exp(-i\omega_\nu t_3) + \left(\exp(k_\nu t_2) - 1\right)\right] \end{aligned} \tag{F5}$$

$$Z_{ab}^{3}\left(t_1,t_2,t_3\right)=F_a^{00}F_b^{00}+\sum_{\nu=1}^{2}F_a^{00}F_{b\nu}^{01}\exp\left[\left(i\omega_\nu-k_\nu\right)t_1\right]+F_{a\nu}^{01}F_b^{00}\exp\left[-\left(i\omega_\nu+k_\nu\right)t_3\right] \\ +\delta_{ab}F_a^{00}F_{a\nu}^{01}\exp\left[\left(i\omega_\nu-k_\nu\right)t_2\right] \tag{F6}$$

Appendix G

This Appendix presents the multi-mode harmonic Brownian oscillator (BO) model employed in this work. We summarize the key equations specific to the systems investigated in this chapter. The general formulation of the BO model has been discussed in detail elsewhere.[1,9,11] Hamiltonians describing the bath and system-bath interaction, which are components of Equation (7.1), are given by[1]

$$H_{Bath} = \frac{1}{2}\sum_j \left[\frac{P_j^2}{M_j} + M_j \bar{\Omega}_j^2 Q_j^2 \right] + \frac{1}{2}\sum_\alpha \left[\frac{p_\alpha^2}{m_\alpha} + m_\alpha \bar{\omega}_\alpha^2 \left(q_\alpha - \sum_j \frac{z_{j\alpha}}{m_\alpha \bar{\omega}_\alpha^2} Q_j \right)^2 \right] \quad \text{(G1)}$$

$$H_{Sys-Bath} = \sum_m \sum_j \bar{h}_{m,j} Q_j B_m^\dagger B_m \quad \text{(G2)}$$

Both H_{Bath} and $H_{Sys-Bath}$ distinguish between the primary, Q_j, and secondary, q_α, oscillators. Here $P_j, \bar{\Omega}_j, M_j$ ($p_\alpha, \bar{\omega}_\alpha, m_\alpha$) are the momenta, frequencies, and masses of the primary (secondary) coordinates. The primary oscillators couple linearly to electronic excitations at the pigment sites, m, with the coupling strength $\bar{h}_{m,j} = M_j \bar{\Omega}_j^2 d_{m,j}$, where $d_{m,j}\sqrt{M_j \bar{\Omega}_j}$ is the dimensionless displacement in Q_j from its equilibrium position. The secondary oscillators interact with the primary oscillators through the coupling parameter, $z_{j\alpha}$, but do not influence the electronic structure of the system directly.

It is useful to point out two fundamental assumptions made in the present applications to APC and CPC, which distinguish it from a more general treatment. First, it is assumed that different pigment sites do not interact with the same primary oscillator (i.e., no shared modes). This aspect of the model is reasonable given that the intermolecular distances within the dimers of both APC and CPC are approximately 2 nm. Moreover, contributions from

shared modes were ruled out in our earlier experimental investigations.[2,12,13] Second, we assume that the primary oscillators influence the site energies in H_{Sys}^{el} and H_{Sys}^{vb} but not the electrostatic couplings. This approximation is motivated, in part, by the limited empirical parameters available. However, it can also be justified by the relatively small size of J_{mn} (-150 cm^{-1}) compared to the E_m (≥ 15300 cm^{-1}). This second assumption is implicit in the form of $H_{Sys-Bath}$ given in Equation (G2).

The spectral density at pigment site m is conveniently written as

$$C_m''(\omega) = -\frac{\bar{h}_{m,j}^2}{2}\sum_j \int_{-\infty}^{\infty} dt \exp(i\omega t)\left\langle \left[Q_j(t), Q_j(0) \right] \right\rangle \qquad \text{(G3)}$$

by assuming that the primary oscillators are uncorrelated. Similarly, the spectral density of the secondary oscillators is given by

$$K_\alpha''(\omega) = -\frac{1}{2}\int_{-\infty}^{\infty} dt \exp(i\omega t)\left\langle \left[q_\alpha(t), q_\alpha(0) \right] \right\rangle \qquad \text{(G4)}$$

With these spectral densities in hand, closed forms of the correlation functions appropriate for the treatment of intermolecular and intramolecular modes can be found in the limits of small and large friction imposed on the primary oscillators, Q_j, by the secondary oscillators, q_α. The amount of friction, in turn, determines the rate at which thermally driven fluctuations of the site energies relax. The form of the spectral density, $C_m''(\omega)$, is governed by the relative sizes of the oscillator frequencies, Ω_j, and the friction

$$\gamma_j(\omega) = \frac{1}{M_j \omega}\sum_\alpha z_{j\alpha}^2 K_\alpha''(\omega) \qquad \text{(G5)}$$

Limiting forms of $C_m''(\omega)$ are conveniently found by assuming that $\gamma_j(\omega)$ is frequency-independent, which signifies that the thermal motions of the bath are fast compared to those of the Q_j. When $\gamma_j >> \Omega_j$, the spectral density is given by

$$C_j''(\omega) = 2\lambda_j' \frac{\omega\Lambda_j}{\omega^2 + \Lambda_j^2} \tag{G6}$$

where $\lambda_j' = \left(2M_j\bar{\Omega}_j^2\right)^{-1}$ and $\Lambda_j = \bar{\Omega}_j^2/\gamma_j$. In the opposite limit, the spectral density is written as

$$C_j''(\omega) = \frac{1}{2M_j\Omega_j}\left[\delta\left(\omega-\Omega_j\right)-\delta\left(\omega+\Omega_j\right)\right] \tag{G7}$$

Equations (7.3) and (7.4) are respectively obtained by combining the overdamped and underdamped versions of $C_j''(\omega)$ with Equation (G3).

Intermolecular and intramolecular modes involving the phycocyanobilim pigments of APC and CPC are well-described in the overdamped and underdamped limits of the BO model, respectively. Liquid water, which likely makes a significant contribution to the fastest solvation processes in these proteins,[2,12,14] has a low-frequency Raman spectrum dominated by nuclear motions at frequencies less than 200 cm^{-1}. By contrast, strongly coupled intramolecular modes of phycocyanobilin pigments are found throughout the fingerprint region (e.g., 500-2000 cm^{-1}).[15-17] In addition to possessing lower frequencies, the intermolecular modes of the environment (i.e., solvent) that couple to the pigments (i.e., solute) generally also have strong interactions with secondary solvation layers (i.e., large $z_{j\alpha}$ in Equation (G5)), and therefore satisfy the limit $\gamma_j >> \Omega_j$. On the other hand, the intramolecular modes of the phycocyanobilins (e.g., stretching and bending above 500 cm^{-1})

are generally underdamped (i.e., narrow line widths are observed in Raman spectra) because they have relatively weak interactions with the environments surrounding the pigments.

Appendix H

This Appendix defines the notation used in Section 9.4.1. This notation closely resembles that used in Reference [18]. Further background on line broadening in excitonic systems can be found elsewhere.[1,10,11] The Hamiltonian of the aggregate is given by

$$H = H_{Sys} + H_{Bath} + H_{Sys-Bath} \tag{H1}$$

where the system Hamiltonian is

$$H_{Sys} = \sum_{m}^{N} E_m B_m^{\dagger} B_m + \sum_{m}^{N} \sum_{n \neq m}^{N} J_{mn} B_m^{\dagger} B_n \tag{H2}$$

E_m is the energy for molecule m, J_{mn} is the coupling between molecular sites m and n, H_{Bath} is the Hamiltonian for the bath and $H_{Sys-Bath}$ describes the system-bath coupling. For N molecular sites, H_{Sys} block diagonalizes into a 1×1 block for the ground state, an $N\times N$ block in the basis states representing single excitations, and a $N(N-1)/2 \times N(N-1)/2$ block corresponding to basis states with two excitation on different sites. The eigenvectors, $\phi_{\alpha m}$, in Eq. (9.2) represent the single exciton excited states found by diagonalization of the $N\times N$ block. For example, the wavefunction for single exciton state α is given by

$$|\psi_{\alpha}\rangle = \sum_{m}^{N} \phi_{\alpha m} |m\rangle \tag{H3}$$

$H_{Sys-Bath}$ is given by

$$H_{Sys-Bath} = \sum_{m} \sum_{n} q_{mn} B_m^{\dagger} B_n \tag{H4}$$

Fluctuations of the mn element of H_{Sys} are induced by the operator on the bath coordinates, q_{mn}. For example, the autocorrelation functions for fluctuations of the energies at molecular sites m and n are $\langle q_{mm}(t)q_{mm}(0)\rangle$ and $\langle q_{nn}(t)q_{nn}(0)\rangle$, whereas the cross-correlation function for fluctuations at sites m and n is given by $\langle q_{mm}(t)q_{nn}(0)\rangle$. These three correlation functions are related by the Cauchy-Schwartz inequality

$$\langle q_{mm}(t)q_{nn}(0)\rangle \le \sqrt{\langle q_{mm}(t)q_{mm}(0)\rangle\langle q_{nn}(t)q_{nn}(0)\rangle} \qquad \text{(H5)}$$

A correlation paramter, $-1 \le \eta_{mn} \le 1$, can be introduced to rewrite Eq. (H5) as

$$\langle q_{mm}(t)q_{nn}(0)\rangle = \eta_{mn}\sqrt{\langle q_{mm}(t)q_{mm}(0)\rangle\langle q_{nn}(t)q_{nn}(0)\rangle} \qquad \text{(H6)}$$

where η_{mn} interpolates between the fully anti-correlated, $\eta_{mn} = -1$, and fully correlated, $\eta_{mn} = 1$, limits.

Appendix I. Response Functions in Homogeneous Limit Without Coherence Transfer

This Appendix presents expressions for four terms in the material response function valid in the homogeneous limit of line broadening.[1,11] Feynman diagrams corresponding to these terms are given in Figure 10.3(a). Index g represents the ground electronic state, whereas a, b and c are dummy indices corresponding to all excited state energy levels.

$$ {}^{0}R_1\left(t_1,t_2,t_3\right)=\left(\frac{i}{\hbar}\right)^3\sum_{ab}\mu_{ag}\mu_{gb}\mu_{bg}\mu_{ga}I_{ag}\left(t_1\right)I_{ab}\left(t_2\right)I_{ag}\left(t_3\right) \qquad \text{(I1)} $$

$$ {}^{0}R_1^{*}\left(t_1,t_2,t_3\right)=\left(\frac{i}{\hbar}\right)^3\sum_{abc}\mu_{ga}\mu_{cg}\mu_{bc}\mu_{ab}I_{ga}\left(t_1\right)I_{ca}\left(t_2\right)I_{ba}\left(t_3\right) \qquad \text{(I2)} $$

$$ {}^{0}R_2\left(t_1,t_2,t_3\right)=\left(\frac{i}{\hbar}\right)^3\sum_{ab}\mu_{gb}\mu_{ag}\mu_{bg}\mu_{ga}I_{gb}\left(t_1\right)I_{ab}\left(t_2\right)I_{ag}\left(t_3\right) \qquad \text{(I3)} $$

$$ {}^{0}R_2^{*}\left(t_1,t_2,t_3\right)=\left(\frac{i}{\hbar}\right)^3\sum_{abc}\mu_{cg}\mu_{ga}\mu_{bc}\mu_{ab}I_{cg}\left(t_1\right)I_{ca}\left(t_2\right)I_{ba}\left(t_3\right) \qquad \text{(I4)} $$

where

$$ I_{ab}\left(t\right)=\theta\left(t\right)\exp\left(-\omega_{ab}t-\Gamma_{ab}t\right) \qquad \text{(I5)} $$

Appendix J. Response Functions in Homogeneous Limit With Coherence Transfer

This Appendix presents response functions corresponding to each Feynman diagram in Figure 10.3(b). Index g represents the ground electronic state, whereas a, b, c, d and e are dummy indices running over all excited state energy levels.

$$ {}^{1}R_1(t_1,t_2,t_3) = \left(\frac{i}{\hbar}\right)^3 \sum_{abc} \left\langle \alpha_{bg}\beta_{ga}\gamma_{gb}\phi_{cg} \right\rangle K_{ag,cg}(t_1) I_{cb}(t_2) I_{cg}(t_3) \qquad \text{(J1)} $$

$$ {}^{2}R_1(t_1,t_2,t_3) = \left(\frac{i}{\hbar}\right)^3 \sum_{abc} \left\langle \alpha_{bg}\beta_{ga}\gamma_{gb}\phi_{cg} \right\rangle I_{ag}(t_1) K_{ab,cb}(t_2) I_{cg}(t_3) \qquad \text{(J2)} $$

$$ {}^{3}R_1(t_1,t_2,t_3) = \left(\frac{i}{\hbar}\right)^3 \sum_{abc} \left\langle \alpha_{bg}\beta_{ga}\gamma_{gb}\phi_{cg} \right\rangle I_{ag}(t_1) I_{ab}(t_2) K_{ag,cg}(t_3) \qquad \text{(J3)} $$

$$ {}^{1}R_2^{*}(t_1,t_2,t_3) = \left(\frac{i}{\hbar}\right)^3 \sum_{abcd} \left\langle \alpha_{ag}\beta_{gc}\gamma_{db}\phi_{ba} \right\rangle K_{cg,dg}(t_1) I_{da}(t_2) I_{ba}(t_3) \qquad \text{(J4)} $$

$$ {}^{2}R_2^{*}(t_1,t_2,t_3) = \left(\frac{i}{\hbar}\right)^3 \sum_{abcde} \left\langle \alpha_{ag}\beta_{gc}\gamma_{eb}\phi_{bd} \right\rangle I_{cg}(t_1) K_{ca,ed}(t_2) I_{bd}(t_3) \qquad \text{(J5)} $$

$$ {}^{3}R_2^{*}(t_1,t_2,t_3) = \left(\frac{i}{\hbar}\right)^3 \sum_{abcde} \left\langle \alpha_{ag}\beta_{gc}\gamma_{cb}\phi_{ed} \right\rangle I_{cg}(t_1) I_{ca}(t_2) K_{ba,ed}(t_3) \qquad \text{(J6)} $$

$$ {}^{2}R_2(t_1,t_2,t_3) = \left(\frac{i}{\hbar}\right)^3 \sum_{abc} \left\langle \alpha_{bg}\beta_{ga}\gamma_{gb}\phi_{cg} \right\rangle I_{gb}(t_1) K_{ab,cb}(t_2) I_{cg}(t_3) \qquad \text{(J7)} $$

$$ {}^{3}R_2(t_1,t_2,t_3) = \left(\frac{i}{\hbar}\right)^3 \sum_{abc} \left\langle \alpha_{bg}\beta_{ga}\gamma_{gb}\phi_{cg} \right\rangle I_{gb}(t_1) I_{ab}(t_2) K_{ag,cg}(t_3) \qquad \text{(J8)} $$

$$ {}^{1}R_{1}^{*}\left(t_1,t_2,t_3\right)=\left(\frac{i}{\hbar}\right)^{3}\sum_{abcd}\left\langle \alpha_{cg}\beta_{gd}\gamma_{db}\phi_{ba}\right\rangle K_{gc,ga}\left(t_1\right)I_{da}\left(t_2\right)I_{ba}\left(t_3\right) \qquad \text{(J9)} $$

$$ {}^{2}R_{1}^{*}\left(t_1,t_2,t_3\right)=\left(\frac{i}{\hbar}\right)^{3}\sum_{abcd}\left\langle \alpha_{ag}\beta_{gc}\gamma_{be}\phi_{ed}\right\rangle I_{ga}\left(t_1\right)K_{ca,bd}\left(t_2\right)I_{ed}\left(t_3\right) \qquad \text{(J10)} $$

$$ {}^{3}R_{1}^{*}\left(t_1,t_2,t_3\right)=\left(\frac{i}{\hbar}\right)^{3}\sum_{abcde}\left\langle \alpha_{ag}\beta_{gc}\gamma_{cd}\phi_{be}\right\rangle I_{ga}\left(t_1\right)I_{ca}\left(t_2\right)K_{da,be}\left(t_3\right) \qquad \text{(J11)} $$

where $K_{ab,cd}\left(t\right)$ and $\Phi_{ab,cd}$ are given by Eqs. (10.17) and (10.18), respectively.

Appendix K. Total Response Function

This appendix presents the total nonlinear response function used to compute signals by numerical integration of Eq. (10.2). The use of dummy indices allows application to arbitrary systems (e.g. the model system of Figure 10.4(b)). Only resonant terms survive integration of Eq. (10.2).

$$R_1(t_1,t_2,t_3)=\left(\frac{i}{\hbar}\right)^3\sum_{ab}\left\langle\alpha_{bg}\beta_{ga}\gamma_{gb}\phi_{ag}\right\rangle\left\{J_{ag}(t_1)I_{ab}(t_2)I_{ag}(t_3)+I_{ag}(t_1)J_{ab}(t_2)I_{ag}(t_3)\right.$$
$$\left.+I_{ag}(t_1)I_{ab}(t_2)J_{ag}(t_3)\right\}+{}^1R_1(t_1,t_2,t_3)+{}^2R_1(t_1,t_2,t_3)+{}^3R_1(t_1,t_2,t_3) \quad \text{(K1)}$$

$$R_2^*(t_1,t_2,t_3)=\left(\frac{i}{\hbar}\right)^3\sum_{abc}\left\langle\alpha_{ag}\beta_{gc}\gamma_{cb}\phi_{ba}\right\rangle\left\{J_{cg}(t_1)I_{ca}(t_2)I_{ba}(t_3)+I_{cg}(t_1)J_{ca}(t_2)I_{ba}(t_3)\right.$$
$$\left.+I_{cg}(t_1)I_{ca}(t_2)J_{ba}(t_3)\right\}+{}^1R_2^*(t_1,t_2,t_3)+{}^2R_2^*(t_1,t_2,t_3)+{}^3R_2^*(t_1,t_2,t_3) \quad \text{(K2)}$$

$$R_2(t_1,t_2,t_3)=\left(\frac{i}{\hbar}\right)^3\sum_{ab}\left\langle\alpha_{bg}\beta_{ga}\gamma_{gb}\phi_{ag}\right\rangle\left\{J_{gb}(t_1)I_{ab}(t_2)I_{ag}(t_3)+I_{gb}(t_1)J_{ab}(t_2)I_{ag}(t_3)\right.$$
$$\left.+I_{gb}(t_1)I_{ab}(t_2)J_{ag}(t_3)\right\}+{}^1R_2(t_1,t_2,t_3)+{}^2R_2(t_1,t_2,t_3)+{}^3R_2(t_1,t_2,t_3) \quad \text{(K3)}$$

$$R_1^*(t_1,t_2,t_3)=\left(\frac{i}{\hbar}\right)^3\sum_{abc}\left\langle\alpha_{ag}\beta_{gc}\gamma_{cb}\phi_{ba}\right\rangle\left\{J_{ga}(t_1)I_{ca}(t_2)I_{ba}(t_3)+I_{ga}(t_1)J_{ca}(t_2)I_{ba}(t_3)\right.$$
$$\left.+I_{ga}(t_1)I_{ca}(t_2)J_{ba}(t_3)\right\}+{}^1R_1^*(t_1,t_2,t_3)+{}^2R_1^*(t_1,t_2,t_3)+{}^3R_1^*(t_1,t_2,t_3) \quad \text{(K4)}$$

where

$$J_{ab}(t)=I_{ab}(t)\exp(-\chi_{ab}t) \quad \text{(K5)}$$

and

$$\chi_{ab}=\sum_{cd}\kappa_{ab,cd}\Phi_{ab,cd} \quad \text{(K6)}$$

Appendix L. Calculating Linear Absorption Spectra With Coherence Transfer

The linear absorption spectra, $\varepsilon(\omega)$, in Figures 10.4, 10.5 and 10.13 are calculated with

$$\varepsilon(\omega) = \sum_a \left|\mu_{ag}\right|^2 \mathrm{Re}\int_0^\infty dt \exp\left[i\left(\omega-\omega_{ag}\right)t - \Gamma_{ag}t - \chi_{ag}t\right] \tag{L1}$$

where χ_{ag} is given by Eq. (K6).

REFERENCES

(1) Abramavicius, D.; Mukamel, S. *Chem. Rev.* 2004, *104*, 2073.

(2) Womick, J. M.; Moran, A. M. *J. Phys. Chem. B* 2009, *113*, 15747.

(3) Hochstrasser, R. M. *Chem. Phys.* 2001, *266*, 273.

(4) Dreyer, J.; Moran, A. M.; Mukamel, S. *Bull. Korean Chem. Soc.* 2003, *24*, 1091.

(5) Zhang, J. M.; Zhao, F. L.; Zheng, X. G.; Wang, H. Z.; Yang, T.-S.; Hayashi, M.; Lin, S. H. *J. Photochem. Photobiol. B: Biol.* 1999, *53*, 128.

(6) Debreczeny, M. P.; Sauer, K.; Zhou, J.; Bryant, D. A. *J. Phys. Chem.* 1995, *99*, 8412.

(7) Debreczeny, M. P.; Sauer, K.; Zhou, J.; Bryant, D. A. *J. Phys. Chem.* 1995, *99*, 8420.

(8) Riter, R. E.; Edington, M. D.; Beck, W. F. *J. Phys. Chem. B*` 1997, *101*, 2366.

(9) Abramavicius, D.; Palmieri, B.; Voronine, D. V.; Sanda, F.; Mukamel, S. *Chem. Rev.* 2009, *109*, 2350.

(10) Cho, M. *Chem. Rev.* 2008, *108*, 1331.

(11) Mukamel, S. *Principles of Nonlinear Optical Spectroscopy*; Oxford University Press: New York, 1995.

(12) Womick, J. M.; Moran, A. M. *J. Phys. Chem. B* 2009, *113*, 15771.

(13) Womick, J. M.; Miller, S. A.; Moran, A. M. *J. Chem. Phys.* 2010, *133*, 024507.

(14) Homoelle, B. J.; Edington, M. D.; Diffey, W. M.; Beck, W. F. *J. Phys. Chem. B* 1998, *102*, 3044.

(15) Szalontai, B.; Gombos, Z.; Csizmadia, V.; Csatorday, K.; Lutz, M. *Biochemistry* 1989, *28*, 6467.

(16) Szalontai, B.; Gombos, Z.; Csizmadia, V.; Bagyinka, C.; Lutz, M. *Biochemistry* 1994, *33*, 11823.

(17) Andel III, F.; Murphy, J. T.; Haas, J. A.; McDowell, M. T.; van der Hoef, I.; Lugtenburg, J.; Lagarias, J. C.; Mathies, R. A. *Biochemistry* 2000, *39*, 2667.

(18) Venkatramani, R.; Mukamel, S. *J. Chem. Phys.* 2002, *117*, 11089.